FILM MODELS FOR TRANSPORT PHENOMENA WITH FOG FORMATION

with application to plastic heat exchangers and condensers

PROEFSCHRIFT

ter verkrijging van de graad van doctor
aan de Technische Universiteit Eindhoven,
op gezag van de Rector Magnificus,
prof.ir. M. Tels, voor een commissie
aangewezen door het College van Dekanen,
in het openbaar te verdedigen op
vrijdag 7 september 1990 te 14.00 uur

door

HENRICUS JOZEF HUBERTUS BROUWERS

geboren op 6 juni 1963 te Maastricht

Dit proefschrift is goedgekeurd door de promotoren:

prof.dr. A.K. Chesters

prof.dr.ir. J. Berghmans (Katholieke Universiteit van Leuven)

Aan mijn ouders

Mijn erkentelijkheid gaat uit naar het direktorium van Akzo Research Laboratories Arnhem voor de toestemming tot publikatie van dit onderzoek. Veel dank ben ik verschuldigd aan ir. G. Vegt en ir. H.P. Korstanje voor de gelegenheid die zij mij hebben geboden in het kader van mijn werkzaamheden te promoveren. De plezierige samenwerking met mijn collega's binnen het laboratorium, met name met de Hr. J.H. van de Straat, de Hr. E. Heuveling en de Hr. D.A. Klarenberg van de warmtewisselaars-groep, heb ik steeds bijzonder op prijs gesteld.

De discussies met prof.dr. A.K. Chesters hebben veel bijgedragen aan het totstandkomen van dit proefschrift.

Grote waardering heb ik voor de prettige samenwerking met dr. C.W.M. van der Geld, ing. J.M.W.M. Schoonen, de Hr. F.A. Filippini (medewerkers van de vakgroep WOC), ing. H. van Vredendaal (afstudeerder TUE), Stan Beekmans (stagiaire HTS Eindhoven) en Paul Maclean (trainee University of Strathclyde) bij het bouwen van een meetopstelling en het uitvoeren van metingen aan een kunststof warmtewisselaar bij de faculteit Werktuigbouwkunde van de Technische Universiteit Eindhoven.

ERRATA

1. p. 44, eq. (1.55), for "$\frac{1}{3}$" read "$-\frac{1}{3}$".
2. p. 45, eq. (1.56), for "0.764" read "0.1685" (= 0.764/4).
3. p. 47, 2nd par., 4th line, for "saturation" read "supersaturation".
4. p. 47, 2nd par., 6th line, for "saturation" read "supersaturation".
5. p. 83, eq. (2.59), for "$(t_i - t)$" read "$(t_i - \bar{t})$".
6. p. 84, fig. 2.4, for "$\Theta_{c,f3}$" read "$\Theta_{c,f2}$".
7. p. 85, 1st par., 1st line, for "equations (2.60)" read "equation (2.60)".
8. p. 87, 2nd par., 3rd line, for "saturation model" read "supersaturation model".
9. p. 95, 1st par., 1st line, for "a undisturbed" read "an undisturbed".
10. p. 97, 3rd par., 2nd line, for "(3.14) and (3.18)" read "(3.14), (3.17) and (3.18)".
11. p. 103, eq. (3.34), for "$(t - \bar{t}_{in})$" read "$(\bar{t} - t_{in})$".
12. p. 112, table 3.3, for "0.0144" read "0.0147" and for "0.00003" read "0.0003".
13. p. 112, 3rd par., 2nd line, for "$\alpha = 2485.938$, $\beta = 48.745$ and $\gamma = 6825.112$" read "$\alpha = 48.75$, $\beta = 6825.7$ and $\gamma = 5.144$".
14. p. 113, 2nd par., 8th line, for "convective mass" read "convective heat and mass".
15. p. 119, 2nd par., 1st line, for "have applied" read "have been applied".
16. p. 130, fig. 4.3, for "$\bar{c}(X+dX, Z) := \bar{c}(Z, Z)$" read "$\bar{c}(X+dX, Z) := \bar{c}(X, Z)$".
17. p. 143, 2nd par., 2nd line, for "Mizushina" read "Mizushina *et al.*".
18. p. 144, fig. 4.6, for "$w_g(X+dX, Z) := w_g(Z, Z)$" read "$w_g(X+dX, Z) := w_g(X, Z)$".
19. p. 145, eq. (4.52), for "$2LB\dot{m}$" read "$-2LB\dot{m}$".
20. p. 159, 1st par., 1st line, for "global" read "overall".
21. p. 194, 3rd par., 2nd line, for "have to" read "have to be".
22. p. 197, 3rd par., 11th line, for "Two" read "Three".
23. p. 239, 1st par., 5th line, for "c_a" read "c_a^+" (twice).
24. p. 246, 3rd par., 1st line, for "bulk" read "film".
25. p. 259, 1st par., 1st line, for "does depart" read "does not depart".
26. p. 261, 8th line, for "cross–sectional" read "cross–sectional area"
27. p. 262, 26th line, for "equation (5.46)" read "equation (4.56)".

CONTENTS

page

GENERAL INTRODUCTION 11

1. THE CLASSICAL FILM MODEL

§1.1 Introduction 15
§1.2 The film equations and their solutions 17
§1.3 Correction factors for the effect of the induced velocity 21
§1.4 Application of the film model to channel flow 26
§1.5 Relation between c and t in the film and the path of $\bar{c}$ and $\bar{t}$ 38
§1.6 Laminar flow 42
§1.7 Concluding remarks 45

2. THE FOG FILM MODEL

§2.1 Introduction 47
§2.2 Film analysis 49
§2.3 Results of numerical solution 59
§2.4 Asymptotic approximation solution 66
§2.5 Results of asymptotic solution 72
§2.6 Application of the fog film model to channel flow 74
§2.7 The effect of fog and induced velocity on nickel evaporation into helium 81
§2.8 Conclusions 85

3. THE COMPOUND FOG FILM MODEL

§3.1 Introduction 87

§3.2 Asymptotic analysis of the film for a negligible induced velocity (NIV) 88

§3.3 Application of the NIV fog film model to channel flow 97

§3.4 Results of NIV fog film model and introduction of compound fog film model 106

§3.5 Comparison of the fog film model with convective models and experiments 111

§3.6 Conclusions 118

4. HEAT AND MASS TRANSFER IN CROSSFLOW PLASTIC HEAT EXCHANGERS

§4.1 Introduction 121

§4.2 Heat transfer without condensation 122

§4.3 Partial water–vapour condensation 129

§4.4 Pure steam condensation 142

§4.5 Computational results 147

§4.6 Experiments 156

§4.7 Concluding remarks 162

5. FILM CONDENSATION OF A PURE VAPOUR ON NON–ISOTHERMAL VERTICAL PLATES

§5.1 Introduction 165

§5.2 Formulation of basic equations 166

§5.3 Solutions in closed form 175

§5.4 Numerical evaluation 184

§5.5 Asymptotic analysis and approximation solution 188

§5.6 Experiments 192

§5.7 Conclusions 200

APPENDIX A: BASIC EQUATIONS OF THE FILM 203

APPENDIX B: THE LOCATION OF G(t) WITH RESPECT TO F(t) 209

APPENDIX C: THE SATURATION LINE 217

APPENDIX D: TRUNCATION ERROR ANALYSIS 223

APPENDIX E: WATER CONDENSATION ON PLASTIC CHANNEL PLATES 225

APPENDIX F: THE IMPROVED TANGENCY CONDITION 233

APPENDIX G: EXPERIMENTAL DATA OF PLASTIC HEAT EXCHANGER 249

APPENDIX H: UNCERTAINTY ANALYSIS 257

SYMBOLS 261

REFERENCES 265

SUMMARY 277

SAMENVATTING 281

CURRICULUM VITAE 285

GENERAL INTRODUCTION

The present research was dictated by the need to develop a numerical model of plastic gas–liquid compact heat exchangers, as depicted in figure 1. These crossflow heat exchangers have been developed at Akzo's research institute and are made entirely from polyvinylidene fluoride (PVDF) or polypropylene (PP). The heat exchangers consist of plates containing small channels and hence possess only primary, or direct, heat transfer surfaces.

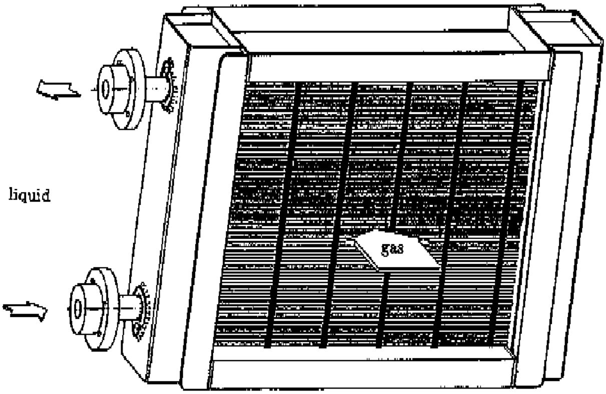

Figure 1 The plastic heat exchanger.

The use of plastic as material permits the heat exchangers to be used for heat recovery from, sometimes corrosive, process gases. Condensable components in the gas, such as water–vapour, sulphur oxides and nitrogen oxides, may form condensate films along the corrosion–resistant walls. The maximum operational temperatures of the PP and PVDF heat exchangers –when properly cooled– are limited to 100°C and 200°C respectively.

As the costs of the heat exchangers are directly related to the heat exchanging surface area, there is a need to determine the required heat transfer surface as accurately as possible. The rating of a heat exchanger is adapted to the specific process requirements of the customer. As such dimensioning is preferably performed on the customer's premises, the calculation should be executable on a personal computer (PC). Yet, the modelling should be based on reliable expressions for heat and mass transfer, taking into account the special features of plastic heat exchangers.

The gas and liquid flows entering the heat exchanger spread approximately equally over the various channels of the heat exchanger. This allows the analysis to be limited to the consideration of one plate. Both of the flows involved are laminar under standard operating conditions, their Reynolds number being in the range $200 < \mathrm{Re} < 2000$. A glance at figure 1 reveals that the transfer between the fluids is a three–dimensional process; the physical properties vary in the direction of both fluids flows and also across the channels. However, employing the mean mixed values (*i.e.* the values that would result after mixing of the flow across a channel) of temperatures and water–vapour mass fraction, the modelling problem becomes two–dimensional. For the simplest case, heat transfer without condensation on the gas side, this approach results in a set of differential equations whose solution is well documented in the literature.

In the case of partial vapour condensation the temperature of condensate–gas interface is not known explicitly, and is furthermore non–uniform. For pure vapour condensation this temperature is known, being equal to the saturation temperature of the vapour, but here the vapour mass flux to the condensate is unknown. In both cases however, the unknown quantity follows from a local energy balance of heat fluxes to and from the condensate surface. A second complication when condensation occurs is that the heat and mass transfer on the gas side is enhanced by the transport of vapour (corresponding, effectively, to "suction" through a porous boundary). In this thesis the classical film model is adopted to account for this effect, since it provides local correction factors for the transfer rates and simple first order differential equations for the decrement in temperature, mass flow and pressure in a closed channel. In the past this one–dimensional model, which neglects convective and diffusive transport in the direction of flow, has proven satisfactory in many practical applications. In chapter 1 the model is reviewed and extended to include the effect of mass transfer on pressure drop. Some of the resulting pressure drop predictions are compared with results, both theoretical and experimental, of previous investigators.

Exploratory computations of heat transfer from mixtures of non–condensables and water–vapour reveal that the mixed mean water–vapour fraction and temperature of the gas mixture may correspond to supersaturation, so that fog is likely to be formed in the gas flow. Fog formation alters heat and mass transfer rates from gas to wall and hence the performance of the heat exchanger. Moreover, the occurrence and rate of fog formation is of utmost importance. In processes aimed solely at heat recovery it is an undesired phenomenon since the formed droplets represent a yield loss and are difficult to remove. For gas washing applications however, both the droplets and condensate films are very well suited to absorb toxic and/or corrosive gas components (implying that the heat exchanger should be used in combination with a fog removal device).

In chapter 2 therefore the film model is extended to include possible fog formation, assuming no supersaturation to be possible, the so–called saturation condition. This chapter yields new expressions and procedures, accounting for the combined effects of fog formation and suction/injection, for the dimensioning of heat exchanging devices, such as condensers and evaporators. In chapter 3, on the basis of an alternative approach, similar, but far simpler results are achieved. In both chapters the suggested film model approach for fog formation is compared with theoretical and practical results of previous investigators.

In chapter 4 the fog film model is applied to actual water–vapour air mixtures and water flowing through the plastic heat exchanger, and assessed against performed measurements. Both the fog film models of chapter 2 and 3 are applied and their results compared mutually, and with predictions of the conventional film model of chapter 1. A special feature of water–vapour condensation on plastic channel plates is employed in the condensation model, namely a negligible temperature variation across the condensate film. This feature of the process reduces the complexity of the physical model substantially since condensate production and flow are decoupled from transfer processes on the gas side. It also implies that the models are invariant with respect to the orientation of the heat exchanger to the vertical.

For pure vapours other than water however, the simplification of an isothermal film does not apply. This complication is considered in chapter 5, where the condensation of pure vapour and its interaction with condensate, channel plates, and orientation to the vertical is analyzed in detail. One of the results of this study, which is in fact an extension of isothermal "Nusselt" plate condensation to non–isothermal plates, is the recognition of two governing non–dimensional numbers. The theoretical predictions are compared with performed experiments for a broad range of values of both non–dimensional numbers.

1. THE CLASSICAL FILM MODEL

§1.1 Introduction

For large mass transfer rates heat and diffusional mass transfer, as well as exerted friction, from a fluid to a wall are influenced by the extra flow due to the mass transfer (corresponding, effectively, to suction or injection). In the past corrections for this influence have been derived from three approximate theories or models: the boundary layer model, the penetration model, and the film model. Reviews of these models are found in Bird *et al.* (1960) and Sherwood *et al.* (1975). The film model is physically the most simple description of the effect of the additional induced velocity, traditionally referred to as "convective velocity", "bulk velocity" or "Stefan flow". The model idealizes the transition between the fluid properties and those at the wall as occurring entirely within a thin film next to the wall. In this film, the influence of convection parallel to the wall is furthermore neglected.

Though the correction factors supplied by the film model are based on a simple physical model, they are widely used in engineering applications, *e.g.* by Perry and Green (1984) or V.D.I. (1988). This is due to the fact that the physical accuracy of the correction factors is generally sufficiently high for engineering end purposes, and they are easily applicable.

Stefan (1873) was the first to study, experimentally and theoretically, the diffusional mass transfer in a stagnant film, including the induced velocity. Ackermann (1937) examined the effect of this induced velocity on both heat and mass transfer in a film. Colburn and Drew (1937) independently did the same, and applied the film model to the case of closed channel flow. Mickley *et al.* (1954) derived the three now well–known film model correction factors for mass, heat and momentum transfer, which can be applied to any process of importance. Additionally, they compared the predictions of the film model with those of the boundary layer model, performed experiments, and found satisfying agreement. However, they did not consider the flow of a mixture through a confined space, such as a channel.

As a complete review of the film model –to the author's knowledge– is absent, and in this thesis the model will be employed and extended to include the effect of fog formation, the model is discussed in this chapter in some detail. The three film model correction factors are derived for a binary mixture, consisting of a vapour and inert gases. Subsequently, the correction factors are applied to the flow through a channel, resulting in expressions for the temperature and vapour mass fraction drop. Furthermore, on the basis of the film model correction factor for friction and an incremental momentum balance, a compact equation is derived predicting the pressure drop in a channel in the presence of the induced velocity. This equation, which is derived here in this form for the first time, will extensively be compared with results of several previous investigators. The formation of fog in a film and in a flowing mixture is visualized in a plot, depicting the relation between temperature and vapour mass fraction in the film and path of the mean mixed values with respect to the saturation line. A typical feature of the film model with respect to the laminar flow regime, namely identical thermal and diffusional film thicknesses, is discussed in the last but one paragraph.

As said, in this chapter the film model of a binary mixture is studied. In the past the results of this model have also fruitfully been used to describe the transfer in multicomponent mixtures. The diffusion of each component is then analyzed independently, thus considered as "non–interactive", from all other components. However, Cussler (1976), Webb *et al.* (1981) and Webb and Sardesai (1981) examined for which exceptional circumstances diffusional interactions among the diffusing components become relevant. For these rare cases a more complicated "interactive" model as derived by Krishna and Standart (1976) is needed. The film model expressions based on the analysis of a binary mixture are then no longer accurate enough.

§1.2 The film equations and their solutions

In this section the equations describing heat, mass and momentum transfer in a film of a binary mixture, wherein there is an induced velocity caused by diffusion, are derived and solved analytically. The solutions are employed in the next section to define the film model correction factors.

Mass transfer

Consider a film containing non–condensable gases and a vapour, as depicted in figure 1.1, through which there is a transfer of heat, mass and momentum in the y–direction, with flow parallel to the wall in the x–direction.

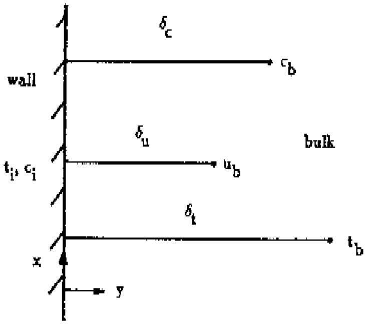

Figure 1.1 The film.

At the "wall" (y=0), *e.g.* denoting the surface of a liquid film, the vapour mass fraction is c_i and the temperature t_i. At a distance δ_c the bulk vapour mass fraction, c_b, is attained, at a distance δ_t the bulk temperature, t_b, and at a distance δ_u the bulk velocity relative to the wall, u_b. For the purposes of the present analysis the physical properties in the film are assumed to be constant and the mixture to behave as an ideal, incompressible, and Newtonian gas.

The full Fickian diffusion equation, *e.g.* see Merk (1957), without source terms reads:

$$\rho \left(\frac{\partial c}{\partial \Upsilon} + u \frac{\partial c}{\partial x} + v \frac{\partial c}{\partial y}\right) = \rho \mathbb{D} \left(\frac{\partial^2 c}{\partial x^2} + \frac{\partial^2 c}{\partial y^2}\right) \quad . \tag{1.1}$$

Attention is restricted here to steady situations, for which therefore the first term, $\partial c / \partial \Upsilon$, is identically zero. In many cases the variation of c (and t and u) is small enough for the terms involving $\partial / \partial x$ to be neglected as well; in this way the "film model" is obtained, for which equation (1.1) reduces to:

$$\rho v \frac{dc}{dy} = \rho \mathbb{D} \frac{d^2 c}{dy^2} \quad . \tag{1.2}$$

In equation (1.2) the convective velocity v is caused by diffusion of vapour through the mixture, and is derived in appendix A as:

$$v = - \frac{\mathbb{D}}{1 - c} \frac{dc}{dy} \quad . \tag{1.3}$$

When this velocity is substituted into equation (1.2), an ordinary differential equation of c in y is obtained. The boundary conditions on c read:

$$c(y = 0) = c_i \quad , \tag{1.4}$$

and:

$$c(y = \delta_c) = c_b \quad . \tag{1.5}$$

Combining and solving equations (1.2) and (1.3), and applying boundary conditions (1.4) and (1.5), yields the distribution of the vapour fraction in the film as a function of y:

$$c(y) = 1 - (1 - c_i)\, e^{\frac{y}{\delta_c} Ln\left[\frac{1 - c_b}{1 - c_i}\right]} \quad . \tag{1.6}$$

Heat transfer

In order to investigate the effect of the induced velocity on heat transfer, attention is now focussed on the energy equation of the film. Again neglecting variations of t in the x–direction, for the film this equation is derived in appendix A as:

$$\rho c_{p,v} v \frac{dt}{dy} = k \frac{d^2t}{dy^2} \quad , \tag{1.7}$$

with as boundary conditions on t:

$$t(y = 0) = t_i \quad , \tag{1.8}$$

$$t(y = \delta_t) = t_b \quad . \tag{1.9}$$

Substitution of equations (1.3) and (1.6) into equation (1.7), solution of the resulting equation, and application of boundary conditions (1.8) and (1.9) now produces as temperature profile in the film:

$$t(y) = (t_b - t_i) \left[\frac{e^{\frac{y}{\mathrm{Le}_v \delta_c} Ln\left(\frac{1 - c_b}{1 - c_i}\right)} - 1}{e^{\frac{\delta_t}{\mathrm{Le}_v \delta_c} Ln\left(\frac{1 - c_b}{1 - c_i}\right)} - 1} \right] + t_i \quad , \tag{1.10}$$

where Le_v denotes the modified Lewis number.

Momentum transfer

To examine the influence of the induced velocity on the wall shear stress, the momentum equation for the x–direction is investigated. Again neglecting gradients of properties in the x–direction, as well as volume forces, this equation reads:

$$\rho v \frac{du}{dy} = \eta \frac{d^2u}{dy^2} \quad , \tag{1.11}$$

with appropriate boundary conditions on u at the wall and bulk:

$$u(y = 0) = 0 \quad , \tag{1.12}$$

$$u(y = \delta_u) = u_b \quad . \tag{1.13}$$

Substituting equations (1.3) and (1.6) in equation (1.11), solving the resulting equation and applying boundary conditions (1.12) and (1.13) results in:

$$u(y) = u_b \left[\frac{e^{\frac{y}{\mathrm{Sc}\,\delta_c} Ln\left[\frac{1 - c_b}{1 - c_i}\right]} - 1}{e^{\frac{\delta_u}{\mathrm{Sc}\,\delta_c} Ln\left[\frac{1 - c_b}{1 - c_i}\right]} - 1} \right] . \tag{1.14}$$

In this equation the Schmidt number Sc has been introduced.

In this paragraph the vapour concentration, temperature and velocity profiles in the film have been derived, represented by equations (1.6), (1.10) and (1.14), respectively. On the basis of these solutions correction factors are arrived at in the next section.

§1.3 Correction factors for the effect of the induced velocity

In this section the classical film model correction factors are introduced by comparing the transfer rates in the binary film with and without induced velocity.

Mass transfer

The mass transfer from the fluid to the wall is governed by Fick's law:

$$\dot{m} \equiv - \rho\, v(y = 0) = \frac{\rho D}{1 - c} \left.\frac{dc}{dy}\right|_{y=0} . \tag{1.15}$$

Without taking account of the induced velocity, the mass transfer is simply described by:

$$\dot{m} = g_m \frac{c_b - c_i}{1 - c_i} , \tag{1.16}$$

because without induced velocity the profile of c (and t and u) as a function of y is a straight line (the limiting cases of equation (1.6), (1.10) and (1.14) for small c). Equation (1.16) indicates that the mass flux is small for $c_b << 1$ and $c_i << 1$, that is to say, dilute vapour mixtures. Equation (1.16) provides the reference level, which must now be corrected for the effect of an appreciable induced velocity. In equation (1.16) the transfer coefficient of mass is given by:

$$g_m = \frac{\rho\mathfrak{D}}{\delta_c} \quad . \tag{1.17}$$

To derive the diffusional transport of mass from the mixture to the wall, equations (1.15) and (1.17) are applied to equation (1.6):

$$\dot{m} = -\, g_m \, Ln\left[\frac{1 - c_b}{1 - c_i}\right] \quad . \tag{1.18}$$

This logarithmic expression for the diffusional mass flux is the original result of Stefan (1873). The film model correction factor is now introduced by comparing the expression for the transfer rate with induced velocity with that without. That is to say, on a comparison of equation (1.18) with equation (1.16), the classical film model correction factor is derived:

$$\Theta_c = \frac{-\,\phi_c}{e^{-\,\phi_c} - 1} \quad , \tag{1.19}$$

with as diffusional dimensionless mass flux in equation (1.19):

$$\phi_c = \frac{\dot{m}}{g_m} \quad , \tag{1.20}$$

where $\dot{m}$ follows from equation (1.18).

Heat transfer

The heat transfer from the fluid to the wall is described by Fourier's law as:

$$q = k \left. \frac{dt}{dy} \right|_{y=0} \quad . \tag{1.21}$$

For a negligible induced velocity the transferred heat through the film is simply given by:

$$q = h_g \left(t_b - t_i \right) \quad , \tag{1.22}$$

which serves as reference level for the effect of the induced velocity on heat transfer. The heat transfer coefficient in equation (1.22) is defined as:

$$h_g = \frac{k}{\delta_t} \quad . \tag{1.23}$$

The heat transfer from fluid to wall is obtained by combining equations (1.10), (1.18), (1.21) and (1.23):

$$q = h_g \left(t_b - t_i \right) \left[\frac{- \frac{\dot{m} c_{p,v}}{h_g}}{e^{- \frac{\dot{m} c_{p,v}}{h_g}} - 1} \right] \quad . \tag{1.24}$$

On a comparison of equation (1.24) with equation (1.22) the following film model correction factor is derived:

$$\Theta_t = \frac{-\phi_t}{e^{-\phi_t} - 1} , \tag{1.25}$$

with as thermal dimensionless mass flux in equation (1.25):

$$\phi_t = \frac{\dot{m} c_{p,v}}{h_g} . \tag{1.26}$$

The thermal correction factor (1.25) is commonly referred to as Ackermann correction factor.

Momentum transfer

The exerted shear stress by the fluid on the wall is governed by Newton's law as:

$$\tau = \eta \left. \frac{du}{dy} \right|_{y=0} . \tag{1.27}$$

Without mass transfer the shear stress is described by:

$$\tau = \tfrac{1}{2} \rho \, f \, u_b^2 , \tag{1.28}$$

with as friction coefficient defined:

$$f = \frac{2\eta}{\rho u_b \delta_u} . \tag{1.29}$$

This friction factor is usually called Fanning friction factor. The interfacial shear stress exerted by the fluid on the wall is determined with equations (1.14), (1.18), (1.27) and (1.29):

$$\tau = \tfrac{1}{2}\,\rho\,\mathrm{f}\,\mathrm{u}_\mathrm{b}^2 \left[\frac{-\dfrac{2\dot{\mathrm{m}}}{\rho\mathrm{f}\,\mathrm{u}_\mathrm{b}}}{e^{-\dfrac{2\dot{\mathrm{m}}}{\rho\mathrm{f}\,\mathrm{u}_\mathrm{b}}} - 1} \right] \quad . \tag{1.30}$$

On a comparison of equation (1.30) with equation (1.28) the film model correction factor for momentum transfer is obtained:

$$\Theta_\mathrm{u} = \frac{-\,\phi_\mathrm{u}}{e^{-\,\phi_\mathrm{u}} - 1} \quad , \tag{1.31}$$

with as frictional dimensionless mass flux in equation (1.31):

$$\phi_\mathrm{u} = \frac{2\dot{\mathrm{m}}}{\rho\mathrm{f}\,\mathrm{u}_\mathrm{b}} \quad . \tag{1.32}$$

The correction factor (1.31) for interfacial shear stress was first derived by Mickley *et al.* (1954).

For condensation problems, $c_b > c_i$ and thus $\dot{m} > 0$, the correction factors (1.19), (1.25) and (1.31) are larger than unity. On the other hand, for wall evaporation, $c_b < c_i$ and $\dot{m} < 0$, the correction factors are smaller than unity. For small mass transfer rates, $\dot{m} \simeq 0$ or $(c_b \; c_i)/(1 - c_i) \simeq 0$, the correction factors tend asymptotically to unity. Or in other words, the induced velocity plays no role of importance and consequently, uncorrected heat transfer, mass transfer and friction predictions will suffice.

The diffusional mass flux $\dot{m}$ in equations (1.20), (1.26) and (1.32) is taken from equation (1.18). For injection or suction problems with an imposed mass flux, this mass flux can be substituted in these equations to determine the three film model correction factors. Thus, identical correction factors follow from the film model equations with a constant imposed mass flux in the film which, like the diffusionally induced mass flux, is independent of y; this can be verified by considering equation (A.4).

Mizushina *et al.* (1978) among others, successfully employed the thermal correction factor in describing the heat transfer of a pure superheated vapour in the presence of a condensation mass flux. Surface injection and suction in tubes with porous walls have been the subject of numerous experiments and calculations. In the recent article of Wang and Tu (1988) results of these efforts have been found in good agreement with the film model correction factors for friction and mass transfer. Summarizing, though the film model correction factors are here derived on the basis of a diffusional mass flux, they can be derived from and applied to imposed suction and injection as well. For this reason in what follows the terms "suction" and "injection" will be used to indicate situations involving respectively mass transfer to and from a wall, even if this mass transfer is due to condensation or evaporation.

§1.4 Application of the film model to channel flow

In the previous section correction factors have been introduced to account for the effect of the induced velocity on mass and heat transfer and on shear stress. In this section the practical use and application of these factors in incompressible convective channel flow is demonstrated. The approach is based on the global conservation laws of mass, energy and momentum and is applicable to any cross–sectional channel shape and geometry.

Mass balance

The gas mixture flows through the channel in the x–direction. Between the mixture and the wall of the channel there exists a transfer of mass, heat and momentum. The mean mixed values of vapour mass fraction and temperature in a cross–section (*i.e.* the values that would result after mixing of a cross–section), are denoted by $\bar{c}$ and $\bar{t}$, respectively.

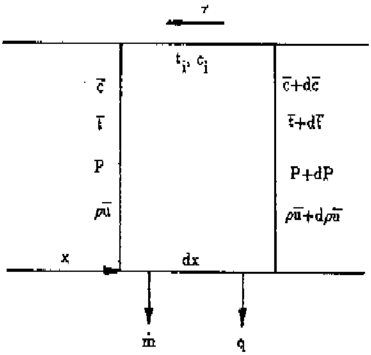

Figure 1.2 The channel.

A differential mass balance for an element dx, as shown schematically in figure 1.2, yields:

$$\frac{d(\rho\bar{u})}{dx} = -\frac{4}{D_h}\dot{m} = -\frac{4}{D_h} g_m \Theta_c \frac{\bar{c}-c_i}{1-c_i} \quad . \qquad (1.33)$$

In this equation the hydraulic diameter D_h is defined as four times the cross–sectional area divided by the perimeter of the channel and $\bar{u}$ is the mixture's mean velocity. The mass transfer coefficient is given by equation (1.17), in which is substituted:

$$\delta_c = \frac{D_h}{Sh} \quad , \tag{1.34}$$

where Sh represents the local convective flow Sherwood number for low mass transfer rates, pertaining to the considered channel geometry. The implicit assumption is thus made that δ_c is not itself a significant function of the mass transfer rates. Moreover, as first order approximation in the film model correction factors c_b (and u_b) is replaced by $\bar{c}$ (and $\bar{u}$), and the film thickness δ_c is approximated by equation (1.34).

For a binary mixture, the change in mass flow through the channel is related to the vapour mass fraction by:

$$(\rho\bar{u})(x)\,(1-\bar{c}(x)) = (\rho\bar{u})(x{=}0)\,(1-\bar{c}(x{=}0)) \quad . \tag{1.35}$$

Equation (1.33) then yields:

$$\frac{d\bar{c}}{dx} = \frac{-\,4g_m}{D_h(\rho\bar{u})\,(x{=}0)}\,\Theta_c\,\frac{\bar{c}-c_i}{1-c_i}\,\frac{(1-\bar{c})^2}{(1-\bar{c}(x{=}0))} \quad . \tag{1.36}$$

Equation (1.35) prescribes mathematically the mass conservation of the inert components entering and flowing through the channel. Equation (1.36), with application of equations (1.18)–(1.20), is rewritten as:

$$\frac{d\bar{c}}{dx} = \frac{4g_m}{D_h(\rho\bar{u})(x{=}0)}\,Ln\left[\frac{1-\bar{c}}{1-c_i}\right]\frac{(1-\bar{c})^2}{(1-\bar{c}(x{=}0))} \quad . \tag{1.37}$$

Energy balance

The change of the mean mixed bulk temperature $\bar{t}$ of the mixture flowing through the channel is obtained by employing an incremental energy balance, see figure 1.2:

$$\frac{d\bar{t}}{dx}\,\rho\bar{u}(x)\,\frac{D_h}{4}\,c_p - \dot{m}\,(\bar{t}-t_i)\,c_{p,v} = -q = -h_g\,\Theta_t\,(\bar{t}-t_i) \quad . \tag{1.38}$$

Equation (1.38) is, with equations (1.26) and (1.35), rewritten for a binary mixture as:

$$\frac{d\bar{t}}{dx} = \frac{-4h_g}{c_p D_h (\rho\bar{u})(x{=}0)}\,(\Theta_t - \phi_t)\,(\bar{t}-t_i)\,\frac{(1-\bar{c})}{(1-\bar{c}(x{=}0))} \quad . \tag{1.39}$$

In equations (1.26), (1.38) and (1.39) h_g is defined by equation (1.23) with as film thickness applied:

$$\delta_t = \frac{D_h}{Nu} \quad , \tag{1.40}$$

where Nu is the local convective flow Nusselt number at low mass transfer rates belonging to the studied channel shape. With equation (1.25) it can be verified that $\Theta_t(\phi_t) - \phi_t$ is identical with $\Theta_t(-\phi_t)$. This implies that these identical functions are smaller than unity for suction and larger than unity for injection; $\Theta_t(\phi_t)$ and its reflection in the vertical axis $\Theta_t(-\phi_t)$ are depicted in figure 1.3. Suction thus enhances the heat transfer at the wall, while the temperature drop of the mixture nevertheless becomes smaller as mass is absorbed at the wall. This opposite conduction of heat flux and temperature alteration has already been noticed and discussed by Colburn and Drew (1937) when applying the film model to heat and mass transfer in channel flow. Subsequent workers applied the film model to combined heat and diffusional mass transfer in condensers and evaporators and found in good agreement with practice, *e.g.* see the results of Webb and Sardesai (1981) or the procedures recommended by V.D.I. (1988).

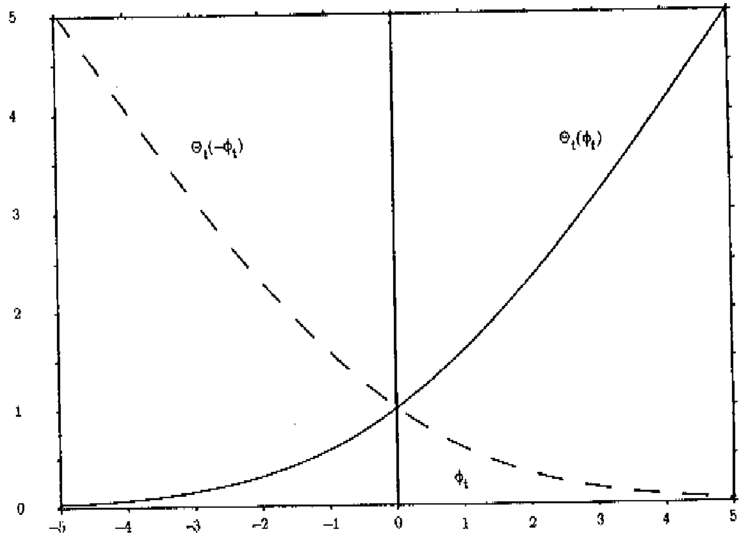

Figure 1.3 Ackermann correction function and its reflection in the vertical axis.

Momentum balance

An expression for the pressure drop in a channel follows from a differential momentum balance on the material between the planes x and x+dx, see figure 1.2:

$$\frac{dP}{dx} + \frac{d(\rho\overline{u^2})}{dx} = -\tau\frac{4}{D_h} = -\Theta_u \tfrac{1}{2}\rho\,\bar{u}^2 f\frac{4}{D_h} \quad . \tag{1.41}$$

The second term on the left hand side represents the vapour deceleration or acceleration owing to suction or injection, respectively. In equations (1.41) the coefficient f is the local coefficient at low mass transfer rates pertaining to the considered channel shape. Substituting equations (1.32) and (1.33) and rearranging equation (1.41) yields:

$$\frac{dP}{dx} = -\frac{2\rho f\bar{u}(x)^2}{D_h}\left(\Theta_u - 2\frac{\overline{u^2}}{\bar{u}^2}\phi_u\right) \quad . \tag{1.42}$$

In deriving equation (1.42) the variation of the mixture's density and momentum flux coefficient (which is the ratio of mean square and square mean velocity) in the direction of x have been considered as zero: within the accuracy of the present model this distinction is minor.

Result (1.42), the film model expression for the pressure drop, has –to the author's knowledge– never been obtained before. It is therefore compared extensively in the following with results of experimental and theoretical studies of flow through closed channels with porous walls in the presence of imposed suction and injection. In the past considerable effort has been expended to this flow since it has been applied to transpiration cooling and boundary layer control, and is also found in membranes for production of uranium–235, artificial kidney dialysis and culturing of animal cells. In all studied papers it has been assumed that the laminar or turbulent porous channel flow is self–similar. The self–similarity is defined as a state of flow in which a local velocity distribution divided by the cross–sectional average velocity does not vary in the flow direction (*i.e.* invariant momentum flux coefficient), and it offers the advantage of simplifying the equations of continuity and motion considerably.

Fully developed laminar fluid flow between parallel plates and in circular tubes with surface injection and suction has been studied analytically by many investigators. For both cases the governing continuity and Navier–Stokes equations were reduced to a single, fourth order, non–linear ordinary differential equation. This equation was initially solved using perturbation methods and subsequently using numerical integration.

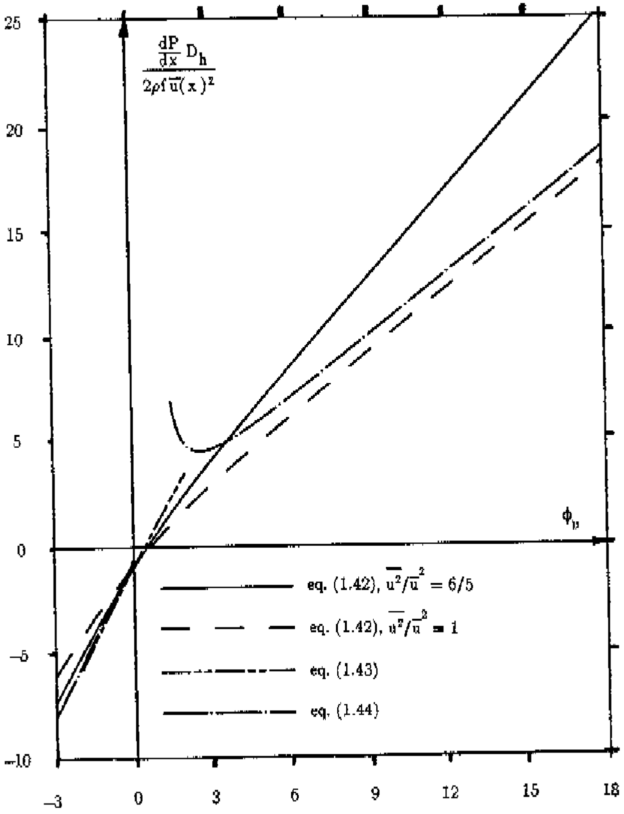

Figure 1.4 Pressure drop of laminar flow between parallel plates in the presence of suction and injection.

A listing of all relevant papers on flow between parallel plates can be found in the notes by Terrill (1964, 1965), particular reference being made here to the contributions of Berman (1953), Yuan (1956) and Berman (1956). The second order approximation for $|\phi_u| < 1/3$ of the differential pressure variation reads:

$$\frac{dP}{dx} = -\frac{2\rho f\overline{u}(x)^2}{D_h}\left(1 - \frac{81}{35}\phi_u + 3\,\frac{468}{26950}\phi_u^2\right) \quad , \qquad (1.43)$$

and the asymptotic approximation for $|\phi_u| > 1/3$:

$$\frac{dP}{dx} = -\frac{2\rho f\overline{u}(x)^2}{D_h}\left(\frac{2.049}{3} - \frac{\pi^2}{4}\phi_u\right) \qquad (\phi_u < -1/3) \ ,$$

$$\frac{dP}{dx} = -\frac{2\rho f\overline{u}(x)^2}{D_h}(-\phi_u)\left[\frac{3\phi_u}{3\phi_u - 1}\right]^2\left[1 + \frac{6}{(3\phi_u - 1)^2} + \frac{53.5}{(3\phi_u - 1)^3}\right] \qquad (\phi_u > 1/3). \qquad (1.44)$$

In figure 1.4 the dimensionless pressure gradient is depicted, according to equations (1.42)–(1.44), as a function of the dimensionless suction rate ϕ_u. In equation (1.42) the momentum flux coefficient 6/5 is substituted, derived from undisturbed Poiseuille flow, *i.e.* $\phi_u = 0$, between parallel plates, see table 1.1.

Figure 1.4 shows the trend that the film model underpredicts the effect of large injection rates and overpredicts the effect of large suction rates on the pressure drop. This can be understood from the fact that the velocity profile in the center of the channel steepens slightly and flattens substantially ("plug flow") for large injection and suction, respectively. Hence for large suction rates the momentum flux coefficient will tend to unity, while for injection the momentum flux coefficient will even be larger than the values listed in table 1.1. To illustrate the pertinent influence of the momentum flux coefficient on the pressure drop predictions, equation (1.42) is also drawn in figures 1.4 with a momentum flux coefficient of unity substituted.

	laminar flow		turbulent flow	
	parallel plates	circular tube	parallel plates	circular tube
$\overline{u^2}/\bar{u}^2$	6/5	4/3	$(1+n)^2/(2+n)n$	$(1+n)^2(1+2n)^2/2n^2(2+n)(2+2n)$
f	24/Re	16/Re	$0.079/Re^{0.25}$	$0.079/Re^{0.25}$

Table 1.1 Neutral ($\phi_u = 0$) friction coefficients and momentum flux coefficients (n denotes the turbulent power–law exponent).

For injection the prediction is worse, as expected, while for large suction rates the determined pressure drop is indeed in better agreement with the referred results.

Perturbation solutions of the governing equations of laminar flow through porous circular tubes for large and small $|\phi_u|$ have been derived by Yuan and Finkelstein (1956) and Terrill and Thomas (1969). Some of these theoretical predictions have been confirmed experimentally by Bundy and Weissberg (1970). For $|\phi_u| < 1/4$ as first order approximation for the pressure drop was obtained:

$$\frac{dP}{dx} = -\frac{2\rho f \bar{u}(x)^2}{D_h}(1 - 3\,\phi_u) \quad , \tag{1.45}$$

and as approximation for $|\phi_u| > 1/4$:

$$\frac{dP}{dx} = -\frac{2\rho f \bar{u}(x)^2}{D_h}(1.3253 - 2.4674\,\phi_u) \qquad (\phi_u < -1/4) \quad ,$$

$$\frac{dP}{dx} = -\frac{2\rho f \overline{u}(x)^2}{D_h}(-\phi_u)\left[1+\frac{1}{\phi_u}+\frac{7}{4\phi_u^2}+\frac{21}{4\phi_u^3}\right] \qquad (\phi_u > -1/4) \ . \tag{1.46}$$

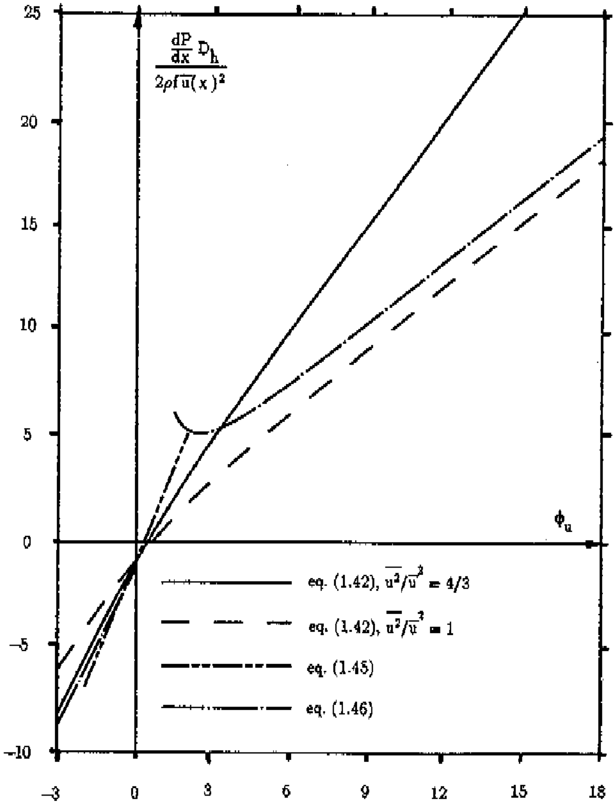

Figure 1.5 Pressure drop of laminar flow in a circular tube in the presence of suction and injection.

In figure 1.5 equations (1.45), (1.46) and (1.42), with as momentum flux coefficients 1 and 4/3 substituted, are drawn. This latter value is based on the parabolic velocity profile of Hagen–Poiseuille flow in a tube, in the absence of suction and injection, see table 1.1. Figure 1.5 indicates that the film model with a momentum flux coefficient of 4/3 substituted is in reasonable agreement with the asymptotic results for small $|\phi_u|$. In contrast to flow between parallel plates, the referred authors found that the profiles flatten both for injection and suction. Figure 1.5 confirms that the effect of a flatter profile is more pronounced for suction (likewise laminar flow between parallel plates); equation (1.42) with momentum flux coefficient unity substituted is indeed in better agreement.

Pressure drop of turbulent flow through circular tubes, in the presence of surface injection and suction, has been the subject of numerous experimental and theoretical works in the past. In figure 1.6 the line based on the injection experiments of Olson and Eckert (1966) is depicted. The Reynolds number Re ranged from 28,000 up to 82,000. One of their findings was that the velocity field in the tube becomes fully developed within 12 tube diameters. The concept of self–similarity of the velocity field formed the basis of comprehensive suction computations performed by Kinney and Sparrow (1970). In figure 1.6 their result for Re = 50,000 is drawn. Mizushina *et al.* (1975) derived an empirical relation for the pressure drop as a function of the suction rate. This relation is based on both suction and injection experiments, Re ranging from 9,000 to 102,500. The suction rate $-v(y=0)/\overline{u}$ range of their experiments was confined from −0.017 to 0.019, see figure 1.6.

In this figure also equation (1.42) has been drawn with 4f set equal to 0.023 and a momentum flux coefficient of 1 and 1.02. The value of f is obtained from the intersection of all lines, depicted in figure 1.6, with the vertical axis, corresponding, to the neutral case of neither suction nor injection. This friction coefficient of turbulent flow through a circular tube corresponds, according to Blasius' equation, see table 1.1, with a Reynolds number of about 36,000, which is indeed within the range investigated by the various authors. The momentum flux coefficient listed in table 1.1 follows from the developed turbulent flow power–law velocity profile in the tube, see Ward–Smith (1980). With power–law exponent n = 7 substituted, this value of n pertains to the afore–said Reynolds number, the mentioned momentum flux coefficient 1.02 is obtained.

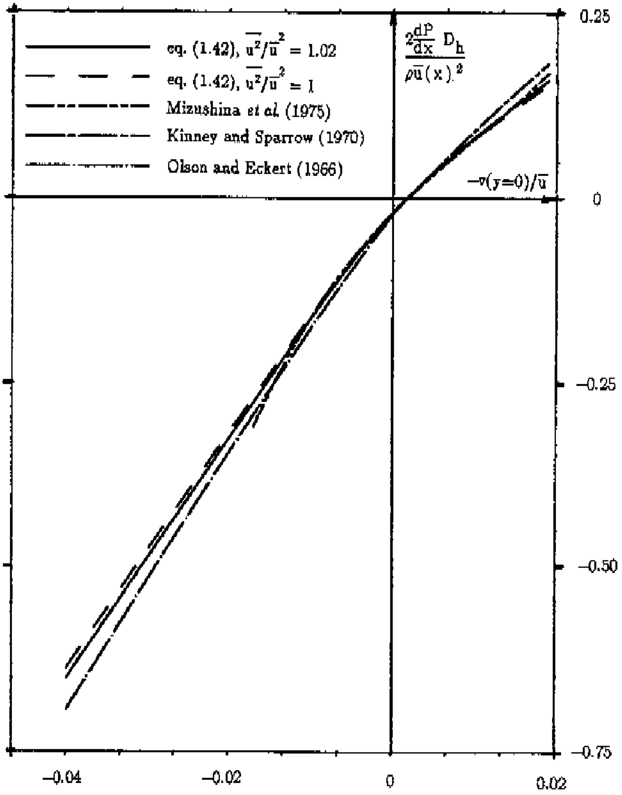

Figure 1.6 Pressure drop of turbulent flow through a circular pipe in the presence of suction and injection.

Figure 1.6 indicates the good agreement between the original and compact equation (1.42), and all results of afore–mentioned investigators, in particular when the momentum flux coefficient of 1.02 is applied. The agreement remains within 10 per cent for the largest suction rate, and within 8 per cent for the largest injection rate. These large values of $|v(y=0)/\bar{u}|$ are typical of tubes with porous walls; diffusional "injection" or "suction" rates in evaporators or condensers are usually smaller.

In figures 1.4–1.6 the enhancement of the pressure drop is illustrated as the injection rate rises, due to the amount of added gas to be accelerated. One can also see the sign change of the pressure drop for sufficiently large suction rates, caused by the momentum decrease of flowing fluid. From equations (1.42) and (1.31) the non–dimensional mass flux pertaining to the zero pressure drop situation is derived analytically as:

$$\phi_u = Ln\left[\frac{2\overline{u^2}/\bar{u}^2}{2\overline{u^2}/\bar{u}^2 - 1}\right] \quad . \tag{1.47}$$

The strength of equations (1.42) and (1.47) lies in the fact they are not limited to one channel shape or one Reynolds number. To apply these simple and compact equations one only needs to know, for a given channel shape, the uncorrected friction factor as a function of the Reynolds number, and the ratio of mean square and square mean velocity. This ratio is in general close to unity for turbulent flow, but a better prediction is obtained when the momentum flux coefficient is actually assessed and applied. For laminar flow the momentum flux coefficient is evidently unequal to unity, but can readily be obtained from a consideration of the neutral velocity profile in the channel.

§1.5 Relation between c and t in the film and the path of $\bar{c}$ and $\bar{t}$

In previous sections film model correction factors have been derived and applied to the case of closed channel flow. In this section the relation of vapour mass fraction and temperature in the film with respect to the saturation line is discussed, in particular the possible crossing of this line. Furthermore, attention is focussed on the path of the mean mixed values $\bar{t}$ and $\bar{c}$ of a binary mixture flowing through a channel, and the entering of these properties into the supersaturated region. Special attention is paid to a binary mixture for which:

$$\mathrm{Nu} = \mathrm{Sh} \quad , \tag{1.48}$$

or:

$$\frac{\delta_c}{\delta_t} = \frac{\mathrm{Nu}}{\mathrm{Sh}} = 1 \quad , \tag{1.49}$$

see equations (1.34) and (1.40), corresponding to equal temperature and diffusion film thicknesses. Both equalities apply to any heat and mass transfer problem, either convective or non–convective, either laminar or turbulent, for a Lewis number Le equal to unity. They also apply to laminar flow with a Lewis number unequal to unity, as will be discussed in the next section.

To express the vapour mass fraction as a function of the temperature in the film, the coordinate y/δ_c is eliminated from equations (1.6) and (1.10), resulting in:

$$c = G(t) = 1 + (c_i - 1)\left[\frac{t - t_i}{t_b - t_i}\left[e^{\frac{\delta_t}{\mathrm{Le}_v \delta_c} Ln\left[\frac{1 - c_b}{1 - c_i}\right]} - 1\right] + 1\right]^{\mathrm{Le}_v} \quad . \tag{1.50}$$

$$(t_i \leq t \leq t_b)$$

Equation (1.50) relates c and t in the film. Both for condensation (that is to say $c_b > c_i$) and for evaporation ($c_b < c_i$), G(t) proves to be a monotonically increasing function of t. This property follows from the first derivative of G(t) with respect to t. Differentiating G(t) twice with respect to t makes it further clear that G(t) is convex for $Le_v < 1$ with condensation or evaporation, while G(t) is concave for $Le_v > 1$ with condensation or evaporation. For $Le_v = 1$, G(t) is a straight line, both for evaporation and condensation.

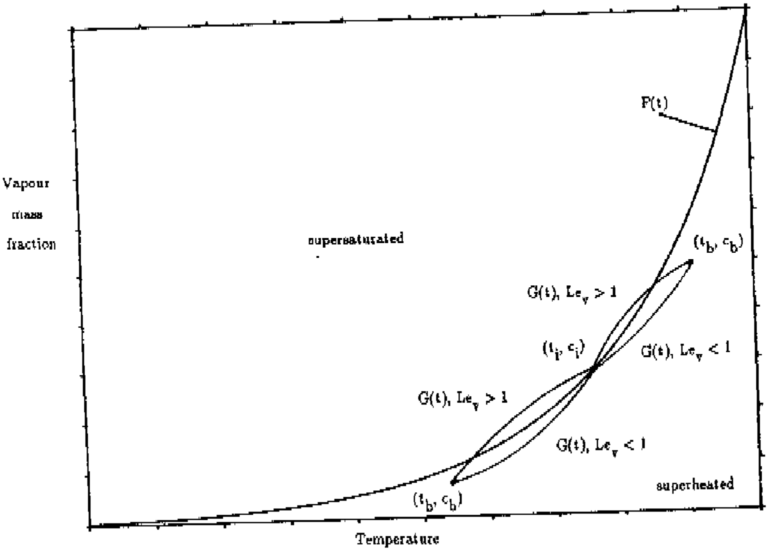
F(t)
Vapour mass fraction
supersaturated
(t_b, c_b)
G(t), $Le_v > 1$
(t_i, c_i)
G(t), $Le_v < 1$
G(t), $Le_v > 1$
G(t), $Le_v < 1$
superheated
(t_b, c_b)
Temperature

Figure 1.7 Behaviour of G(t), $\delta_t = \delta_c$.

In figure 1.7 the possible shapes of G(t) for equal film thicknesses (corresponding to equality (1.49)) are depicted. In fact y acts as a parameter of each curve depicted in this figure. In the figure the saturation line F(t) of the mixture concerned is also drawn.

It can be seen that a part of the film is supersaturated, even when (t_b, c_b) is situated in the superheated region. The part of the film that is positioned in the supersaturated region, is thermodynamically in a unstable state. As a result condensation takes place and fog is created: by homogeneous nucleation and heterogeneous condensation on foreign particles, see Steinmeyer (1972). Where fog is formed, the basic diffusion and energy equations are locally altered. In appendix A the governing equations of the fogging part of the film are derived.

In order to study the behaviour of the bulk, or mean mixed temperature, $\bar{t}$ and vapour concentration, $\bar{c}$, of a binary mixture flowing through a channel, the coordinate x is eliminated from equations (1.37) and (1.39). Substituting equations (1.17), (1.18), (1.23), (1.25), (1.26), (1.34) and (1.40), assuming uniform interface conditions, separating of the variables $\bar{t}$ and $\bar{c}$, and integrating yields:

$$\bar{c} = \overline{G}(\bar{t}) = 1 + \tag{1.51}$$

$$(c_i - 1)\left[\left(\frac{\bar{t} - t_i}{\bar{t}(x=0) - t_i}\right)^{\frac{Sh}{NuLe}}\left[e^{\frac{Sh}{Le_v Nu} Ln\left[\frac{1 - \bar{c}(x=0)}{1 - c_i}\right]} - 1\right] + 1\right]^{\frac{Le_v Nu}{Sh}} ,$$

where the values of $\bar{c}$ and $\bar{t}$ at an arbitrarily chosen location, $x = 0$ (for instance the entrance of a channel), have been applied to determine the integration constant.

One can readily see that to $Le = 1$, in view of equality (1.49), applies:

$$\overline{G}(\bar{t}) = G(t) \ . \tag{1.52}$$

This result is very interesting because for $Le = 1$ the binary mixture's mean mixed temperature and vapour mass fraction ($\bar{t}$, $\bar{c}$) evidently "walk", while the mixture flows through the channel, along $G(t)$ towards (t_i, c_i), see figure 1.7. In other words, the curve $G(t)$ then acts as streamline for ($\bar{t}$, $\bar{c}$), independent of Le_v, although this curve is originally derived from the temperature and vapour concentration relationship in the film. For Le unequal to unity, however, it can be seen that the mixture follows $\overline{G}(\overline{t})$, but not G(t).

Figure 1.7 also indicates that under certain circumstances the mean mixed properties may enter the supersaturated area, which will result in a supersaturated mixture when the flow through the channel in a cross–section is mixed. Colburn and Drew (1937) already remarked that a mixture's bulk temperature and vapour fraction in a condenser may cross the saturation line and enter the supersaturated region. On the other hand, if the curvature of G(t) is sharp enough ($Le_v < 1$), it is possible that the c–t relation in the film, as well as the path of the mean mixed values, remains in the superheated region, even if the mixture enters the channel saturated. It is interesting to notice that the bulk can be superheated or saturated, while G(t) is situated in the supersaturated region. It also possible that the bulk properties move to enter the supersaturated region, while G(t) is located in the superheated region. Hence it is important to distinguish two kinds of supersaturation and fog formation, namely:

- fog formation in the film,
- fog formation in the bulk, owing to the entering of the bulk properties into the supersaturated region.

In the former discussions Le and Le_v have been treated as independent variables. However, it should be realized that Le and Le_v are coupled by equation (A.13), and therefore become identical when the vapour mass fraction tends to unity. Consequently, for large vapour fractions Le_v unequal to unity implies Le unequal to unity as well.

§1.6 Laminar flow

Two specific features of the film model for Le = 1 have been mentioned, namely equal temperature and diffusion film thicknesses and the path of change in the mixture's mean mixed properties lying along G(t), see equation (1.52). In some situations, however, Nu =

Sh can still apply, even when Le is not equal to unity. Examples are heat and mass transfer in the absence of (free or forced) convection, or fully developed laminar channel flow. In common heat transfer devices this type of flow is rarely found, which may be the reason that this special case has not been examined in detail yet. It will now be demonstrated that for laminar flow situations Nu = Sh is an acceptable approximation, even for Lewis numbers unequal to unity and in the presence of entry effects.

As example the laminar flow of an air water–vapour mixture between parallel plates is considered more closely. The mean Nusselt number for forced convective laminar flow through this channel configuration is given by Stephan (1959) as:

$$\overline{Nu} = 7.55 + \frac{0.024\ (RePrD_h/B)^{1.14}}{1\ +\ 0.0358\ (RePrD_h/B)^{0.64}\,Pr^{0.17}}\ , \tag{1.53}$$

in which the hydraulic diameter D_h equals twice the the gap height of the duct, and the Reynolds number Re is based on this hydraulic diameter. The channel length is represented by B. By replacement in equation (1.53) of $\overline{Nu}$ by $\overline{Sh}$ and the Prandtl number Pr by the Schmidt number Sc, the following relation for the mean Sherwood number is obtained:

$$\overline{Sh} = 7.55 + \frac{0.024\ (RePrD_h/B)^{1.14}\ Le^{1.14}}{1\ +\ 0.0358\ (RePrD_h/B)^{0.64}\,Pr^{0.17}\,Le^{0.81}}\ . \tag{1.54}$$

In equations (1.53) and (1.54) the first (constant) term on the right hand side represents the fully developed laminar flow Nusselt/Sherwood number, while the second term accounts for the enhanced transfer due to hydraulic and thermal/diffusional entry effects.

For air and water–vapour the Prandtl number is 0.7 and the Schmidt number about 0.55. As entry effects cannot be neglected, and Le is not equal to unity, $\overline{Sh}$ will not exactly be equal to $\overline{Nu}$. However, when (typical of situations to be considered later) the above values of Pr and Sc, a large Re of 2000, and a unfavourable D_h/B ratio of 1/19, are substituted in equations (1.53) and (1.54), one finds $\overline{Sh} = 9.26$ and $\overline{Nu} = 9.66$. This small difference between both numbers makes equality (1.48) an acceptable approximation, in particular when the physical accuracy of equations like (1.53) and (1.54) as such is considered: Hwang and Fan (1964) showed the accuracy of equation (1.53) is typically of a few per cent.

Thus, even for Le unequal to unity, with modest entry effects, equality (1.48) is acceptable for flow through parallel plates, and also for many other channel configurations, of course. This can be verified by considering forced convective laminar flow Nusselt number correlations for diverse channel shapes, which have been documented by Shah and London (1978). The only requirement, in fact, is that B/D_h is large enough, and Le is close enough to unity.

For turbulent flow, on the other hand, the approximation $\overline{Nu} = \overline{Sh}$ is less acceptable. For this flow situation Nu and Sh are often correlated by the Chilton–Colburn analogy:

$$\frac{Nu}{Sh} = Le^{\frac{1}{3}} \quad . \tag{1.55}$$

A substitution of Le = 0.55/0.7 in equation (1.55) indicates that this quotient differs more than 8 per cent from unity, which is twice the maximum error involved in approximation (1.48) in the laminar case.

The Nusselt and Sherwood number correlations for forced convective laminar flow between parallel plates have already been presented. For completeness, the friction coefficient is mentioned in the following as well. The mean friction coefficient for laminar fluid flow between parallel plates has been determined by Liu (1974):

$$\bar{f} = \frac{24}{Re} + 0.674 \frac{D_h}{B} \quad , \tag{1.56}$$

valid for $B/D_h Re$ larger than 0.01. The first term on the right hand side of equation (1.56) represents the fully developed laminar flow friction factor, the second term accounts for the increment in the friction factor by entry effects.

§1.7 Concluding remarks

As the film model plays an important role in the practical description of heat and mass transfer processes, this model has been discussed in some detail in this chapter. First, the three classical film model correction factors for energy, mass and momentum transfer have been derived for a diffusion induced velocity in a binary mixture. They can however be generalized to situations involving suction and injection. Moreover, in the past the results have successfully been applied to multicomponent diffusion problems as well.

Subsequently, the film model correction factors have been applied to closed channel flow and universal expressions derived for the mean mixed vapour mass fraction, temperature, and pressure variation along the channel. The latter appears to be a new equation, and has been found in good functional accord with various non–diffusional suction and injection results of previous workers. The momentum flux coefficient (ratio of mean square velocity and square mean velocity) in a channel proved to be an important parameter in predicting the laminar flow pressure variation in the presence of suction and injection. As the turbulent flow velocity profile approximates plug flow, this coefficient is there close to unity.

The local vapour mass fraction in the film has been expressed as a function G(t) of the local temperature. The relation between G(t) and the onset of fog formation in the film has been discussed. In following chapters G(t) will fruitfully be employed to investigate the possible fog formation in a film and a flowing mixture. Furthermore, it has been demonstrated the mean mixed vapour fraction $\bar{c}$ and temperature $\bar{t}$ of a binary mixture follow the relation G(t) for Le = 1, while flowing through a closed channel. Considering the path of $\bar{t}$ and $\bar{c}$ (represented by $\bar{G}(\bar{t})$) with respect to the saturation line, it has been seen that these properties may enter the supersaturated region (implying formation of fog in the bulk) or, on the other hand, remain in the superheated region.

For a Lewis number Le equal to unity the film thicknesses for heat and mass transfer are the same. These film thicknesses are also equal for non–convective problems, and very nearly equal in most laminar convective flow situations, when the Lewis number is not exactly equal to unity.

2. THE FOG FILM MODEL

§2.1 Introduction

In the film considered in the previous chapter fog can be formed, if the temperature and vapour fraction profiles and/or the bulk properties' path cross the saturation line. The classical film model analysis with resulting correction factors is then no longer valid and applicable, since in the supersaturated film the energy and diffusion equation are altered.

Supersaturation in mixtures has been the subject of many studies in the past, relevant contributions are discussed briefly in the following. Piening (1933) observed no fog formation in slightly supersaturated clean air water–vapour mixtures, owing to the absence of foreign nuclei. Based on homogeneous nucleation at a critical saturation level, numerous problems concerning supersaturated gas mixtures have been treated. Turkdogan (1964) and Turkdogan and Mills (1964) introduced the "critical saturation model" (CSM) to describe the wall evaporation of metals into a helium atmosphere. For the same purpose this CSM has been employed and extended by Rosner (1967), by Rosner and Epstein (1968) and Sekulić (1985) to model wall condensation of water–vapour in moist air, by Epstein and Rosner (1970) to investigate methyl alcohol evaporation into an air atmosphere, and by Hayashi *et al.* (1976, 1978) to describe the naphtalene sublimation into air.

In an early paper, Johnstone *et al.* (1950) observed, if sufficient foreign nuclei are present, that fog formation sets in as soon as supersaturation takes place. Assuming no supersaturation to be possible, the so–called saturation condition, they derived an erroneous expression to investigate the conditions for fog formation, see appendix F. The saturation condition has been employed fruitfully by Hills and Szekely (1964, 1969), Toor (1971a, 1971b) and Aref'yev and Averkiyev (1979) to investigate one–dimensional film systems. Forced convective wall condensation of water–vapour in air has been modelled two–dimensionally by Hijikata and Mori (1973), Legay–Desesquelles and Prunet–Foch (1985, 1986), and Hayashi *et al.* (1981). Free convective wall condensation of water–vapour in moist air has been studied successfully with the saturation condition by Koch (1986).

The central point of interest in all mentioned elaborations, except Aref'yev and Averkiyev (1979), is the absence of a film analysis including fog formation and an appreciable induced velocity. But in the previous chapter we have seen that in many practical situations the induced velocity plays a role of major importance, and that the basic film model approach is well suited to account for this velocity. In their original paper Aref'yev and Averkiyev (1979) presented a film analysis of a mixture consisting of air and water–vapour under evaporation conditions. Saturated bulk conditions and equal thermal and diffusional film thicknesses were considered and hence the entire film was assumed to be saturated. Their numerical results indicated the significant effect of fog formation on heat and mass transfer rates. However, superheated bulk conditions and the possible existence of both superheated and saturated regions in the film were not considered, nor the application of the fog film model to channel flow.

In this chapter therefore a complete film model analysis is presented, whereby a superheated bulk and unequal film thicknesses are allowed. First, the conditions for fog formation are analyzed thoroughly. Subsequently, the existence and magnitude of superheated and saturated regions in the film is determined precisely, illustrating the role of the decisive parameter Le_V (it will be demonstrated that superheating in the film is possible for $Le_V < 1$, notwithstanding a saturated bulk). The governing equation of diffusion and energy in the fogging region, coupled with the saturation condition, is first solved numerically. The possible existence of both a saturated and superheated region in the film, and the effect of fog formation on heat and mass transfer, is illustrated in various saturated air water–vapour mixtures.

Next, an asymptotic analysis is carried out, yielding an excellent approximate solution of the fog layer's governing non–linear equation. This solution supplies reliable analytical expressions for the correction factors, which are suitable for the dimensioning of heat exchanging devices, such as condensers or evaporators. The application of the fog film model to closed channel flow is demonstrated in detail and illustrated by means of a flow chart. In the last but one section the approximate solution is applied to evaporation of nickel into helium. The solution is compared with results of foregoing studies which neglected the effects of both the induced velocity and fog formation on evaporation rates.

§2.2 Film analysis

In this section the heat and mass transfer in a film as described in §1.2 is analyzed, extended to include the possibility of fog formation. An elementary study of the vapour mass fraction and gas temperature profiles in the film yield the exact circumstances needed for fog formation. The alternative diffusion and energy equation, in the case of fog formation coupled with the saturation condition, are then derived and solved numerically. Correction factors are then introduced which will be compared in the next section with the correction factors for the conventional film model without fog formation.

Relation (1.50) describes mathematically the connection between the vapour concentration c and the temperature t in the film of a binary mixture. This curve can be located such that it crosses the saturation line F(t) of the vapour. In figure 1.7 two examples were drawn for either suction or injection situations. The possible intersection of G(t) and F(t), enabling the formation of fog, is now examined by considering the slope conditions:

$$\left.\frac{dF}{dt}\right|_{t_i} < \left.\frac{dG}{dt}\right|_{t_i} = Le_v \, \frac{c_i - 1}{t_b - t_i} \left[e^{\frac{\delta_t}{Le_v \delta_c} Ln\left[\frac{1 - c_b}{1 - c_i}\right]} - 1 \right] \quad , \tag{2.1}$$

for suction and, with a rearranged right hand side;

$$\left.\frac{dF}{dt}\right|_{t_i} > \left.\frac{dG}{dt}\right|_{t_i} = \frac{\delta_t}{\delta_c}\frac{\Theta_c}{\Theta_t}\frac{c_b - c_i}{t_b - t_i} \quad , \tag{2.2}$$

for injection. In equation (2.2) the conventional film model correction factors (1.19) and (1.25) have been inserted. When equations (2.1) and (2.2) are not satisfied, the curve G(t) is situated entirely in the superheated region, and fog will not be formed, see figure 1.7 for two examples. Consequently, the classical film model corrections remain valid. However, when these requirements are not satisfied, the curve (1.50) intersects the saturation line. Assuming no supersaturation to be possible, fog will then be formed in part, or all of the film. In appendix B the use of criteria (2.1) and (2.2) is discussed in detail. The film, superheated and/or saturated, is analyzed below.

The first step is to divide the film into a fog or saturated layer ($0 \le y \le \delta_a$) and a superheated layer ($\delta_a \le y \le \delta_c$ or δ_t). The fog layer thickness δ_a lies between zero (*i.e.* no fog formation) and δ_c or δ_t, when the entire film is saturated. But δ_a is at the present unknown and will be determined later on. Plural saturated and superheated regions in the film have been excluded implicitly, though it is demonstrated in appendix B this feature cannot be proved mathematically for $Le_v < 1$. Secondly, at the boundary of the superheated and saturated regions the temperature is denoted by:

$$t(y = \delta_a) = t_a \quad , \tag{2.3}$$

and the vapour mass fraction must obey the requirement:

$$c(y = \delta_a) = c_a \quad . \tag{2.4}$$

The vapour mass fraction up to and including the boundary of the saturated region is related to the temperature by the saturation condition:

$$c = F(t) \qquad (t_i \le t \le t_a) \quad . \qquad (2.5)$$

This so-called saturation condition has been utilized frequently in the past, as discussed in the introduction. The saturation condition holds in general when sufficient particles are present in the mixture which can serve as nuclei for condensation. According to Steinmeyer (1972) these conditions are indeed often fulfilled in practical situations. The level of supersaturation, which thermodynamically always must be non-zero, can then be considered as negligibly small. Moreover, for the analysis it is in fact not relevant which relation between c and t in the fog region is selected, which is to say that F(t) can also be the result of a CSM, here the saturation condition is employed in view of its convenience and accuracy to most practical situations.

In the analysis of the fog layer the droplets created (and transported, *e.g.* by thermophoresis) are not explicitly considered and the physical properties in the superheated and saturated mixture are therefore assumed to be identical. This approach is quite acceptable since the fraction of droplets in mixtures is usually very small.

In the superheated region the diffusion equation (1.2) with induced velocity (1.3) is still valid. Solving this equation with boundary conditions (1.5) and (2.4) yields:

$$c(y) = 1 - (1 - c_a)\, e^{\frac{y - \delta_a}{\delta_c - \delta_a} Ln\left[\frac{1 - c_b}{1 - c_a}\right]} \qquad (\delta_a \le y \le \delta_c) \quad . \qquad (2.6)$$

The temperature distribution is obtained by solving equation (1.7) with application of equation (2.6) and boundary conditions (1.9) and (2.3), resulting in the temperature profile:

$$t(y) = (t_b - t_a)\left[\frac{e^{\frac{y-\delta_a}{Le_v(\delta_c-\delta_a)}Ln\left[\frac{1-c_b}{1-c_a}\right]} - 1}{e^{\frac{\delta_t-\delta_a}{Le_v(\delta_c-\delta_a)}Ln\left[\frac{1-c_b}{1-c_a}\right]} - 1}\right] + t_a \quad (\delta_a \leq y \leq \delta_t)\ . \tag{2.7}$$

Eliminating $(y - \delta_a)/(\delta_c - \delta_a)$ from equations (2.6) and (2.7) results in the following relation between c and t in the superheated region:

$$c = G(t) = 1 + (c_a - 1)\left[\frac{t - t_a}{t_b - t_a}\left[e^{\frac{\delta_t-\delta_a}{Le_v(\delta_c-\delta_a)}Ln\left[\frac{1-c_b}{1-c_a}\right]} - 1\right] + 1\right]^{Le_v} \quad (t_a \leq t \leq t_b)\ . \tag{2.8}$$

For $\delta_a = 0$ (*i.e.* $t_a = t_i$ and $c_a = c_i$) solutions (2.6)–(2.8) reduce to the solutions (1.6), (1.10) and (1.50) of the conventional film.

At the boundary of the saturated and superheated region the concentration and temperature (and physical properties) are continuous, as are the energy and mass flux:

$$\underset{\text{saturated region}}{k\left.\frac{dt}{dy}\right|_{y=\delta_a}} = \underset{\text{superheated region}}{k\left.\frac{dt}{dy}\right|_{y=\delta_a}}\ , \tag{2.9}$$

and for the diffusion equation:

$$\underset{\text{saturated region}}{\left.\frac{\rho\mathbb{D}}{1-c}\frac{dc}{dy}\right|_{y=\delta_a}} = \underset{\text{superheated region}}{\left.\frac{\rho\mathbb{D}}{1-c}\frac{dc}{dy}\right|_{y=\delta_a}}\ . \tag{2.10}$$

The temperature and vapour concentration in the superheated region are already known, see equations (2.6) and (2.7), but in the saturated region they have yet to be determined. However, in the saturated region the concentration and temperature are coupled by the saturation function (2.5). Combining equations (2.9) and (2.10) to eliminate the y–dependence and applying equations (2.5) and (2.8) yields as tangency condition:

$$\left.\frac{dF}{dt}\right|_{t_a} = \left.\frac{dG}{dt}\right|_{t_a} = Le_v \frac{c_a - 1}{t_b - t_a}\left[e^{\frac{\delta_t - \delta_a}{Le_v(\delta_c - \delta_a)} Ln\left[\frac{1 - c_b}{1 - c_a}\right]} - 1\right] \quad . \qquad (2.11)$$

Equation (2.11) prescribes continuity of the first derivative dc/dt as given by equation (2.8) in the superheated region and by equation (2.5) in the fog layer. Additional information about use and features of equation (2.11) is given in appendix B. Equation (2.11) contains two unknowns, namely t_a and δ_a (since $c_a = F(t_a)$). In order to derive a second equation with both unknowns and to complete the analysis of the film, attention is now focussed on the fog layer next to the wall ($0 \leq y \leq \delta_a$).

In the fog layer vapour disappears by spontaneous condensation and as a result of the droplet formation latent heat is liberated. In this layer the energy and diffusion equation, as derived in appendix A, therefore read:

$$k \frac{d^2t}{dy^2} + \frac{\rho \mathbb{D} c_{p,v}}{1 - c} \frac{dc}{dy} \frac{dt}{dy} = - H_{lat}\, K \quad , \qquad (2.12)$$

$$\rho \mathbb{D} \frac{d^2c}{dy^2} + \frac{\rho \mathbb{D}}{1 - c} \frac{dc}{dy} \frac{dc}{dy} = K\,(1 - c) \quad , \qquad (2.13)$$

with as respective boundary conditions (1.8) and (2.3), and (1.4) and (2.4). In equations (2.12) and (2.13) K represents the mass of formed fog in the mixture per unit volume.

Eliminating K from these equations produces:

$$\mathrm{Le}_v \frac{d^2t}{dy^2} - \frac{d\,Ln(1 - c)}{dy}\frac{dt}{dy} = \frac{H_{lat}}{c_{p,v}}\frac{d^2Ln(1 - c)}{dy^2} \quad . \tag{2.14}$$

This equation is an ordinary non–linear second order differential equation in t with respect to the coordinate y, since c is expressed by the saturation equation (2.5) as a function of t. As a solution in closed form is not possible, the boundary value problem (2.14), with boundary conditions (1.8) and (2.3), is solved numerically with a standard shooting method. Detailed information about this solution technique is found in Hall and Watt (1976). In order to prepare equation (2.14) for this solution method, the dimensionless variable:

$$Y = \frac{y}{\delta_a} \quad , \tag{2.15}$$

is substituted into equation (2.14). By this substitution equation (2.14) remains exactly the same form, but the domain of integration is transformed into $0 \leq Y \leq 1$.

The second equation containing t_a and δ_a is now obtained by combining the numerical solution of equation (2.14), and equations (2.7), (2.9) and (2.15):

$$\frac{\delta_c}{\delta_a} = 1 + \frac{1}{\mathrm{Le}_v \left.\frac{dt}{dY}\right|_{Y=1}} \left[\frac{(t_b - t_a)\,Ln\left[\frac{1 - c_b}{1 - c_a}\right]}{e^{\frac{\delta_t - \delta_a}{\mathrm{Le}_v(\delta_c - \delta_a)} Ln\left[\frac{1 - c_b}{1 - c_a}\right]} - 1} \right] \quad . \tag{2.16}$$

In this equation the first derivative of the temperature with respect to Y in Y = 1 is supplied by the numerical solution of equation (2.14).

The combined iteration of equations (2.11) and (2.16) yields δ_a and t_a. To employ this simultaneous iteration the boundary problem (2.14) has to be solved for every value of t_a during the iteration. To decouple both equations and reduce the computational effort, equality (1.49) could from now on be supposed to be valid. Rather than setting Nu = Sh, though it is acceptable for many transfer processes, the magnitude of the term $(\delta_t - \delta_a)/(\delta_c - \delta_a)$ is evaluated in the following.

In the case in which no fog is formed in the film, so that K is identically zero in equation (2.13), the vapour mass fraction, c_a, at location $y = \delta_a$ is given by:

$$\frac{\delta_c}{\delta_c - \delta_a} = \frac{Ln(1 - c_b) - Ln(1 - c_i)}{Ln(1 - c_b) - Ln(1 - c_a)} , \tag{2.17}$$

since then $Ln(1 - c)$ depends linearly on y in both the saturated and superheated region. If equation (2.17) is supposed to be valid when fog is present and is inserted into equation (2.11), δ_a is eliminated from the right hand sides of equations (2.11) and (2.16). Hence, equation (2.11) produces readily t_a, and with this t_a equation (2.14) is solved, and with the numerical solution δ_a is obtained explicitly from equation (2.16). A similar simplification follows in fact from inserting equality (1.49), as discussed above.

However, equation (2.17) is only an approximation when $K \neq 0$ and the error involved by assuming (2.17) has to be assessed. The amount of formed fog has been derived in appendix A, expressed by equation (A.17). It has furthermore been discussed in this appendix that the amount of produced fog is greatest where the temperature of the fog layer is lowest. For evaporation this temperature corresponds to t_a, while for condensation this temperature is found at the interface, thus $t = t_i$. Equation (2.17) is violated the most if this maximum value of K is supposed to apply throughout the entire fog region. Integrating equation (2.13) twice with respect to y, and application of boundary conditions (1.4) and (2.4) then yields:

$$Ln(1-c(y)) = -\tfrac{1}{2}p\left(\frac{y}{\delta_a}\right)^2 + \left(Ln\left[\frac{1-c_a}{1-c_i}\right] + \tfrac{1}{2}p\right)\frac{y}{\delta_a} + Ln(1-c_i) \qquad (0 \le y \le \delta_a) \quad , \tag{2.18}$$

where p follows from equations (2.15) and (A.17):

$$p = \frac{\delta_a^2}{\rho\mathbb{D}}K = \frac{(Le_v - 1)\left[\frac{1}{1-F}\frac{dF}{dt}\right]^2 + Le_v\frac{1}{1-F}\frac{d^2F}{dt^2}}{Le_v + \frac{H_{lat}}{c_{p,v}}\frac{1}{1-F}\frac{dF}{dt}}\left(\frac{dt}{dY}\right)^2 \ . \tag{2.19}$$

The relation between film thicknesses and vapour fraction follows from combining equations (2.6), (2.10) and (2.18), yielding:

$$\frac{\delta_c}{\delta_c - \delta_a} = \frac{Ln(1-c_b) - Ln(1-c_i)}{Ln(1-c_b) - Ln(1-c_a)}(1+\epsilon) \quad , \tag{2.20}$$

with:

$$\epsilon = \frac{\tfrac{1}{2}p}{Ln(1-c_b) - Ln(1-c_i)} \quad , \tag{2.21}$$

as a measure of the error occasioned by assuming equation (2.17). Equation (2.17) is rewritten as:

$$\frac{\delta_t - \delta_a}{\delta_c - \delta_a} = 1 + \left(\frac{\delta_t}{\delta_c} - 1\right)\frac{Ln(1-c_b) - Ln(1-c_i)}{Ln(1-c_b) - Ln(1-c_a)} \quad . \tag{2.22}$$

For wall evaporation the actual effect of $\delta_t \neq \delta_c$ is greater than expressed by this equation and equation (2.17), as $\dot{\epsilon} > 0$, while for condensation equations (2.17) and (2.22) exaggerate this effect, since then $\epsilon < 0$. However, equation (2.22) reckons to some extent with unequal thermal and diffusional film thicknesses, while its application decouples equations (2.11) and (2.16) and therefore reduces the computational effort. From now on ϵ is therefore considered to be zero, the actual magnitude of ϵ is assessed in the next section for some practical situations.

The correction factors of heat and mass transfer will now be derived. With equations (1.23) and (2.15), the transferred heat (1.21) is written as:

$$q = h_g \frac{\delta_t}{\delta_a} \frac{dt}{dY}\bigg|_{Y=0} \quad . \tag{2.23}$$

Comparing equation (2.23) with the heat flux in a film without fog and without induced velocity, represented by equation (1.22), yields as correction factor:

$$\Theta_{t,f} = \frac{\dfrac{\delta_t}{\delta_a} \dfrac{dt}{dY}\bigg|_{Y=0}}{(t_b - t_i)} \quad . \tag{2.24}$$

The mass flux from gas to wall is governed by equation (1.15). Combining this equation with equation (2.5) results in:

$$\dot{m} = \frac{\rho D}{1 - F(t_i)} \frac{dF}{dt}\bigg|_{t_i} \frac{dt}{dy}\bigg|_{y=0} \quad . \tag{2.25}$$

A comparison of equation (2.25) with equation (1.16) and application of equations (1.17) and (2.15) results in the following correction factor for diffusion:

$$\Theta_{c,f} = \frac{\dfrac{\delta_c}{\delta_a} \left.\dfrac{dF}{dt}\right|_{t_i} \left.\dfrac{dt}{dY}\right|_{Y=0}}{(c_b - c_i)} \quad . \tag{2.26}$$

The gradient of temperature at $Y = 0$, appearing in equations (2.23), (2.24) and (2.26), follows from the numerical solution of equation (2.14). It can easily be verified that in general between the fog correction factors for mass and heat transfer, $\Theta_{c,f}$ and $\Theta_{t,f}$ respectively, the relation exists:

$$\Theta_{c,f} = \frac{t_b - t_i}{c_b - c_i} \left.\frac{dF}{dt}\right|_{t_i} \frac{\delta_c}{\delta_t} \Theta_{t,f} \quad , \tag{2.27}$$

owing to the saturation condition (2.5) in the fog layer.

An additional interesting property which can be determined with the numerical solution of the combined energy and diffusion equation (2.14) is the amount of formed fog in the saturated layer:

$$\dot{m}_f = \int_{y=0}^{\delta_a} K \, dy \quad . \tag{2.28}$$

Applying equations (1.23), (2.12) and (2.15), equation (2.28) yields:

$$\dot{m}_f = \frac{h_g}{H_{lat}} \frac{\delta_t}{\delta_a} \left[\left.\frac{dt}{dY}\right|_{Y=0} - \left.\frac{dt}{dY}\right|_{Y=1} - \frac{1}{Le_v} \int_{Y=0}^{1} \frac{1}{1 - c} \frac{dc}{dY} \frac{dt}{dY} \, dY \right] \quad . \tag{2.29}$$

The first derivatives of t with respect to Y in $Y = 0$ and $Y = 1$ follow from the numerical solution of equation (2.14); this solution is also employed to calculate numerically the integral in equation (2.29) with Simpson's rule.

The amount of formed fog, represented by equation (2.28), is the same for evaporation and condensation, which is explained as follows. Equation (2.14) remains the same form when y is replaced by the coordinate $\delta_a - y$, only the boundary conditions (1.8) and (2.3) being exchanged. In other words, evaporation conditions become condensation conditions, or vice versa. The solution of the equation (2.14) with exchanged boundary conditions is therefore the reflection of the original equation's solution in the line $y = 0.5\delta_a$, hence t(y) curves for evaporation and condensation are symmetrical with respect to the line $y = 0.5\delta_a$. A similar consideration of equations (2.28) and (2.13) provides evidence that the amount of fog formed for condensation and evaporation is positive and equal.

A complete analysis has been given in this section of a film with possible formation of fog. Equations (2.1) or (2.2) serve to examine whether fog is formed; when this is the case tangency condition (2.11), combined with approximation (2.22), provides the boundary of the saturated and superheated regions (t_a, c_a). Ultimately, the numerical solution of the governing equation (2.14) provides the temperature and coupled vapour concentration in the saturated region, yielding the fog layer's thickness (2.16), the correction factors (2.24) and (2.26), and the quantity of fog formed (2.29).

§2.3 Results of numerical solution

The influence of fog formation on heat and mass transfer will be greatest when the entire film is saturated. That is to say, when the bulk temperature t_b and bulk vapour fraction c_b are situated on the saturation line. In a condenser or evaporator this condition corresponds to a saturated mixture entering and flowing through a channel. To indicate the effect of fog formation results are presented based on the model derived in the previous section. As example saturated air water–vapour mixtures at low temperatures and vapour mass fractions are considered, as well as saturated mixtures at high temperatures and vapour fractions. Both mixtures are examined under condensation conditions, thus $c_b > c_i$, and equal thermal and diffusion film thicknesses. The former conditions are for instance found in air–conditioning devices, while the latter are typical of condensers.

	Le_v	$\Theta_{t,fl}/\Theta_t$	$\Theta_{c,fl}/\Theta_c$	$\dot{M}_{fl}$	$\overline{\dot{M}}_{fl}$	$q_{tot,fl}/q_{tot}$	$\lvert\epsilon\rvert$
$t_b = 30^\circ C$	0.50	1.218	0.924	0.391	0.393	1.000	0.096
$c_b = 0.0264$	0.75	1.192	0.901	0.350	0.352	1.000	0.120
	1.00	1.170	0.883	0.316	0.317	1.000	0.136
	1.25	1.153	0.868	0.288	0.289	1.000	0.148
$t_b = 60^\circ C$	0.50	2.418	0.791	2.050	2.091	1.002	0.736
$c_b = 0.1318$	0.75	2.301	0.723	1.883	1.919	1.001	0.805
	1.00	2.180	0.671	1.731	1.762	1.001	0.819
	1.25	2.073	0.630	1.601	1.629	1.000	0.810

Table 2.1 Results of numerical solution for $(t_i, c_i) = (20^\circ C, 0.0144)$, $\delta_a/\delta_c = \delta_a/\delta_t = 1$ for all cases.

For the first case considered, (t_i, c_i) is set equal to $(20^\circ C, 0.0144)$; this point is situated on the saturation line of a air water–vapour mixture under atmospheric conditions, as derived in appendix C. The bulk values (t_b, c_b) are successively set equal to $(30^\circ C, 0.0264)$ and $(60^\circ C, 0.1318)$, all situated on the same saturation function. The latent to specific heat ratio $H_{lat}/c_{p,v}$ of water–vapour is set equal to 1200 K. Calculations are carried out for Le_v equal to 0.5, 0.75, 1 and 1.25.

Evaluating equation (2.11) showed that for all cases the entire film is fogged, thus $\delta_a = \delta_c = \delta_t$ and $(t_a, c_a) = (t_b, c_b)$. Substituting the greatest t_b in equation (C.12) produces as maximum $H(t_b = 60^\circ C) = 0.13$, which is well below the smallest Le_v, namely $Le_v = 0.5$. The afore–said values assure that Le_v is greater than $H(t)$ in all considered fogging films, which is a condition for $K > 0$, see appendix A. In table 2.1 the correction factors according to equations (2.24) and (2.26), compared with the conventional correction factors (1.25) and (1.19) respectively, are listed. In this table also the dimensionless fog formation:

$$M_f = \frac{\dot{m}_f H_{lat}}{h_g(t_b - t_i)} \quad , \tag{2.30}$$

is inserted. This number is the ratio of transported sensible heat (heat transferred by conduction) through the film, in the case of no fog formation and no induced velocity, to created latent heat in the film by fog formation and in the presence of an induced velocity.

The large deviation of the correction factor ratios from unity illustrates the substantial influence of fog formation on both heat and mass transfer. The sensible heat transfer ratio is larger than unity, which would be expected since spontaneous condensation in the film causes extra sensible heat generation. This condensation is at the expense of the diffusional vapour transport from bulk to wall. Indeed the ratio of the diffusion correction factors is smaller than unity. For small vapour mass fractions, the latent (this is heat transferred by transport of vapour and liberation of latent heat) and sensible heat transfer in a heat exchanger are of the same magnitude. Because both kinds of heat transfer are seriously affected by fog formation, it is interesting to calculate the total amount of transferred latent and sensible heat from film to wall:

$$q_{tot} = q + \dot{m}\, H_{lat} \quad , \qquad (2.31)$$

for the classical film model and fog film model. In table 2.1 the ratio of q_{tot} according to the numerical solution and according to the conventional film model is listed. All tabled values are close to unity, implying the total amount of transported heat is hardly altered by fog formation, only the contribution of latent and sensible heat is different. Toor (1971a) derived analytically that in a film without induced velocity, $1 - c_i \cong 1$ and $Le = 1$, the ratio of transferred heat is exactly equal to unity. As the physical situations of table 2.1 are similar, one can conclude that the numerically obtained ratios are in agreement with the afore–said analytical result.

In table 2.1 also the maximum error introduced by assumption (2.17) (or equivalent equation (2.22)) is listed, ϵ defined by equation (2.21). The error increases with increasing fog formation levels, which might be expected, but remains within an acceptable magnitude for realistic conditions (the upper ones of table 2.1).

For the second group of calculations (t_i, c_i) is set equal to (94.81°C, 0.75), and the bulk values (t_b, c_b) equal to (97.63°C, 0.875) and (99.90°C, 0.995). All points are again situated on the saturation line of an air water–vapour mixture. These temperatures and concentrations are relevant to condensers. The calculations are carried out for Le_v equal to 0.8, 0.9, 1 and 1.1, the same latent to specific heat ratio, and equal thermal and diffusion film thicknesses. The values of Le_v are different from those of the previous set of calculations since an evaluation of equation (2.1) indicated that for all afore–mentioned condenser conditions and Le_v equal to 0.5 and 0.75, fog is not formed at all. For these small Le_v values the convex curve (1.50) is entirely situated in the superheated region. Thus, although the interface and bulk properties are both situated on the saturation line, fog is not formed. Consequently, the conventional correction factors (1.19), (1.25) and (1.31) retain their validity for these cases.

	Le_v	$\Theta_{t,fl}/\Theta_t$	$\Theta_{c,fl}/\Theta_c$	$\dot{M}_{fl}$	$\overline{\dot{M}}_{fl}$	δ_a/δ_c	$q_{tot,fl}/q_{tot}$	$H(t_a)$
$t_b = 97.63°C$	0.80	1.019	0.999	0.031	0.026	0.37	1.000	0.77
$c_b = 0.875$	0.90	1.062	0.999	0.121	0.121	1.00	1.000	0.84
	1.00	1.098	0.999	0.198	0.198	1.00	1.000	0.84
	1.10	1.129	0.999	0.261	0.261	1.00	1.001	0.84
$t_b = 99.90°C$	0.80	1.000	1.000	0.000	0.000	0.00	1.000	0.71
$c_b = 0.995$	0.90	1.080	0.999	0.356	0.346	0.14	1.000	0.82
	1.00	1.191	0.999	0.778	0.780	1.00	1.000	0.99
	1.10	1.298	0.998	1.132	1.135	1.00	1.000	0.99

Table 2.2 Results of numerical solution for $(t_i, c_i) = (94.81°C, 0.75)$.

In table 2.2 the calculated correction factor ratios and dimensionless fog formation levels are listed for the cases considered. As for some cases the film is now partly or even entirely superheated, the dimensionless fog layer thickness δ_a/δ_c is also included in this table, $0 \leq \delta_a/\delta_c = \delta_a/\delta_t \leq 1$. In figure 2.1 the determined temperature and concentration profiles in the film, with y as parameter, for $Le_v = 0.8$ and 0.9 are drawn as example. For $Le_v = 0.8$ the curve $G(t)$ is situated in the superheated region, as correctly predicted by equation (2.1). According to this equation fog is formed for $Le_v = 0.9$. With equation (2.11) the border of the superheated region (t_a, c_a) has been determined. In figure 2.1 the continuity of the first derivative dc/dt at the boundary between saturated and superheated zones is evident. In table 2.2 or figure 2.1 it can be seen that for the examined situations the film can be entirely superheated, partly superheated and saturated, or entirely saturated. The correction factor ratios for heat and mass transfer differ most from unity, of course, when the entire film is saturated. For $Le_v \geq 1$ the entire film is always saturated when the bulk is saturated.

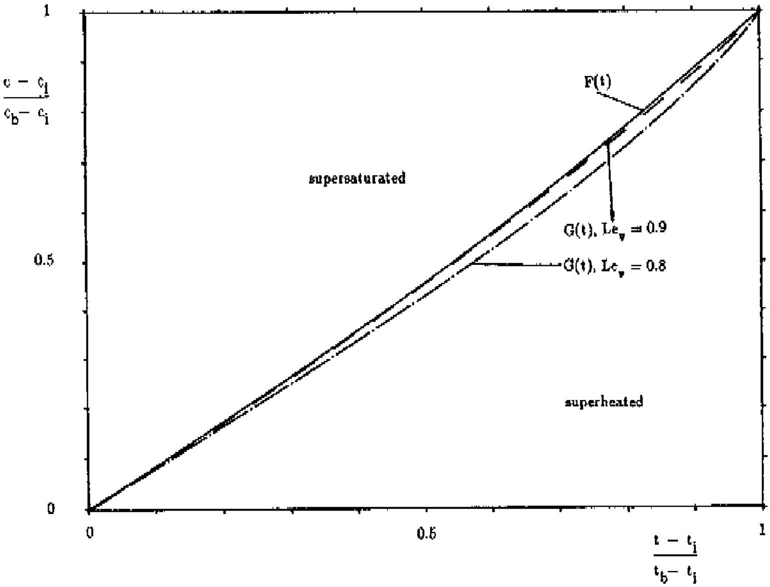

Figure 2.1 Behaviour of vapour concentration and temperature in the film with respect to saturation line, $(t_i, c_i) = (94.81^\circ C, 0.75)$ and $(t_b, c_b) = (99.90^\circ C, 0.995)$.

This feature of the film for $Le_v = 1$ was employed implicitly by Aref'yev and Averkiyev (1979) and is explained in appendix B. In table 2.2 $H(t_a)$ has been included, see equation (C.12), with $t_a = t_i$ substituted for a superheated film and $t_a = t_b$ for an entirely saturated film. One can readily see that the maximum $H(t_a)$ of the film is smaller than Le_v for all cases examined, thus $K > 0$ is assured. In appendix B it is deduced that t_a is always such that $H(t_a) < Le_v$ is fulfilled.

A glance at the total transferred heat and the diffusion correction factor ratios shows that these are now both nearly unity, even for completely saturated films. This means that fog formation does not seriously affect the vapour diffusion and latent heat transfer in condensers. In condensers, however, the main part of transferred heat is latent heat; Sparrow *et al.* (1967), for example, demonstrated that the sensible heat transfer is negligibly small because the temperature difference between wall and bulk is very small. As the diffusional mass transfer is hardly altered by fog formation, not only the overall heat transfer in a condenser will be the same in the case of fog formation, but also the dominant latent mode of heat transfer will remain the same. Or in other words, for condenser calculations the conventional film model will predict heat and mass transfer rates sufficiently accurately, with or without fog formation.

The relatively unimportant effect of fog formation in condensers is once more illustrated by the small amount of fog formed, see $\dot{M}_f$ in table 2.2. One must be aware when the actual amount of formed fog is considered, that the temperature differences (t_b – t_i) pertaining to table 2.1 are much larger than those pertaining to table 2.2. As the maximum introduced error ϵ, which is correlated with K and $\dot{m}_f$, is also much smaller for the here studied physical situations, it has not been listed in table 2.2.

In the analysis of the previous section no attention has been paid to the film momentum equation in the case of fog formation, nor has there been derived a correction factor for friction in a fogged film. The correction for suction or injection is only of importance when the vapour mass fractions are large. The calculation of diffusional mass transfer in the case of fog formation has shown that the diffusion profile in the film is significantly altered only for small vapour mass fractions. But for small vapour mass fractions the mass flux as such is small and thus the friction correction factor close to unity. For large vapour fractions the correction becomes important, but for this case the concentration profile, and pertaining mass flux, is nearly unchanged by fogging.

Accordingly, the author confines himself by suggesting a substitution of the mass flux in the conventional correction factor (1.31) will be a good approximation of the true friction correction factor. The substituted mass flux may be calculated by either the classical or the fog film model.

§2.4 Asymptotic approximation solution

In the previous section the coupled energy and diffusion equation (2.14) of the fog layer has been solved numerically. To this end, a standard shooting method was employed to solve the boundary value problem. This numerical method consists of a combined integration and iteration routine to find a solution which satisfies both boundary conditions (1.8) and (2.3). In the context of an operating heat exchanger t_i and $c_i = F(t_i)$ have to be calculated iteratively, since the interface temperature and concentration in a evaporator or condenser have to obey a local energy balance, and are not known *a priori*. The coupled application of an iteration for t_i, and a shooting method to solve equation (2.14) for each cycle of this iteration, yields long computation times. The derivation of an asymptotic approximate solution of equation (2.14) is therefore desirable and this is presented in this section.

In order to derive an approximate solution of equation (2.14), an assessment of the order of magnitude of the diverse terms is first carried out. For small vapour mass fractions the first term on the left hand side of equation (2.14) is of about the same magnitude as the term on the right hand. The latter is of importance because, even for small c, this term is large by virtue of the presence of the latent specific heat ratio. This becomes evident when the typical values appearing in table 2.1 are considered and one realizes that Le_v is of order unity and $H_{lat}/c_{p,v}$ is of order 120–1200 K for most vapours. The second and non–linear term on the left hand side is very small when compared with the two afore–said terms of equation (2.14). For large vapour mass fractions (see table 2.2 for typical values of c and t) the term on the right hand side completely dominates both the other terms in equation

(2.14). Thus again, the non–linear term plays no role of importance.

The considerations of small and large vapour concentrations yield the relative unimportance of the second and non–linear term on the left hand side of equation (2.14). Evaluating the equation without this non–linear term yields indeed a promising agreement between the reduced solution and the complete numerical solution of equation (2.14). Yet, a much better agreement is obtained by assessing the contribution of this term to the complete solution.

The non–linear term only becomes of some importance for large vapour fractions, when it exceeds the other term on the left hand side of equation (2.14). But again it must be stressed that under these circumstances both terms are small in comparison with the term on the right hand side of the equation. Mathematically, then, for large vapour fractions the solution of:

$$\frac{d^2 Ln(1-c)}{dy^2} = 0 \quad , \tag{2.32}$$

accurately approximates the complete solution of equation (2.14). Integration of equation (2.32) and application of the boundary conditions (1.4) and (2.4) yields:

$$c(y) = 1 - (1 - c_i)\, e^{\frac{y}{\delta_a} Ln\left[\frac{1 - c_a}{1 - c_i}\right]} \qquad (0 \le y \le \delta_a) \quad . \tag{2.33}$$

This solution for the saturated layer, combined with solution (2.6) for the superheated layer, corresponds exactly to the undisturbed diffusion profile (1.6) of a film without fog formation. This is the reason that for large vapour fractions the conventional diffusional correction factor without fog almost coincides with that of the film model with fog, as confirmed by the numerical results listed in table 2.2.

To obtain a higher order approximate solution of equation (2.14), the zero–order solution (2.33) is substituted in the non–linear term of equation (2.14):

$$\mathrm{Le_v}\,\frac{d^2t}{dy^2} - \frac{1}{\delta_a}\,Ln\left[\frac{1 - c_a}{1 - c_i}\right]\frac{dt}{dy} = \frac{H_{lat}}{c_{p,v}}\,\frac{d^2Ln(1 - c)}{dy^2} \quad . \tag{2.34}$$

The asymptotic solution (2.33) has been substituted in the non–linear term since only for large vapour fractions this term becomes of some importance. For small vapour fractions this term is still dominated by both other terms appearing in equation (2.14) or (2.34). Equation (2.34) is integrated twice with respect to y:

$$\mathrm{Le_v}\,t(y) - \frac{1}{\delta_a}\,Ln\left[\frac{1 - c_a}{1 - c_i}\right]\int_{y=0}^{y} t(y)\,dy = \frac{H_{lat}}{c_{p,v}}\,Ln(1 - c(y)) + K_1\,y + K_2 \qquad (0 \le y \le \delta_a) \quad . \tag{2.35}$$

Applying boundary conditions (1.4), (1.8), (2.3) and (2.4) yields the integration constants:

$$K_1 = \frac{\mathrm{Le_v}\,(t_a - t_i)}{\delta_a} - \frac{1}{\delta_a}\,Ln\left[\frac{1 - c_a}{1 - c_i}\right]\left[\frac{H_{lat}}{c_{p,v}} + \frac{1}{\delta_a}\int_{y=0}^{\delta_a} t\,dy\right] \quad , \tag{2.36}$$

and:

$$K_2 = \mathrm{Le_v}\,t_i - \frac{H_{lat}}{c_{p,v}}\,Ln(1 - c_i) \quad . \tag{2.37}$$

The integral appearing in equation (2.36) is assessed with the help of the zero–order solution (2.33). This equation constitutes an expression for c as a function of y, while t as a function of y is needed to solve the integral. In the fog layer, however, c is determined by the saturation function (2.5) as a function of t, and conversely, t is a known function of c. In appendix C the inverse relation is derived for an air water–vapour mixture. However, this complex relation permits no further analytic treatment of the integral. As a compromise, therefore, the saturation line in the saturated region is now roughly approximated as a straight line between (t_i, c_i) and (t_a, c_a):

$$t = F^{\mathrm{inv}}(c) \cong \frac{c - c_i}{c_a - c_i}(t_a - t_i) + t_i \qquad (c_i \le c \le c_a) \quad . \qquad (2.38)$$

In equation (2.38) for c the zero–order solution (2.33) is again substituted and the integral in equation (2.36) is solved analytically as follows:

$$\frac{1}{\delta_a}\int_{y=0}^{\delta_a} t\,dy = \frac{t_a(1 - c_i) - t_i(1 - c_a)}{c_a - c_i} + \frac{t_a - t_i}{Ln\left[\frac{1 - c_a}{1 - c_i}\right]} \quad . \qquad (2.39)$$

Substitution of equation (2.39) into equation (2.36) now yields:

$$K_1 = (Le_v - 1)\,\frac{(t_a - t_i)}{\delta_a} - \frac{1}{\delta_a}\,Ln\left[\frac{1 - c_a}{1 - c_i}\right]\left\{\frac{H_{lat}}{c_{p,v}} + \frac{t_a(1 - c_i) - t_i(1 - c_a)}{c_a - c_i}\right\} \quad . \qquad (2.40)$$

A complete approximate solution (2.35), combined with equations (2.37) and (2.40), of equation (2.14) has now been realized. The dimensionless fog layer thickness is obtained by combining equations (2.5), (2.7), (2.9), (2.22), (2.35) and (2.40):

$$\frac{\delta_c}{\delta_a} = 1 + \frac{1}{Le_v}\left[\frac{(t_b - t_a)Ln\left[\frac{1-c_b}{1-c_a}\right]}{e^{\frac{1}{Le_v}Ln\left[\frac{1-c_i}{1-c_a}\right] + \frac{\delta_t}{Le_v\delta_c}Ln\left[\frac{1-c_b}{1-c_i}\right]} - 1}\;\frac{(Le_v +}{(Le_v - 1)}\right. \tag{2.41}$$

$$\left.\frac{\frac{H_{lat}}{c_{p,v}}\,\frac{1}{1-c_a}\left.\frac{dF}{dt}\right|_{t_a}\;)}{(t_a - t_i) - Ln\left[\frac{1-c_a}{1-c_i}\right]\left[\frac{H_{lat}}{c_{p,v}} - t_a + \frac{t_a(1-c_i) - t_i(1-c_a)}{c_a - c_i}\right]}\right] .$$

The thermal correction factor follows from equations (1.21)–(1.23):

$$\Theta_{t,f} = \frac{\delta_t\left.\frac{dt}{dy}\right|_{y=0}}{(t_b - t_i)} \; . \tag{2.42}$$

The first derivative of t with respect to y at the wall, according to the approximate solution, is determined with the help of equations (2.5), (2.35) and (2.40):

$$\delta_t\left.\frac{dt}{dy}\right|_{y=0} = \frac{\delta_t}{\delta_a} \cdot \tag{2.43}$$

$$\frac{(Le_v - 1)(t_a - t_i) - Ln\left[\frac{1-c_a}{1-c_i}\right]\left[\frac{H_{lat}}{c_{p,v}} - t_i + \frac{t_a(1-c_i) - t_i(1-c_a)}{c_a - c_i}\right]}{Le_v + \frac{H_{lat}}{c_{p,v}}\,\frac{1}{1-c_i}\left.\frac{dF}{dt}\right|_{t_i}} .$$

The dimensionless fog layer thickness in this equation is given by equation (2.41). The diffusional correction factor pertaining to the approximate solution can easily be obtained by combining equations (2.27) and (2.42):

$$\Theta_{c,f} = \frac{\delta_c \left.\frac{dF}{dt}\right|_{t_i} \left.\frac{dt}{dy}\right|_{y=0}}{(c_b - c_i)} \quad . \tag{2.44}$$

The amount of formed fog is determined by equation (2.13) and (2.28):

$$\dot{m}_f = \rho D \left(\left.\frac{dLn(1 - c)}{dy}\right|_{y=0} - \left.\frac{dLn(1 - c)}{dy}\right|_{y=\delta_a} \right) \quad . \tag{2.45}$$

This equation, combined with equations (1.23), (2.35) and (2.36), is written as:

$$\dot{m}_{f2} = \frac{h_g}{H_{lat}} \left[\delta_t \left.\frac{dt}{dy}\right|_{y=0} - \delta_t \left.\frac{dt}{dy}\right|_{y=\delta_a} + \frac{\delta_t}{\delta_a} \frac{(t_a - t_i)}{Le_v} Ln\left[\frac{1 - c_a}{1 - c_i}\right] \right] \quad . \tag{2.46}$$

The first derivative of t in y = 0 in equation (2.46) follows from equation (2.43), the first derivative in $y = \delta_a$ is calculated by combining equations (2.5), (2.35) and (2.40):

$$\delta_t \left.\frac{dt}{dy}\right|_{y=\delta_a} = \frac{\delta_t}{\delta_a} \cdot \tag{2.47}$$

$$\frac{(Le_v - 1)(t_a - t_i) - Ln\left[\frac{1 - c_a}{1 - c_i}\right] \left[\frac{H_{lat}}{c_{p,v}} - t_a + \frac{t_a(1 - c_i) - t_i(1 - c_a)}{c_a - c_i}\right]}{Le_v + \frac{H_{lat}}{c_{p,v}} \frac{1}{1 - c_a} \left.\frac{dF}{dt}\right|_{t_a}} \quad .$$

The dimensionless fog layer thickness appearing in equations (2.43), (2.46) and (2.47) follows from equation (2.41).

§2.5 Results of asymptotic solution

In this section similar calculations to those presented in §2.3 are carried out to compare the predictions of the asymptotic approximate solution with those of the complete numerical solution.

	Le_v	$\Theta_{t,f2}/\Theta_t$	$\Theta_{c,f2}/\Theta_c$	$\dot{M}_{f2}$	$\bar{\dot{M}}_{f2}$	$q_{tot,f2}/q_{tot}$	$\|\epsilon\|$
$t_b = 30^\circ C$	0.50	1.218	0.924	0.391	0.393	1.000	0.096
$c_b = 0.0264$	0.75	1.192	0.901	0.350	0.352	1.000	0.120
	1.00	1.170	0.883	0.316	0.317	1.000	0.136
	1.25	1.153	0.868	0.288	0.289	1.000	0.148
$t_b = 60^\circ C$	0.50	2.411	0.789	2.035	2.068	0.999	0.736
$c_b = 0.1318$	0.75	2.297	0.721	1.871	1.915	0.999	0.802
	1.00	2.177	0.670	1.722	1.760	1.000	0.817
	1.25	2.071	0.629	1.594	1.627	1.000	0.809

Table 2.3 Results of approximate solution for $(t_i, c_i) = (20^\circ C, 0.0144)$, $\delta_a/\delta_c = \delta_a/\delta_t = 1$ for all cases.

In tables 2.3 and 2.4 the results of these calculations are listed which correspond with the computational results of the complete model, as listed in tables 2.1 and 2.2, respectively. To determine the boundary of saturation (t_a, c_a), equation (2.11) has again been employed, yielding identical (t_a, c_a) and $H(t_a)$ again, of course, for all cases examined.

A comparison of all values listed in tables 2.1–2.4, shows the maximum discrepancy between numerical and approximate solutions is of about a few per mille. Even for the largest difference between (t_i, c_i) and (t_b, c_b), the agreement is still very good. This large difference belongs to unrealistically large sensible and latent heat fluxes from gas to wall. It will therefore not be found in ordinary heat exchangers or condensers, it has only been selected to create some deviation between the numerical and approximate solutions.

One can furthermore conclude from tables 2.1 and 2.3 that the error decreases with increasing Le_v.

	Le_v	$\Theta_{t,f2}/\Theta_t$	$\Theta_{c,f2}/\Theta_c$	$\dot{M}_{f2}$	$\overline{\dot{M}}_{f2}$	δ_a/δ_c	$q_{tot,f2}/q_{tot}$	$H(t_a)$
$t_b = 97.63°C$	0.80	1.019	0.999	0.031	0.026	0.37	1.000	0.77
$c_b = 0.875$	0.90	1.062	0.999	0.121	0.121	1.00	1.000	0.84
	1.00	1.098	0.999	0.198	0.198	1.00	1.000	0.84
	1.10	1.129	0.999	0.260	0.261	1.00	1.000	0.84
$t_b = 99.90°C$	0.80	1.000	1.000	0.000	0.000	0.00	1.000	0.71
$c_b = 0.995$	0.90	1.080	0.999	0.356	0.346	0.14	1.000	0.82
	1.00	1.191	0.999	0.777	0.780	1.00	1.000	0.99
	1.10	1.298	0.998	1.130	1.135	1.00	1.000	0.99

Table 2.4 Results of approximate solution for $(t_i, c_i) = (94.81°C, 0.75)$.

For larger Le_v the first term on the left hand side of equation (2.14) gains importance and dominates more the second term, resulting in a smaller deviation. For small vapour fractions it is namely important for the approximation to be accurate that both Le_v and $H_{lat}/c_{p,v}$ are large. For large vapour mass fractions however, the error slightly increases with larger Le_v, see tables 2.2 and 2.4. For these physical situations it is important that $H_{lat}/c_{p,v}$ is large and consequently the right hand side of equation (2.14) dominates both terms on the left hand side. The approximation is based on the fact that $H_{lat}/c_{p,v}$ is large. For water–vapour this ratio is close to 1200 K, but for a lot of other vapours it is a factor 10 smaller. A repetition of all calculations, with $H_{lat}/c_{p,v}$ set equal to 120 K and all other values unchanged, indicated however that the approximation solution is still correct within a few per cent. Since this error is quite acceptable, the approximate solution is not only applicable to water–vapour, but to most other vapours as well.

In tables 2.1–2.4 only results pertinent to conditions found in air–conditioning devices and condensers have been listed. Computations carried out for intermediate vapour fractions and temperatures, for instance found in exhaust gases from dryers, indicate that the agreement is of the same high level as in the cases studied in detail here. Furthermore, since the temperature as a function of y in the fog layer has been found to be similar for evaporation and condensation, the approximation is applicable to evaporation processes as well.

§2.6 Application of the fog film model to channel flow

In preceding sections the conditions have been discussed under which fog formation in the film occurs and modified correction factors derived. In this section the use of this extended film model is demonstrated. This model includes the possibility that the bulk properties move to enter the supersaturated region and that, as a result, bulk fog is created. Similar to the conventional film model, here the bulk values t_b and c_b are taken to be sufficiently approximated by the mixed mean values of these quantities in a cross–section.

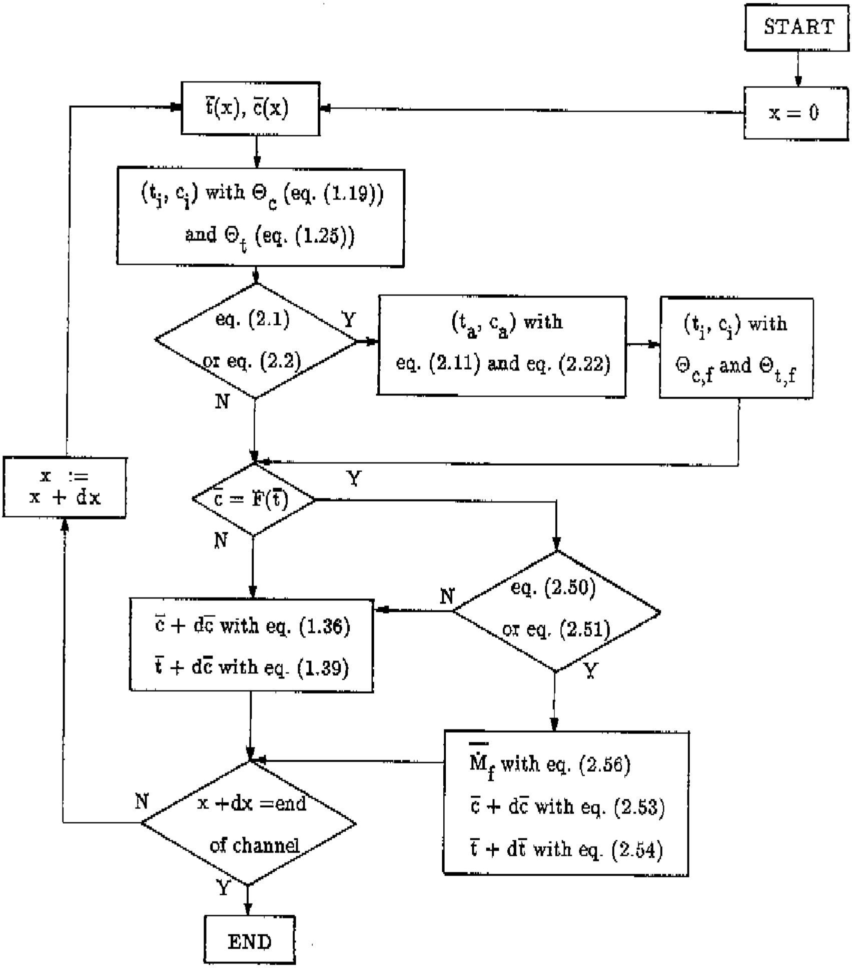
START
x = 0
$\bar{t}(x)$, $\bar{c}(x)$
(t_i, c_i) with Θ_c (eq. (1.19)) and Θ_t (eq. (1.25))
eq. (2.1) or eq. (2.2)
Y
N
(t_a, c_a) with eq. (2.11) and eq. (2.22)
(t_i, c_i) with $\Theta_{c,f}$ and $\Theta_{t,f}$
$\bar{c} = F(\bar{t})$
Y
N
eq. (2.50) or eq. (2.51)
N
Y
$\bar{c} + d\bar{c}$ with eq. (1.36)
$\bar{t} + d\bar{c}$ with eq. (1.39)
$\bar{\dot{M}}_f$ with eq. (2.56)
$\bar{c} + d\bar{c}$ with eq. (2.53)
$\bar{t} + d\bar{t}$ with eq. (2.54)
x +dx =end of channel
N
Y
x := x + dx
END

Figure 2.2 Flow chart of the applied fog film model.

A flow chart, drawn in figure 2.2, illustrates the procedure followed.

Determination of interface conditions (t_i, c_i)

As discussed in a preceding section, in evaporators or condensers the interface temperature t_i and associated vapour mass fraction c_i (= $F(t_i)$) is determined by a local energy balance. The net latent and sensible heat flux from or to an interface must be zero, the fluxes on the gas side being given by the conventional film model corrections for heat and mass transfer. Once t_i has been obtained, equation (2.1) or equation (2.2) for suction or injection, respectively, is employed to determine whether the vapour concentration/temperature line (1.50) is located in the supersaturated region. These conventional film model expressions are based on the assumption of no intersection of this relation with the saturation line. If this proves indeed to be the case, the t_i and fluxes calculated, according to equations (2.1) or (2.2), are correct and the amount of fog formed in the film equal to zero.

If, on the other hand, an intersection between equation (1.50) and saturation line is detected, an alternative procedure has to be followed. First, the temperature and vapour concentration (t_a, c_a) on the boundary of the saturated and superheated region is determined numerically with the help of equations (2.11) and (2.22). By employing a local energy balance, t_i is then re-determined. But during this iterative procedure now the fog correction factors $\Theta_{c,f}$ and $\Theta_{t,f}$ are utilized to predict the transfer on the gas side.

Incremental mass and energy balances

As long as the bulk (or mean mixed flow) is not saturated (that is to say, ($\bar{t}$, $\bar{c}$) is located in the superheated region) the mixture's incremental temperature and vapour concentration change are still governed by equations (1.38) and (1.36). Note that it is possible for fog to be predicted in the film without the bulk flow being saturated. Physically this means that if the flow in a cross-section were mixed, fog present near the wall would evaporate on contact with the superheated core flow.

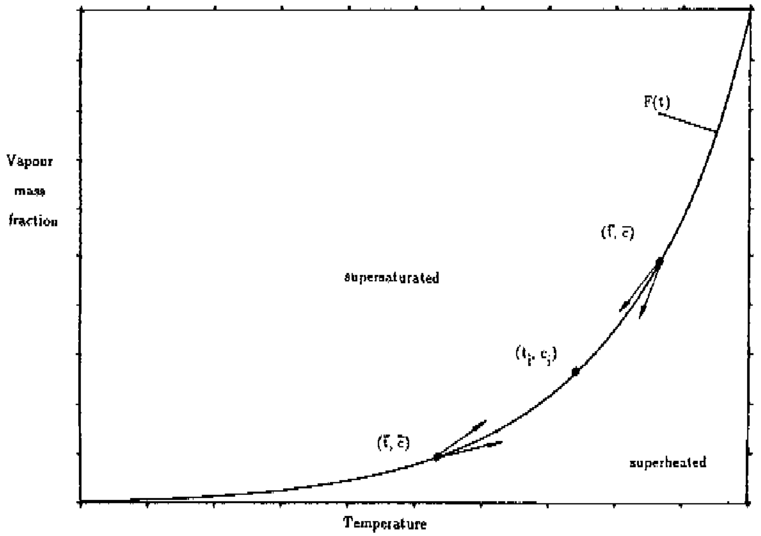
F(t)
$(\bar{t}, \bar{c})$
Supersaturated
(t_i, c_i)
$(\bar{t}, \bar{c})$
superheated
Vapour mass fraction
Temperature

Figure 2.3 Path of mixture's bulk properties $(\bar{t}, \bar{c})$.

The slope of the $(\bar{t}, \bar{c})$ path in the case of fog formation in the film is now obtained by combining equations (1.36) and (1.38), and applying equations (1.17), (1.23), (2.25), (2.27) and (2.42):

$$\frac{d\bar{c}}{d\bar{t}} = \frac{d\bar{G}}{d\bar{t}} = \frac{1}{Le}\,\frac{-\dfrac{1-\bar{c}}{1-c_i}\left.\dfrac{dF}{dt}\right|_{t_i}}{\dfrac{1}{Le_v}\,\dfrac{\bar{t}-t_i}{1-c_i}\left.\dfrac{dF}{dt}\right|_{t_i}-1} \tag{2.48}$$

In chapter 1 we have deduced the path of the bulk properties for the case that the film is superheated. For the case fog is formed in the film a similar result is now obtained by separating the variables $\bar{c}$ and $\bar{t}$ and integrating:

$$\bar{c} = \bar{G}(\bar{t}) = 1-(1-\bar{c}(x=0))\left[\frac{(\bar{t}-t_i)\left.\dfrac{dF}{dt}\right|_{t_i}-Le_v(1-c_i)}{(\bar{t}(x=0)-t_i)\left.\dfrac{dF}{dt}\right|_{t_i}-Le_v(1-c_i)}\right]^{\frac{Le_v}{Le}} , \tag{2.49}$$

whereby as boundary condition the vapour fraction and temperature at an arbitrary location, $x = 0$, has been applied. Equations (2.48) and (2.49) are used to detect the intersection of the path of the bulk properties and the saturation line. Equation (1.51) for a superheated film and equation (2.49) for a (partly) saturated film hold up to the point when the bulk flow is saturated ($\bar{c} = F(\bar{t})$) and the path of the mixture's bulk properties is directed into the supersaturated region, see figure 2.3.

For condensation the condition for entry of the bulk into the supersaturated region then corresponds mathematically to:

$$\frac{d\bar{G}}{d\bar{t}} < \left.\frac{dF}{dt}\right|_{\bar{t}} , \tag{2.50}$$

and for evaporation:

$$\frac{d\overline{G}}{d\overline{t}} > \left.\frac{dF}{dt}\right|_{\overline{t}} \quad . \tag{2.51}$$

The incremental mass balance in the case of such a saturated bulk flow (*i.e.* one which would be supersaturated and therefore fogged after mixing of a cross–section) flowing through a channel reads:

$$\frac{d(\rho\overline{u})}{dx} = -\frac{4}{D_h}\left[g_m\,\Theta_c\,\frac{\overline{c} - c_i}{1 - c_i} + \overline{\dot{m}}_f\right] \quad . \tag{2.52}$$

Neglecting the fraction of fog droplets, for a binary mixture the channel mass flux $(\rho\overline{u})(x)$ can again be expressed in terms of the vapour concentration by equation (1.35), yielding:

$$\frac{d\overline{c}}{dx} = \frac{-\,4g_m}{D_h(\rho\overline{u})(x=0)}\left[\Theta_c\,\frac{\overline{c} - c_i}{1 - c_i} + \frac{\overline{\dot{m}}_f}{g_m}\right]\frac{(1 - \overline{c})^2}{(1 - \overline{c}(x=0))} \quad . \tag{2.53}$$

The differential energy equation for the supersaturated bulk flow becomes:

$$\frac{d\overline{t}}{dx} = \frac{-\,4h_g}{c_p D_h(\rho\overline{u})(x=0)}\left[\Theta_t - \frac{g_m c_{p,v}}{h_g}\,\Theta_c\,\frac{\overline{c} - c_i}{1 - c_i} - \frac{H_{lat}\overline{\dot{m}}_f}{h_g(\overline{t} - t_i)}\right](\overline{t} - t_i)\,\frac{(1 - \overline{c})}{(1 - \overline{c}(x=0))} \quad . \tag{2.54}$$

As the fraction of droplets is very small, it is expected not to alter the mixture's physical properties significantly.

In the energy equation the created bulk fog appears as a heat source, and in the gas mass conservation relation as a sink of matter. This bulk fog weakens the temperature drop and increases the fall in vapour fraction in situations with wall condensation. For wall evaporation, the formed fog increases the temperature rise and reduces the vapour fraction increment in a channel. The amount of fog in the bulk gas flow is such that the mixture's bulk properties ($\bar{t}$, $\bar{c}$) follow the saturation line. Mathematically the effective amount of fog is therefore calculated by requiring that:

$$\frac{d\overline{G}}{d\bar{t}} = \left.\frac{dF}{dt}\right|_{\bar{t}} . \tag{2.55}$$

With the help of equations (1.17), (1.23), (1.34), (1.40), (2.30) and (2.53)–(2.55), the corresponding dimensionless amount of bulk fog can be determined as:

$$\overline{\dot{M}}_f = \frac{\Theta_t \left.\frac{dF}{dt}\right|_{\bar{t}} - \frac{Sh}{Nu}\,\Theta_c\,\frac{\bar{c} - c_i}{1 - c_i}\left[\frac{1}{Le_v}\left.\frac{dF}{dt}\right|_{\bar{t}} + \frac{1}{Le}\,\frac{1 - \bar{c}}{\bar{t} - t_i}\right]}{\left.\frac{dF}{dt}\right|_{\bar{t}} + (1 - \bar{c})\,\frac{Le_v}{Le}\,\frac{c_{p,v}}{H_{lat}}} . \tag{2.56}$$

For a mixture with a (partly) saturated film and with bulk properties that enter the supersaturated region, the fog film model correction factors $\Theta_{t,f}$ and $\Theta_{c,f}$, instead of Θ_t and Θ_c, respectively, should be used in equations (2.52)–(2.54) and (2.56).

In tables 2.1–2.4 the bulk fog formation according to equation (2.56) has been included with the Lewis number in equations (1.51), (2.48) and (2.56) chosen as unity and equality (1.48) substituted. The amount of formed fog in the film is smaller than, but close to, the bulk fog for all examined cases where the entire film was saturated ($\delta_a = \delta_c = \delta_t$).

On the other hand, the formed fog in the film is larger than the bulk fog when the film is partly superheated. This result would in fact be expected: the smaller the saturated part of the film is, the closer the correction factors approximate the conventional correction factors. For Le = 1 the bulk properties ($\bar{t}$, $\bar{c}$), according to the conventional film model, are directed along $\overline{G}(t)$, which coincides with G(t), see §1.5. This implies when a larger part of the film is situated in the superheated region, ($\bar{t}$, $\bar{c}$) is less directed into the saturated region and more directed along G(t). This phenomenon becomes more pronounced when a larger part of the film is superheated, which is indeed confirmed by tables 2.2 and 2.4. It is interesting to observe that in such cases fog is present in a part of the film near the wall and in the bulk, both regions separated by a superheated film part. Furthermore, for an entirely superheated film, *e.g.* see figure 2.1 for G(t) pertaining to $Le_v = 0.8$, the mixture follows this curve. This means that the bulk remains entirely within the superheated region while flowing through a channel: equations (1.51) and (2.50) then predict no entering of the bulk properties into the supersaturated region and hence bulk fog is not formed.

§2.7 The effect of fog and induced velocity on nickel evaporation into helium

One field of problems involving the combined effects of induced velocity and fog formation, is the evaporation of iron/nickel alloys into stagnant helium. The enhancement of evaporation by fog formation has been described theoretically by Turkdogan (1964), Rosner (1967) and Hills and Szekely (1964, 1969), and investigated experimentally by Turkdogan and Mills (1964). The two former investigators treated supersaturation in the gas in terms of a CSM. In both papers the assumption was made that the temperature field in the film is undisturbed by fog formation and therefore remains a linear function of the coordinate. This representation of the process is only allowed for cases where the vapour is extremely dilute. On the basis of a combined analysis of the energy and diffusion equations, coupled with the basic saturation condition, Hills and Szekely (1969) obtained good agreement with the experimental data of Turkdogan and Mills (1964). In their analysis of nickel evaporation, however, the induced velocity in the film was not taken into account. In this section therefore their model's domain of validity is extended by application of the approximate solution of §2.4.

The total absolute pressure P_{tot} of the system amounts to 1 atmosphere (= 1.01325 bar) and the bulk properties concerned are: $\bar{t} = 77^\circ C$, $\bar{c} = 0$. The interface vapour fraction c_i is a function of t_i and follows from appendix C. The liquid saturation pressure is applicable since $t_i \geq 1500^\circ C$, which is well above the melting point of nickel ($\cong 1455^\circ C$). In the vicinity of the wall the fog droplets are in liquid state as well of course; but Turkdogan (1964) furthermore discussed that the droplets remain also in a liquid state for temperatures of 300—400°C below the melting temperature. As the coupled heat and mass transfer is governed in the vicinity of the surface, and the difference between liquid and solid vapour pressure is modest for $t < 1100^\circ C$, the liquid vapour pressure is taken to prevail in the entire film.

In view of Le being close to unity (typically Le = 2.2, see Rosner (1967)) and the absence of externally imposed flow, the approximation $\delta_t = \delta_c$ is applicable. The specific heat of the mixture follows from the expression for perfect monatomic gases:

$$c_p = \frac{5R}{2M} \quad , \tag{2.57}$$

where R is the universal gas constant, see appendix C. The mean molecular mass M is evaluated with the help of the arithmetic mean of the mole fractions of nickel and helium at the interface and bulk. The specific heat $c_{p,v}$ of nickel follows readily from equation (2.57) when $M = M_v$ is substituted. Substituting all afore–said values in equation (2.11) yields as boundary of saturated and superheated region ($t_a = 79.5^\circ C$, $c_a \cong 0$). Since $t_i \geq 1500^\circ C$ the conclusion can be drawn that $(t_a, c_a) \cong (\bar{t}, \bar{c})$ and hence $\delta_a/\delta_c = \delta_a/\delta_t \cong 1$: thus an entirely fogging film, which has been assumed implicitly in fact by Hills and Szekely (1969). Substituting these values into equations (2.43) and (2.44) now yields as correction factor for the effect of injection and fog formation on mass transfer:

$$\Theta_{c,f2} = \frac{\left(\frac{c_p}{c_{p,v}}\,Le - 1\right)(\bar{t} - t_i) + Ln(1 - c_i)\left[\frac{H_{lat}}{c_{p,v}} + \frac{(\bar{t} - t_i)(1 - c_i)}{-c_i}\right]\left.\frac{dF}{dt}\right|_{t_i}}{-\,Le\,\frac{c_p}{c_{p,v}}\,c_i - \frac{H_{lat}}{c_{p,v}}\,\frac{1}{1 - c_i}\,\left.\frac{dF}{dt}\right|_{t_i}\,c_i} \qquad (2.58)$$

The approximate solution can be applied as both $H_{lat}/c_{p,v}$ and Le_v are large; $H_{lat}/c_{p,v} \cong$ 18000 K ($H_{lat} = 6.38\ 10^6$ J/kg, see Smithells (1976)) and $17 < Lec_p/c_{p,v} \equiv Le_v < 33$ (c_p depends on t_i). In §2.5 we have seen that for moderate temperatures, $t_i \leq 2500°C$ ($c_i \leq 0.66$), the accuracy of the asymptotic solution improves with larger $H_{lat}/c_{p,v}$ and Le_v.

For $c_i << 1$ equation (2.58) is approximated by:

$$\Theta_{c,f2} = \frac{Le\ (t_i - t) + \frac{H_{lat}}{c_p}\,c_i\,\left.\frac{dF}{dt}\right|_{t_i}}{c_i Le + c_i\,\frac{H_{lat}}{c_p}\,\left.\frac{dF}{dt}\right|_{t_i}} \qquad (2.59)$$

When Le = 1 is substituted this correction factor clearly corresponds with "Sh/Nu" ("eq. (14)", in which the second bracket of the numerator should be placed after the last term) of Hills and Szekely (1969). For $c_i dF/dt(t=t_i) \cong 0$ equation (2.59) further reduces to:

$$\Theta_{c,f2} = \frac{t_i - \bar{t}}{c_i} \frac{dF}{dt}\bigg|_{t_i} , \tag{2.60}$$

which corresponds with "j''_{max}/j''_{min}" ("eq. (17)" with $\mathcal{S} = 1$) of Rosner (1967) when $c_i^{-1} dF/dt(t_i) \equiv F^{-1}(t_i) dF/dt(t_i) \cong \beta\,[K]/T^2$ (see equations (C.3) and (C.8)) is substituted.

The resulting correction factors for evaporation are now calculated for interface temperatures ranging from 1500°C up to 2500°C, and drawn in figure 2.4. In this figure also the experimental data of Turkdogan and Mills (1964) and theoretical CSM predictions of Turkdogan (1964) and Rosner (1967) are depicted, taken from Hills and Szekely (1969).

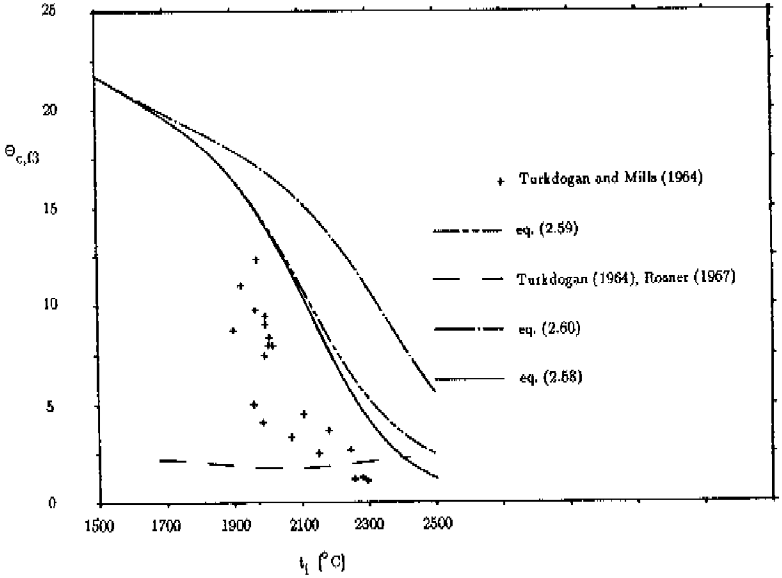

Figure 2.4 Mass transfer correction factors for evaporation of nickel into helium.

The figure shows the enhancement of the evaporation rates, $\Theta_{c,f2} > 1$, by fog formation in the film. Equations (2.60) clearly overestimates this enhancement because it does not account for the effect of liberated latent heat on the temperature profile in the film. The principle difference between equation (2.58) and equation (2.59) is caused by the allowance, made in the former, for the reducing effect of injection on evaporation. The difference between the two increases with increasing t_i and c_i, as might be expected. For $t_i = 2500^\circ C$ injection already causes a reduction of about 50 per cent, which will rise dramatically when the boiling temperature of nickel ($\cong 2915^\circ C$) is approached (that is to say, c_i approaches unity). Equation (2.58), however, still overpredicts $\Theta_{c,f2}$, owing to the assumption of the saturation condition. If the effect of supersaturation in the mixture were taken into account, $\Theta_{c,f2}$ would be further reduced.

§2.8 Conclusions

The conventional film model issues from heat, mass and momentum transfer in a film next to a wall. In this chapter it has been demonstrated with slope conditions (2.1) and (2.2) for wall condensation and wall evaporation, respectively, that in a binary mixture a part of or the entire film is supersaturated. On the basis of the saturation condition the existence and magnitude of the fogging film region have been determined and calculated.

The solution of the governing non–linear basic equation of diffusion and energy in the fog layer has been found both numerically and approximately with an asymptotic analysis. Evaluating the heat and mass transfer rates proved the large influence of fog formation. In particular for small vapour fractions, the effect of fog formation on the contributions of latent and sensible heat transfer is significant, as well as the amount of produced fog. On the other hand, the mass transfer in a mixture with large vapour mass fractions, diffusional latent heat transfer is the dominant mode in a condenser or evaporator, is hardly not affected by fog formation. To all physical situations applies that the total amount of transferred heat is nearly the same as for a film without fog formation.

For large vapour fractions the temperature and vapour fraction in the film, correlated by $G(t)$, can be situated in the superheated region, even when the bulk is saturated. This is due to the fact that for large vapour fractions and $Le_v < 1$ the curvature of $G(t)$ is such that it lies entirely in the superheated region and consequently, the classical film model remains valid. The major role of Le_v is once more emphasized when K, which should be positive in the fog layer, is considered. This condition is fulfilled for $Le_v \geq 1$, but not guaranteed for $Le_v < 1$. The computational examples in this chapter disclosed however that $K > 0$ in all fog layers considered.

The here derived approximate solution has been compared for condensation in various air water–vapour mixtures with the complete numerical solution of the governing equation in the fog layer. Numerous calculations indicate the reliability of this solution to condensation and evaporation, and applicability to most other vapours as well.

An alternative way of adequate describing heat and mass transfer in condensers and evaporators, allowing fog formation in the film and/or in the bulk flow, has been discussed in great detail. The recommended new procedure is illustrated by means of a flow chart. It corrects both the local transfer coefficients and direction of the bulk properties' path in the presence of both an induced velocity and fog formation (in the film and/or in the bulk of the mixture).

In the previous section the approximate solution has been utilized to predict the evaporation of nickel into helium, in particular its enhancement by fog formation and reduction by the induced velocity. Comparing the results with those of previous investigators, it was demonstrated that at higher interface temperatures and vapour fractions the enhancement is significantly reduced by the injection effect. The investigation further suggested that a combined consideration of the induced velocity and possible supersaturation would result in a still better representation of the system examined.

3. THE COMPOUND FOG FILM MODEL

§3.1 Introduction

The classical film model correction factors for the effect of suction and injection were derived and applied in chapter 1 and extended to include the formation of fog in chapter 2. This new film model provides correction factors which account for the effect of both an induced velocity and fog formation. In chapter 2 the calculated results illustrated that for small vapour mass fractions, implying in turn small induced velocities, the effect of fog formation on heat and mass transfer is greatest. As this interaction between fog–related heat and mass transfer is extremely interesting and the governing equations are significantly simplified without induced velocity, in this chapter the limiting case is analyzed in which fog is formed in the film but the vapour mass fraction is small.

Formation of fog in dilute vapour non–condensables mixtures has been the subject of numerous investigations in the past. In the introduction of chapter 2 the studies based on the critical saturation model (CSM) and on the saturation condition have already been discussed. Studies of fog formation in dilute one–dimensional systems, in combination with the saturation condition, have been carried out by Hills and Szekely (1964, 1969) and Toor (1971a, 1971b). The former investigators proceeded from saturated bulk properties and an entirely saturated film. By the latter, employing the tangency condition, the existence of a saturated region and its boundary with the superheated region were determined. All presented theories, however, were limited to cases where Le = 1 (and $\delta_t = \delta_c$) and not brought within the scope of a general fog film model which can be applied to convective heat and mass transfer.

Here then, a film of a binary mixture with any Le value will be considered but without induced velocity, this physical simplification being permissible when the vapour mass fraction is sufficiently small. The error, introduced by omitting this velocity, will be assessed thoroughly by means of an asymptotic analysis.

The possible existence and magnitude of a fog layer in the film will be determined and explained graphically. The simplified governing equations of heat and mass transfer in the film are treated analytically and compact and useful correction factors are derived. These correction factors for heat and mass transfer give a clear insight into the influence of the diverse parameters on fog formation.

The film model approach to fog formation is then applied to closed channel flow and analytical expressions for the bulk vapour mass fraction and bulk temperature variation in the channel derived. Since attention is focussed only on the interaction between the energy and diffusion equations when fog is formed (and not on the effect and presence of the induced velocity in these equations), the analysis presented here will not yield a correction for the friction coefficient, as this is affected only by suction or injection.

Furthermore, it will be demonstrated that the derived fog correction factors can be adapted easily to heat and mass transfer in the presence of suction or injection. In this way a compound fog film model is derived which is based on relatively simple equations, and can be applied to heat and mass transfer in the presence of both fog formation and an induced velocity. Finally, the fog film model is compared extensively with theoretical and experimental results of two–dimensional free and forced convective heat and mass transfer analyses, performed by previous investigators.

§3.2 Asymptotic analysis of the film for a negligible induced velocity (NIV)

The present analysis is based on:

- the saturation condition, and
- no induced velocity (NIV).

The first assumption has already been discussed in the previous chapter. The error introduced by not taking the induced velocity into account is assessed with the help of an asymptotic analysis of equations (1.6) and (1.10) for small vapour mass fractions. The underlying theory of the applied techniques can be found in the standard work of Van Dyke (1975).

When:

$$\epsilon_1 = \frac{c_b(x=0) - c_i}{1 - c_i} \quad , \tag{3.1}$$

tends to zero, equation (1.6) can be approximated by:

$$\frac{c - c_i}{c_b - c_i} = \frac{y}{\delta_c}\left(1 + O\{\epsilon_1\}\right) \quad , \tag{3.2}$$

and equation (1.10) by:

$$\frac{t - t_i}{t_b - t_i} = \frac{y}{\delta_t}\left(1 + O\{\frac{\epsilon_1}{Le_v}\}\right) \quad . \tag{3.3}$$

In equation (3.1) the entrance vapour mass fraction $c_b(x=0)$ figures since this is the most extreme condition. In a channel the local bulk vapour mass fraction is always situated between the entry value and the vapour fraction at the wall c_i. The magnitude of Le_v, appearing in equations (1.10) and (3.3), is usually of order unity. Equations (3.2) and (3.3) indicate that the vapour fraction and temperature profiles tend to linear functions of y as $|\epsilon_1|$ becomes small, which is for instance the case for mixtures with dilute vapour.

The solutions of the diffusion equation (1.2) and the energy equation (1.7) are exactly straight lines when the induced velocity (1.3) is not included in these equations. The error magnitude of omitting the induced velocity from both basic equations is thus governed by the second term on the right hand sides of equations (3.2) and (3.3). When the vapour fractions c_i and c_b, and the modified Lewis numbers Le_v listed in tables 2.1 or 2.3 are considered, it is evident that the magnitude of ϵ_1 and hence the introduced error, is very small. In particular when one realizes that the largest tabulated difference between bulk and interface properties is so large that it will practically never be found in common situations.

Since the temperature and vapour mass fraction profiles tend to a linear dependence on y for small vapour mass fractions, the relation between c and t will be linear as well. The relation between c and t in a film with induced velocity, represented by equation (1.50), is furthermore linear if Le_v is equal to unity, regardless of the magnitude of ϵ_1. G(t) therefore tends to a linear function of t if both ϵ_1 and ϵ_2 are close to zero, where:

$$\epsilon_2 = Le_v - 1 \quad . \tag{3.4}$$

Thus equation (1.50) can be asymptotically expanded for small ϵ_1 and ϵ_2 as:

$$c = G(t) = c_i + (c_b - c_i)\,\frac{\delta_t}{\delta_c}\left[\frac{t - t_i}{t_b - t_i}\right](1 + O\{\epsilon_1\ \epsilon_2\}) \quad (t_i \le t \le t_b). \tag{3.5}$$

Equations (3.2), (3.3) and (3.5) indicate the small influence of the induced velocity for small ϵ_1. Accordingly, in this chapter the induced velocity is not considered and the first order approximations of equations (1.6) and (1.50), and zero-order approximation of equation (1.10) (which correspond with equations (3.2), (3.5) and (3.3), respectively, with $\epsilon_1 = 0$ substituted) for small ϵ_1 will be employed from now on.

To verify whether fog is formed, equation (3.5), with ϵ_1 set equal to zero, is employed. Substituting equation (3.5) into slope condition (2.1) for suction yields:

$$\left.\frac{dF}{dt}\right|_{t_i} < \left.\frac{dG}{dt}\right|_{t_i} = \frac{c_b - c_i}{t_b - t_i}\frac{\delta_t}{\delta_c} \quad , \tag{3.6}$$

and applying equation (3.5) in equation (2.2) for injection yields:

$$\left.\frac{dF}{dt}\right|_{t_i} > \left.\frac{dG}{dt}\right|_{t_i} = \frac{c_b - c_i}{t_b - t_i}\frac{\delta_t}{\delta_c} \quad . \tag{3.7}$$

The possible intersection of the saturation line, implying the formation of fog, is detected with equations (3.6) and (3.7).

When these equations predict formation of fog in the film, see figure 3.1, a superheated and a saturated region are distinguished. In $0 \leq y \leq \delta_a$ the film is saturated, and in $\delta_a \leq y \leq \delta_c$ or δ_t the film is superheated. The fog film thickness δ_a is yet to be determined. At the boundary of the superheated and saturated regions the temperature and vapour fraction are defined by equations (2.3) and (2.4), respectively. In the superheated region, defining:

$$\epsilon_3 = \frac{c_b - c_a}{1 - c_a} \quad , \tag{3.8}$$

the zero–order approximation for small $|\epsilon_3|$ of the temperature, represented by equation (2.7), reads:

$$t(y) = \frac{t_b\,(y - \delta_a) - t_a\,(y - \delta_t)}{(\delta_t - \delta_a)} \qquad (\delta_a \leq y \leq \delta_t) \quad . \tag{3.9}$$

The first order approximation for small $|\epsilon_3|$ of the vapour fraction, represented by equation (2.6), in the superheated region reads:

$$c(y) = \frac{c_b\,(y - \delta_a) - c_a\,(y - \delta_c)}{(\delta_c - \delta_a)} \qquad (\delta_a \le y \le \delta_c) \ . \tag{3.10}$$

Eliminating y from equations (3.9) and (3.10) results in:

$$c = G(t) = \frac{t - t_a}{t_b - t_a}\frac{\delta_t - \delta_a}{\delta_c - \delta_a}(c_b - c_a) + c_a \qquad (t_a \le t \le t_b) \ . \tag{3.11}$$

Relation (3.11) is linear since both c and t depend linearly on y in the superheated region. Equation (3.11) is in fact the first order approximation of equation (2.8) for small $|\epsilon_3|$.

As no solution in closed form for the fog layer's governing equations was derived in chapter 2, it is not possible to derive approximate expressions for small $|\epsilon_3|$ from them. Accordingly, the basic equations are first linearized and then solved. The linearized diffusion equation in the fog layer (equation (A.11), in the limit of small c) reads:

$$\rho\mathbb{D}\,\frac{d^2c}{dy^2} = K \ , \tag{3.12}$$

with associated boundary conditions (1.4) and (2.4). The energy equation in the fog layer, without induced velocity reads:

$$k\,\frac{d^2t}{dy^2} = -\,H_{lat}\,K \ , \tag{3.13}$$

with appropriate boundary conditions (1.8) and (2.3). In the fog layer, $0 \le y \le \delta_a$, and on the borders $y = 0$ and $y = \delta_a$, the vapour fraction is related to the temperature by the saturation line (2.5). The amount of formed fog K is eliminated from equations (3.12) and

(3.13), the resulting equation is integrated twice with respect to y, and boundary conditions (1.4), (1.8), (2.3) and (2.4) are applied, yielding:

$$\frac{H_{lat}}{c_p} c(y) + \mathrm{Le}\, t(y) = \frac{H_{lat}}{c_p} \frac{y\ (c_a - c_i)\ +\ c_i\delta_a}{\delta_a} + \qquad (0 \le y \le \delta_a)$$

$$\mathrm{Le}\,\frac{y\ (t_a - t_i)\ +\ t_i\delta_a}{\delta_a} \qquad (3.14)$$

this equation is an implicit solution of t as a function of y, because c is prescribed by equation (2.5), in the range $t_i \le t \le t_a$, as a function of t.

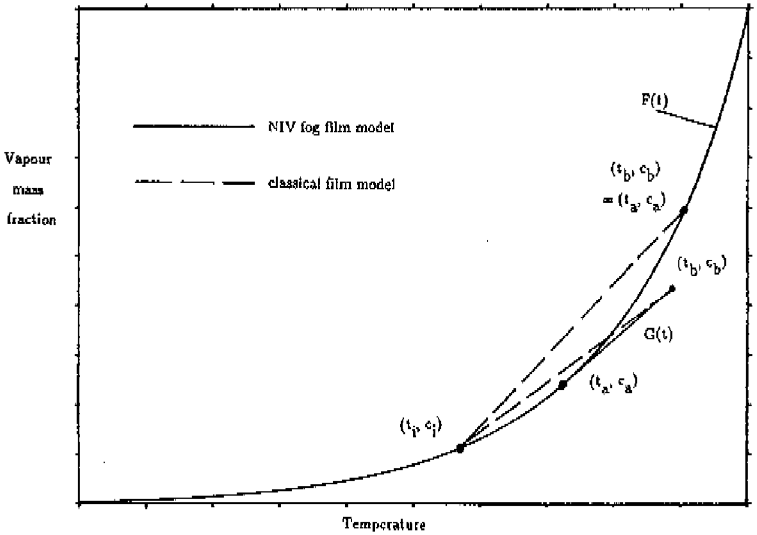

Figure 3.1 Determination of the boundary (t_a, c_a) of the superheated and saturated regions for two (t_b, c_b), $\delta_t = \delta_c$.

On the border of the superheated and saturated region the vapour fraction and temperature profiles obey the gradient–continuity conditions (2.10) and (2.9), respectively. Combining these equations to eliminate y, and substituting equations (3.11) and (2.5) yields:

$$\left.\frac{dF}{dt}\right|_{t_a} = \left.\frac{dG}{dt}\right|_{t_a} = \frac{c_b - c_a}{t_b - t_a}\frac{\delta_t - \delta_a}{\delta_c - \delta_a} \quad . \tag{3.15}$$

Equation (3.15) prescribes mathematically that (t_a, c_a) is situated on the saturation line in such a way that the straight line (3.11) of the superheated region is tangent in (t_a, c_a) to the saturation line (2.5). Thus (t_a, c_a) coincide with (t_b, c_b) when the bulk is saturated, implying that the entire film is saturated when the bulk is saturated. This feature of the film for small vapour mass fractions (or for $Le_v = 1$) is explained in appendix B. In figure 3.1 the determination of (t_a, c_a) is represented graphically for the cases of a saturated and a superheated mixture.

The dimensionless fog layer thickness follows from equation (2.9), combined with equations (3.9), (3.14), (3.15) and the first order approximation of equation (2.17) for small $|\epsilon_1|$ and $|\epsilon_3|$:

$$\frac{c_b - c_a}{c_b - c_i} = \frac{\delta_c - \delta_a}{\delta_c} \quad , \tag{3.16}$$

as:

$$\frac{\delta_a}{\delta_t} = \frac{Le\,(t_a - t_i) + \dfrac{H_{lat}}{c_p}(c_a - c_i)}{Le\,(t_b - t_i) + \dfrac{H_{lat}}{c_p}(c_b - c_i)\,\dfrac{\delta_t}{\delta_c}} \quad . \tag{3.17}$$

Equation (3.16) is based on the assumption of a undisturbed (linear) vapour profile in the saturated part of the film; it is introduced to retain in the analysis the option of unequal thermal and diffusional film thicknesses. In the previous chapter it was shown that the introduced error can be neglected for practical situations, see tables 2.1 and 2.3.

The correction factor for transferred heat is now obtained by comparing the heat transfer with fog formation with the heat transfer without fog formation, resulting in expression (2.42). Differentiating (3.14) with respect to y, applying the saturation condition (2.5), and substituting (3.17) into equation (2.42) results, according to the NIV fog film model, in the following thermal correction factor:

$$\Theta_{t,f3} = \frac{1 + \frac{H_{lat}}{c_p}\frac{1}{Le}\frac{c_b - c_i}{t_b - t_i}\frac{\delta_t}{\delta_c}}{1 + \frac{H_{lat}}{c_p}\frac{1}{Le}\left.\frac{dF}{dt}\right|_{t_i}} . \qquad (3.18)$$

The NIV correction factor for mass transfer is obtained by application of equations (2.27) and (3.18):

$$\Theta_{c,f3} = \frac{1 + \left[\frac{H_{lat}}{c_p}\frac{1}{Le}\frac{c_b - c_i}{t_b - t_i}\frac{\delta_t}{\delta_c}\right]^{-1}}{1 + \left[\frac{H_{lat}}{c_p}\frac{1}{Le}\left.\frac{dF}{dt}\right|_{t_i}\right]^{-1}} . \qquad (3.19)$$

The correction factors (3.18) and (3.19) are very compact and useful results, since they follow directly from the local bulk conditions (t_b, c_b), the interface conditions (t_i, c_i), and the saturation line F(t). To determine the correction factors the iterative calculation of (t_a, c_a) using equation (3.15), and of the dimensionless fog film thickness (3.16), are not necessary.

Moreover, the analytical expressions for the correction factors clarify the influence of the diverse parameters and numerical results listed in tables 2.1 and 2.3. When fog condition (3.6) for condensation and equation (3.7) for evaporation are considered, one can readily see that $\Theta_{t,f3}$ is larger and smaller than unity for condensation and evaporation, respectively. A similar consideration of equation (3.19), in combination with equations (3.6) and (3.7), yields that $\Theta_{c,f3}$ is smaller and larger than unity for condensation and evaporation, respectively.

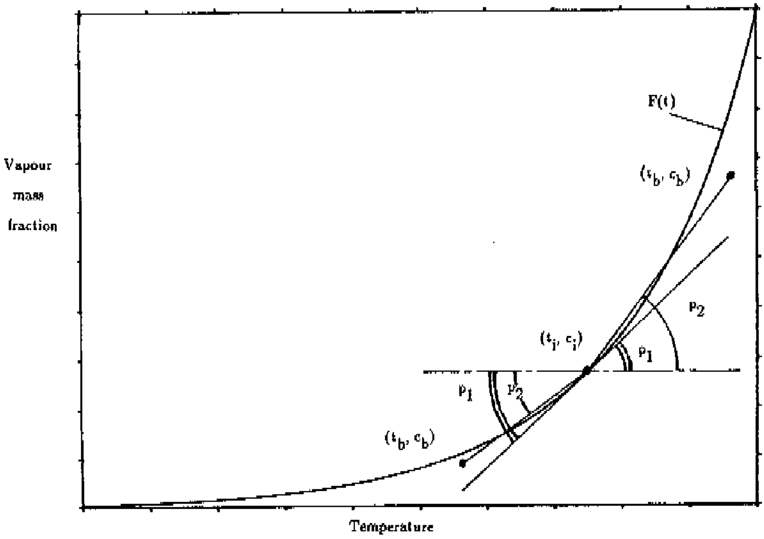

Figure 3.2 Graphical representation of the effect of fog formation, $\delta_t = \delta_c$.

Furthermore, the thermal correction factor deviates more, and the diffusion correction factor less, from unity for larger $H_{lat}/c_p Le$. When it is born in mind that $H_{lat}/c_p Le \equiv$

$H_{lat}/c_{p,v}Le_v$, this feature of $\Theta_{t,f}$ and $\Theta_{c,f}$ is indeed confirmed by the results listed in tables 2.1 and 2.3. In figure 3.2 features of $\Theta_{t,f3}$ and $\Theta_{c,f3}$ are illustrated graphically for evaporation and condensation; *tan*(p_1) corresponds to dF/dt in t_i and *tan*(p_2) to $(c_b-c_i)/(t_b-t_i)$. Figure 3.2 also indicates that the the correction factor differs most from unity when the bulk properties (t_b, c_b) are situated on the saturation line F(t), *i.e.* when the entire film is saturated.

Toor (1971a) derived analytically for $1 - c_i \cong 1$, $Le = 1$ and $\delta_t = \delta_c$ that the total (latent and sensible) heat transferred at the wall is not affected by fog formation. A glance at equations (1.15)–(1.17), (1.21)–(1.23), (2.31), (2.42), (2.44), (3.18) and (3.19) indicates that this feature of the film is also found when $Le \neq 1$ and $\delta_t \neq \delta_c$.

The dimensionless amount of fog formed (2.30) in the fog layer follows from equations (2.5), (2.28), (3.13), (1.23), (3.14) and (3.18):

$$M_{f3} = \Theta_{t,f3}\left[1 - \frac{1 + \frac{H_{lat}}{c_p}\frac{1}{Le}\left.\frac{dF}{dt}\right|_{t_i}}{1 + \frac{H_{lat}}{c_p}\frac{1}{Le}\left.\frac{dF}{dt}\right|_{t_a}}\right] . \tag{3.20}$$

This expression and equation (3.18) indicate the augmentation of the NIV dimensionless fog formation with an increase in the difference between interface properties (t_i, c_i) and boundary properties (t_a, c_a), as well when H_{lat}/c_pLe is enlarged.

§3.3 Application of the NIV fog film model to channel flow

The application of the NIV fog model to the laminar or turbulent flow of a binary mixture through a channel is now discussed in detail. The governing equations for the vapour fraction and temperature alteration in the channel are derived for three possible cases: no fog formed; fog formed in the film but not in the bulk since the mean mixed condition corresponds to superheat; fog formed both in the film and in the bulk, which is saturated. Solutions in closed form will be provided for all three cases. It will be demonstrated that the applied NIV fog film model exhibits interesting features for Le equal to unity.

Transfer of heat and mass without fog formation

Consider the flow of a binary mixture through a channel of any given shape and in which there is a transfer of heat and mass from gas to a wall, and the vapour mass fraction is small, so that $|\epsilon_1|$ is close to zero. When equations (3.6) and (3.7) predict no formation of fog, the conventional film model is applicable. For small transfer rates ($\phi_t \cong 0$ and $\phi_c \cong 0$) the classical correction factors Θ_t and Θ_c tend to unity: for small $|\epsilon_1|$ the zero–order approximation of the differential energy balance (1.39) reads:

$$\frac{d\bar{t}}{dx} = \frac{-4h_g}{c_p D_h (\rho\bar{u})(x{=}0)} (\bar{t} - t_i) \quad , \tag{3.21}$$

with as boundary condition the mean mixed temperature at the beginning of the channel:

$$\bar{t}(x{=}0) = t_{in} \quad . \tag{3.22}$$

As the interface properties (t_i, c_i) are assumed to be constant in the gas channel, equation (3.21) can be integrated and boundary condition (3.22) applied, yielding:

$$\bar{t}(x) = t_i + (t_{in} - t_i)\, e^{\frac{-4h_g x}{c_p D_h (\rho\bar{u})(x=0)}} \quad . \tag{3.23}$$

The first order approximation for small $|\epsilon_1|$ of mass balance (1.36) reads:

$$\frac{d\bar{c}}{dx} = \frac{-4g_m}{D_h(\rho\bar{u})(x=0)}(\bar{c} - c_i) \ , \tag{3.24}$$

with as bulk vapour mass fraction at the entrance of the channel:

$$\bar{c}(x=0) = c_{in} \ . \tag{3.25}$$

Solving equation (3.24) analytically with application of boundary condition (3.25) produces:

$$\bar{c}(x) = c_i + (c_{in} - c_i)\, e^{\frac{-4g_m x}{D_h(\rho\bar{u})(x=0)}} \ . \tag{3.26}$$

Equations (3.23) and (3.26) give the bulk properties as a function of the coordinate in the direction of the flow, when the entire flow is superheated. These equations show that the mixed mean properties in the channel will lie between the interface values and entry values, which would be expected.

To determine the path of the bulk properties, the coordinate x is eliminated from equations (3.23) and (3.26), and equations (1.17), (1.23), (1.34) and (1.40) are substituted, yielding:

$$\frac{d\bar{c}}{d\bar{t}} = \frac{d\bar{G}}{d\bar{t}} = \frac{Sh}{LeNu}\frac{\bar{c} - c_i}{\bar{t} - t_i} \ . \tag{3.27}$$

This expression reveals that $\overline{G}(\bar{t})$ is a monotonically increasing function of $\bar{t}$. Equation (3.27) furthermore illustrates that for Le equal to unity, and hence also the applicability of equation (1.48), the mean mixed properties follow the relation between c ant t in the superheated film represented by equation (3.5). The classical –no fog– film model exhibits the feature of equality (1.52) as well, as was proved in §1.5. So, the fact that for the special case of small $|\epsilon_1|$ the same behaviour is found, is in fact to be expected.

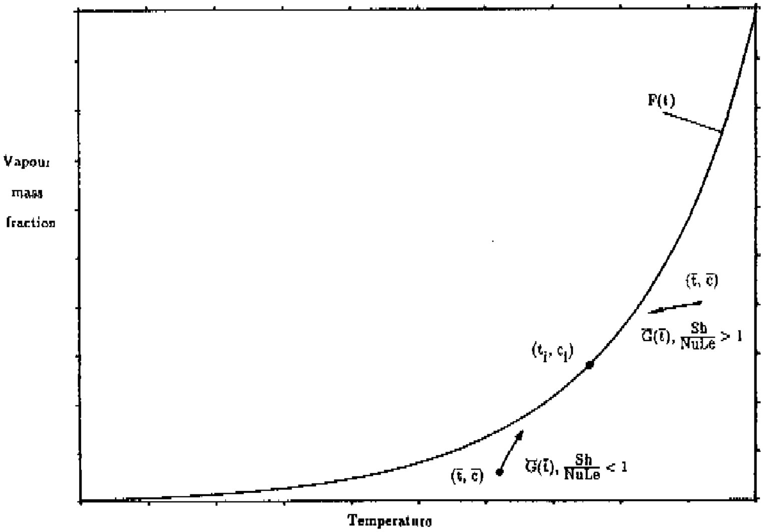

Figure 3.3 Path of bulk properties in the case of no fog formation.

The variables $\bar{c}$ and $\bar{t}$ in equation (3.27) are separated and integrated. Applying boundary conditions (3.22) and (3.25) then yields:

$$\bar{c} = \bar{G}(\bar{t}) = c_i + (c_{in} - c_i)\left[\frac{\bar{t} - t_i}{t_{in} - t_i}\right]^{\frac{Sh}{NuLe}} \quad . \tag{3.28}$$

For Sh/NuLe > 1 and condensation or Sh/NuLe < 1 and evaporation, $\bar{G}(\bar{t})$ proves to be a concave curve. For Sh/NuLe < 1 and condensation or Sh/NuLe > 1 and evaporation, $\bar{G}(\bar{t})$ is a convex curve. For Sh/NuLe = 1, $\bar{G}(\bar{t})$ is a straight line, both for condensation or evaporation. These properties follow from the second derivative of $\bar{G}(\bar{t})$ with respect to $\bar{t}$.

As schematically depicted in figure 3.3, the bulk properties may move to intersect the saturation line, before which the film will become partially saturated. The governing equations of this physical situation are discussed below.

Heat and mass transfer with fog formation in the film but not in the bulk

When only a part of the film is saturated (as predicted by equations (3.6) or (3.7)) the bulk (which is to say: mean mixed) situation may correspond to superheat. The differential energy balance then reads:

$$\frac{d\bar{t}}{dx} = \Theta_{t,f3} \frac{-4h_g}{c_p D_h (\rho\bar{u})(x=0)} (\bar{t} - t_i) \quad , \tag{3.29}$$

with boundary condition (3.22) and the differential vapour fraction balance:

$$\frac{d\bar{c}}{dx} = \Theta_{c,f3} \frac{-4g_m}{D_h (\rho\bar{u})\,(x=0)} (\bar{c} - c_i) \quad , \tag{3.30}$$

with equation (3.25) as appropriate boundary condition.

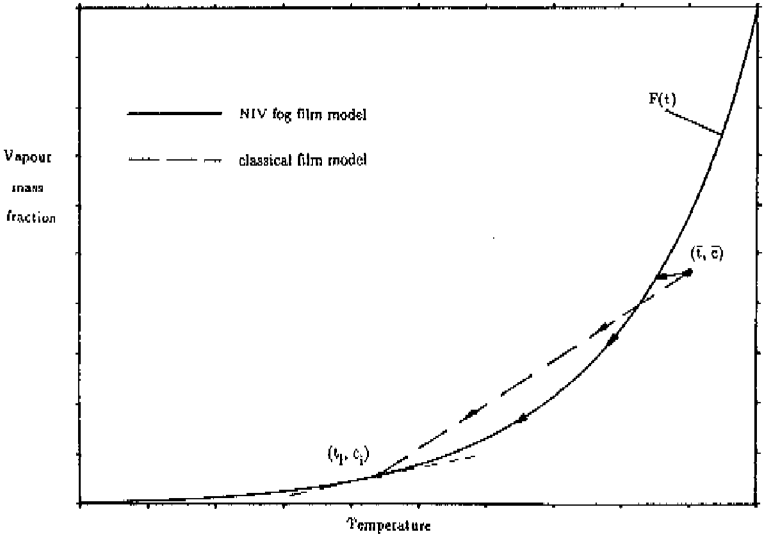

Figure 3.4 Path of bulk properties in the case of wall condensation and fog formation, Le = 1.

The differential equations (3.29) and (3.30) are coupled because in the correction factors (3.18) and (3.19) $\bar{t}$ and $\bar{c}$ appear. Combining equation (3.29) and (3.30) to eliminate x and substitution of equations (1.17), (1.23) and (2.27) yields:

$$\frac{d\bar{c}}{d\bar{t}} = \frac{d\bar{G}}{d\bar{T}} = \frac{1}{Le}\left.\frac{dF}{dt}\right|_{t_i} \quad . \tag{3.31}$$

In order to express $\bar{c}$ as a function of $\bar{t}$, equation (3.31) is integrated with respect to $\bar{t}$, and equations (3.22) and (3.25) are applied, yielding:

$$\bar{c} = \bar{G}(\bar{t}) = c_{in} + (\bar{t} - t_{in}) \frac{1}{Le} \frac{dF}{dt}\bigg|_{t_i} \quad . \tag{3.32}$$

Equation (3.32) is substituted into equation (3.18) to eliminate $\bar{c}$, and the result is substituted in equation (3.29). The variables $\bar{t}$ and x in the resulting differential equation are separated and equations (1.34) and (1.40) inserted, producing:

$$\frac{1 + \frac{H_{lat}}{c_p} \frac{1}{Le} \frac{dF}{dt}\Big|_{t_i}}{\bar{t} - t_i + \frac{H_{lat}}{c_p} \frac{Sh}{LeNu} \left(c_{in} - c_i + (\bar{t} - t_{in}) \frac{1}{Le} \frac{dF}{dt}\Big|_{t_i}\right)} d\bar{t} = \frac{-4h_g}{c_p D_h (\rho\bar{u})(x{=}0)} dx \quad . \tag{3.33}$$

Integrating (3.33) partially and applying boundary condition (3.22) yields:

$$Ln\left[\frac{\bar{t} - t_i + \frac{H_{lat}}{c_p} \frac{Sh}{LeNu} \left(c_{in} - c_i + (t - \bar{t}_{in}) \frac{1}{Le} \frac{dF}{dt}\Big|_{t_i}\right)}{t_{in} - t_i + \frac{H_{lat}}{c_p} \frac{Sh}{LeNu} (c_{in} - c_i)}\right] = \frac{1 + \frac{H_{lat}}{c_p} \left(\frac{1}{Le}\right)^2 \frac{Sh}{Nu} \frac{dF}{dt}\Big|_{t_i}}{1 + \frac{H_{lat}}{c_p} \frac{1}{Le} \frac{dF}{dt}\Big|_{t_i}} \; \frac{-4h_g x}{c_p D_h (\rho\bar{u})(x{=}0)} \quad . \tag{3.34}$$

Equation (3.34) prescribes explicitly the temperature $\bar{t}(x)$ of the gas in the channel when fog is formed in the film and the bulk is still superheated. Substitution of $\bar{t}(x)$ according to equation (3.34) into equation (3.32) yields the local bulk vapour mass fraction in the channel.

Equation (3.31) indicates that, when fog is formed in a part of the flow and Le = 1, the bulk properties shift in the direction of the saturation curve parallel to the line tangent to F(t) in (t_i, c_i), as illustrated in figure 3.4. The shape of this path, which is a straight line, does however not depend on the magnitude of Sh/NuLe.

The bulk properties follow the path until the saturation curve is reached. The behaviour of the mixture once the bulk is saturated is discussed below. When the heat and mass transfer in a channel is described without heeding the intersection of saturation line and formation of fog, the bulk properties ($\bar{t}$, $\bar{c}$) may enter the supersaturated region following $\bar{G}(\bar{t})$. This phenomenon is described by equation (3.28) and illustrated in figures 3.3 and 3.4.

Heat and mass transfer with fog formation in the bulk

The last physical situation concerns a saturated bulk flow in which fog is formed. The entire film is then also saturated, thus (t_a, c_a) coincide with ($\bar{t}$, $\bar{c}$). This property of the NIV analysis is mathematically prescribed by equation (3.15) and is illustrated in figure 3.1. The conditions when fog remains in the gas flow are governed by equations (2.50) or (2.51), in which equation (3.31) is substituted. The created bulk fog keeps the bulk properties on the saturation line; $\bar{c} = F(\bar{t})$. The differential energy balance in the case of fogged bulk flow reads:

$$\frac{d\bar{t}}{dx} = \frac{-4h_g}{c_p D_h (\rho\bar{u})(x=0)} \left[\Theta_{t,f3}\,(\bar{t} - t_i) - \frac{\overline{\dot{m}_{f3}} H_{lat}}{h_g}\right] , \tag{3.35}$$

with belonging boundary condition (3.22). The differential vapour fraction balance is given as:

$$\frac{d\bar{c}}{dx} = \frac{-4g_m}{D_h(\rho\bar{u})\,(x=0)}\left[\Theta_{c,f3}\,(\bar{c}-c_i) + \frac{\bar{\dot{m}}_{f3}}{g_m}\right] , \tag{3.36}$$

with boundary condition (3.25). The quantity of fog is such that equation (2.55) is fulfilled. This means mathematically that the mixture follows the saturation line while flowing through the channel. With equations (1.17), (1.23), (2.27), (2.30), (2.55), (3.35) and (3.36) the dimensionless quantity of fog in the bulk flow is obtained as:

$$\bar{M}_{f3} = \Theta_{t,f3}\left[1 - \frac{1 + \frac{H_{lat}}{c_p}\frac{1}{Le}\left.\frac{dF}{dt}\right|_{t_i}}{1 + \frac{H_{lat}}{c_p}\left.\frac{dF}{dt}\right|_{\bar{t}}}\right] . \tag{3.37}$$

The thermal NIV correction factor figuring in this equation is found in equation (3.18). For Le = 1 the amount of bulk fog, given by equation (3.37), is identical to that created in the film, given by equation (3.20).

The differential equations (3.35) and (3.36) are coupled because $\bar{c} = F(\bar{t})$. Hence, only $\bar{t}(x)$ has to be determined. Equation (3.37), with application of equation (2.30), is substituted in equation (3.35):

$$\frac{d\bar{t}}{dx} = \Theta_{t,f3}\,\frac{-4h_g}{c_p D_h(\rho\bar{u})(x=0)}\,(\bar{t}-t_i)\,\frac{1 + \frac{H_{lat}}{c_p}\frac{1}{Le}\left.\frac{dF}{dt}\right|_{t_i}}{1 + \frac{H_{lat}}{c_p}\left.\frac{dF}{dt}\right|_{\bar{t}}} . \tag{3.38}$$

By substitution of equations (1.34) and (1.40) into equation (3.18), substitution of the result in equation (3.38), and separation of the variables $\bar{t}$ and x, one finds:

$$\frac{1 + \dfrac{H_{lat}}{c_p} \left.\dfrac{dF}{dt}\right|_{\bar{t}}}{\bar{t} - t_i + \dfrac{H_{lat}}{c_p} \dfrac{Sh}{NuLe} (\bar{c} - c_i)} d\bar{t} = \frac{-4h_g}{c_p D_h (\rho \bar{u})(x=0)} dx \quad . \tag{3.39}$$

The left hand side of this equation can be integrated analytically with respect to $\bar{t}$ when the product Sh/NuLe equals unity (which implies Le = 1 for most practical cases since Sh/Nu $\cong$ Le^p, where $0 \leq p < 1$, *e.g.* see equation (1.55)). Setting this product equal to unity, equation (3.39) is partially integrated and coupled boundary conditions (3.22) and (3.25) applied:

$$\frac{\bar{t}(x) - t_i + \dfrac{H_{lat}}{c_p} \dfrac{1}{Le} (\bar{c}(x) - c_i)}{t_{in} - t_i + \dfrac{H_{lat}}{c_p} \dfrac{1}{Le} (c_{in} - c_i)} = e^{\dfrac{-4h_g x}{c_p D_h (\rho \bar{u})(x=0)}} \quad . \tag{3.40}$$

Equation (3.40) gives the temperature $\bar{t}(x)$ implicitly as a function of x, because $\bar{c}(x) = F(\bar{t}(x))$. The bulk temperature and vapour mass fraction follow the saturation line in the direction of (t_i, c_i) while flowing through the channel, see figure 3.4.

§3.4 Results of the NIV fog film model and introduction of compound fog film model

The results of the fog model here derived will be calculated for the underlying conditions of tables 2.1–2.4 ($\delta_t = \delta_c$): one should keep in mind that $H_{lat}/c_p Le$ is identical to $H_{lat}/c_{p,v} Le_v$. On the basis of the here derived NIV fog correction factors and classical film model correction factors, compounded correction factors are introduced which account for both fog formation and the presence of an induced velocity. To determine fog formation use has been made of slope condition (2.1).

	Le_v	$\Theta_{t,f3}$	$\Theta_{t,f3}\Theta_c/\Theta_t$	$\Theta_{c,f3}$	$\overline{\dot{M}}_{f4}$
$t_b = 30^\circ C$	0.50	1.222	1.215	0.922	0.392
$c_b = 0.0264$	0.75	1.192	1.189	0.899	0.351
	1.00	1.169	1.169	0.882	0.317
	1.25	1.151	1.152	0.868	0.288
$t_b = 60^\circ C$	0.50	2.538	2.387	0.781	2.065
$c_b = 0.1318$	0.75	2.328	2.281	0.717	1.902
	1.00	2.169	2.169	0.667	1.753
	1.25	2.044	2.069	0.629	1.626

Table 3.1 Results of the NIV and compound fog film models for $(t_i, c_i) = (20^\circ C, 0.0144)$.

The mass transfer correction factor $\Theta_{c,f3}$ listed in table 3.1 agrees extremely well with the ratio of the overall correction factor (taking account both of fog formation and induced velocity) to the classical correction factor (taking account of an induced velocity, only), $\Theta_{c,f1}/\Theta_c$ in table 2.1 and $\Theta_{c,f2}/\Theta_c$ in table 2.3. This implies that the overall correction factor for fog formation and induced velocity can be approximated by multiplication of the correction factor of the NIV fog film model with the classical film model correction factor:

$$\Theta_{c,f4} = \Theta_c \, \Theta_{c,f3} \quad . \tag{3.41}$$

Thus the introduced correction factor $\Theta_{c,f4}$ is compounded from the conventional correction factor Θ_c which accounts for suction or injection, and an independent NIV correction factor $\Theta_{c,f3}$ which accounts for fog formation only.

	Le_v	$\Theta_{t,f3}$	$\Theta_{t,f3}\Theta_c/\Theta_t$	$\Theta_{c,f3}$	$\overline{M}_{f4}$
$t_b = 97.63^\circ C$	0.80	1.097	1.017	0.998	0.025
$c_b = 0.875$	0.90	1.097	1.060	0.998	0.121
	1.00	1.097	1.097	0.998	0.198
	1.10	1.096	1.128	0.998	0.261
$t_b = 99.90^\circ C$	0.80	1.000	1.000	1.000	0.000
$c_b = 0.995$	0.90	1.189	1.077	0.997	0.345
	1.00	1.188	1.188	0.996	0.778
	1.10	1.188	1.295	0.996	1.133

Table 3.2 Results of the NIV and compound fog film models for $(t_i, c_i) = (94.81^\circ C, 0.75)$.

In table 3.2 the corresponding results are presented for the physical situations of tables 2.2 or 2.4. A comparison of the values in the tables again indicates the good agreement of the compounded correction factor with those of more profound analyses. Even for the typical condenser conditions listed in table 3.2, involving a significant induced velocity, the accuracy of the compounded correction factor is astonishing good.

On the other hand, the thermal correction factor $\Theta_{t,f3}$, listed in table 3.2, does not agree with the quotient of the thermal fog film model correction factor and the Ackermann correction factor, $\Theta_{t,f1}/\Theta_t$ and $\Theta_{t,f2}/\Theta_t$ in tables 2.2 and 2.4, respectively. In other words, multiplying the thermal NIV fog correction factor derived here by the Ackermann correction factor yields no satisfactory compound thermal correction factor. In general, all thermal and diffusional correction factors of the fog film models obey basic equation (2.27), thus the heuristically constructed correction factors $\Theta_{c,f4}$ and $\Theta_{t,f4}$ have to meet these requirements as well. As $\Theta_{c,f3}$ and $\Theta_{t,f3}$ fulfill equation (2.27), the thermal correction factor $\Theta_{t,f3}$ has to be multiplied by the same factor as $\Theta_{c,f3}$, that is to say Θ_c:

$$\Theta_{t,f4} = \Theta_c \, \Theta_{t,f3} \quad . \tag{3.42}$$

This thermal fog correction factor has been divided by the Ackermann correction factor Θ_t and the result listed in tables 3.1 and 3.2. These tables reveal that the constructed fog thermal correction factor (3.42) agrees well when it is compared with the results listed in tables 2.1–2.4. Moreover, extensive calculations have been carried out with numerous other physical conditions, Le_v and $H_{lat}/c_{p,v}$. All calculations proved that the accuracy is of the same order as the examples treated here. This implies $\Theta_{c,f4}$ and $\Theta_{t,f4}$ are good approximations for the fog film model correction factors, accounting for both the influence of fog and the induced velocity.

The compound fog film model is applied in the same way to closed channel flow as the fog film models treated in chapter 2. The procedure is described in §2.6 and figure 2.2, and illustrated here by figure 3.5. The main difference is that, to determine $\Theta_{t,f4}$ and $\Theta_{c,f4}$, the boundary properties (t_a, c_a) do not have to be calculated iteratively. This essential simplification is a major advantage since it reduces the complexity of the fog model and the needed computational time.

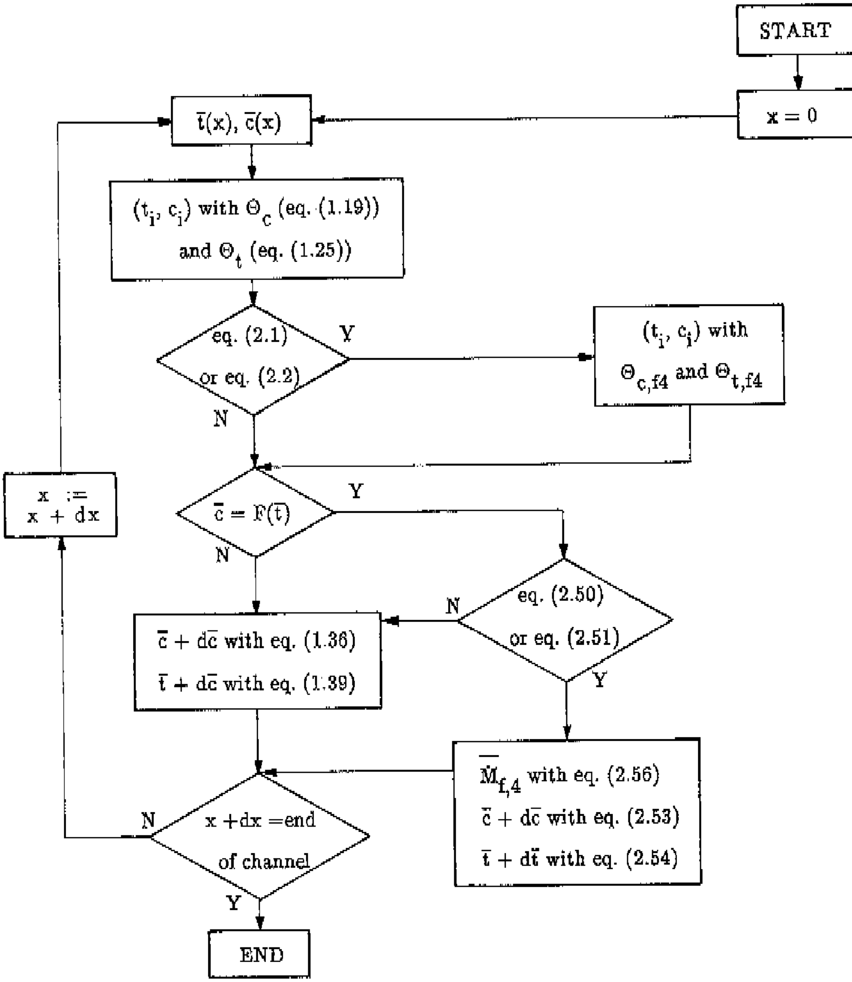
START
x = 0
$\bar{t}(x), \bar{c}(x)$
(t_i, c_i) with Θ_c (eq. (1.19)) and Θ_t (eq. (1.25))
eq. (2.1) or eq. (2.2)
Y
N
(t_i, c_i) with $\Theta_{c,f4}$ and $\Theta_{t,f4}$
$\bar{c} = F(\bar{t})$
Y
N
eq. (2.50) or eq. (2.51)
N
Y
$\bar{c} + d\bar{c}$ with eq. (1.36)
$\bar{t} + d\bar{c}$ with eq. (1.39)
$\bar{\dot{M}}_{f,4}$ with eq. (2.56)
$\bar{c} + d\bar{c}$ with eq. (2.53)
$\bar{t} + d\bar{t}$ with eq. (2.54)
x := x + dx
N
x +dx =end of channel
Y
END

Figure 3.5 Flow chart of the applied compound fog film model.

Furthermore, the forms of Θ_c, $\Theta_{t,f3}$ and $\Theta_{c,f3}$ as such are far less complex than the expressions derived in the previous chapter and hence are much faster to determine.

In tables 3.1 and 3.2 the amount of formed bulk fog, according to the compound fog film model derived here, is listed. Calculating equation (2.56) to determine the dimensionless bulk fog, Le has again be set equal to unity and equality (1.48) substituted. The calculated rates agree well with the corresponding ones listed in tables 2.1–2.4, once more proving the reliability of the compound fog film model expressions.

§3.5 Comparison of the fog film model with convective models and experiments

In this section the non–convective fog film model is compared with comprehensive models and experiments of previous investigators. These two–dimensional models concern laminar free and forced convective heat and mass transfer of dilute water–vapour air mixtures to a wall, the presence of fog being described by the saturation condition.

Free convective heat and mass transfer

Koch (1986) investigated the free convective boundary layer flow along a vertical cryosurface with wall condensation. To this end the governing equations of continuity, momentum, energy, molecular diffusion, and particle diffusion were derived and solved numerically. In the thesis it was demonstrated that the thermophoresis of particles is a significant mode of mass transfer when the interface temperature is below about $-10^\circ C$; it even dominates molecular mass transfer if $t_i \leq -60^\circ C$. The theoretical model was furthermore found in good agreement with performed condensation experiments on a plate of 1 m height. In table 3.3 two examples are listed, which will be compared with the predictions of the fog film model.

The total mean mass flux to the wall consists of two parts, namely mass transfer by particle and by molecular diffusion. As in this thesis only the effect of fog formation on the (molecular) diffusion and energy equations is examined, in table 3.3 also the purely molecular diffusion part, denoted as a_c, is included (taken from "Bild 5.20"), as well as the diffusion mass transfer without fog formation. Dividing both diffusion mass transfer rates then produces the correction factors for mass transfer. The diffusion correction factor obtained in this way can be compared with the predictions of the analysis presented here, since thermophoresis does not affect the coupled diffusion and energy equation.

Accordingly, $\Theta_{c,f3}$, see equation (3.19), is determined for the corresponding physical situations of Koch (1986): Le = 0.85, H_{lat}/c_p = 2490 K. For free convection Sh/Nu (= δ_t/δ_c) is approximated by equation (1.55).

	experimental	theoretical		no fog	theoretical	eq.(3.19)
c_b	$\overline{\dot{m}}_{tot}$ [kg/m²s]	$\overline{\dot{m}}_{tot}$ [kg/m²s]	a_c	$\overline{\dot{m}}$ [kg/m²s]	$a_c\overline{\dot{m}}_{tot}/\overline{\dot{m}}$	$\Theta_{c,f3}$
0.3 $F(t_b)$	1.08 10^{-5}	1.12 10^{-5}	0.63	1.51 10^{-5}	0.46	0.43
0.6 $F(t_b)$	1.72 10^{-5}	1.63 10^{-5}	0.52	3.16 10^{-5}	0.26	0.25

Table 3.3 Free convective mass transfer of water–vapour air mixtures, t_b = 20°C ($F(t_b)$ = 0.0144), to a vertical wall, t_i = – 30°C and $c_i = F(t_i)$ = 0.00003.

To compose the saturation line (C.7), the Rankine–Kirchhoff equation is furthermore used for the water–vapour pressure (α = 2485.938, β = 48.745 and γ = 6825.112, see equations (C.1) and (C.3)), and P_{tot} = 1 bar. This liquid–water vapour pressure is employed, though the fog layer near the wall is below the solidification temperature of water. It was stated and employed by Koch (1986) that the droplets are in a metastable liquid state and hence the mentioned saturation pressure of liquid water can be used. At the solid surface the saturation pressure of ice, of course, prevails, but the distinction with the water pressure is minor there and moreover, $c_i << c_b$. In table 3.3 the calculated $\Theta_{c,f3}$ for the two examined cases are listed.

The computed diffusion correction factors in table 3.3 show that the fog film model mass transfer predictions are in good agreement; the deviation of $\Theta_{c,f3}$ from unity is predicted within 6 %. One should also realize that the results of Koch (1986) in table 3.3 are based on the combined analysis of particle and molecular diffusion, and that a_c (the ratio of the molecular diffusion mass flux to the total mass flux at the surface) is read off graphically. In order to obtain data which can be compared more accurately with the fog film model, Koch and Straub (1990) utilized the numerical model to predict the free convective mass transfer to a surface with $t_i = 0^\circ C$, $t_b = 40^\circ C$, and $c_b = 0.3\ F(t_b)$ or $c_b = 0.6\ F(t_b)$, thus excluding a relevant effect of thermophoresis.

For $c_b = 0.3\ F(t_b)$ the entire film is superheated, this follows from slope condition (3.6). The same equation is in fact used by Koch (1986) and Koch and Straub (1990), yielding the same conclusion of course. For $c_b = 0.6\ F(t_b)$ fog formation takes place in the mixture. Numerical calculations have been carried out with fog formation and thermophoresis suppressed, thermophoresis suppressed only, and with the complete model.

	no fog	fog	ratio	eq. (3.18)
x [m]	q [W/m^2]	q [W/m^2]	$\Theta_{t,f}$	$\Theta_{t,f3}$
0.05	213.0	300.9	1.41	1.47
0.5	118.7	169.2	1.42	1.47
1	99.70	142.5	1.43	1.47

Table 3.4 Free convective heat transfer of water–vapour air mixtures, $t_b = 40^\circ C$ and $c_b = 0.6\ F(t_b)$ $(F(t_b) = 0.0471)$, to a vertical wall, $t_i = 0^\circ C$ and $c_i = 0.00381$.

The computations revealed that the solutions for thermophoresis included and suppressed are practically identical, implying that thermophoresis is indeed a negligible phenomenon for the interface and bulk conditions considered. Some determined heat fluxes to the wall are summarized in table 3.4, while in table 3.5 the mass fluxes are listed.

One can readily see that the transfer rates depend on the coordinate x, which constitutes the distance from the upper end of the vertical plate. The tables also indicate that the ratio of fog and no fog rates is nearly uniform, thus independent of the level of heat and mass transfer. This aspect of the effect of fog formation is in qualitative accord with the film model approach, since the resulting correction factors only depend on interface and bulk conditions as well. The constant local transfer rates ratios furthermore imply that the total (and mean) heat and mass transfer fog/no fog ratios will have the same value as well. This might be the reason why the overall agreement in table 3.3 is so good.

	no fog	fog	ratio	eq. (3.19)
x [m]	$\dot{m}$ [kg/m²s]	$\dot{m}$ [kg/m²s]	$\Theta_{c,f}$	$\Theta_{c,f3}$
0.05	$1.391\ 10^{-4}$	$1.017\ 10^{-4}$	0.73	0.71
0.5	$0.776\ 10^{-4}$	$0.559\ 10^{-4}$	0.72	0.71
1	$0.652\ 10^{-4}$	$0.469\ 10^{-4}$	0.72	0.71

Table 3.5 Free convective mass transfer of water–vapour air mixtures, $t_b = 40^\circ C$ and $c_b = 0.6\ F(t_b)$ $(F(t_b) = 0.0471)$, to a vertical wall, $t_i = 0^\circ C$ and $c_i = 0.00381$.

In tables 3.4 and 3.5 the NIV correction factors for fog formation are also included, in which Le = 0.86 and $H_{lat}/c_p = 2413$ K have been substituted. The computed correction factors illustrate the reasonable agreement between the solution of the comprehensive free convective boundary layer equations, and those of the basic fog film model. The deviation of the heat transfer ratios from unity agree within 11 %, whereas the mass transfer ratios agree within 7 %.

Forced convective heat and mass transfer

Forced convective laminar flow between parallel plates (in the diffusional and thermal entrance region) with wall condensation of various dilute water–vapour in air has been investigated theoretically and experimentally by Hayashi *et al.* (1981). The governing equations of continuity, diffusion and energy were derived, solved numerically and found in good agreement with performed experiments. On the basis of the saturation condition and a consideration of the vapour fraction and temperature profiles Hayashi *et al.* (1981) derived the following condition for fog formation:

$$p = \frac{c_b - c_i}{t_b - t_i} \frac{1}{\left.\frac{dF}{dt}\right|_{t_i}} > \frac{Nu}{Sh} \quad , \tag{3.43}$$

which is identical to the fog film model condition (3.6) (p was referred to as "$1/T^*$"). It was furthermore derived that to the considered entrance region applies:

$$\frac{\delta_c}{\delta_t} = \frac{Nu}{Sh} = Le^{-0.36} = 1.05 \quad , \tag{3.44}$$

as Le = 0.875 for the studied mixtures. The theoretical and experimental results indicated that $\Theta_{t,f}$ and $\Theta_{c,f}$ (referred to as "Nu/Nu_0" and "Sh/Sh_0", respectively) depend more on p than on the local transfer rate (governed by the dimensionless distance from the entrance, referred to as: "Gz_t" and "Gz_c"). This observation is in qualitative accord with the principle of the fog film model.

In order to compare the results of Hayashi *et al.* (1981) quantitatively with the predictions of the fog film model, correction factors $\Theta_{t,f3}$ and $\Theta_{c,f3}$, represented by equations (3.18) and (3.19), are determined for the process concerned.

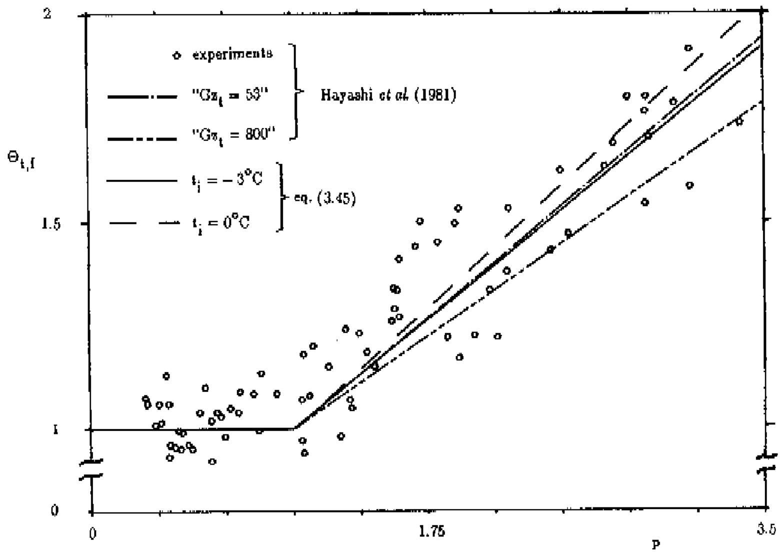

Figure 3.6 Effect of fog formation on forced convective heat transfer from a water–vapour air mixture to a wall in the presence of wall condensation.

With equation (3.43) equation (3.18) is therefore rewritten as:

$$\Theta_{t,f3} = \frac{1 + \frac{H_{lat}}{c_p} \frac{Sh}{LeNu} \left.\frac{dF}{dt}\right|_{t_i} p}{1 + \frac{H_{lat}}{c_p} \frac{1}{Le} \left.\frac{dF}{dt}\right|_{t_i}} , \tag{3.45}$$

and equation (3.19) as:

$$\Theta_{c,f3} = \Theta_{t,f3} \frac{Nu}{Sh} \frac{1}{p} \quad . \tag{3.46}$$

As relevant data in equations (3.45) and (3.46) are now substituted the afore–said values of Le and Nu/Sh, and $t_i = -3^{\circ}C$, $\bar{H}_{lat}/c_p = 2500$ K. In equation (3.45) the first derivative of the water–vapour air saturation line is employed, derived in appendix C. In figures 3.6 and 3.7 the experimental data and theoretical results of Hayashi *et al.* (1981) are depicted (which were also based on $t_i = -3^{\circ}C$), as well the computational results of equations (3.45) and (3.46).

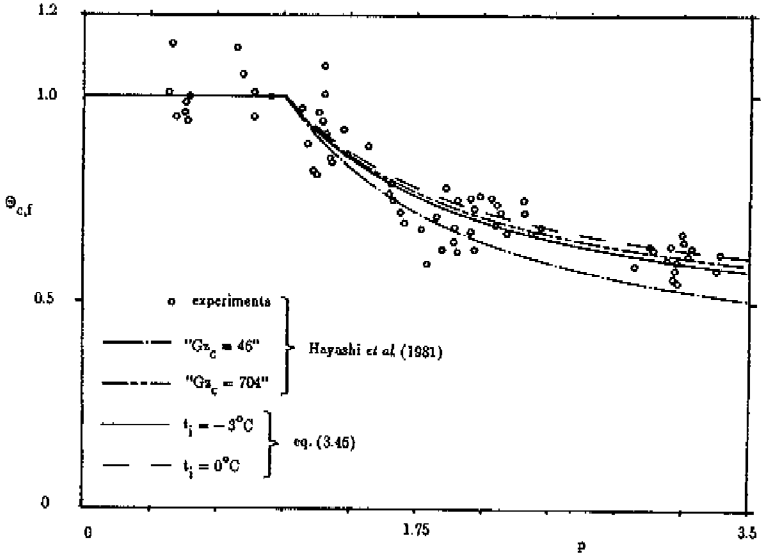

Figure 3.7 Effect of fog formation on forced convective mass transfer from a water–vapour air mixture to a wall in the presence of wall condensation.

Both figures illustrate the excellent agreement of the NIV fog film model with the theoretical and experimental results concerned. Some experimental results in figure 3.6, however, are typically situated above the theoretical predictions. These exceptions, though the deviations are modest, can be attributed to the variation in wall temperature during the experiments; t_i ranged from $-3^\circ C$ up to $0^\circ C$. Hence, equations (3.45) and (3.46) are also evaluated with $t_i = 0^\circ C$ and all other values unchanged; the obtained results are also depicted in figures 3.6 and 3.7. One can see in figure 3.7 that the effect of a higher t_i is minor, while in figure 3.6 the line pertaining to $t_i = 0^\circ C$ has a steeper slope and is indeed in better agreement with some experimental data.

In this section the predictions of the NIV fog film model have been compared with those of convective and hence more comprehensive studies. This important comparison justifies the film model approach to fog formation, since it agrees with a deviation of typically 10 %. In chapter 1 it has been discussed and demonstrated that the conventional film model allows for the induced velocity with a similar accuracy, which is well acceptable for engineering end purposes. It is noteworthy that if the induced velocity were included in the analyses of Koch (1986) and Hayashi *et al.* (1981), the effect of fog formation on transfer rates (and related correction factors) would be the same. In §3.4 we have seen namely that both for fog and no fog formation the heat and mass transfer is enhanced equally by the condensation–induced velocity.

§3.6 Conclusions

In this chapter a film of a binary mixture has been examined in which there is a transfer of heat and mass. In this film the induced velocity has been assumed absent. The error introduced by leaving this velocity out of consideration has been assessed thoroughly by means of an asymptotic analysis.

In the film with no induced velocity (NIV) fog is allowed to take place. First, a complete analysis has been given, on the basis of the saturation condition, of the presence and extent of a fog layer and a superheated layer. The governing equations of both regions have been derived, solved, and analytical expressions for the heat and mass transfer have been derived. On the basis of these expressions compact NIV film model correction factors have been introduced, and the influence of the diverse parameters discussed.

Subsequently, the simple NIV fog film model correction factors have applied to the flow of a mixture, with a small vapour mass fraction, through a channel. Three possible physical cases have been examined, namely a superheated flow without fog formation, a superheated bulk flow with fog formation in the film, and a saturated bulk flow with fog formation. For all three cases solutions in closed form have been obtained, describing and illustrating the mixture's mean mixed temperature and vapour mass fraction behaviour with respect to the saturation line.

Calculation of the correction factors for realistic cases of fog formation in various air water–vapour mixtures indicated the significant effect of fog formation on heat and mass transfer. Furthermore, the NIV fog film model correction factors have been combined with the classical film model correction factors. These latter correction factors only allow for the effect of the induced velocity on heat and mass transfer, and not for the influence of fog formation. The compounded correction factors account for both formation of fog and the induced velocity. As these correction factors are sufficiently accurate and described by simple expressions, they are suited and recommended for future engineering calculations.

The fog film model correction factors have been compared with experimental and extensive theoretical studies of forced and free convective heat and mass transfer. Both studies concerned wall condensation of dilute water–vapour in air and the effect of fog formation, with neglect of the induced velocity. The predictions of the basic NIV fog film model have been found in good accord with the results of the comprehensive studies considered. This important comparison justifies the film model approach to fog formation.

4. HEAT AND MASS TRANSFER IN CROSSFLOW PLASTIC HEAT EXCHANGERS

§4.1 Introduction

In chapter 1 the classical film model has been reviewed and extended. In chapters 2 and 3 formation of fog has been taken into account. Here now, in this chapter the heat and mass transfer in the plastic heat exchanger, see figure 4.1, is analyzed and modelled.

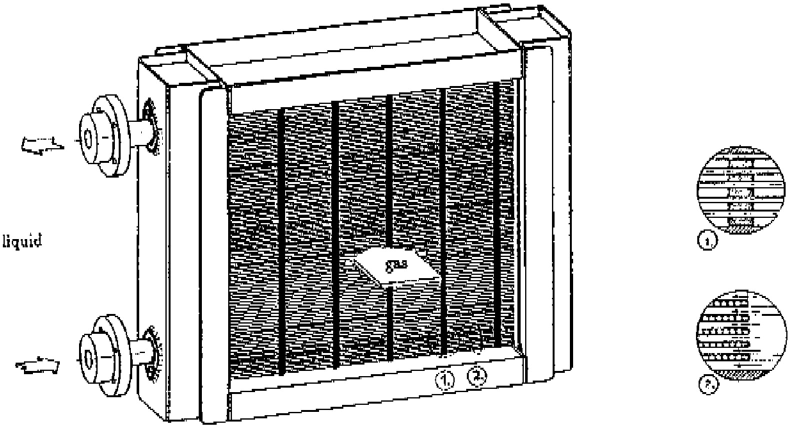

Figure 4.1 The plastic heat exchanger.

First, the governing equations describing the heat transfer between gas and liquid, without any condensation at the gas side, are derived. Analytical solutions in closed form of these classical equations have been provided by previous investigators. Subsequently, the equations of partial and pure water–vapour condensation are formulated, taking superheating and large vapour mass fractions into account. The effect of the induced velocity on latent and sensible heat transfer is predicted with the film model, which has been discussed in the first chapter.

The possible formation of fog in the gas flow is examined and described with the fog film models of chapters 2 and 3. The resulting local equations are first solved to predict the rates of mass and energy transfer. A set of partial differential equations is then integrated to carry the solution forward over an increment of area. As the plastic heat exchanger operates in crossflow, the resulting exit vapour mass fraction, mass flow, gas temperature and produced fog are not uniform, and do not necessarily have to be in thermodynamic equilibrium after mixing. Accordingly, expressions are derived describing the stable state of the gas after mixing, resulting effectively in fog creation or dissolution.

Some characteristic features of the heat exchanger are illustrated by application of the models to various mixtures of air and water–vapour. The theoretical predictions are compared with experiments, carried out with a PVDF heat exchanger placed in a wind tunnel, to verify the models presented in this chapter.

§4.2 Heat transfer without condensation

In this section the heat transfer between gas and liquid is discussed without any condensation at the gas side. Condensation will not take place when the gas is heated in the heat exchanger, or when the gas is cooled and the coldest spot in the heat exchanger is hotter than the dew point of the mixture or saturation temperature of pure vapour. The exact condition for condensation will be specified at the end of this section.

The gas flows between the channel plates in the direction of X, the liquid through the plates in the direction of Z , see figure 4.2. The coordinates X and Z have been rendered dimensionless by means of the net width B and length L of the plate, respectively:

$$X = \frac{x}{B} \quad , \tag{4.1}$$

$$Z = \frac{z}{L} \quad . \tag{4.2}$$

The net effective width of the plate B relates to the total width B_{tot} minus the thickness of a partition wall times the number of channels, see figures 4.1(2) and 4.2. The net length L is formed by the total length of the plate minus the total length taken up by the intermediate reinforcements of the plates, see figure 4.1(1). In figure 4.1 one can see that their relative distance is of magnitude B_{tot}.

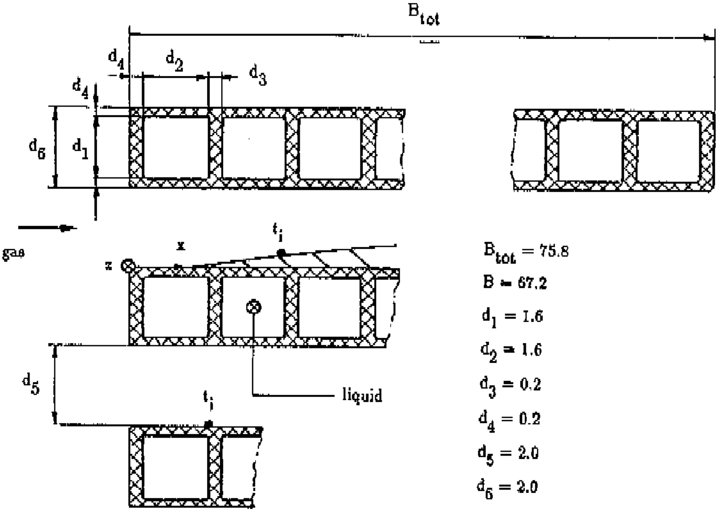
B_{tot}
d_4
d_2
d_3
d_4
d_6
d_1
gas
x
z
t_i
d_5
t_i
liquid
$B_{tot} = 75.8$
$B = 67.2$
$d_1 = 1.6$
$d_2 = 1.6$
$d_3 = 0.2$
$d_4 = 0.2$
$d_5 = 2.0$
$d_6 = 2.0$

Figure 4.2 Heat transfer between channel plates (sizes in mm).

The different gas and liquid temperatures cause sensible heat transfer between both fluids. An energy balance for an element dXdZ, see figure 4.2, yields:

$$\bar{h}_g (\bar{t}_g - t_i) = \bar{h}_{pl} (t_i - \bar{t}_l) \quad . \tag{4.3}$$

Here $\bar{t}_g(X, Z)$ and $\bar{t}_l(X, Z)$ represent the mixed mean temperatures of gas and liquid respectively. All (physical) properties of the gas are from now assigned the subscipt "g" to distinguish them from the liquid properties. By making use of the mixed mean temperatures the three-dimensional process in the heat exchanger is simplified to a two-dimensional model.

The heat transfer coefficient $\bar{h}_g$ from gas to wall is defined as:

$$\bar{h}_g = \frac{k_g \overline{Nu}_g}{D_{h,g}} = \frac{k_g \overline{Nu}_g}{2 d_5} \quad , \tag{4.4}$$

$\bar{h}_g$ proves to be about 55 W/m^2K if the correlation (1.53) of Stephan (1959) ($Nu_{g,\infty} = 7.55$), the hydraulic diameter of the gas channel, see figure 4.2, and the physical properties of air, see V.D.I. (1988), are substituted. The mean heat transfer coefficient $\bar{h}_{pl}$ of the plate consists of two parts:

$$\frac{1}{\bar{h}_{pl}} = \frac{1}{\bar{h}_w} + \frac{1}{\bar{h}_l} \quad , \tag{4.5}$$

the mean heat transfer coefficient $\bar{h}_w$ of the plate wall is defined as:

$$\bar{h}_w = \frac{k_w}{d_4} \quad , \tag{4.6}$$

and proves to be about 950 W/m^2K if the thermal conductivity of PVDF, 0.19 W/mK, and average wall thickness d_4 are substituted. The mean heat transfer coefficient $\bar{h}_l$ from wall to liquid is defined as:

$$\bar{h}_l = \frac{\overline{Nu}_l k_l}{D_{h,l}} = \frac{\overline{Nu}_l k_l}{d_l} \quad . \tag{4.7}$$

The mean forced convective laminar flow Nusselt number is taken from Dennis *et al.* (1959) ($Nu_{l,\infty} = 2.98$). This correlation only accounts for the effect of the thermal entry length, not the hydraulic. Neti and Eichhorn (1983) demonstrated numerically that the hydrodynamic development region has little effect for $Pr_l > 6$ and $Re_l Pr_l D_{h,l}/L < 120$. As these conditions are satisfied in the channels of the heat exchanger, the correlation Dennis *et al.* (1959) can be used. When this correlation is substituted in equation (4.7), together with the thermal conductivity of water, see V.D.I. (1988), and the hydraulic diameter d_l of the channel, see figure 4.2, a value of $\bar{h}_l$ of at least 1500 W/m^{2}K is obtained. The Sieder and Tate correction for the dynamic viscosity variation across the channel, mentioned in V.D.I. (1988), is not included in equation (4.7). As $\bar{h}_l$ is much larger than $\bar{h}_g$ and $\bar{h}_w$, the temperature (and dynamic viscosity) variation will be small.

The heat exchange yields an alteration of the bulk gas and liquid temperatures. For the liquid the differential energy balance relation reads:

$$\frac{w_l c_{p,l}}{BL} \frac{\partial \bar{t}_l}{\partial Z} = 2\bar{h}_{pl} (t_i - \bar{t}_l) \quad , \tag{4.8}$$

subject to boundary condition:

$$\bar{t}_l(X, Z{=}0) = t_{l,in} \quad . \tag{4.9}$$

To the gas applies:

$$\frac{w_g c_{p,g}}{BL} \frac{\partial \bar{t}_g}{\partial X} = 2\bar{h}_g \, (t_i - \bar{t}_g) \quad , \tag{4.10}$$

with associated boundary condition:

$$\bar{t}_g(X=0, Z) = t_{g,in} \quad . \tag{4.11}$$

The factor two in equations (4.8) and (4.10) takes into account the heat transfer at both sides of the plate. The gas mass flow through one gas channel is given by the total gas mass flow, divided by the number of plates. The liquid mass flow per plate is equal to the total liquid mass flow divided by the number of channel plates, times the number of times the liquid passes the heat exchanger. In figure 4.1 a heat exchanger with two liquid passes is depicted as example. Equation (4.3) is now rewritten, yielding t_i as a combination of $\bar{t}_g$ and $\bar{t}_l$. The result is substituted in equations (4.8) and (4.10), yielding:

$$\frac{\partial \bar{t}_l}{\partial Z} = NTU_l \, (\bar{t}_g - \bar{t}_l) \quad , \tag{4.12}$$

and:

$$\frac{\partial \bar{t}_g}{\partial X} = NTU_g \, (\bar{t}_l - \bar{t}_g) \quad , \tag{4.13}$$

respectively. In both equations the number of transfer units are introduced as:

$$NTU_l = \frac{2\bar{h}_{tot} LB}{w_l c_{p,l}} \quad , \tag{4.14}$$

and:

$$\mathrm{NTU}_g = \frac{2\bar{h}_{tot}LB}{w_g c_{p,g}} \quad . \tag{4.15}$$

The mean total heat transfer coefficient $\bar{h}_{tot}$ from gas to liquid, figuring in equations (4.14) and (4.15), is defined as:

$$\frac{1}{\bar{h}_{tot}} = \frac{1}{\bar{h}_{pl}} + \frac{1}{\bar{h}_g} = \frac{1}{\bar{h}_w} + \frac{1}{\bar{h}_l} + \frac{1}{\bar{h}_g} \quad , \tag{4.16}$$

see equation (4.5). In order to find out whether condensation takes place on the plates at the gas side, the minimum plate surface temperature $t_i(1,0)$ is determined. Equation (4.13), combined with equations (4.9) and (4.11), is solved at $Z = 0$. The result is substituted into equation (4.3) and equation (4.16) applied, yielding as minimum surface temperature:

$$t_i(X{=}1, Z{=}0) = t_{l,in} + (t_{g,in} - t_{l,in}) \frac{\bar{h}_{tot}}{\bar{h}_{pl}} e^{-\mathrm{NTU}_g} \quad . \tag{4.17}$$

Water will not condense if the temperature of this coldest spot on the plate is higher than the saturation temperature t_{sat} of pure steam or the dew point temperature t_{dew} of a mixture. Both temperatures are derived in appendix C for pure steam and mixtures of air and water–vapour.

The solution of the coupled equations (4.12) and (4.13), with boundary conditions (4.9) and (4.11), depends only on both numbers of transfer units. These crossflow equations have been solved by many investigators, starting with Nusselt (1911). In the letter of

Baclic and Heggs (1985) a broad review is presented of all treatments and equivalent solutions of these classical equations. Here the solution of Mason (1954) is employed and discussed further. The mean exit temperature of the liquid is defined as:

$$\bar{t}_l(Z{=}1) = \int_{X=0}^{1} \bar{t}_l(X, Z{=}1)\,dX \quad , \tag{4.18}$$

and according to Mason (1954) is given by:

$$\bar{t}_l(Z{=}1) = NTU_l\ S(NTU_l, NTU_g) \quad , \tag{4.19}$$

where:

$$S(NTU_l, NTU_g) = \frac{1}{NTU_l NTU_g} \sum_{n=0}^{\infty} \left(1 - e^{-NTU_g} \sum_{i=0}^{n} \frac{NTU_g^i}{i\,!}\right) \left(1 - e^{-NTU_l} \sum_{i=0}^{n} \frac{NTU_l^i}{i\,!}\right) . \tag{4.20}$$

Since a truncation error analysis has not been carried out yet, this is undertaken in appendix D. This analysis reveals that the truncation error is less than 10^{-4} if equation (4.20) is developed up to five terms.

As mass is not transferred, the gas mass flow at the exit of the plates is evidently equal to the entry gas mass flow and the mean exit gas temperature then readily follows from an overall energy balance. In a heat exchanger in which the liquid passes more than one time, see figure 4.1, the heat transfer of each pass has to be calculated in the manner described here. The exit temperature of a pass serves as entry temperature of the following pass, until the liquid leaves the last pass and heat exchanger. The mean exit gas temperature follows from the arithmetic mean of the determined exit gas temperatures of each pass.

§4.3 Partial water–vapour condensation

In this paragraph the partial condensation of water–vapour or steam in the presence of non–condensables is modelled. The equations governing heat and mass transfer due to temperature and concentration differences between gas and condensate surface are derived and solved numerically. The followed procedure is illustrated by means of the flow chart drawn in figure 4.3.

Governing equations

Using equation (4.17) it can be verified whether condensation takes place. When water–vapour condenses on the coldest spot between the plates, it will probably condense at some other locations as well. This can be examined by calculating the local interface temperature $t_i(X, Z)$ by means of equation (4.3), thus assuming *a priori* that there is no condensation.

If no condensation takes place the governing equations (4.12) and (4.13) of the previous section are locally applicable. On the other hand, condensation takes place if:

$$t_{dew} = F^{inv}(\bar{c}) > t_i \quad , \tag{4.21}$$

where $\bar{c}(X, Z)$ denotes the bulk vapour mass fraction of the mixture. In appendix C the saturation function $F(t)$ and its inverse function have been derived for air water–vapour mixtures.

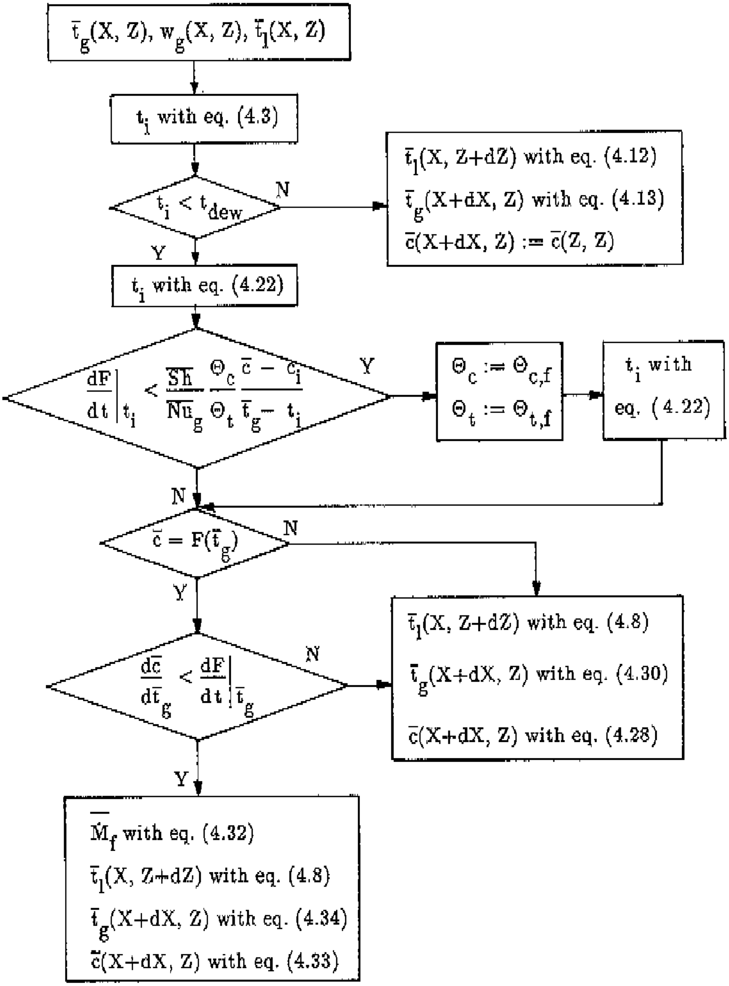
$\bar{t}_g(X, Z)$, $w_g(X, Z)$, $\bar{t}_l(X, Z)$
t_i with eq. (4.3)
$t_i < t_{dew}$
N
Y
$\bar{t}_l(X, Z+dZ)$ with eq. (4.12)
$\bar{t}_g(X+dX, Z)$ with eq. (4.13)
$\bar{c}(X+dX, Z) := \bar{c}(Z, Z)$
t_i with eq. (4.22)
$\left.\frac{dF}{dt}\right|_{t_i} < \frac{\overline{Sh}}{\overline{Nu}_g} \frac{\Theta_c}{\Theta_t} \frac{\bar{c} - c_i}{\bar{t}_g - t_i}$
Y
N
$\Theta_c := \Theta_{c,f}$
$\Theta_t := \Theta_{t,f}$
t_i with eq. (4.22)
$\bar{c} = F(\bar{t}_g)$
N
Y
$\bar{t}_l(X, Z+dZ)$ with eq. (4.8)
$\bar{t}_g(X+dX, Z)$ with eq. (4.30)
$\bar{c}(X+dX, Z)$ with eq. (4.28)
$\frac{d\bar{c}}{d\bar{t}_g} < \left.\frac{dF}{dt}\right|_{\bar{t}_g}$
N
Y
$\overline{\dot{M}}_f$ with eq. (4.32)
$\bar{t}_l(X, Z+dZ)$ with eq. (4.8)
$\bar{t}_g(X+dX, Z)$ with eq. (4.34)
$\bar{c}(X+dX, Z)$ with eq. (4.33)

Figure 4.3 Flow chart of calculational procedure for partial water–vapour condensation.

In the case of condensation a local energy balance for an element dXdZ, see figure 4.1, yields:

$$\dot{m}H_{lat} + \Theta_t \bar{h}_g(\bar{t}_g - t_i) = \bar{h}_{pl}(t_i - \bar{t}_l) \quad . \tag{4.22}$$

The interface temperature $t_i(X, Z)$ in this equation definitely specifies $c_i(X, Z)$ since at the interface the mixture is saturated, that is to say, $c_i = F(t_i)$. The first term on the left hand side of equation (4.22) represents the mass flux towards the condensate film where condensation takes place and the latent heat is liberated, while the second term represents the transported sensible heat, corrected for suction with the conventional Ackermann term.

The mass transport is caused by diffusion from mixture phase to condensate film. According to the classical film model this transport is described as:

$$\dot{m} = \Theta_c \, \bar{g}_m \frac{\bar{c} - c_i}{1 - c_i} \quad . \tag{4.23}$$

In chapter 1 Θ_c and Θ_t have been derived, see equations (1.19) and (1.25), respectively. The mass transfer coefficient from mixture to condensate is defined as:

$$\bar{g}_m = \frac{\rho \mathbb{D} \overline{Sh}}{D_{h,g}} = \frac{\rho \mathbb{D} \overline{Sh}}{2d_5} \quad . \tag{4.24}$$

The mean Sherwood number $\overline{Sh}$ is calculated, according to the Chilton–Colburn analogy, in the same way as the Nusselt number of the gas. In the correlation of Stephan (1959) the Prandtl number Pr is therefore replaced by Schmidt number Sc, see equations (1.53) and (1.54).

The formed condensate drains along the plate surface under the action of gravity. On the right hand side of equation (4.22) the heat transfer resistance of the condensate film has been neglected. In appendix E it is shown that the contribution of this film can be disregarded for pure vapour condensation, because it is so thin. For partial condensation the mass flux towards the film is even smaller than for pure steam condensation. This implies that the heat resistance of the film can safely be neglected in equation (4.22) because the condensate thickness will be smaller as well.

As the intermediate reinforcements between the channel plates approximately have a relative distance B, the flow–off lengths of the condensate film are equal for co–, counter and crosscurrent condensation, see figure 4.4.

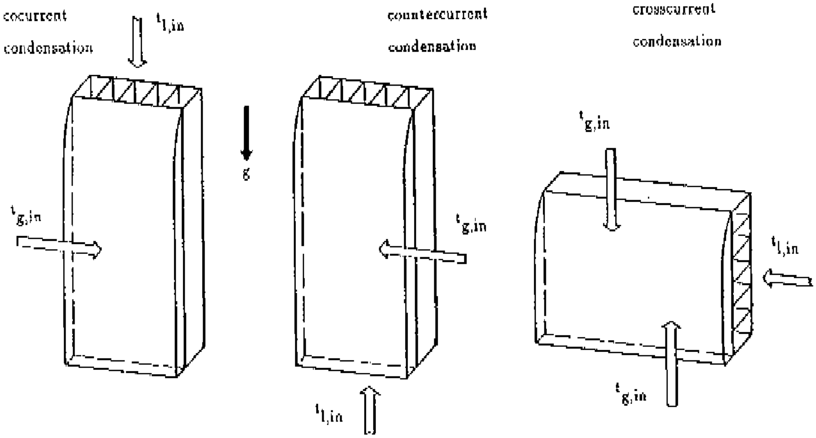
cocurrent
condensation
$t_{l,in}$
$t_{g,in}$
g
countercurrent
condensation
$t_{g,in}$
$t_{l,in}$
crosscurrent
condensation
$t_{g,in}$
$t_{l,in}$
$t_{g,in}$

Figure 4.4 Practical orientations of channel plates towards gravitation.

This means that the equations derived here become valid for these three types of condensation heat transfer. The orientation of the heat exchanger to the vertical is not relevant to the partial and pure vapour condensation models.

In equations (4.22) and (4.23) the classical film model correction factors Θ_c and Θ_t appear. That is to say, it is assumed *a priori* that fog is not formed in the mixture. Using the value of t_i obtained, and associated value of c_i, equation (2.1) is used to examine whether the mixture is supersaturated:

$$\left.\frac{dF}{dt}\right|_{t_i} < \frac{\overline{Sh}}{\overline{Nu}_g}\frac{\Theta_c}{\Theta_t}\frac{\bar{c} - c_i}{\bar{t}_g - t_i} \quad . \tag{4.25}$$

If this equation predicts supersaturation, the value of t_i obtained is not correct and has to be re–determined from equations (4.22) and (4.23) in which the fog film model correction factors $\Theta_{c,f}$ and $\Theta_{t,f}$, derived in chapter 2 or 3, now have to be substituted. These correction factors are based on the saturation condition, which is the most ideal condition for fog formation. In reality supersaturation will always take place to some extent in the gas. Accordingly, the actual heat and mass transfer will lie between the levels predicted by the conventional film model and saturation fog film model.

With the value t_i finally obtained, the differential energy balances for the gas and liquid sides, and the mass balance for the gas side, are derived. The heating of the liquid is described by equation (4.8), with associated boundary condition (4.9). In order to formulate the decrement in total mass flow, vapour mass fraction and mixture temperature, the gas flow between the plates is considered in the following.

For a superheated mixture a differential vapour mass balance yields equation (1.33). This equation is adapted to flow between parallel plates (see figure 4.2) by:

$$\frac{(\rho\bar{u})(X,Z)D_h}{4} = \frac{(\rho\bar{u})(X,Z)d_5}{2} = \frac{w_g(X,Z)}{2L} \quad , \tag{4.26}$$

Combining equations (4.26) and (1.35) yields:

$$\frac{w_g(X,Z)}{w_{g,in}} = \frac{1 - c_{in}}{1 - \bar{c}(X,Z)} \quad , \tag{4.27}$$

which prescribes the conservation of the non–condensables in the mixture. Combining equations (1.33), (4.26) and (4.27) now yields:

$$\frac{\partial \bar{c}}{\partial X} = -\frac{2\bar{g}_m LB}{w_{g,in}} \Theta_c \frac{\bar{c} - c_i}{1 - c_i} \frac{(1 - \bar{c})^2}{1 - c_{in}} \quad , \tag{4.28}$$

with as boundary condition on $\bar{c}$:

$$\bar{c}(X=0,\, Z) = c_{in} \quad . \tag{4.29}$$

The variation of the gas temperature is described by equation (1.38). For flow between parallel plates this equation, with equations (4.4), (4.23), (4.24), (4.26) and (4.27), can be written as:

$$\frac{\partial \bar{t}_g}{\partial X} = -\frac{2\bar{h}_g LB}{w_{g,in} c_{p,g}} \left[\Theta_t - \frac{\overline{Sh}}{Le_v \overline{Nu}_g} \Theta_c \frac{\bar{c} - c_i}{1 - c_i}\right] \frac{1 - \bar{c}}{1 - c_{in}} (\bar{t}_g - t_i) \quad , \tag{4.30}$$

with equation (4.11) as boundary condition.

As soon as the mixture is locally saturated, so that $\bar{c}(X, Z) = F(\bar{t}_g(X, Z))$, and the path of the bulk properties is directed into the supersaturated region, fog is created in the bulk. The behaviour of the bulk properties is examined with the help of equations (4.4), (4.24), (4.28), (4.30) and (2.50):

$$\frac{d\bar{c}}{d\bar{t}_g} = \frac{\overline{Sh}}{Le\overline{Nu}_g} \frac{\Theta_c \frac{\bar{c}-c_i}{1-c_i}(1-\bar{c})}{\left[\Theta_t - \frac{\overline{Sh}}{Le_v \overline{Nu}_g}\Theta_c \frac{\bar{c}-c_i}{1-c_i}\right](t_g - t_i)} < \left.\frac{dF}{dt}\right|_{\bar{t}_g} . \tag{4.31}$$

Fog is formed in the bulk if the resulting bulk properties' path is directed into the supersaturated region. The amount of bulk fog is then governed by equation (2.56):

$$\overline{\dot{M}}_f = \frac{\Theta_t \left.\frac{dF}{dt}\right|_{\bar t_g} - \frac{\overline{Sh}}{\overline{Nu}_g}\Theta_c\frac{\bar c - c_i}{1-c_i}\left[\frac{1}{Le_v}\left.\frac{dF}{dt}\right|_{\bar t_g} + \frac{1}{Le}\frac{1-\bar c}{\bar t_g - t_i}\right]}{\left.\frac{dF}{dt}\right|_{\bar t_g} + (1-\bar c)\frac{Le_v}{Le}\frac{c_{p,v}}{H_{lat}}} . \tag{4.32}$$

The differential mass and energy balances in the case in which bulk fog is created are represented by equations (2.53) and (2.54), respectively. For flow between parallel plates these equations are, with application of equations (2.30), (4.4), (4.24) and (4.26), written as:

$$\frac{\partial\bar c}{\partial X} = -\frac{2\bar h_g LB}{w_{g,in}c_{p,g}}\left[\frac{\overline{Sh}}{\overline{Nu}_g Le}\Theta_c\frac{\bar c - c_i}{1-c_i} + (\bar t_g - t_i)\frac{c_{p,g}}{H_{lat}}\overline{\dot M}_f\right]\frac{(1-\bar c)^2}{1-c_{in}} , \tag{4.33}$$

and:

$$\frac{\partial \bar{t}_g}{\partial X} = -\frac{2\bar{h}_g LB}{w_{g,in} c_{p,g}} \left[\Theta_t - \frac{\overline{Sh}}{Le_v \overline{Nu}_g} \Theta_c \frac{\bar{c} - c_i}{1 - c_i} - \overline{\dot{M}}_f\right] \frac{1 - \bar{c}}{1 - c_{in}} (\bar{t}_g - t_i) \quad , \tag{4.34}$$

respectively. Applying equation (4.27) the effect of formed fog on the mass flow of the mixture is disregarded, because this amount is expected to be very small. For the same reason the influence of the droplets on the physical properties of the mixture is neglected.

Note that the Nusselt number in equations (4.4), (4.25) and (4.30)–(4.34), and the Sherwood number in equations (4.24), (4.25), and (4.30)–(4.34), are based on the initial gas mass flow. In fact the mass flow decreases due to wall condensation and fog formation. However, these numbers do not depend on the magnitude of the mass flow for fully developed laminar flow, and depend only weakly on the mass flow when entry effects are taken into account, see equations (1.53) and (1.54).

In the case of fog formation in the film, the fog film model correction factors $\Theta_{c,f}$ and $\Theta_{t,f}$ are used in equations (4.22), (4.23), (4.28) and (4.30)–(4.34) instead of Θ_c and Θ_t, respectively. The path of the bulk properties is then examined with:

$$\frac{d\bar{c}}{d\bar{t}_g} = \frac{1}{Le} \frac{-\dfrac{1 - \bar{c}}{1 - c_i} \left.\dfrac{dF}{dt}\right|_{t_i}}{\dfrac{1}{Le_v} \dfrac{\bar{t}_g - t_i}{1 - c_i} \left.\dfrac{dF}{dt}\right|_{t_i} - 1} < \left.\frac{dF}{dt}\right|_{\bar{t}_g} \quad , \tag{4.35}$$

instead of equation (4.31). Strictly speaking, equation (4.35) is a combination of equations (4.28) and (4.30), where Θ_c and Θ_t have been replaced by $\Theta_{c,f}$ and $\Theta_{t,f}$, respectively, and equation (2.27) applied. In this chapter both the correction factors based on the asymptotic solution, obtained in chapter 2, as well as the compounded correction factors of chapter 3, are employed, in order to investigate the differences in required calculational time and produced numerical results.

Numerical solution

The modelling of the partial water–vapour condensation process in this section has resulted in a set of equations, applicable to each liquid passage in the heat exchanger. One algebraic equation to determine t_i, and three partial differential equations describing the temperature rise of the liquid and temperature and vapour fraction drop of the gas mixture.

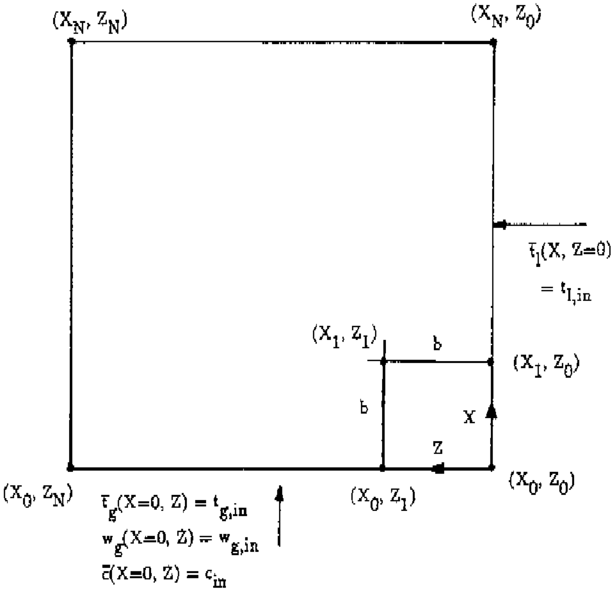
(X_N, Z_N)
(X_N, Z_0)
$\bar{t}_l(X, Z=0)$
$= t_{l,in}$
(X_1, Z_1)
b
(X_1, Z_0)
b
X
Z
(X_0, Z_N)
$\bar{t}_g(X=0, Z) = t_{g,in}$
$w_g(X=0, Z) = w_{g,in}$
$\bar{c}(X=0, Z) = c_{in}$
(X_0, Z_1)
(X_0, Z_0)

Figure 4.5 Discretisation points.

Four different local physical cases at the gas side have been distinguished. Namely heat transfer without condensation, condensation and no fog formation, condensation and fog formation in the film and/or in the bulk. Account has been taken of the exact conditions for these physical situations, and their consequences with respect to the governing equations. To solve the equations numerically per pass, t_i is calculated in $(N+1)^2$ equidistant points in the X–Z plane with a intermediate distance b, see figure 4.5. In $(X=0,\ Z=0)$ $\bar{t}_g$, $\bar{c}$ and $\bar{t}_l$ are known and t_i can be determined. With this t_i, and associated c_i, the values of $\bar{t}_g$, $\bar{c}$ and $\bar{t}_l$ are evaluated in adjacent points with an integration scheme. For stability reasons an implicit Euler's formula is employed to determine $\bar{t}_g(X=b,\ Z=0)$, $\bar{c}(X=b,\ Z=0)$ and $\bar{t}_l(X=0,\ Z=b)$. In these adjacent points the procedure of determining t_i iteratively is repeated, followed by further integration steps, until the borders of the plate have been reached.

The mixing cup temperature of the outflowing liquid after each passage is given by equation (4.18). The exit temperature of each pass serves as the entry temperature for the next pass. The mean exit gas temperature of pass j is described by:

$$\bar{\bar{t}}_{g,j}(X=1) = \frac{1}{\bar{w}_{g,j}(X=1)} \int_{Z=0}^{1} w_g(X=1,\ Z)\ \bar{t}_g(X=1,\ Z)\ dZ \quad , \qquad (4.36)$$

and the mean exit vapour mass fraction as:

$$\bar{\bar{c}}_j(X=1) = \frac{1}{\bar{w}_{g,j}(X=1)} \int_{Z=0}^{1} w_g(X=1,\ Z)\ \bar{c}(X=1,\ Z)\ dZ \quad . \qquad (4.37)$$

In equations (4.36) and (4.37) the mean exit mass gas flow per plate of pass j features:

$$\overline{w}_{g,j}(X=1) = \int_{Z=0}^{1} w_g(X=1, Z)\, dX \quad . \tag{4.38}$$

The integrals appearing in equations (4.36) and (4.37) contain the local exit gas mass flow as weight factor. As the heat and mass transfer takes place in crossflow with the cooling liquid, the exit mass flow will depend on the coordinate Z, the direction of the liquid flow. The gas mass flow follows from the vapour mass fraction via equation (4.27).

The total amount of produced fog in the bulk in pass j is governed by:

$$\overline{w}_{f,j}(X=1) = LB \int_{X=0}^{1} \int_{Z=0}^{1} \overline{\dot{m}}_f\, dXdZ \quad . \tag{4.39}$$

The integrals in equations (4.36)–(4.39) are evaluated numerically by means of Simpson's rule. In general, the mean exit gas flows and temperatures of each pass will be different. The mean exit gas mass flow, per plate, is governed by:

$$\overline{w}_g(X=1) = \frac{1}{n_{pass}} \sum_{j=1}^{n_{pass}} \overline{w}_{g,j}(X=1) \quad , \tag{4.40}$$

and the mean formed fog by:

$$\overline{w}_f(X=1) = \frac{1}{n_{pass}} \sum_{j=1}^{n_{pass}} \overline{w}_{f,j}(X=1) \quad . \tag{4.41}$$

The mean exit gas temperature per plate, taking account of multiple passes, follows from:

$$\bar{t}_g(X=1) = \frac{1}{n_{pass}\bar{w}_g(X=1)} \sum_{j=1}^{n_{pass}} \bar{w}_{g,j}(X=1)\,\bar{t}_{g,j}(X=1) \quad , \tag{4.42}$$

and the mean vapour mass fraction of the gas from:

$$\bar{c}(X=1) = \frac{1}{n_{pass}\bar{w}_g(X=1)} \sum_{j=1}^{n_{pass}} \bar{w}_{g,j}(X=1)\,\bar{c}_j(X=1) \quad . \tag{4.43}$$

In equations (4.42) and (4.43) the exit mass flow of each pass acts as weight factor.

	$(\bar{t}_g(X=1), \bar{c}(X=1))$		
	superheated	saturated	supersaturated
$\bar{w}_f(X=1) = 0$	(i)	(i)	(iii)
$\bar{w}_f(X=1) > 0$	(ii)	(i)	(iii)

(i): $c_{out} = \bar{c}(X=1)$	(ii): $c_{out} > \bar{c}(X=1)$	(iii): $c_{out} < \bar{c}(X=1)$
$t_{g,out} = \bar{t}_g(X=1)$	$t_{g,out} < \bar{t}_g(X=1)$	$t_{g,out} > \bar{t}_g(X=1)$
$w_{g,out} = \bar{w}_g(X=1)$	$w_{g,out} > \bar{w}_g(X=1)$	$w_{g,out} < \bar{w}_g(X=1)$
$w_{f,out} = \bar{w}_f(X=1)$	$w_{f,out} < \bar{w}_f(X=1)$	$w_{f,out} > \bar{w}_f(X=1)$

Table 4.1 Possible conditions of gas and transformation rules.

The mean exit values determined from equations (4.40)–(4.43) are not in general identical with the ultimate exit values after mixing, owing to the crossflow principle and possibility of multiple liquid passages. If the calculated mean values correspond to superheat or saturation, and there is no fog in the gas after the plates, that is $\overline{w}_f(X=1) = 0$, the calculated mean mixed values are identical with the values after mixing, denoted as $t_{g,out}$ and c_{out}. In the case of $\overline{w}_f(X=1)$ not equal to zero, the mean exit values have to be saturated to draw the same conclusion. In table 4.1 both cases are marked by (i).

On the other hand, when the mixture is superheated, and $\overline{w}_f(X=1)$ is not equal to zero, a part of the formed fog between the plates will dissolve after the gas has left the heat exchanger and is mixed; this case is marked in table 4.1 by (ii). The dissolution alters the vapour mass flow:

$$c_{out}\, w_{g,out} - \overline{c}(X=1)\, \overline{w}_g(X=1) = \overline{w}_f(X=1) - w_{f,out} \quad . \tag{4.44}$$

In this equation the index "out" refers to the bulk state of the homogeneous gas after mixing, when it is in thermodynamic equilibrium. The equation contains $w_{g,out}$ since the gas mass flow is also affected by the return of droplets, which have been considered as matter lost between the plates, to the vapour phase. The inert components of the gas mass flow before entering the heat exchanger are not affected in and after the heat exchanger:

$$w_{g,out} = \frac{1 - \overline{c}(X=1)}{1 - c_{out}}\, \overline{w}_g(X=1) = \frac{1 - c_{in}}{1 - c_{out}}\, w_{g,in} \quad . \tag{4.45}$$

The dissolution of fog is at the cost of the gas bulk temperature:

$$\begin{aligned}(t_{g,out} - \overline{t}_g(X=1))\,(c_{p,v}(w_{g,out} - \overline{w}_g(X=1)) + c_{p,g}\overline{w}_g(X=1)) \\ = H_{lat}\,(w_{f,out} - \overline{w}_f(X=1)) \quad .\end{aligned} \tag{4.46}$$

If all fog can be dissolved by the superheated mixture c_{out}, $w_{g,out}$ and $t_{g,out}$ follow directly from equations (4.44)–(4.46), respectively, since $w_{f,out}$ then equals zero. A mixture which is not sufficiently superheated to absorb all fog will become saturated and a part of the fog is left over, that is $w_{f,out}$ is unequal to zero. Equations (4.44)–(4.46), combined with the saturation line (2.5), then yield $t_{g,out}$, $c_{out} = F(t_{g,out})$, $w_{g,out}$ and $w_{f,out}$.

The same set of equations is applied to determine the same physical properties when the mixture leaves the plates supersaturated and fog is created in the mixture by mixing; in table 4.1 these cases are marked by (iii). Steinmeyer (1972) mentioned this mechanism of fog formation by mixing of gas flows with non–uniform vapour fractions and temperatures as one pertinent source of fog formation.

§4.4 Pure steam condensation

When (superheated) steam enters the duct to condense as a film on the plate, the heat transfer will be highest. For a superheated vapour there is, beside the latent heat transfer, also a contribution of sensible heat transfer. This sensible heat transfer results in a decrease of mass transfer towards the plate and hence in the formation of condensate. Taking these effects into account, in this section the governing equations of the process are derived and solved. The procedure followed is illustrated in figure 4.6.

Governing equations

To examine whether condensation takes place, the local interface temperature is determined using equation (4.3), thus assuming condensation will not take place. If the calculated temperature is such that:

$$t_i \geq t_{sat} = A^{inv}(P_v) \quad , \tag{4.47}$$

the assumption of no condensation was correct. The differential energy balances (4.12) and (4.13) are then applicable. In appendix C the inverse Antoine relation $A^{inv}(P_v)$ is given for steam. However, when equation (4.47) is not satisfied, condensation takes place and a local energy balance for an element dXdZ yields equation (4.22), with t_i replaced by t_{sat}:

$$\dot{m}H_{lat} + \left[\frac{-\dfrac{\dot{m}c_{p,v}}{\bar{h}_g}}{e^{-\dfrac{\dot{m}c_{p,v}}{\bar{h}_g}} - 1}\right]\bar{h}_g(\bar{t}_g - t_{sat}) = \bar{h}_{pl}(t_{sat} - \bar{t}_l) \quad . \tag{4.48}$$

The first term on the left hand side of this equation represents the liberated latent heat flux into the condensate film. In the second term the sensible heat flux is taken into account, see equation (1.24), with the Ackermann correction for suction. This Ackermann correction is originally based on the classical film model analysis of a binary mixture presented in chapter 1, but applied in equation (4.48) to non–diffusional condensation of pure vapour.

In appendix E it is demonstrated that for the plastic heat exchanger the dimensionless mass flux ϕ_t is smaller than 1.18. Mizushina (1978) proved the film model to be in good agreement with pure benzene condensation experiments for ϕ_t smaller than 1.4. Furthermore, it is shown in appendix E that the heat transfer coefficient of the water condensate film is very large when compared with $\bar{h}_{pl}$, hence the coefficient of the condensate does not appear in equation (4.48).

The temperature rise of the liquid in the channel plate is described by equation (4.8) with t_i replaced by t_{sat}:

$$\frac{\partial \bar{t}_l}{\partial Z} = \frac{2\bar{h}_{pl} LB}{w_l c_{p,l}} (t_{sat} - \bar{t}_l) \quad , \tag{4.49}$$

with equation (4.9) as boundary condition. As the pressure drop, when compared to the absolute pressure, is very small in the gas channel, see appendix E, t_{sat} is constant in the channel.

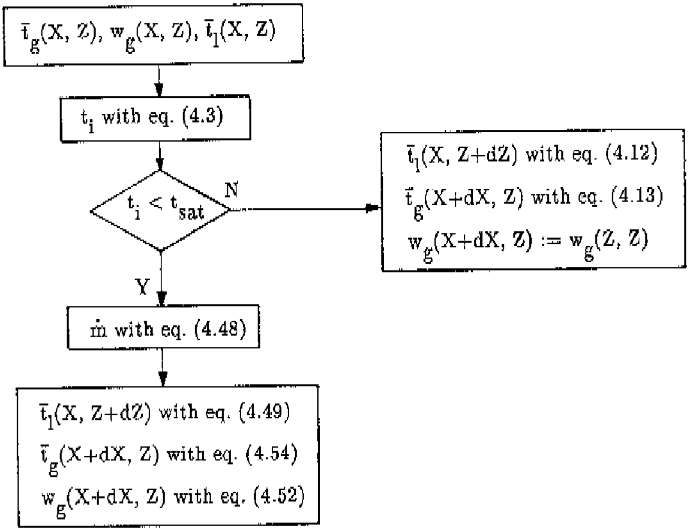
$\bar{t}_g(X, Z)$, $w_g(X, Z)$, $\bar{t}_l(X, Z)$
t_i with eq. (4.3)
$t_i < t_{sat}$
N
$\bar{t}_l(X, Z+dZ)$ with eq. (4.12)
$\bar{t}_g(X+dX, Z)$ with eq. (4.13)
$w_g(X+dX, Z) := w_g(Z, Z)$
Y
$\dot{m}$ with eq. (4.48)
$\bar{t}_l(X, Z+dZ)$ with eq. (4.49)
$\bar{t}_g(X+dX, Z)$ with eq. (4.54)
$w_g(X+dX, Z)$ with eq. (4.52)

Figure 4.6 Flow chart of calculational procedure for pure steam condensation.

When it is further assumed *a priori* that condensation takes place on the entire plate, equation (4.49) can be integrated and boundary condition (4.9) applied, yielding the liquid temperature in the plate:

$$\bar{t}_l(X, Z) = t_{l,in} + (t_{sat} - t_{l,in})\,(1 - e^{-\frac{2\bar{h}_{pl} LB}{w_l c_{p,l}} Z}) \quad . \tag{4.50}$$

The maximum surface temperature $t_i(X=0, Z=1)$ is calculated by substitution of equations (4.50) and (4.11) into equation (4.3), producing:

$$t_i(X=0, Z=1) = t_{l,in} + \frac{\bar{h}_{tot}}{\bar{h}_{pl}}(t_{g,in} - t_{l,in}) + \frac{\bar{h}_{tot}}{\bar{h}_g}(t_{sat} - t_{l,in})\,(1 - e^{-\frac{2\bar{h}_{pl} LB}{w_l c_{p,l}}}) \quad . \tag{4.51}$$

If this temperature is smaller than t_{sat}, the assumption of entire plate condensation was correct. If this assumption was not correct, the liquid temperature is determined by numerical integration of equation (4.49) until the end of the condensation region of the plate is reached. For saturated steam, thus $t_{g,in} = t_{sat}$, the surface temperature never becomes higher than the saturation temperature and equation (4.50) is always applicable.

In contrast to partial vapour condensation, the interface temperature is explicitly known in equation (4.48), namely $t_i = t_{sat}$, and need not to be determined iteratively. Instead of t_i the local mass flux $\dot{m}(X, Z)$ has to be determined iteratively now; with this mass flux known the differential mass and energy balances at the gas side are derived. At the gas side the decrease of the mass flow is described by:

$$\frac{\partial w_g}{\partial X} = 2LB\,\dot{m} \quad , \tag{4.52}$$

with as appropriate boundary condition on w_g:

$$w_g(X=0, Z) = w_{g,in} \quad . \tag{4.53}$$

The variation of gas bulk temperature is given by equation (1.38) with t_i replaced by t_{sat}. This equation is adapted to flow between parallel plates with equation (4.26), and with equation (1.26) expressed as:

$$\frac{\partial \bar{t}_g}{\partial X} = -\frac{2\bar{h}_g LB}{w_g c_{p,g}} (\Theta_t - \phi_t)(\bar{t}_g - t_{sat}) \quad , \tag{4.54}$$

with pertaining boundary condition (4.11). Three first order partial differential equations, coupled by one algebraic equation describe the process of superheated vapour heat and mass transfer. In the case of "whole plate" condensation, *e.g.* saturated steam ($t_{g,in} = t_{sat}$), an analytical solution (4.50) has been derived. In the following a numerical solution procedure is described that provides a solution of the process equations for both "partial" and "total" plate condensation.

Solution procedure

The solution is determined in $(N+1)^2$ discrete points. These points are equidistant in the direction of X and Z, with a intermediate distance b, see figure 4.5. In (X=0 , Z=0) the gas and liquid temperatures are known, being $t_{g,in}$ and $t_{l,in}$, respectively. If the interface temperature according to equation (4.3) is higher than the saturation temperature, no condensation will take place. The liquid and gas temperatures in (X=0, Z=b) and (X=b, Z=0) are then determined by equations (4.12) and (4.13), respectively.

In case condensation takes place $\dot{m}(X=0, Z=0)$ is obtained by numerical iteration of equation (4.48). Subsequently the values $\bar{t}_l(X=0, Z=b)$, $\bar{t}_g(X=b, Z=0)$ and $w_g(X=b, Z=0)$

are determined from equations (4.49), (4.54) and (4.52), respectively. The values of the temperatures and mass flow in these adjacent points are once again evaluated using an implicit Euler's formula. The procedure of iteration and integration is carried out until the boundaries of the plate, ($X=1$, $0 \leq Z \leq 1$) and ($0 \leq X \leq 1$, $Z=1$), have been reached. The mean gas exit temperature and mass flow of pass j are calculated in the discrete points at the edge of the plate, using the expressions (4.36) and (4.38). For multiple passes, with equations (4.40) and (4.42) the mean exit properties per plate are determined. The liquid temperature after each pass follows from equation (4.18), and serves as entry temperature for the following pass.

§4.5 Computational results

Calculations on a PVDF heat exchanger with an effective length of 0.40 m and width of 0.384 m, corresponding to 96 parallel channel plates, have been carried out. The liquid flow passes the channel plates twice, as depicted in figure 4.1. It flows through 48 plates from inlet to opposite headers, is collected there and mixed, and flows then through the 48 other plates to the exit of the heat exchanger. The initial liquid temperature is set equal to 19.5°C for the calculations, the entering gas has a temperature of 62°C and absolute pressure of 1.029 bar. The entry mass fraction of vapour, c_{in}, ranges from zero up to and including 0.142. These entry conditions are such that all aspects of the model treated here will occur, namely no condensation, condensation without fog formation and condensation and fog formation. Moreover, the induced velocity is small for small c_{in}, is larger for larger c_{in}, and is greatest for c_{in} equal to 0.142 (corresponding to a saturated mixture).

The physical properties of both fluids are evaluated at the arithmetic mean of entry and exit temperature, as suggested by V.D.I. (1988). At the gas side all properties are evaluated at the arithmetic mean of entry and exit composition (in mole fractions), except H_{lat}, which is evaluated at t_i. The contributions of both components are weighed by the present mole fraction, for example see equation (F.9), except the thermal conductivity and dynamic viscosity, which are evaluated following Perry and Green (1984), for example see equation (F.25). All physical properties are taken from V.D.I. (1988), except the diffusion coefficient, which is taken from Edwards *et al.* (1979), see equation (F.22).

In figure 4.7 the dimensionless exit temperatures of both fluids, defined as:

$$\zeta = \frac{t - t_{l,in}}{t_{g,in} - t_{l,in}} \quad , \tag{4.55}$$

are depicted as a function of c_{in} for $NTU_g = 0.612$ and $NTU_l = 0.041$, and $NTU_g = 0.710$ and $NTU_l = 0.038$, and in figure 4.8 for $NTU_g = 1.001$ and $NTU_l = 0.039$, and $NTU_g = 1.270$ and $NTU_l = 0.036$. In both plots also the dimensionless exit gas mass flow and fog mass flow are depicted, both flows rendered dimensionless by means of the entry gas mass flow:

$$W = \frac{w}{w_{g,in}} \quad . \tag{4.56}$$

For clarity's sake the dimensionless fog has been multiplied by a factor 10. The predictions of the compound fog film model (for all computations this model proved to produce identical results as the asymptotic fog film model) and the solutions of the classical film model (thus without fog), which are used as reference, are depicted in both figures.

One can see clearly in figures 4.7 and 4.8 that for small c_{in} no condensation takes place in the heat exchanger and consequently the exit mass flows equals the entry mass flow. For $c_{in} \geq 0.017$ condensation and liberation of latent heat sets in in both figures resulting in an exit temperature rise of both fluids and decrease of the exit gas mass flow. For $c_{in} \geq 0.084$ and $c_{in} \geq 0.080$ in figure 4.7 and 4.8, respectively, fog formation near the wall appears to take place, indicated by an augmented temperature fall at the gas side. As long as the bulk is still superheated, formation of fog near the wall causes an enhanced sensible heat transfer; see figure 3.4 for a graphical explanation.

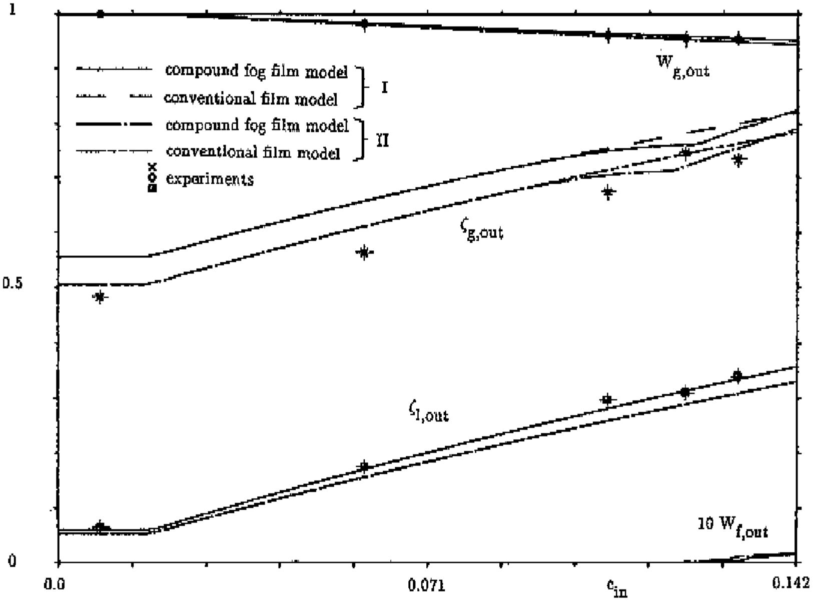

Figure 4.7 Exit properties for $t_{l,in}$ = 19.5°C, $t_{g,in}$ = 62°C, P_{tot} = 102900 Pa, NTU_g = 0.612 and NTU_l = 0.041 (I), and NTU_g = 0.710 and NTU_l = 0.038 (II), according to the fog film model and conventional film model.

For $c_{in} \geq 0.111$ and $c_{in} \geq 0.097$ in figure 4.7 and 4.8, respectively, fog is formed and latent heat is liberated in the bulk and the temperature fall is reduced. As the entry vapour mass fraction is close to the maximum (saturated) value, the bulk properties reach the saturation line sooner and the developed bulk fog rises, see figure 3.4. Consequently, the exit gas temperature even exceeds the value provided by the conventional film model.

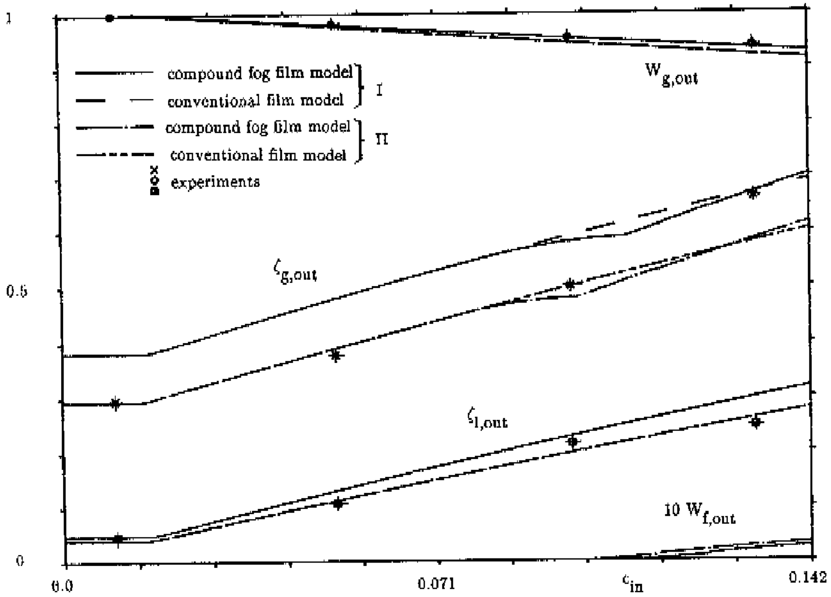

Figure 4.8 Exit properties for $t_{l,in}$ = 19.5°C, $t_{g,in}$ = 62°C, P_{tot} = 102900 Pa, NTU_g = 1.001 and NTU_l = 0.039 (I), and NTU_g = 1.270 and NTU_l = 0.036 (II), according to the fog film model and conventional film model.

Figures 4.7 and 4.8 show that about one third of the initial vapour present in the mixture condenses in the heat exchanger; the level of (wall and droplet) condensed water is represented by the deviation of the dimensionless exit mass flow from unity. One can furthermore observe that the exit gas mass flow and related vapour mass fraction are predicted equally well by both models.

However, the numerical results indicate that the rate of wall condensed water is reduced by fog formation, since a part of the condensed water, of about 5 %, has become fog. Both figures reveal that only a small part of the initial vapour mass flow leaves the heat exchanger as fog. Accordingly, the assumption that the droplets do not affect the physical properties of the gas appears to be correct *a posteriori*. All created fog is however undesired since it is a yield loss and the formed droplets are difficult to remove. Additional computations with $t_{l,in} = 0^{\circ}C$ furthermore revealed that for this realistic condition even 10 % of the condensed water becomes fog, which is a substantial amount.

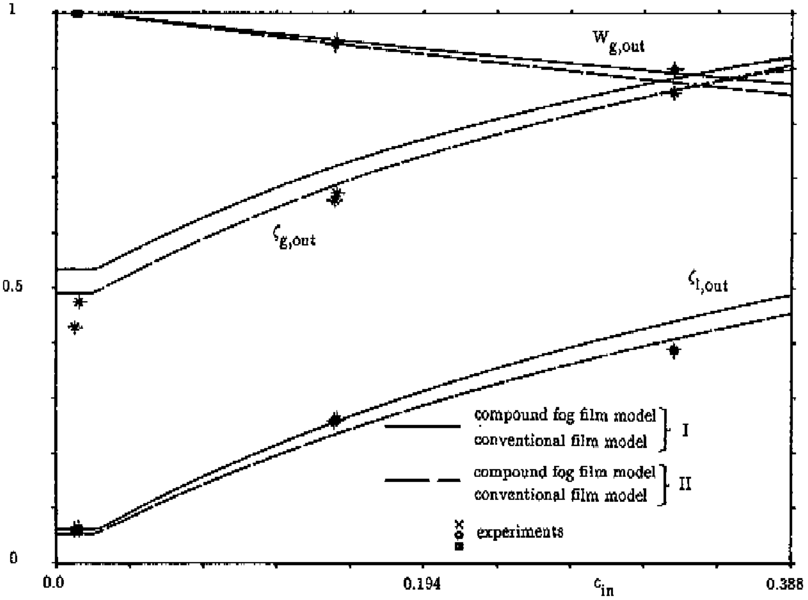

Figure 4.9 Exit properties for $t_{l,in} = 20^{\circ}C$, $t_{g,in} = 82^{\circ}C$, $P_{tot} = 101325$ Pa, $NTU_g = 0.656$ and $NTU_l = 0.042$ (I), and $NTU_g = 0.741$ and $NTU_l = 0.038$ (II), according to the fog film model and conventional film model.

The exit gas which contains fog is saturated. As the exit vapour fraction is predicted equally by both models, and the exit gas temperature of the fog film model exceeds that of the conventional film model, one can conclude that these exit conditions, following the conventional film model, correspond to a supersaturated and unstable mixture.

Further examination of figures 4.7 and 4.8 indicates that the exit water temperature is not affected by fog formation. This would be expected; in chapter 2 and 3 we have already seen that the total (latent and sensible) heat flux towards a wall is not changed by fog formation. Both figures also illustrate that the fog and conventional film model deviate only in the prediction of exit gas temperature. For that matter, this deviation is very modest, typically 1°C. That is to say, the formation of fog and its effect on the process of heat and mass transfer will be hard to verify quantitatively. Particularly when one realizes that a supersaturated mixture actually exhibits behaviour between the predictions of the conventional (*i.e.* perfect non–equilibrium) and fog film model, since the latter is based on the saturation condition (*i.e.* perfect equilibrium between vapour and droplet phase).

In figure 4.9 results of similar calculations are depicted for entry liquid and gas temperatures of 20°C and 82°C, respectively, $P_{tot} = 101325$ Pa, $NTU_g = 0.656$ and $NTU_l = 0.042$, and $NTU_g = 0.741$ and $NTU_l = 0.038$, c_{in} ranging from zero up to and 0.388, which is the maximum and saturated vapour fraction. The figure shows the same trends as figures 4.7 and 4.8. The main difference is that the amount of transferred heat is larger, owing to the larger vapour fractions in the gas. Condensation starts for $c_{in} = 0.019$, which is a higher value than the values we have seen for $t_{g,in} = 62°C$. This is due to the higher temperature of gas and interface.

Fog is not formed in a layer next to the wall, which can be attributed to the curvatures of the relation between temperature and vapour fraction in the film, and the saturation line. For higher vapour mass fractions and $Le_v < 1$ the bulk properties are also less, or not, directed into the supersaturated region and hence bulk fog is not likely to be formed. Accordingly, the solutions of the conventional and fog film model coincide.

The entry gas temperature pertaining to figure 4.10 is 100°C, $t_{l,in} = 20°C$, $P_{tot} = 101325$ Pa, $NTU_g = 0.621$ and $NTU_l = 0.042$, and $NTU_g = 0.742$ and $NTU_l = 0.038$. The largest c_{in} of this figure is unity, which corresponds physically to pure saturated steam entering the heat exchanger; the employed model for this situation has been discussed in §4.4. Figure 4.10 indicates that condensation sets in for $c_{in} = 0.023$ and that for all cases fog is not formed. All the mixtures are again sufficiently superheated, implying that the predictions of the fog film model and conventional film model coincide.

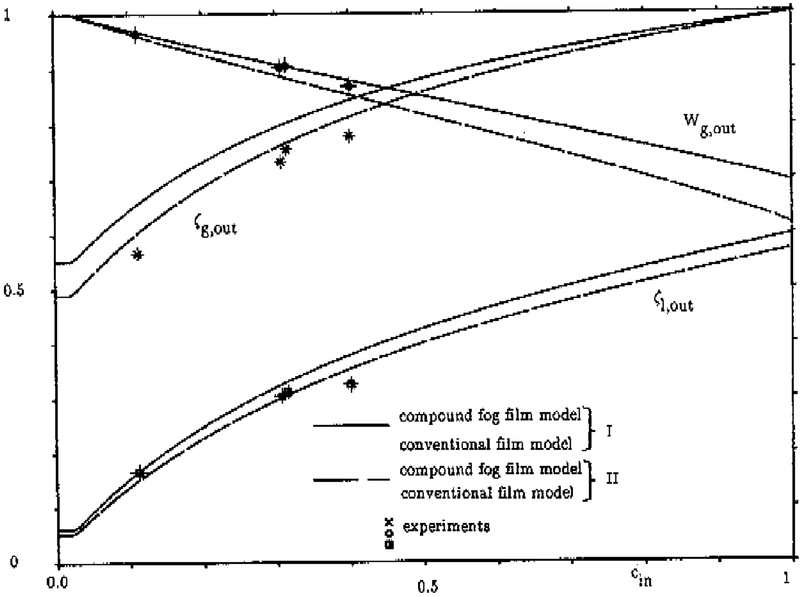

Figure 4.10 Exit properties for $t_{l,in} = 20^\circ C$, $t_{g,in} = 100^\circ C$, $P_{tot} = 101325$ Pa, $NTU_g = 0.621$ and $NTU_l = 0.042$ (I), and $NTU_g = 0.742$ and $NTU_l = 0.038$ (II), according to the fog film model and conventional film model.

In order to indicate some characteristic features of the processes in the heat exchanger, the dimensionless interface temperature is determined for one group of the conditions of figure 4.10 ($NTU_g = 0.742$ and $NTU_l = 0.038$, marked by II). To this end, for a plate of the first pass, $\zeta_i(X=0, Z=0)$, $\zeta_i(1,0)$ and $\zeta_i(0,1)$ are determined, $\zeta_i(0,1)$ represents the maximum and $\zeta_i(1,0)$ the minimum temperature of plate or condensate film, respectively. It can be verified, *e.g.* see figure 4.5, that $\zeta_i(0,1)$ only depends on NTU_l, $\zeta_i(1,0)$ on NTU_g and $\zeta_i(0,0)$ on neither of them.

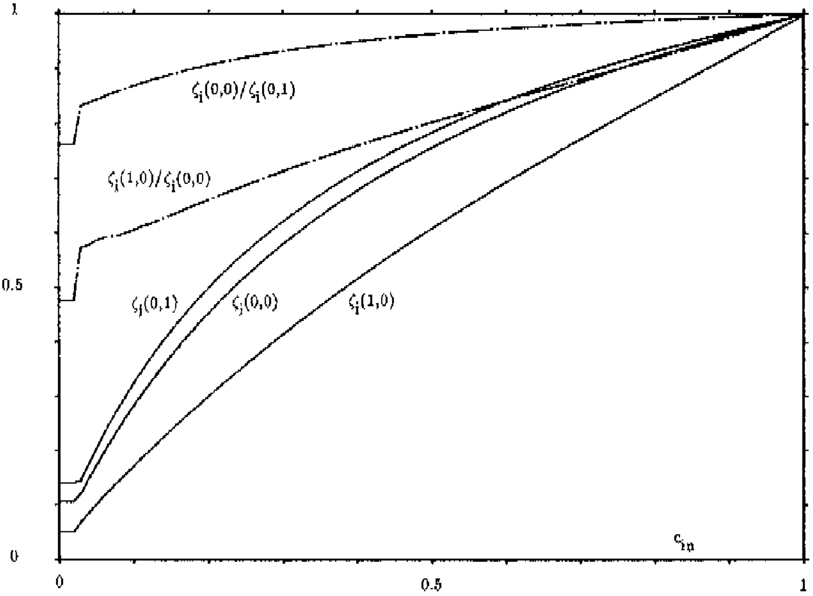

Figure 4.11 Interface temperatures for $t_{l,in} = 20^{\circ}C$, $t_{g,in} = 100^{\circ}C$, $P_{tot} = 101325$ Pa, $NTU_g = 0.742$ and $NTU_l = 0.038$, according to the fog and conventional film model.

For heat transfer without condensation these temperatures are explicitly known, $\zeta_i(0,0)$ is obtained by rewriting equation (4.3) and application of equations (4.9), (4.11), (4.16) and (4.55):

$$\zeta_i(0,0) = \frac{\bar{h}_{tot}}{\bar{h}_{pl}} \ , \tag{4.57}$$

$\zeta_i(1,0)$ follows readily from equations (4.17) and (4.55), and $\zeta_i(0,1)$ is determined by solving equation (4.12) with application of equations (4.9) and (4.11), and substitution of the result in equation (4.55), yielding:

$$\zeta_i(0,1) = 1 - \frac{\bar{h}_{tot}}{\bar{h}_g} e^{-NTU_1} \ . \tag{4.58}$$

For $c_{in} = 1$, the pure steam condensation process, these three temperatures are also known, $\zeta_i(X, Z)$ is uniform and equal to unity, since $t_{sat} = t_{g,in} = 100^\circ C$.

In figure 4.11 $\zeta_i(0,0)$, $\zeta_i(0,1)$ and $\zeta_i(1,0)$ are drawn versus the initial vapour mass fraction. One can notice the smooth transition from heat transfer without condensation, represented by horizontal lines, through partial condensation to pure steam condensation heat transfer. The onset of condensation is indicated by a sudden rise of ζ_i, at first in (X, Z) = (1,0) and subsequently in (0,0) and (0,1). In order to assess the uniformness of ζ_i over the condensate surface, the ratios $\zeta_i(1,0)/\zeta_i(0,0)$ and $\zeta_i(0,0)/\zeta_i(0,1)$ are also depicted in figure 4.11. These lines indicate that the interface temperature is not uniform in both the direction of X and Z; the interface temperature ratios differ significantly from unity, except for c_{in} close to unity. Despite the frequent assumption in conventional condenser analysis of uniform condensate interface temperature, here this temperature substantially depends on the coordinates X and Z. Or, in other words, the processes and pertaining models are essentially two–dimensional.

The accuracy of the numerical procedures has been assessed by varying the number of discretisation points and considering its effect on exit values. These computations revealed that for 15x15 points the numerical error is less than one per cent. For the examined heat exchanger with two passes this grid corresponds to a computational time of 20 seconds on Harris H500 for partial condensation and fog formation, 10 seconds for partial condensation and 5 seconds for pure vapour condensation. These values serve very well the objective of the present investigation, even if on an IBM AT these requisite times will be a factor 5 longer. All computations disclosed that the predictions of the approximate fog film model of chapter 2 are practically identical to those of the compound fog film model, but that the computational time is twice as long.

§4.6 Experiments

The theoretical predictions of the previous section are now compared with some performed experiments. These experiments have been carried out in cooperation with the Mechanical Engineering Department of Eindhoven University of Technology. Main features of test rig and experiments performed have well been reported by Beekmans (1989), Maclean (1989) and Van Vredendaal (1990). Some aspects of apparatus and experiments are summarized below.

Apparatus

The heat exchanger was tested at ambient pressure in a low speed wind tunnel with an entire length of about 16 m, see figure 4.12. Air is transported by means of two fans (2 x 0.88 kW) and heated using metal heat exchangers. In these heat exchangers superheated steam of 150°C with a maximum pressure of 8 bar ($t_{sat} = 140^\circ C$) condenses. The steam is supplied by a boiler with a maximum capacity of 1800 kg/hr. Steam from the same generator is injected into the tunnel to create gas mixtures with arbitrarily desired temperatures and vapour mass fractions.

The flow of the gas mixture is determined with an orifice plate. In the widening funnel of the tunnel a central plate is placed to distribute the gas uniformly over the plates ($\overline{u} < 5$ m/s) of the plastic heat exchanger and avoid preference flows.

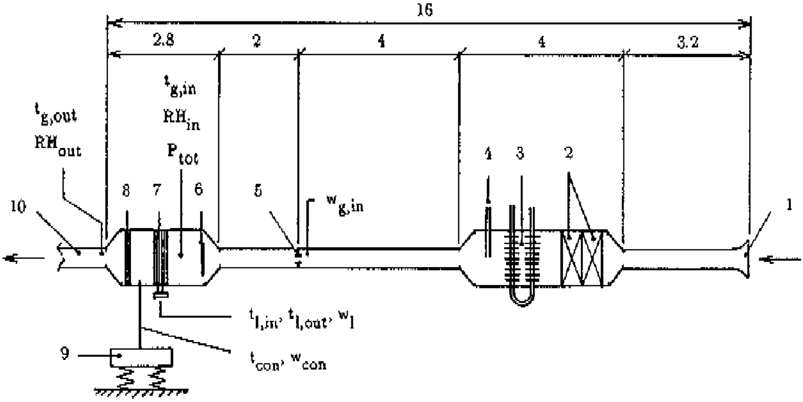

1: inlet, 2: fans, 3: metal heat exchangers, 4: injector, 5: orifice plate, 6: plate,
7: plastic heat exchanger, 8: droplet catcher, 9: weighing–machine, 10: exit

Figure 4.12 Experimental apparatus (sizes in m).

To permit a visual inspection of the phenomena at the gas side (condensation, fog formation), the heat exchanger is placed in a rectangular chamber with 10 mm thick heat–resistant glass walls. A (removable) cover allows further insulation of the tunnel (and glass chambers). The tunnel is heated electrically between steam injector and glass chamber to prevent premature condensation and to shorten the measurement time. After 1 hr a reproducible steady–state situation could usually be obtained. After the heat exchanger a droplet catcher removes large droplets and homogenizes the exit gas flow.

Holes have been provided in the walls of the tunnel (in the glass chamber in front of the heat exchanger and at the end of the narrowing funnel after the heat exchanger) to measure the temperatures and relative humidities of the gas with mercury thermometers and Vaisala HMP–135Y devices. Before the heat exchanger the absolute pressure in the tunnel is determined with an U–tube manometer.

The heat exchanger was placed with respect to gravity such that countercurrent condensation occurs on the 48 plates of the first pass and that cocurrent condensation takes place on the 48 plates of the second pass, see figure 4.4. The rate of produced condensate was measured with the help of a weighing–machine and a chronometer. The temperature of the condensate was measured with a mercury thermometer.

The entry and exit temperatures and flow of the primary water are measured with mercury thermometers and a rotameter, respectively. The demineralized water is draw off and carried back to a closed water circuit. The capacity of this circuit is large enough such that the entry temperature is practically constant ($17.8^\circ C < t_{1,in} < 20.8^\circ C$). Before the measurements were performed all devices have been calibrated.

Results

The depicted experimental results in figure 4.7, taken from in appendix G, and uncertainties in both NTU's, discussed in appendix H, indicate that their NTU_1 ranges from 0.038 to 0.041 and NTU_g from 0.612 to 0.710. These values imply that the experimental dimensionless exit values should be located between the two theoretical situations depicted in figure 4.7. Both cases namely represent the most extreme conditions: the smallest liquid flow and largest gas flow (marked by I), and largest liquid flow in combination with the smallest gas flow (II). For the same reason the selected experimental results, with their uncertainties, for figures 4.8–4.10 have to lie between the depicted theoretical solutions as well. In appendix G all experimental results are documented, supplied with a global energy balance. The vertical and horizontal bars in figures 4.7–4.10 are the ranges of uncertainty in the primary measurements of temperature, relative humidity, condensate weight and time, see appendix H. The results of this appendix indicate that the uncertainties in c_{in}, $\zeta_{l,out}$, $\zeta_{g,out}$ and W_{con} are smaller than 0.0120, 0.0034, 0.0032 and 0.0085, respectively.

The observations of the liquid exit temperatures suggest that the theoretical predictions overestimate the true heat and mass transfer for large condensation rates. This overprediction of heat and mass transfer is attributed to the actual heat resistance of the condensed water, which has been neglected theoretically. During the condensation experiments it was observed that, contrary to the assumptions of the model, the water condensed dropwise on the PVDF channel plates, sometimes forming bridges between to adjacent parallel walls. The figures also show the trend that the theoretical mass transfer rates overestimate the true mass fluxes, while the true sensible heat transfer appears to be better than theoretically expected.

The droplets drain off the plate until a intermediate reinforcement of two plates is reached. These reinforcements stop the flow of the condensate and in this way the negative effect of the condensate is reduced. It is expected that the slightly negative effect of condensate on heat transfer will be reduced if the heat exchanger is placed with respect to gravity such that crosscurrent condensation takes place with the gas flow in the direction of the condensate flow, see figure 4.4.

In the previous section it was explained that it is difficult to detect quantitatively the effect of fog formation on exit properties, and that it can be detected qualitatively only. To this end, a 300 W light was used to illuminate the gas flow in the glass chambers and detect the threshold entry vapour mass fraction that results in fog formation. Fog is first observed in the gas that leaves the plates of the first liquid pass (more specifically: where the cold liquid enters the plates) and subsequently, on increasing c_{in}, after the plates of the second pass. The gas flows are separated by a plate of 0.2 m to avoid direct contact and mixing of both flows. To promote fog formation and avoid supersaturation as much as possible, extra nuclei are added to the gas flow. These nuclei are generated by glowing saw dust at the entrance of the wind tunnel. A typical glowing rate is 0.3 kg saw dust per hour, while the total gas mass flow at the entrance of the tunnel (corresponding to 96 $w_{g,in}$) varies from 0.2 kg/s to 0.5 kg/s, see appendix G. In tables 4.2 and 4.3 the experimentally determined bounding c_{in} (for each pass) of no fog/fog for the underlying conditions of figures 4.7 and 4.8, respectively, are listed. It was noticed that the extra nuclei were needed to create visible fog in the vicinity of the critical c_{in}. For c_{in} that exceed this threshold value significantly nuclei were no longer needed.

In both tables also the theoretical predictions for the onset of film and bulk fog are included. One can see from these tables that fog formation starts for a lower c_{in} when NTU_g is large (which is to say a small gas flow) and NTU_l is small (large liquid flow).

	first pass		second pass	
	film	bulk	film	bulk
$NTU_g = 0.612$, $NTU_l = 0.041$	0.084	0.111	0.104	0.127
$NTU_g = 0.710$, $NTU_l = 0.038$	0.081	0.105	0.100	0.123
Fog observation	0.106		0.121	

Table 4.2 Theoretical and experimental threshold entry vapour mass fractions for film and/or bulk fog formation.

The results indicate that the experimental threshold c_{in} correspond to the theoretical boundaries for developing bulk fog. It is also possible of course that film fog is observed and that the difference in c_{in} (about 0.02) can be attributed to supersaturation. However, in the considered temperature and saturation mass fraction regions ($20^{\circ}C \leq t \leq 62^{\circ}C$, $0.014 \leq F(t) \leq 0.142$) a vapour supersaturation of 0.02 corresponds to a temperature supercooling of about 6.5°C. Such a supercooling level is not likely to take place, in appendix F for instance it can be seen that visible fog formation occurs if supercooling exceeds 1°C to 2°C. Accordingly, the experimental and theoretical results can be considered as an indication for the correctness of the application of the fog film model to channel flow, as described in §2.6 and §3.4.

The main physical feature of the suggested procedures is the distinction between film and bulk fog. Created film fog was neglected as long as the bulk properties are superheated, legitimated by the thinness of the film.

	first pass		second pass	
	film	bulk	film	bulk
$NTU_g = 1.001$, $NTU_l = 0.039$	0.078	0.097	0.094	0.115
$NTU_g = 1.270$, $NTU_l = 0.036$	0.076	0.088	0.087	0.104
Fog observation	0.097		0.111	

Table 4.3 Theoretical and experimental threshold entry vapour mass fractions for film and/or bulk fog formation.

This approach is allowed for turbulent and developing laminar channel flow. In either of these situations one can actually speak of a bulk and a thin film next to the wall where heat and mass are transferred. The gas entering and flowing between the channel plates never attains a parabolic velocity profile as $Re_g > 500$ (the minimum and maximum NTU_g and NTU_l of tables 4.2 and 4.3 correspond to gas flow Reynolds numbers ranging from 520 to 1210 and liquid flow Reynolds numbers ranging from 250 to 300, respectively). Following Ward-Smith (1980) fully developed flow is attained for:

$$\frac{B_{tot}}{D_{h,g}} > 0.04\ \mathrm{Re}_g \quad . \tag{4.59}$$

So for $\mathrm{Re}_g > 500$ the developing length takes at least 20 $D_{h,g}$, while the length of the gas channel B_{tot} approximates 19 $D_{h,g}$, see figure 4.2. Moreover, the droplets on the plates prevent a smooth development of laminar flow and promote transverse mixing in the gas. All these features of the flow between the plates might be the reason why the agreement with the experimental observations is so good.

The suggested fog film model approach to channel flow is less suited for fully developed laminar channel flow of gas mixtures (which is rarely found in engineering applications). Hayashi *et al.* (1981) observed a superheated core in the presence of a fogging layer next to the wall. These regions were observed in mixtures of wall condensing water–vapour and air flowing between parallel plates.

§4.7 Concluding remarks

Two–dimensional crossflow models have been presented which describe the heat transfer in gas–liquid compact heat exchangers. These models involve heat transfer without condensation, pure steam condensation, and condensation and fog formation in the presence of non–condensables. Both the conventional film model of chapter 1 and the fog film models of chapter 2 and 3 have been employed to predict heat and mass transfer. Mixing rules have been derived and used to determine the equilibrium state of the gas after the heat exchanger, possibly resulting in fog formation or dissolution. These general rules can be applied to all practical cases where gas flows are mixed and the mixture's vapour and droplet phase are not in equilibrium.

Numerous heat transfer computations of various air water–vapour mixtures revealed that the compound fog film model of chapter 3 produces identical results to those of the asymptotic fog film model of chapter 2, but that the required computational time of the latter is twice as long. The entire investigation further revealed that the governing equations of all physical situations can be solved within very short calculational time. Hence the presented models and solution procedures are well executable on a PC.

In the case of condensation the results indicated that a considerable part of the initial vapour flow remains as condensate in the heat exchanger; this is due to the compact geometry of channel plates and heat exchanger. The amount of formed bulk fog is found to be very modest for the selected conditions, and can be verified qualitatively only. The heat transfer to the primary liquid is not affected by fog formation, which was already predicted in chapters 2 and 3. A typical result is that, except for small air fractions, the interface temperature of the film is not uniform and dependent on the location in the heat exchanger.

The theoretical predictions have been compared with experimental data obtained with a PVDF heat exchanger. The entry liquid temperature $t_{l,in}$ was about 20°C and $t_{g,in}$ varied from 60°C to 100°C; the entry vapour mass fraction c_{in} ranged from zero up to and 0.40. For $t_{g,in} \cong 80^\circ C$ and $t_{g,in} \cong 100^\circ C$, fog formation is not predicted and not observed. For $t_{g,in} \cong 60^\circ C$ fog formation is predicted and indeed observed. The observations suggest the correctness of the proposed application of the fog film model to channel flow. Probably this qualitative agreement is due to the type of gas flow between the plates: developing forced convective laminar flow.

The condensation model issues from the approximation that the effect of the water condensate film on heat transfer can be disregarded so that the process of heat and mass transfer is driven by the difference between the liquid temperature in the plate and the gas–condensate interface temperature and is not affected by condensate production and flow along the plate. The co– and countercurrent condensation experiments illustrate that this simplification results in an slight overestimation of the heat exchanger's performance, in particular when c_{in} and –dropwise– condensation rate rise (it should be noted that this dropwise condensation is in contrast to the assumption of filmwise condensation). However, for a heat exchanger operating in crosscurrent condensation and cocurrent gas flow the effect of the condensate will be reduced.

If an order of magnitude analysis for another vapour than water also yields the conclusion that the effect of the condensate is small, the presented model can be applied directly to the condensation of that particular vapour. Moreover, though attention was focussed on plastic heat exchangers, the analysis can very well form the basis for modelling the heat transfer in other types of crossflow heat exchangers. One only needs to know the geometry, and pertaining Nusselt number correlations, of both fluid channels.

5. FILM CONDENSATION OF A PURE VAPOUR ON NON–ISOTHERMAL VERTICAL PLATES

§5.1 Introduction

In appendix E it has been assessed that the water condensate film on the plastic channel plate can be considered as isothermal. Moreover, it was demonstrated that the exerted friction on the film and the pressure drop in the gas channel are very small. In other words, the condensate flows approximately as a free falling film in the direction of gravity. For pure vapours other than water however, the heat resistance of the condensate is, in comparison with the plastic channel plate, in general not negligible. Accordingly, in this chapter the heat transfer from a pure vapour to a cooled channel plate is analyzed. The condensing vapour is assumed to be saturated, which is to say $t_{g,in} = t_{sat}$. Sparrow and Eckert (1961) demonstrated theoretically that the effect of superheating on the condensation process is only of minor importance.

Condensation of pure saturated vapours on vertical flat plates has often been examined in the past. Several extensions and improvements have been proposed to the original analysis of Nusselt (1916). Bromley (1952) and Rohsenow (1956) included the heat capacity of the condensate, Sparrow and Gregg (1959) extended this analysis to include the inertia of the condensate, and Koh *et al.* (1961) analyzed additionally the effect of vapour drag. Chen (1961), Koh (1961), and Churchill (1986) derived approximate solutions, accounting for the afore–said effects. However, all condensation problems analyzed thus far have –to the author's knowledge– been limited to isothermal plates. Temperature rises of the cooling liquid as a result of liberated latent heat are neglected. Such temperature rises and their interaction with the condensation process are considered to be important and typical of channel plates.

In this chapter condensation on channel plates is studied both theoretically and experimentally. Taken into account are conduction and convection in the plate, heat transfer in the condensate, and their interactions. Three types of configuration are examined, namely the flow of the condensate under the action of gravity in the direction of the liquid flow, called cocurrent, in opposite direction, called countercurrent and perpendicular to the liquid flow, called crosscurrent condensation. It is assumed that both the liquid and condensate flow are unmixed, and that the physical properties of both fluids are constant. It is furthermore assumed that the condensate forms a laminar non–rippling film on the plate, though it has been recognized in literature, *e.g.* by V.D.I. (1988), that surface waves appreciably enhance the heat transfer. More information about this phenomenon can be found in the recent article of Ünsal (1988), in which the classical Nusselt model is extended with the effect of surface waves.

The governing equations of the three afore–said processes will be derived, made dimensionless, and analytical solutions of these non–linear equations will be provided. It is shown that the processes are governed by two dimensionless groups: the McAdam number Ad, and the number of transfer units NTU. Based on the analytical solutions and an asymptotic analysis, there is derived an approximate result that is compact and accurate for most practical values of these dimensionless groups characterizing the processes. Furthermore, pure steam condensation experiments are carried out on brass and PVDF channel plates to validate the presented models.

§5.2 Formulation of basic equations

Crosscurrent operation

First, the equations of the crosscurrent condensation process will be mathematically formulated, because this is the most general case. The equations of the other situations can easily be derived from the equations for this process. The liquid flowing through the channels has an inlet temperature $t_{l,in}$, which is lower than the saturation temperature t_{sat} of the vapour, see figure 5.1. For the channel plate, an energy balance for an element dxdz involves conduction and convection heat flows within the plate and an inflow of heat from the condensate. This energy balance can be written as:

$$\frac{w_l c_{p,l}}{2B} \frac{\partial \bar{t}_l}{\partial z} = h_{tot} \left(t_{sat} - \bar{t}_l\right) \quad , \tag{5.1}$$

in which h_{tot} is defined as the overall heat transfer coefficient of the condensate and the plate. The factor two on the left hand side accounts for the heat transfer on both sides of the plate.

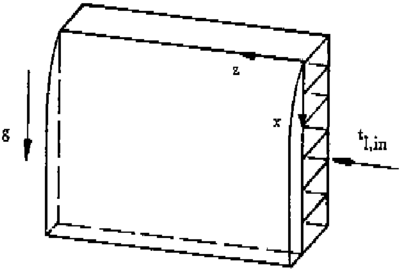

Figure 5.1 Crosscurrent condensation.

The heat transfer coefficient h_{tot} consists of three parts:

$$\frac{1}{h_{tot}} = \frac{1}{h_{con}} + \frac{1}{\bar{h}_w} + \frac{1}{\bar{h}_l} \quad . \tag{5.2}$$

Note that in this chapter h_{tot} is defined otherwise than in the previous chapter. The heat transfer from vapour to film does not appear in the analysis because the vapour is saturated, and thus has the same temperature as the condensate surface. The heat transfer coefficient h_{con} of the condensate, and correlated h_{tot}, are functions of both x and z:

$$h_{con} = \frac{k_{con}}{\delta_{con}} \quad , \tag{5.3}$$

in which k_{con} is the thermal conductivity of the condensate and $\delta_{con}(x,z)$ the film thickness. The contribution of subcooling of the condensate (*i.e.* cooling below the saturation temperature) is neglected because the Kutateladze number Ku_{con} of the relevant condensates is small, *e.g.* see appendix E for the almost isothermal water film on the plastic channel plate. Bromley (1952), Rohsenow (1956) and Sparrow and Gregg (1959) demonstrated that for small Kutateladze numbers convection plays a secondary role because the film is so thin. The heat transfer coefficient $\bar{h}_w$ in equation (5.2) stands for the conduction through the walls of the plate and is defined by:

$$\bar{h}_w = \frac{k_w}{d_4} \quad , \tag{5.4}$$

where d_4 denotes the wall thickness, see figure 4.2. For plastic channel plates the mean forced convection heat transfer coefficient $\bar{h}_1$ in equation (5.2) follows from equation (4.4) and takes the convective heat transfer in the channels into account. For metal channel plates the Nusselt number should be multiplied by a factor two to account for the heat transfer through the intermediate walls in the plate, which act as extra heat transferring surfaces, and the Sieder and Tate correction should be included:

$$\bar{h}_l = \frac{2\overline{Nu}_l k_l}{D_{h,l}} \left[\frac{Pr_l}{Pr_{l,w}}\right]^{0.11} \cong \frac{4\overline{Nu}_l k_l}{(d_1+d_2)} \left[\frac{Pr_l}{Pr_{l,w}}\right]^{0.11} , \tag{5.5}$$

see figure 4.2. In this equation the Sieder and Tate correction appears, see V.D.I. (1988), which plays a role of importance for metal channel plates. In the case of fully developed channel flow the mean Nusselt number $\overline{Nu}_l$ is identical to the local Nusselt number.

The boundary condition on $\bar{t}_l$ reads:

$$\bar{t}_l(x, z=0) = t_{l,in} \quad . \tag{5.6}$$

In order to obtain an equation describing $\delta_{con}(x,z)$, attention is paid to the condensate film. In the momentum equation in the x–direction the inertia terms can be neglected; Sparrow and Gregg (1959) demonstrated that for Prandtl numbers Pr_{con} of the condensate greater than unity these terms may be neglected. The buoyancy force exerted by the vapour on the film can also be neglected, because usually ρ_v/ρ_{con} is small. In appendix E one can see that for water Pr_{con} is larger and ρ_v/ρ_{con} much smaller than unity. The momentum equation in the x–direction then reads:

$$\eta_{con} \frac{\partial^2 u_{con}}{\partial y^2} = -\rho_{con} g \quad . \tag{5.7}$$

In this equation the pressure drop term has not been retained because it is small or even absent, see appendix E. The boundary conditions on u_{con} are:

$$u_{con}(y=0) = 0 \quad , \tag{5.8}$$

$$\left.\frac{\partial u_{con}}{\partial y}\right|_{y=\delta_{con}} = 0 \quad . \tag{5.9}$$

In appendix E it is derived that the exerted friction by flowing gas is small or zero, depending on the orientation of the gas flow towards gravity, and is therefore not mentioned here. Furthermore, Koh (1961) and Koh *et al.* (1961) demonstrated that for small Ku_{con} the drag of the quiescent vapour on the flowing film can be neglected as well, so the zero shear boundary condition is appropriate. Integration of equation (5.7) with respect to y and application of equations (5.8) and (5.9) yields:

$$u_{con}(x,y,z) = \frac{\rho_{con} g}{\eta_{con}} (y\delta_{con} - \tfrac{1}{2}y^2) \quad . \tag{5.10}$$

Using the equation of conservation of mass ($\partial v_{con}/\partial y = -\partial u_{con}/\partial x$), the velocity $v_{con}(x,y,z)$ perpendicular to the plate can be determined as:

$$\frac{\partial v_{con}}{\partial y} = -\frac{\rho_{con} g y}{\eta_{con}} \frac{\partial \delta_{con}}{\partial x} \quad , \tag{5.11}$$

subject to the boundary condition:

$$v_{con}(y{=}0) = 0 \quad . \tag{5.12}$$

By integration of equation (5.11) with respect to y and application of equation (5.12) one finds that:

$$v_{con}(x,y,z) = -\frac{\rho_{con} g y^2}{2\eta_{con}} \frac{\partial \delta_{con}}{\partial x} \quad . \tag{5.13}$$

The amount of condensate $\dot{m}$ passing through an element of area dx at $y = \delta_{con}$ is governed by:

$$\dot{m} = \rho_{con} \left(u_{con} \frac{\partial \delta_{con}}{\partial x} - v_{con}\right)\Big|_{y=\delta_{con}} \quad , \tag{5.14}$$

see figure 5.2.

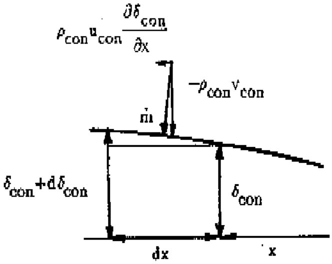
$\rho_{con} u_{con} \frac{\partial \delta_{con}}{\partial x}$
$-\rho_{con} v_{con}$
$\dot{m}$
$\delta_{con}+d\delta_{con}$
δ_{con}
dx
x

Figure 5.2 Vapour flux into condensate film.

Substitution of equations (5.10) and (5.13) into equation (5.14) produces:

$$\dot{m} = \frac{\rho_{con}^2 g}{\eta_{con}} \delta_{con}^2 \frac{\partial \delta_{con}}{\partial x} \quad . \tag{5.15}$$

The amount of liberated heat is the product of the mass flow into the film and latent heat H_{lat}: this liberated latent heat is equal to the heat transported to the liquid:

$$\frac{\rho_{con}^2 g H_{lat}}{\eta_{con}} \delta_{con}^2 \frac{\partial \delta_{con}}{\partial x} = h_{tot} \left(t_{sat} - \bar{t}_l\right) \quad , \tag{5.16}$$

subject to the boundary condition:

$$\delta_{con}(x=0) = 0 \quad . \tag{5.17}$$

In the energy balance (5.16) the subcooling of the condensate has been neglected implicitly, this is only allowed for small Ku_{con}. The non–linear partial differential equations (5.1) and (5.16), coupled by equations (5.2) and (5.3), and boundary conditions (5.6) and (5.17) represent the governing equations of the crosscurrent condensation process.

Countercurrent operation

Next, the countercurrent process is considered, which is depicted in figure 5.3.

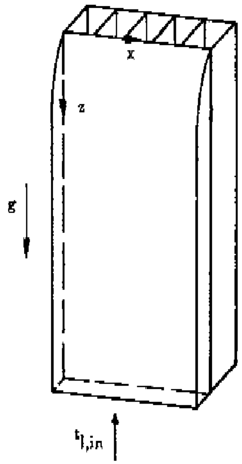

Figure 5.3 Countercurrent process.

The equations describing this process can easily be derived from the equations of the crosscurrent process as:

$$\frac{w_l c_{p,l}}{2B}\frac{d\bar{t}_l}{dz} = -h_{tot}\left(t_{sat} - \bar{t}_l\right) \quad , \tag{5.18}$$

and:

$$\frac{\rho_{con}^2 g H_{lat}}{\eta_{con}}\,\delta_{con}^2\,\frac{d\,\delta_{con}}{dz} = h_{tot}\left(t_{sat} - \bar{t}_l\right) \quad . \tag{5.19}$$

Note that $\bar{t}_l$ and δ_{con} are functions of z only. The boundary conditions become:

$$\bar{t}_l(z{=}L) = t_{l,in} \quad , \tag{5.20}$$

and for equation (5.19):

$$\delta_{con}(z{=}0) = 0 \quad . \tag{5.21}$$

Cocurrent operation

The equations describing the cocurrent process, see figure 5.4, become:

$$\frac{w_l c_{p,l}}{2B}\frac{d\bar{t}_l}{dz} = h_{tot}\left(t_{sat} - \bar{t}_l\right) \quad , \tag{5.22}$$

and:

$$\frac{\rho_{con}^2 g H_{lat}}{\eta_{con}} \delta_{con}^2 \frac{d\delta_{con}}{dz} = h_{tot} (t_{sat} - \bar{t}_l) \quad . \tag{5.23}$$

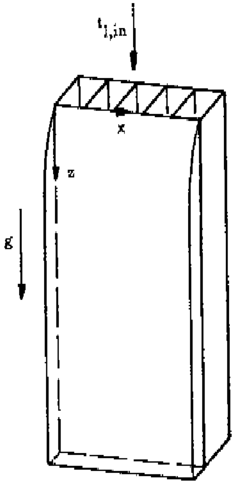

Figure 5.4 Cocurrent process.

The boundary conditions of equations (5.22) and (5.23) read:

$$\bar{t}_l(z=0) = t_{l,in} \quad , \tag{5.24}$$

and:

$$\delta_{con}(z=0) = 0 \quad . \tag{5.25}$$

Faghri and Sparrow (1980) derived similar equations, and integrated them numerically, for co– and countercurrent condensation on a vertical circular tube. The analysis of these equations presented in the following sections can, therefore, right away be applied to both the afore–said processes and pertaining equations.

§5.3 Solutions in closed form

In this section the previously derived differential equations will be set dimensionless and solved in closed form. Dimensionless variables and groups are introduced and defined, and it will be demonstrated that such groups entirely characterize the processes. The three configurations will be treated in a sequence opposite to that employed in the previous section.

Cocurrent process

Equations (5.22) and (5.23), with application of equations (4.2), (4.5), (5.2) and (5.3), can be written in dimensionless form as:

$$\frac{d\zeta}{dZ}(1+\Delta)+\mathrm{NTU}\,\zeta=0 \quad , \tag{5.26}$$

$$\Delta^2(1+\Delta)\frac{d\Delta}{dZ}-\mathrm{Ad}_1\zeta=0 \quad , \tag{5.27}$$

where:

$$\zeta=\frac{t_{sat}-\bar{t}_1}{t_{sat}-t_{1,in}} \quad , \tag{5.28}$$

$$\Delta = \frac{\delta_{con}\bar{h}_{pl}}{k_{con}} \quad , \tag{5.29}$$

$$\mathrm{NTU} = \frac{2\bar{h}_{pl}BL}{w_l c_{p,l}} \quad , \tag{5.30}$$

$$\mathrm{Ad}_l = \frac{\bar{h}_{pl}^4 \eta_{con} L\,(t_{sat} - t_{l,in})}{\rho_{con}^2 H_{lat} k_{con}^3 g} \quad , \tag{5.31}$$

and with boundary conditions:

$$\zeta(Z=0) = 1 \quad , \tag{5.32}$$

$$\Delta(Z=0) = 0 \quad . \tag{5.33}$$

The number of transfer units NTU is inversely proportional to the liquid capacity flow through the plate and Ad_l is the ratio, to the fourth power, of the total heat transfer coefficient of the plate and the heat transfer coefficient of the condensate film. Note that ζ and NTU are defined otherwise here than in the previous chapter. By adding equations (5.26) and (5.27), integrating with respect to Z, and applying equations (5.32) and (5.33), the following relation for Δ and ζ can be obtained:

$$\zeta = -\frac{\mathrm{NTU}}{3\,\mathrm{Ad}_l}\,\Delta^3 + 1 \quad . \tag{5.34}$$

Equation (5.34) is substituted in equation (5.26) and integrated to give:

$$Ln(p^3+1)-\left[\frac{3\,Ad_1}{NTU}\right]^{\frac{1}{3}}\left[3p-Ln(p+1)+\tfrac{1}{2}Ln(p^2-p+1)\right.$$
$$\left.-\sqrt{3}\,arctan\left(\frac{2}{\sqrt{3}}p-\frac{1}{\sqrt{3}}\right)\right]=-NTU\ Z+K_1\quad, \tag{5.35}$$

where:

$$p=(\zeta-1)^{\frac{1}{3}}\quad. \tag{5.36}$$

By application of boundary condition (5.32) K_1 is obtained:

$$K_1=-\tfrac{\pi}{6}\sqrt{3}\left[\frac{3\,Ad_1}{NTU}\right]^{\frac{1}{3}}\quad. \tag{5.37}$$

Values of $\zeta(Z{=}1)=\zeta_{out}$, and hence for the outlet temperature of the liquid, can be determined iteratively with equations (5.35)–(5.37) for any given NTU and Ad_1. Note that $1-\zeta_{out}$ represents what is sometimes called the heat exchanger effectiveness. The maximum possible exit temperature, $\bar{t}_l(X{=}1)=t_{sat}$, corresponds with $\zeta_{out}=0$.

Countercurrent process

Equations (5.18) and (5.19) of the countercurrent process are set dimensionless by introducing equations (4.2), (4.5), (5.2), (5.3) and (5.28)–(5.31):

$$\frac{d\zeta}{dZ}(1+\Delta)-NTU\ \zeta=0\quad, \tag{5.38}$$

$$\Delta^2(1+\Delta)\frac{d\Delta}{dZ} - Ad_1\zeta = 0 \quad , \tag{5.39}$$

and equations (5.20) and (5.21) become:

$$\zeta(Z{=}1) = 1 \quad , \tag{5.40}$$

$$\Delta(Z{=}0) = 0 \quad . \tag{5.41}$$

Equations (5.38) and (5.39) are added, then integrated with respect to Z, and equations (5.40) and (5.41) are applied, yielding:

$$\zeta = \frac{NTU}{3\,Ad_1}\,\Delta^3 + \zeta(Z{=}0) \quad . \tag{5.42}$$

Using equation (5.42) to eliminate Δ in equation (5.38) and integrating the resulting equation with respect to Z yields:

$$\begin{aligned} &Ln(p^3+1) + \left[\frac{3\,Ad_1}{NTU}\,\zeta(Z{=}0)\right]^{\frac{1}{3}} \left[3p - Ln(p+1) + \right. \\ &\left. \tfrac{1}{2}\,Ln(p^2-p+1) - \sqrt{3}\ arctan\!\left(\frac{2}{\sqrt{3}}\,p - \frac{1}{\sqrt{3}}\right)\right] = NTU\ Z + K_2 \quad , \end{aligned} \tag{5.43}$$

where:

$$p = \left[\frac{\zeta}{\zeta(Z{=}0)} - 1\right]^{\frac{1}{3}} \quad . \tag{5.44}$$

By substituting ζ(Z=0) into equation (5.43):

$$K_2 = \tfrac{\pi}{6}\sqrt{3}\left[\frac{3\,\mathrm{Ad}_1}{\mathrm{NTU}}\,\zeta(Z{=}0)\right]^{\frac{1}{3}} \quad . \tag{5.45}$$

The unknown $\zeta(Z{=}0) = \zeta_{out}$ can be evaluated for any NTU and Ad_1 by numerical iteration of equations (5.43)–(5.45).

Crosscurrent process

The crosscurrent equations, equations (5.1) and (5.16), are set dimensionless by equations (4.1), (4.2), (4.5), (5.2), (5.3) and (5.28)–(5.30) and:

$$\mathrm{Ad}_2 = \frac{\bar{h}_{pl}^4\,\eta_{con}\,B\,(t_{sat} - t_{l,in})}{\rho_{con}^2\,H_{lat}\,k_{con}^3\,g} \quad . \tag{5.46}$$

The number Ad_2 has the same physical meaning as Ad_1, but this McAdam number contains B as flow–off length. The equations become:

$$\frac{\partial\zeta}{\partial Z}(1 + \Delta) + \mathrm{NTU}\,\zeta = 0 \quad , \tag{5.47}$$

$$\Delta^3\,(1 + \Delta)\,\frac{\partial\Delta}{\partial X} - \mathrm{Ad}_2\zeta = 0 \quad . \tag{5.48}$$

The boundary conditions of these coupled partial differential equations are:

$$\zeta(X, Z{=}0) = 1 \quad , \tag{5.49}$$

$$\Delta(X{=}0,\, Z) = 0 \quad . \tag{5.50}$$

To solve the above non–linear problem the following procedure will be employed. Instead of $\zeta(X, Z)$ the mean temperature $\overline{\zeta}(X, Z)$ will be determined, defined as:

$$\overline{\zeta}(X, Z) = \int_0^X \zeta(X, Z)\, dX \quad . \tag{5.51}$$

Combining equations (5.48), (5.50) and (5.51) yields:

$$\overline{\zeta} = \frac{1}{3Ad_2} \Delta^3 (1 + \tfrac{3}{4}\Delta) \quad . \tag{5.52}$$

Integrating equation (5.47) with respect to X and substitution of equation (5.51):

$$\frac{\partial \overline{\zeta}}{\partial Z} = -\,NTU \int_0^X \frac{\zeta}{1 + \Delta}\, dX \quad . \tag{5.53}$$

Combining equations (5.48) and (5.53):

$$3Ad_2 \frac{\partial \overline{\zeta}}{\partial Z} = -\,NTU\ \Delta^3 \quad , \tag{5.54}$$

and equations (5.52) and (5.54) produce:

$$3\,(1 + \frac{1}{\Delta})\ \partial\Delta = -\,NTU\ \partial Z \quad . \tag{5.55}$$

Integrating equation (5.55):

$$3Ln\Delta + 3\Delta = -Z\ \mathrm{NTU} + K_3(X) \quad . \tag{5.56}$$

The integration function $K_3(X)$ can be determined by combination of equations (5.48) and (5.49):

$$\Delta^3(Z=0)\ (1 + \tfrac{3}{4}\Delta(Z=0)) = 3Ad_2X \quad . \tag{5.57}$$

Equations (5.56) and (5.57) yield:

$$3Ln\Delta - 3Ln\Delta(Z=0) + 3\Delta - 3\Delta(Z=0) = -Z\ \mathrm{NTU} \quad . \tag{5.58}$$

For any NTU and Ad_2 it is possible to determine $\bar{\zeta}(X=1,\ Z=1) = \zeta_{out}$ by successive numerical iteration of the analytically obtained equations (5.57) and (5.58), and relation (5.52).

Condensate production and Reynolds number

An important unknown is the amount of energy transferred and condensate produced per unit time. The simplest way to determine it is to employ an overall energy balance:

$$w_{con}H_{lat} = w_1 c_{p,1}\,(t_{1,out} - t_{1,in}) \quad , \tag{5.59}$$

where w_{con} represents the total mass flow of vapour to both films. In the employed energy balance the subcooling of the condensate is neglected again, which is allowed for small Ku_{con}'s. Equation (5.59) is set dimensionless by applying equations (5.28), (5.30) and:

$$\dot{M}_{con} = \frac{w_{con} H_{lat}}{2BL\bar{h}_{pl}(t_{sat} - t_{l,in})} \quad . \tag{5.60}$$

Equation (5.59) becomes:

$$\dot{M}_{con} = \frac{1 - \zeta_{out}}{NTU} \quad . \tag{5.61}$$

Here, ζ_{out} follows from equations (5.35)–(5.37) for the cocurrent process, from equations (5.43)–(5.45) for the countercurrent process, and from equations (5.52), (5.57) and (5.58) for the crosscurrent process.

The Reynolds number of the condensate is defined as:

$$Re_{con} = \frac{u_{con} \delta_{con} \rho_{con}}{\eta_{con}} \quad , \tag{5.62}$$

and is at most where the condensate leaves the plate. For the co– and countercurrent process a global mass balance of vapour entering the condensate films and condensate flowing off the plate and leaving the films yields:

$$Re_{con} \leq \frac{w_{con}}{2 \eta_{con} B} \quad . \tag{5.63}$$

For crosscurrent condensation the Reynolds number of the off–flowing condensate varies with z. That is to say, with the distance from the entry of the coolant, see figure 5.1. The maximum condensate production and Reynolds number is found at z=0. In appendix E, equation (E.1), an expression for the maximum local mass flux $\dot{m}$ is derived. A global mass balance and substitution of equation (E.1) yields as maximum Reynolds number for the crosscurrent process:

$$\mathrm{Re}_{\mathrm{con}} = \frac{\bar{h}_{\mathrm{pl}}(t_{\mathrm{sat}} - t_{\mathrm{con,w}})B}{H_{\mathrm{lat}}\eta_{\mathrm{con}}} < \frac{\bar{h}_{\mathrm{pl}}(t_{\mathrm{sat}} - t_{1,\mathrm{in}})B}{H_{\mathrm{lat}}\eta_{\mathrm{con}}} \quad , \tag{5.64}$$

since the channel plate/condensate interface temperature $t_{\mathrm{con,w}}$ is greater than $t_{1,\mathrm{in}}$.

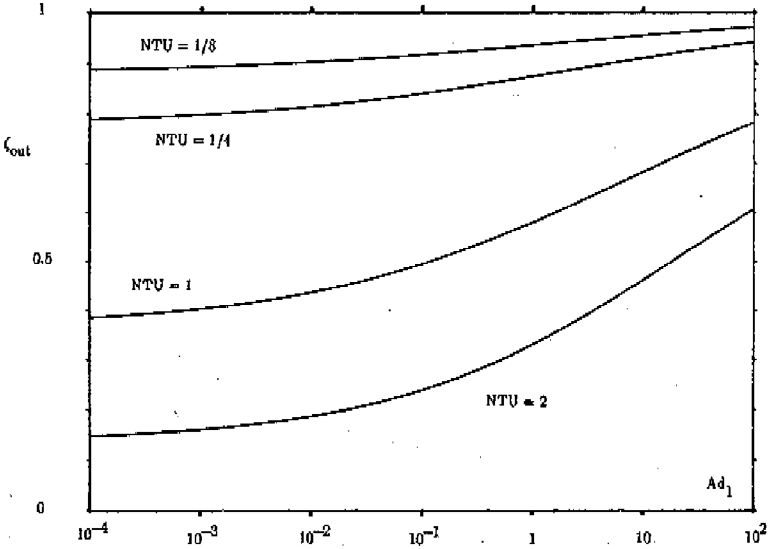

Figure 5.5 Variation of ζ_{out} with Ad_1 for the cocurrent process.

According to V.D.I. (1988) the condensate film is in the laminar flow regime for $\mathrm{Re}_{\mathrm{con}}\mathrm{Pr}_{\mathrm{con}}^{0.95} < 640$.

§5.4 Numerical evaluation

In the previous sections the governing equations for the three relevant process configurations were formulated, non–dimensionalized and solved. Implicit algebraic relations were obtained between ζ_{out}, the numbers NTU and Ad_1 or Ad_2. In this section results will be presented of numerical calculations of ζ_{out} for several values of NTU and Ad_1 or Ad_2.

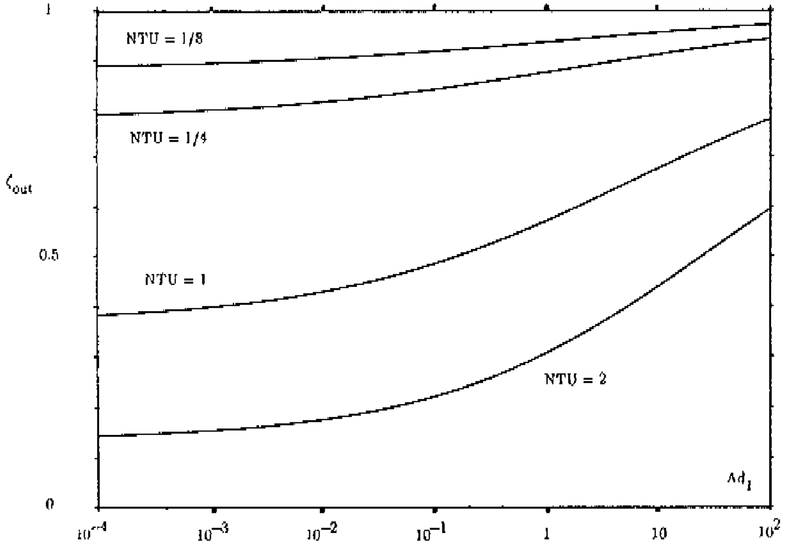

Figure 5.6 Variation of ζ_{out} with Ad_1 for the countercurrent process.

Values of Ad_1 ranging between 10^{-4} and 10^2 are substituted into equations (5.35)–(5.37) and (5.43)–(5.45), while NTU is set equal to 2, 1, 0.25 and 0.125. These ranges of NTU and

Ad_1 extend well beyond most current practical applications. In figures 5.5 and 5.6 the iterated ζ_{out} is plotted against Ad_1, for the co– and countercurrent process, respectively.

The exit temperatures of the countercurrent process are somewhat higher than the exit temperatures of the cocurrent process, in particular for high NTU, but the difference is very small. It should be borne in mind that a higher ζ_{out} implies a lower exit temperature, see equation (5.28).

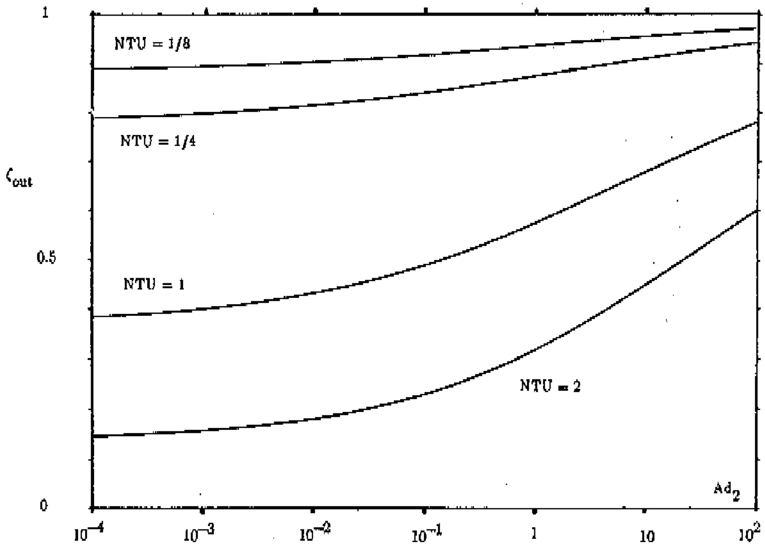

Figure 5.7 Variation of ζ_{out} with Ad_2 for the crosscurrent process.

To calculate ζ_{out} for the crosscurrent case, equations (5.52), (5.57) and (5.58) are successively iterated after substituting values for NTU = 2, 1, 0.25 and 0.125, while Ad_2 varies between 10^{-4} and 10^2. In figure 5.7, ζ_{out} is depicted against Ad_2. It is striking that figures 5.5–5.7 almost coincide when $Ad_1 = Ad_2$, that is when length and width of the plate are equal. This implies that, if L = B, the orientation of the plate towards gravity is not important anymore.

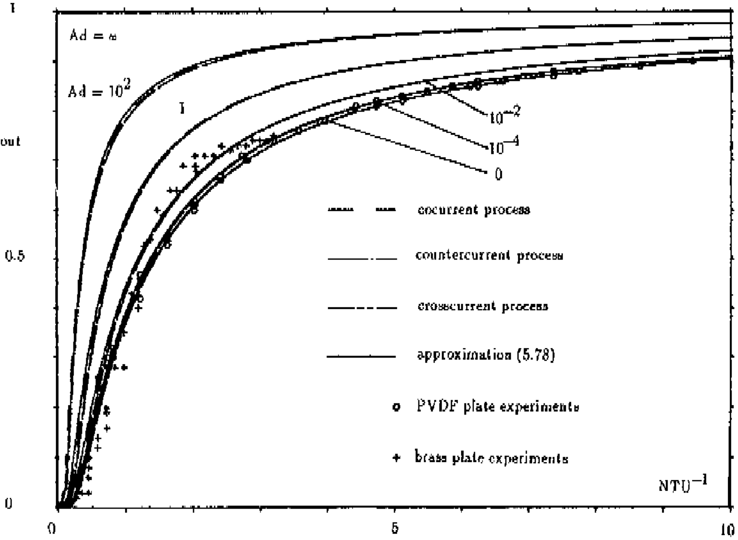

Figure 5.8 Variation of ζ_{out} with NTU^{-1} for the co–, counter–, and crosscurrent process, according to approximation (5.78) and experiments.

Furthermore, it can be concluded that for values of L/B > 1 (because of the application of channel plates this is often the case in plastic heat exchangers) crosscurrent condensation will lead to higher take–off temperatures of the liquid and higher condensate productions. This might be expected because the flow–off length of the condensate is shorter. For reasons of brevity the dimensionless variable Ad is introduced, Ad stands for Ad_1 for co–

and countercurrent condensation, see equation (5.31), and Ad stands for Ad_2 for crosscurrent condensation, see equation (5.46).

Next the exit temperatures for the three processes are calculated for Ad = 10^{-4}, 10^{-2}, 1, and 10^2, while NTU^{-1} is varied between 0 and 10. In figure 5.8, ζ_{out} is drawn versus NTU^{-1}. Again it is obvious that for $Ad_1 = Ad_2$ the exit temperatures are almost the same. It also shows that the exit temperatures tend to zero, for all Ad's, when the liquid flow is nearly zero. Hence, the exit temperatures are equal to t_{sat}, and decrease when the liquid flow increases.

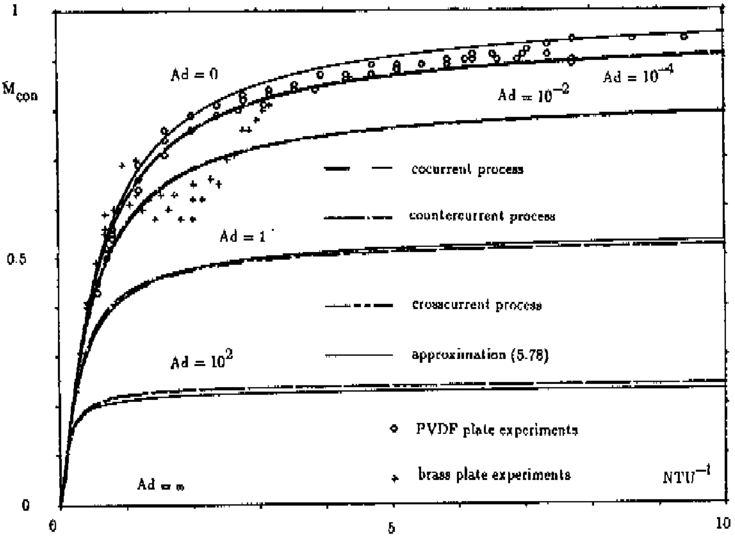

Figure 5.9 Variation of $\dot{M}_{con}$ with NTU^{-1} for the co–, counter–, and crosscurrent process, according to approximation (5.78) and experiments.

Figure 5.8 confirms the expected trend with the exit temperatures for large Ad decreasing more strongly when the liquid flow increases. For large Ad the heat transfer resistance of the film is important when compared with that of the plate. So, when the liquid flow increases the thicker condensate film, for large Ad, will considerably affect the exit temperature. For small Ad, on the contrary, the thickness and heat transfer resistance of the condensate film are of minor importance, even when the liquid flow and condensate production increase.

In figure 5.9 the dimensionless mass transfer $\tilde{M}_{con}$ is plotted against NTU^{-1} for the same values of Ad as is done in the previous figure, using equation (5.61). For small values of NTU^{-1}, increasing the liquid flow results in increasing condensation rates, although the exit temperature decreases. But a further increase of the flow, however, will not lead to any significant increase of the condensate production and energy transfer. Both the liquid flow and the plate area have to be increased to achieve higher condensate productions, see equations (5.30), (5.60) and (5.61).

§5.5 Asymptotic analysis and approximation solution

When attention is paid to figures 5.5–5.7, the supposition arises that there are limiting values of ζ_{out} for large and small Ad's. This supposition is examined in some detail for the crosscurrent process, using asymptotic methods, see Van Dyke (1975). This analysis forms the basis of an approximate solution, which will be introduced at the end of this section.

Small values of Ad imply a poor heat transfer coefficient of the plate and a good heat transfer coefficient of the condensate, see equations (5.31) and (5.46), whereas the inverse is true of large values of Ad. For intermediate Ad's, the heat transfer coefficients of plate and condensate film are of about the same magnitude.

For small values of Ad_2, which may occur when steam condenses on a plastic channel plate, the following perturbation expansions can be applied:

$$\zeta(X,Z) = \zeta_0(X,Z) + O(\epsilon) \quad , \tag{5.65}$$

$$\Delta(X,Z) = \epsilon\,(\Delta_0(X,Z) + O(\epsilon)) \quad , \tag{5.66}$$

where:

$$\epsilon = (3Ad_2)^{\frac{1}{3}} \quad . \tag{5.67}$$

Substituting equations (5.65)–(5.67) into equations (5.47) and (5.48), equating the coefficients of equal power of ϵ and solving the resulting equations for the zero–order terms yield:

$$\zeta_0 = e^{-NTU\ Z} \quad , \tag{5.68}$$

$$\Delta_0 = (X\ e^{-NTU\ Z})^{\frac{1}{3}} \quad . \tag{5.69}$$

Applying equation (5.51) gives:

$$\zeta_{out} = \bar{\zeta}_0(X{=}1,\ Z{=}1) = e^{-NTU} \quad . \tag{5.70}$$

This zero–order solution suggests that for small Ad_2 the heat transfer coefficient of the condensate film is negligibly large compared with the heat transfer coefficient $\bar{h}_{pl}$ of the channel plate. The film on the plate can be considered to be isothermal and its presence disregarded. In figures 5.8 and 5.9 the zero–order solution has been drawn.

For large values of Ad_2, *e.g.* when isopropanol or toluene condenses on a metal channel plate, the perturbation expansions:

$$\zeta(X,Z) = \zeta_0(X,Z) + O(\epsilon) \quad , \tag{5.71}$$

$$\Delta(X,Z) = \frac{1}{\epsilon}\left(\Delta_0(X,Z) + O(\epsilon)\right) \quad , \tag{5.72}$$

where:

$$\epsilon = (3Ad_2)^{-\frac{1}{4}} \quad , \tag{5.73}$$

can be applied. Equations (5.71)–(5.73) are substituted into equations (5.47) and (5.48). Equating coefficients of equal power of ϵ and solving the resulting equations for the zero–order terms yield:

$$\zeta_0 = 1 \quad , \tag{5.74}$$

$$\Delta_0 = (\tfrac{4}{3}X)^{\frac{1}{4}} \quad . \tag{5.75}$$

Application of equation (5.51) gives:

$$\zeta_{out} = \bar{\zeta}_0(X=1,\, Z=1) = 1 \quad . \tag{5.76}$$

The zero–order solutions (5.74) and (5.75) represent –in dimensionless form– the classical Nusselt type condensation on an isothermal plate with temperature $t_{1,in}$. In figures 5.8 and 5.9 this zero–order solution is depicted. An analogous reflection of the equations (5.26) and (5.27) from the cocurrent process, and (5.38) and (5.39) from the countercurrent process, for large and small Ad_1, yields the same limiting values for ζ_{out} and the same physical interpretations.

The asymptotic analyses for large and small Ad's indicate that ζ_{out} is situated between the line pertaining to $\mathrm{Ad} = 0$, represented by equation (5.70), and $\mathrm{Ad} = \infty$, represented by equation (5.76):

$$e^{-\mathrm{NTU}} \leq \zeta_{\mathrm{out}} \leq 1 \quad . \tag{5.77}$$

This implies graphically that in figures 5.8 and 5.9 the situation of ζ_{out} and $\dot{M}_{\mathrm{con}}$, respectively, is bounded by both limiting cases. These lines have been depicted in both figures.

The drawn lines, plotted in figures 5.8 and 5.9, represent an approximate solution of the broken lines, which are the solutions in closed form. The approximate function is based on the knowledge of the asymptotic behaviour of ζ_{out} for large and small Ad's, which is the same for the three processes, and figures 5.5–5.9 for intermediate Ad's. This approximation of ζ_{out} is an explicit function of NTU and Ad:

$$\zeta_{\mathrm{out}} = \left(e^{-\mathrm{NTU}} - 1\right) \left[\frac{e^{\frac{\mathrm{NTU}}{2}}}{e^{\frac{\mathrm{NTU}}{2}} + (0.55\mathrm{Ad})^{0.3}} \right] + 1 \quad . \tag{5.78}$$

Equation (5.78) tends to the limiting values of ζ_{out} for large and small Ad's, and matches these values properly for intermediate Ad's. Furthermore, ζ_{out} tends to zero when the liquid flow tends to zero, independent of Ad, and tends to unity when the liquid flow tends to infinity. These physical properties are both essential to the processes and also satisfied by equation (5.78). The amount of condensate production can be evaluated with equation (5.61).

§5.6 Experiments

In the past pure vapour condensation experiments on isothermal plates have been reported, *e.g.* steam condensation by Slegers and Seban (1970) and Ratiani and Shekriladze (1964), to validate the Nusselt condensation model. These efforts were limited to experiments on isothermal plates, thus only verifying the special case Ad = ∞. Accordingly, pure steam condensation experiments with other Ad values have been carried out, the results of these experiments are discussed in this section.

Apparatus

The low pressure steam used is supplied by the central boiler–house. The water is degassed before boiling and consequently is not expected to contain any non–condensables.

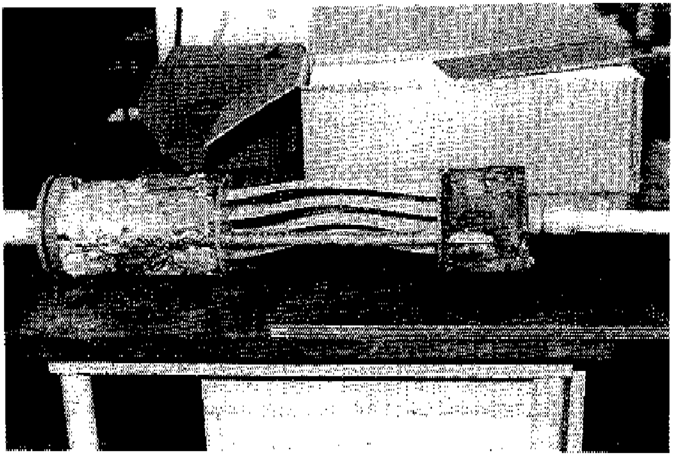

Figure 5.10 Tested PVDF channel plates.

The steam has an absolute pressure P_v of 2.25 bar, with a pertaining saturation temperature t_{sat} of 124°C, and is a little superheated; $t_{g,in} = 135°C$. This degree of superheat is however insignificant, *e.g.* see Sparrow and Eckert (1961) or Minkowycz and Sparrow (1966), and the steam can therefore be considered as saturated. The steam enters a cylindrical chamber with thick (20 mm) PVDF walls to condense on four parallel channel plates, see figure 5.10. The distance between the plates is such that interactions between the condensation processes on the separate plates are excluded. The entire test chamber is thermally insulated with plastic foam to avoid undesired heat transfer. The entering coolant, water, has during the experiments an inlet temperature $t_{l,in}$ of about 11°C. The various temperatures of test rig are measured with laboratory mercury thermometers, and the coolant flow with calibrated flow meters.

	PVDF	brass
B_{tot} (mm)	40.2	40
d_1 (mm)	1.4	3.4
d_2 (mm)	1.6	3.4
d_3 (mm)	0.4	0.6
d_4 (mm)	0.3	0.3
d_5 (mm)	40	40
d_6 (mm)	2.0	4.0
k_w (W/mK)	0.19	85
$\bar{h}_w$ (W/m²K)	633.3	28.3 10^4

Table 5.1 Properties and dimensions of tested channel plates (see figure 4.2).

At the start of the experiments, the condensate in the connection tubes was removed by blowing through steam. By injecting steam, with zero coolant flow, the air present was driven out of the test chamber through a venting hole in the bottom.

In order to create two different McAdam numbers PVDF and brass (DIN Ms 63) channel plates have been tested. Because of the poor thermal conductivity of PVDF the pertaining Ad will be small. The difference with the larger Ad of the brass plate is furthermore increased by adapting the orientation of the rig with respect to the vertical: the vapour condenses cocurrentwise on the brass plates and crosscurrentwise on the PVDF plates. In table 5.1 the dimensions of both set–ups are listed. The NTU is simply varied by adjustment of the liquid mass flow through the plates.

Results

To obtain NTU^{-1} and Ad the physical properties of both fluids have to be determined. As these properties depend on temperature, the proper reference temperatures have to calculated.

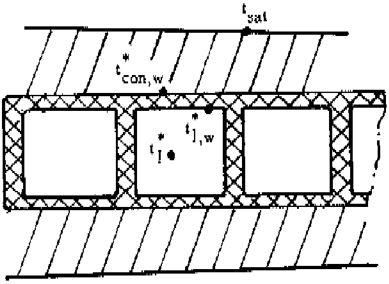

Figure 5.11 Heat transfer from vapour–condensate surface to coolant.

In both characterizing dimensionless groups $\bar{h}_{pl}$ appears, defined by equation (4.5). The heat transfer coefficient $\bar{h}_W$ of the walls follows from equation (5.4) and is listed in table 5.1. The heat transfer coefficient from channel plate to coolant follows from equations (4.4) and (5.5) for the plastic and brass channel plates, respectively. In this chapter the correlation of Dennis *et al.* (1959) is employed for the average laminar convective flow Nusselt number, as in both plates the flow remains in the laminar flow regime. This correlation only accounts for the effect of the thermal entry length, not the hydrodynamic. Neti and Eichhorn (1983) demonstrated numerically that the hydrodynamic development region has little effect for $Pr_l > 6$ and $Re_l Pr_l D_{h,l}/L < 120$. As these conditions are satisfied in the tested channel plates, the correlation of Dennis *et al.* (1959) can be used. The physical properties of the coolant are evaluated at:

$$t_l^* = \frac{t_{l,in} + t_{l,out}}{2} \quad , \tag{5.79}$$

as suggested by V.D.I. (1988).

To calculate the coolant Prandtl number at the brass wall, $Pr_{l,w}$, the temperature at the wall needs to be known, see equation (5.5). This temperature follows from the energy balance:

$$\bar{h}_w \left(t^*_{con,w} - t^*_{l,w}\right) = \bar{h}_l \left(t^*_{l,w} - t^*_l\right) \quad , \tag{5.80}$$

see figure 5.11. The mean wall reference temperature is derived from equation (5.80) as:

$$t^*_{l,w} = \frac{t^*_{con,w}\bar{h}_w + t^*_l \bar{h}_l}{\bar{h}_w + \bar{h}_l} \quad . \tag{5.81}$$

The mean reference interface temperature $t^*_{con,w}$ at condensate—plate surface follows from the energy balance:

$$\bar{h}_{pl}\,(t^*_{con,w} - t^*_l) = \bar{h}_{con}\,(t_{sat} - t^*_{con,w}) \quad . \tag{5.82}$$

This equation is rewritten to obtain as reference temperature:

$$t^*_{con,w} = \frac{\bar{h}_{con} t_{sat} + \bar{h}_{pl} t^*_l}{\bar{h}_{con} + \bar{h}_{pl}} \quad . \tag{5.83}$$

The mean heat transfer coefficient of the Nusselt condensation model is given by Bird *et al.* (1960) as:

$$\bar{h}_{con} = \tfrac{4}{3}\left[\frac{\rho^2_{con} H_{lat} k^3_{con} g}{4\eta_{con}(L \text{ or } B)(t_{sat} - t^*_{con,w})}\right]^{\frac{1}{4}} \quad . \tag{5.84}$$

For co– and countercurrent condensation L should be used in equation (5.84), while for crosscurrent condensation B should be used, corresponding with the flow–off lengths of the processes concerned. Following Minkowycz and Sparrow (1966), the properties of the water condensate are evaluated at reference temperature:

$$t^*_{con} = \frac{t_{sat} + 2t^*_{con,w}}{3} \quad , \tag{5.85}$$

except H_{lat}, which is evaluated at t_{sat}. To determine $\bar{h}_l$ and $\bar{h}_{con}$, the reference temperatures $t^*_{l,w}$ and $t^*_{con,w}$ have to be known to determine the physical properties of both fluids. These heat transfer coefficients, however, depend on the physical properties. A successive substitution method is used to determine the matching $\bar{h}_l$, $\bar{h}_{con}$, $t^*_{l,w}$, and $t^*_{con,w}$. The $t^*_{con,w}$ determined in this way is furthermore used to evaluate the physical properties of the condensate figuring in Ad, see equations (5.31), (5.46) and (5.85).

In figures 5.8 and 5.9 the results of the experiments on brass and PVDF plate are depicted as a function NTU^{-1}. The largest NTU^{-1} of the PVDF plate corresponds to $\mathrm{Re}_l = 993$ and $\mathrm{Re}_{con}\mathrm{Pr}_{con}^{0.95} = 13$; consequently, both fluids are in the laminar flow regime. The Ad of the PVDF experiments increased with rising NTU^{-1} from $0.8\ 10^{-5}$ to $1.1\ 10^{-5}$. This minor variation is due to the poor heat transfer coefficient of the plastic walls (see table 5.1): though the heat transfer from coolant to wall is enhanced by larger mass flows, entry effects cause a $\bar{h}_l$ range from 1300 W/m²K to 1900 W/m²K, $\bar{h}_{pl}$ and Ad remain dominated by $\bar{h}_w$. Figures 5.8 and 5.9 illustrate the excellent agreement between experiment and the theory, which predicted almost no influence of the formed condensate on heat transfer for small values of Ad.

In both figures the experimental results of the condensation on the brass plate are also drawn as a function of NTU^{-1}. The largest NTU^{-1}in these plots, $\mathrm{NTU}^{-1} = 3.2$, corresponds to $\mathrm{Re}_l = 2218$ and $\mathrm{Re}_{con}\mathrm{Pr}_{con}^{0.95} = 209$. During the experiments $\bar{h}_l$ increased from 1300 W/m²K to 2800 W/m²K with increasing NTU^{-1}, owing to entry effects. As $\bar{h}_l$ dominates $\bar{h}_{pl}$, see table 5.1, $\bar{h}_{pl}$ and Ad are nearly enhanced to the same extent as $\bar{h}_l$: Ad increased from $0.29\ 10^{-2}$ to $8.4\ 10^{-2}$ with increasing coolant flow.

Figures 5.8 and 5.9 illustrate the departure from theory for very small and large NTU^{-1}. The discrepancy for very small NTU^{-1} is attributed to the contribution of unavoidable leakage heat flows to the coolant in the brass plate. Accordingly, too high exit temperatures are measured. Some ζ_{out} are even situated below the curve pertaining to Ad = 0, which is physically impossible. Beyond $\mathrm{NTU}^{-1} = 1$ the experimental exit temperatures are situated between the curves Ad = 0 and Ad = 10^{-2}, and are thus in agreement with the theoretical prediction. However, for $\mathrm{NTU}^{-1} > 2$ the experimental ζ_{out} intersects the curve Ad = 10^{-2} and tends to approach the curve Ad = 0, though the experimental Ad approximates $8.4\ 10^{-2}$. This implies that the measured value of ζ_{out} is smaller than predicted, that is to say, the calculated exit temperature is too low. The heat transfer from vapour to coolant is apparently better than predicted by theory. Two possible departures from the ideal model conditions are:

- ripples on the condensate surface,
- dropwise condensation,
- forced vapour flow in the test chamber.

In literature the appearance of ripples is often quoted as major explanation for the Nusselt condensation model underpredicting the heat transfer from condensate to wall.

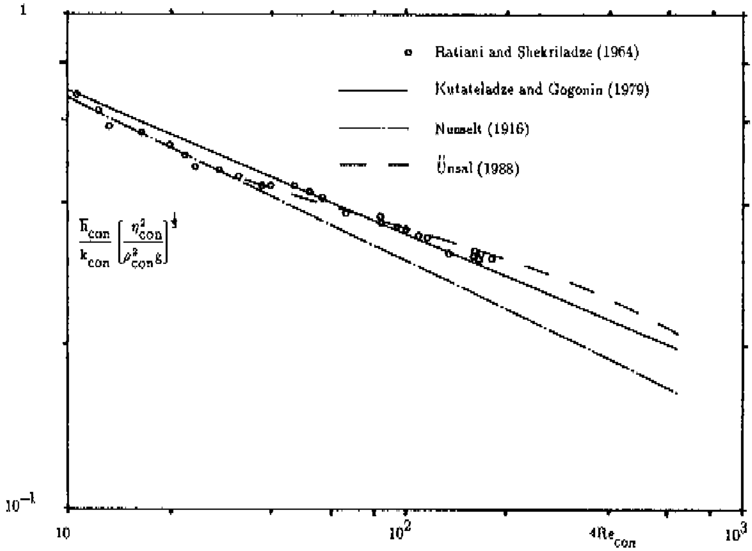

Figure 5.12 Condensation heat transfer according to Nusselt (1916), Ünsal (1988), Ratiani and Shekriladze (1964) and Kutateladze and Gogonin (1979).

For all experiments the dimensionless combination Ku_{con}/Pr_{con} was much smaller than 0.1, implying that the results of the model of Ünsal (1988) can be applied (Ku_{con}/Pr_{con} is referred to as "F" in this note).

The heat transfer through a condensate film with ripples is compared in this note with a film without ripples; the Nusselt solution. One of the results, relevant here, is that for $4\mathrm{Re}_{\mathrm{con}} = 400$, the heat transfer from condensate to plate is augmented by ripples by at most a factor 1.5, see figure 5.12 for a comparison with Nusselt's solution. An additional requirement for this value to be attained is that the dimensionless surface tension number (referred to as "N") is smaller than 12,347. For all condensation experiments however, this number proved to be of order 23,000, so the effect of surface ripples should be less pronounced.

In figure 5.12 experimental data of Ratiani and Shekriladze (1964) are also shown, as well as the simple correction for the effect of waves following Kutateladze and Gogonin (1979):

$$\Theta_{\mathrm{con}} = \mathrm{Re}_{\mathrm{con}}^{0.04} \qquad (5.86)$$

where Θ_{con} is a correction factor for the Nusselt condensation heat transfer coefficient (5.84), and $\mathrm{Re}_{\mathrm{con}}$ the maximum Reynolds number of the condensate. Figure 5.12 illustrates the fair agreement between the result of the comprehensive analysis of Ünsal (1988), the compact correction suggested by Kutateladze and Gogonin (1979), and experiments performed by Ratiani and Shekriladze (1964). However, all experimental and theoretical results indicate that ripples alone cannot account for the calculated heat transfer being too poor. For when Ad is divided by 5, corresponding with the suspected effect of waves to the fourth power, the calculated exit temperature is still too low.

During the experiments it was not possible to watch the plates and verify whether film condensation actually occurred. However, the experimental and theoretical results indicate that the discrepancy between the results depends on the coolant mass flow (and related condensation rate), revealing that the deviation cannot be explained from possible dropwise condensation only. Moreover, dropwise condensation is not expected to take place. This is because the brass plates do not have smooth and clean surfaces as they are constructed from square channels joined by soldering.

The amount of steam injected in the test chamber and condensed on the plates increases with higher coolant flow rates. For the PVDF plate the steam flow reaches a maximum rate of 9 kg/hr, while for the brass plate the maximum steam mass flow amounts 44 kg/hr, owing to the excellent heat transfer in this plate. Though the steam is injected by two injectors, provided with many holes directed away from the channel plates, it is suspected that the condensate films are disturbed, or even blown off the plates, by the incoming steam. The effect of forced flow in the test chamber was also considered by Slegers and Seban (1970) as the most acceptable explanation for their experimental results being 20 % above theory. During their experiments, for that matter, the maximum amount of injected steam was only about 1 kg/hr.

§5.7 Conclusions

Based on the assumption of Nusselt type condensation, which has been found to be consistent in the past for most of the vapours applied, an analysis has been carried out of the condensation processes on non–isothermal plates. Three configurations have been examined and compared: namely cocurrent, countercurrent and crosscurrent condensation. The governing equations have been derived, analyzed and solved. The major results obtained are given below:

- the process is governed by the McAdam number and the number of transfer units,
- for small liquid flows the exit temperature is equal to the saturation temperature, independent of Ad,
- for large and small Ad's, the asymptotic behaviour of the three processes are equal,
- for square plates (L = B), the take–off temperatures for all the three situations are

nearly the same, but if L > B the crosscurrent condensation will result in higher take–off temperatures and condensation rates,

- for small values of Ad, the condensate film can be considered isothermal,
- for large values of Ad, the plate can be considered isothermal, corresponding to Nusselt condensation on an isothermal plate,
- at certain mass flows, dependent on Ad, a further increase in liquid flow will not result in increasing condensation rates. Only an increase in both plate area and liquid flow will result in higher condensate productions.

With knowledge of the asymptotic behaviour of the governing equations, there has been constructed an accurate and compact approximation function for the exit temperature, valid for all configurations of condensation. Experiments performed on PVDF channel plates confirm that the predictions of the model are essentially correct. The theoretical predictions of condensation on brass plates correspond with experiments only in a limited range of the dimensionless numbers. Complete agreement with theory might have been obtained if perfect thermal insulation and quiescent vapour conditions had been more nearly achieved.

APPENDIX A: BASIC EQUATIONS OF THE FILM

In this appendix the induced velocity in a stagnant film, consisting of a vapour and non–condensables, is derived with the continuity equations of both components. Additionally, on basis of Fick's law of diffusion and the obtained expression of the induced velocity, the diffusion equation of the vapour in the film is derived. Furthermore, the energy equation is derived, including the induced velocity. Both equations are also given for the case fog is formed in the film. The mass of formed fog per unit volume follows from combining both equations, which are coupled in the fogging part of the film. An account of the employed basic conservation laws is found in Merk (1957).

The continuity equation of the non–condensables in a film reads:

$$\frac{d(\rho_n v_n)}{dy} = 0 \quad . \tag{A.1}$$

In this equation differentials with respect to the coordinates x and z and time Υ do not appear, since in the film only variations of y are relevant and we are only interested in steady situations, see figure 1.1. Integrating equation (A.1) with respect to y and application of the boundary condition on the non–condensables' velocity:

$$v_n(y{=}0) = 0 \quad , \tag{A.2}$$

yields as velocity of the non–condensables in the film:

$$v_n(y) = 0 \quad . \tag{A.3}$$

Boundary condition (A.2) arises from the fact the wall is impermeable to the non–condensables. Solution (A.3) represents physically that the non–condensable components are quiescent in the entire film. The continuity equation of the vapour component reads:

$$\frac{d(\rho_v v_v)}{dy} = 0 \quad , \tag{A.4}$$

in the case of no fog formation and:

$$\frac{d(\rho_v v_v)}{dy} = K \quad , \tag{A.5}$$

in the case fog is formed. In this equation K represents the rate of disappearance of vapour due to condensation, or fog formation. In a film without fog formation, *e.g.* the classical film, this term is evidently identical to zero; equation (A.4). Fick's equation of the diffusing vapour component in the direction of y reads:

$$\rho_v \, (v_v - v) = - \rho \mathbb{D} \, \frac{dc}{dy} \quad , \tag{A.6}$$

where the vapour mass fraction is defined as:

$$c = \frac{\rho_v}{\rho} = \frac{\rho_v}{\rho_v + \rho_n} \quad . \tag{A.7}$$

In equation (A.6) ρ, v and $\mathbb{D}$ represent the mixture's density, velocity and binary diffusion coefficient, respectively. In equation (A.6) only Fickian diffusion is included, diffusion by pressure or external forces is absent. In this equation thermo–diffusion, or Soret effect, is not analyzed either. For pressures and temperatures found in ordinary heat transfer devices, the Soret and Dufour (or diffusion–thermo) effect have commonly been recognized as second order phenomena. For mixtures of air and wall condensing water–vapour in particular, Minkowycz and Sparrow (1966) demonstrated both theoretically and experimentally that these effects play no role of importance.

The mixture's mass flux is related to the mass fluxes of the components by:

$$\rho v = \rho_v v_v + \rho_n v_n = \rho_v v_v \quad , \tag{A.8}$$

wherein equation (A.3) has been substituted. Combining equations (A.6)–(A.8) produces as induced velocity:

$$v = -\frac{\mathbb{D}}{1 - c}\frac{dc}{dy} \quad , \tag{A.9}$$

caused by the diffusion of vapour. The induced velocity v is negative for suction, *e.g.* condensation, and positive for injection, *e.g.* evaporation. Substitution of equations (A.8) and (A.9) into equations (A.4) and (A.5) yield as diffusion equations:

$$\rho\mathbb{D}\,\frac{d^2 Ln(1 - c)}{dy^2} = 0 \quad , \tag{A.10}$$

and:

$$\rho\mathbb{D}\,\frac{d^2 Ln(1 - c)}{dy^2} = -K \quad , \tag{A.11}$$

respectively. Result (A.10) is employed in chapter 1, see equations (1.2) and (1.3), and equation (A.11) in chapter 2, see equation (2.13).

The energy equation, neglecting the Soret and Dufour effect, viscous dissipation, heat sources or radiation, reads:

$$\rho\mathbb{D}\,(c_{p,n} - c_{p,v})\,\frac{dc}{dy}\frac{dt}{dy} + \rho c_p v\,\frac{dt}{dy} = k\,\frac{d^2t}{dy^2} \quad . \tag{A.12}$$

It is noted that the first term on the left hand side, due to Ackermann (1937), is not always included in the literature, though it is in fact of major influence. Substituting equation (A.9) in equation (A.12) and applying the following relation between the specific heat of the mixture and its composition:

$$c_p = c\,c_{p,v} + (1-c)\,c_{p,n} \quad , \tag{A.13}$$

yields:

$$-\frac{\rho\mathbb{D}c_{p,v}}{1-c}\,\frac{dc}{dy}\frac{dt}{dy} = k\,\frac{d^2t}{dy^2} \quad . \tag{A.14}$$

With fog formation as internal heat source the energy equation reads:

$$-\frac{\rho\mathbb{D}c_{p,v}}{1-c}\,\frac{dc}{dy}\frac{dt}{dy} = k\,\frac{d^2t}{dy^2} + H_{lat}K \quad . \tag{A.15}$$

In the case of fog formation equations (A.11) and (A.15) are coupled by relation (2.5). To determine the amount of produced fog, these equations are combined, yielding:

$$\frac{d^2t}{dy^2} = \frac{\dfrac{H_{lat}}{c_{p,v}} \dfrac{d^2Ln(1-F)}{dt^2} + \dfrac{dLn(1-F)}{dt}}{Le_v - \dfrac{H_{lat}}{c_{p,v}} \dfrac{dLn(1-F)}{dt}} \left(\frac{dt}{dy}\right)^2 , \tag{A.16}$$

in this equation Le_v represents the modified Lewis number. Result (A.16) is then substituted in equation (A.15) and equation (2.5) applied to produce:

$$K = \rho\mathbb{D} \frac{(Le_v - 1)\left[\dfrac{1}{1-F}\dfrac{dF}{dt}\right]^2 + Le_v \dfrac{1}{1-F}\dfrac{d^2F}{dt^2}}{Le_v + \dfrac{H_{lat}}{c_{p,v}} \dfrac{1}{1-F}\dfrac{dF}{dt}} \left(\frac{dt}{dy}\right)^2 , \tag{A.17}$$

The linearized form of equation (A.17) for small F, with Le = 1 substituted, corresponds to the expression ("eq. (7)", K is referred to as "r_3") of Toor (1971a) for the mass of fog formation per unit volume. The amount of fog formation is positive definite for $Le_v \geq 1$, since $c = F(t) < 1$ and the first and second derivative of the function F(t) with respect to t are usually positive, *e.g.* see appendix C for the saturation line of an air water–vapour mixture. The feature of K being larger than zero for $Le_v = 1$ has been employed implicitly by Aref'yev and Averkiyev (1979). For $Le_v < 1$, however, the fog formation can become zero or even negative, thus fog formation ends. Mathematically fog formation in the film ends when the numerator of equation (A.17) becomes zero (or negative):

$$Le_v \leq H(t) = \frac{\left[\dfrac{dF}{dt}\right]^2}{\left[\dfrac{dF}{dt}\right]^2 + (1-F)\dfrac{d^2F}{dt^2}} . \tag{A.18}$$

Differentiating H(t) with respect to t and considering that $d^3F/dt^3 > 0$ it can be verified that dH/dt > 0 and hence H(t) is a monotonically increasing function of t. As example in appendix C the fog condition function H(t), which depends on the saturation line F(t) only, is drawn for an air water–vapour mixture. To permit K > 0 in a fog film Le_v must be larger than the maximum H(t) of the film. Toor (1971b) assumed implicitly that K > 0 in analyzing fog formation of dilute water–vapour in air. This assumption appears to be correct *a posteriori*, since $Le_v \cong 0.5$ for the mixtures considered and hence $H(t) < Le_v$ in the film, see figure C.2.

In order to investigate the expiration of K, equation (A.17) is differentiated with respect to t, equation (A.16) substituted, and rewritten as:

$$\frac{dK}{dt} = \frac{-\rho\mathbb{D}\left(\frac{dt}{dy}\right)^3}{\left[Le_v - \frac{H_{lat}}{c_{p,v}}\frac{d\,Ln(1-F)}{dt}\right]^2} \Bigg[\left(Le_v\frac{d^3Ln(1-F)}{dt^3} + 2\frac{d\,Ln(1-F)}{dt}\frac{d^2Ln(1-F)}{dt^2}\right) \left(Le_v - \frac{H_{lat}}{c_{p,v}}\frac{d\,Ln(1-F)}{dt}\right) + \left(Le_v\frac{d^2Ln(1-F)}{dt^2} + \left(\frac{d\,Ln(1-F)}{dt}\right)^2\right) \left(3\frac{H_{lat}}{c_{p,v}}\frac{d^2Ln(1-F)}{dt^2} + 2\frac{d\,Ln(1-F)}{dt}\right)\Bigg] \quad (A.19)$$

It can be verified, which will not be done here, that the second factor of the right hand side of equation (A.19) is positive in the fogging region. One can therefore readily conclude that the sign of dK/dt is opposite to the sign of dt/dy. That is to say, bearing in mind that K > 0, K is greatest at y = 0 for condensation (since dt/dy < 0 in the film), while the maximum K is found at $y = \delta_a$ for evaporation (dt/dy > 0).

APPENDIX B: THE LOCATION OF G(t) WITH RESPECT TO F(t)

Introduction

In chapters 2 and 3 the location of relation (1.50) with respect to the saturation line F(t) has been examined with slope conditions (2.1) and (2.2) for suction and injection, respectively, and is illustrated in figure 1.7 (with application of equation (1.49)).

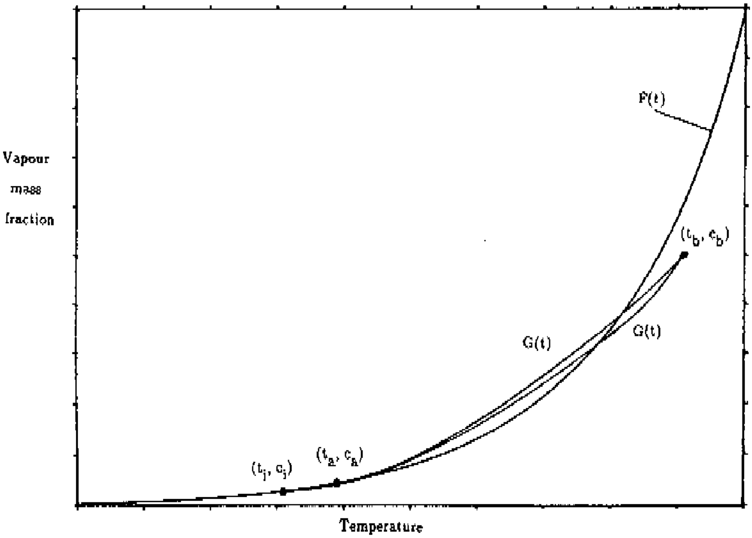

Figure B.1 Incorrect use of equations (2.1) and (2.11).

When these equations predict supersaturation, the border of the saturated region (t_a, c_a) is furthermore detected iteratively with tangency condition (2.11) in combination with equation (2.22). In this appendix remarks are made regarding the use of both procedures. Furthermore, the special case where the bulk properties are saturated is discussed in detail. At the end of this appendix it is demonstrated that the saturated region will never attain the temperature at which the formed fog per unit volume becomes zero.

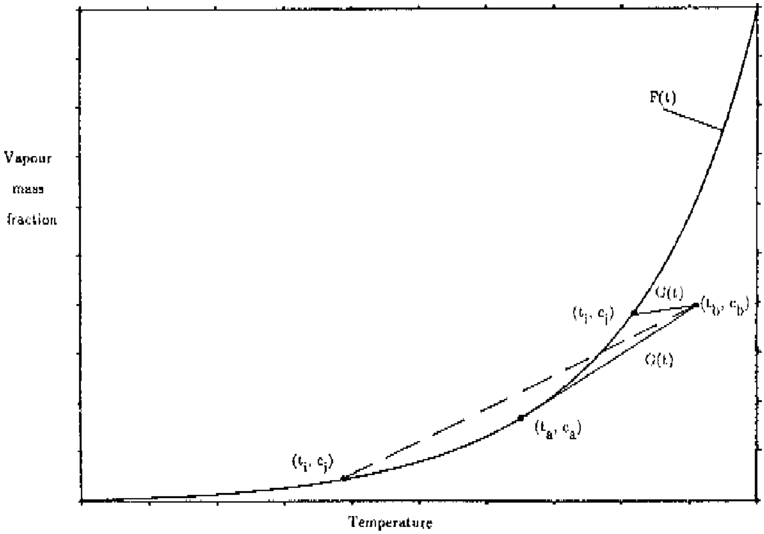

Figure B.2 Determination of t_a for two (t_i, c_i) and $Le_v = 1$.

As a similar consideration applies to evaporation, only condensation cases are discussed here. In this appendix, for reasons of convenience, equation (1.49) is assumed to be valid.

Slope condition

When equation (2.1) predicts that G(t) is entirely situated in the superheated region of the c–t plot, one assumes this curve does not intersect with F(t) between (t_i, c_i) and (t_b, c_b). At the interface the vapour fraction is related to the temperature by:

$$c_i = F(t_i) \quad , \tag{B.1}$$

e.g. see figures 1.7 and 2.1. For $Le_v \geq 1$ this assumption is certainly correct, this follows from the shapes of F(t) and G(t). F(t) is a convex curve, while G(t) is a concave curve for $Le_v > 1$ and a straight line for $Le_v = 1$. In §1.5 these properties of G(t) are discussed.

On the other hand, for $Le_v < 1$, G(t) is a convex curve as well. Thus even when equation (2.1) predicts no fog formation, it is theoretically possible that G(t) and F(t) intersect between t_i and t_b. In figure B.1 an incorrect prediction and use of criterion (2.1) is depicted.

Tangency condition

When equation (2.1) predicts intersection, and hence a saturated region in the film, the boundary temperature t_a and vapour fraction c_a of the saturated region have to be determined. According to the saturation condition they have to obey the continuity equation:

$$c_a = F(t_a) = G(t_a) \quad . \tag{B.2}$$

On basis of the gradient continuity equations (2.9) and (2.10) the properties t_a and c_a have also to fulfill the tangency condition:

$$\left.\frac{dF}{dt}\right|_{t_a} = \left.\frac{dG}{dt}\right|_{t_a} \quad , \tag{B.3}$$

where:

$$\left.\frac{dG}{dt}\right|_{t_a} = \mathrm{Le}_v \frac{c_a - 1}{t_b - t_a}\left[e^{\frac{1}{\mathrm{Le}_v} Ln\left[\frac{1 - c_b}{1 - c_a}\right]} - 1\right] \quad . \tag{B.4}$$

Equation (B.4) follows from combined equations (1.49) and (2.11). Equations (B.2) and (B.3) demand mathematically that the relation (2.8) between c and t in the superheated part of the film, passes in tangentially to the saturation line F(t), which relates c and t in the fog region of the film.

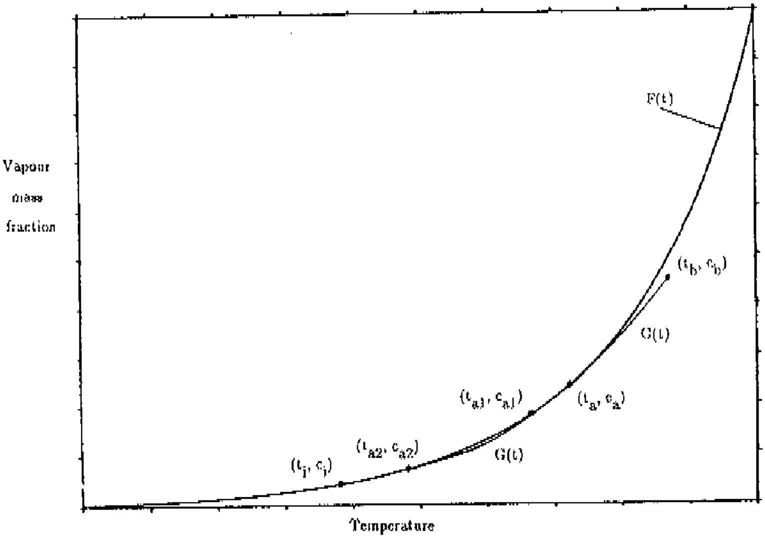

Figure B.3 The c–t relation in a film with two superheated and saturated regions.

For $Le_v \geq 1$ it is evident that there exists only one (t_a, c_a) that satisfies equations (B.2) and (B.3), owing to the shape of G(t). As long as the left hand side of equation (B.3) is smaller than the right hand side during the iteration of t_a, the sought t_a must be larger. In figure B.2 the procedure of determining t_a is drawn for for $Le_v = 1$, thus G(t) being a straight line, see equations (1.49) and (2.8). For iterations with $Le_v \neq 1$, the same iteration criterion is used in this thesis.

Implicitly it has been assumed for $Le_v < 1$ that when a t_a is obtained, the convex curves G(t) and F(t) do not intersect between t_a and t_b. In figure B.1 a t_a and G(t) are given which do not obey this assumption. For $Le_v < 1$ it is even possible that several superheated and and saturated regions exist in the film. In figure B.3 a c–t relation of a film is illustrated in which two superheated and two saturated regions are found. In both (t_{a1}, c_{a1}) and (t_{a2}, c_{a2}) the curve G(t), of the intermediate superheated region, has to pass in tangentially to the curve F(t), as in both these boundaries the continuity equation (B.3) has to be fulfilled. Here the possible existence of more than one superheated region is excluded and therefore not further examined.

Saturated bulk

Special attention is required in the case where the bulk properties (t_b, c_b) are saturated, thus are situated on the saturation line:

$$c_b = F(t_b) \quad . \tag{B.5}$$

With equations (B.2), (B.4) and (B.5) it can be verified, with application of l'Hopital's rule, that:

$$\lim_{t_a \to t_b} \left.\frac{dG}{dt}\right|_{t_a} = \left.\frac{dF}{dt}\right|_{t_a} \quad . \tag{B.6}$$

Equation (B.6) indicates mathematically that $(t_a, c_a) = (t_b, c_b)$ is a correct solution of equation (B.3), independent of Le_v ($Le_v > 0$), and it means physically that the entire film is saturated. For $Le_v \geq 1$, fog will always be formed in the entire film, and the solution $t_a = t_b$ is the only one possible, as explained graphically in figure B.4, with $Le_v > 1$ as example.

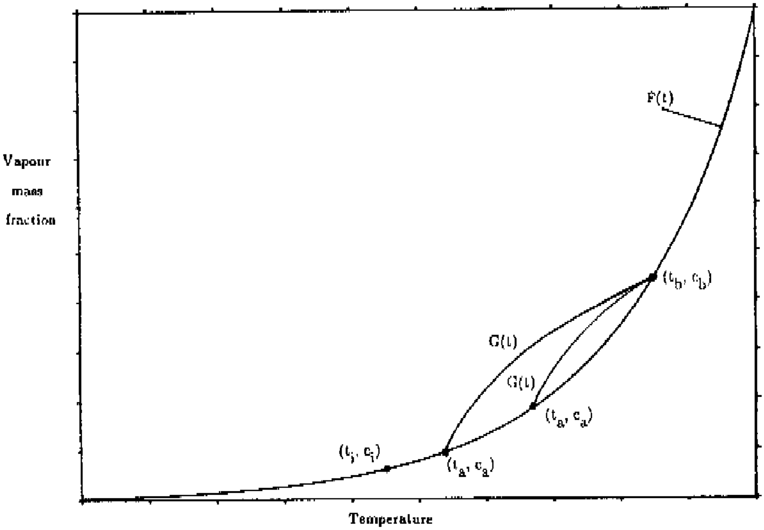

Figure B.4 Determination of t_a for $Le_v > 1$ and saturated bulk properties (t_b, c_b).

For $Le_v < 1$, however, other relations between c and t in the film are possible. The film can for instance be entirely superheated, this is examined with equation (2.1). As example in figure 2.1 an obtained c–t relation is drawn of an entirely superheated film ($Le_v = 0.8$). When fog is predicted by equation (2.1), the film may turn out to be partly superheated when a t_a is found that is smaller than t_b. In figure 2.1 the c–t relation of a partly superheated film is depicted ($Le_v = 0.9$). The boundary (t_a, c_a) in this film has been obtained by means of the procedure previously discussed in this appendix. Physically both depicted relations of c–t in the film are preferable to the pure mathematical solution $t_a = t_b$. Moreover, when the values of Le_v and the fog condition function $H(t_a)$ in table 2.1 are considered, it can be observed that the solution $t_a = t_b$ is not possible, since $Le_v < H(t_b)$ and indeed $H(t_a) < Le_v$. In the next section it is demonstrated that one can always find such a t_a for $Le_v < 1$.

For small vapour mass fractions and regardless the value of Le_v, the entire film is fogging, as follows from tables 2.1 and 2.3. In chapter 3 namely it is derived that for small c, G(t) tends to a straight line. Furthermore, for small vapour mass fractions $Le_v > H(t_b)$ and consequently $K > 0$ is guaranteed, see tables 2.1 and 2.3.

Figure 2.1 also illustrates the correct assumption that F(t) and G(t) do not intersect in the superheated region. In chapter 3 it is demonstrated the curvature of G(t) is more pronounced for larger c, while F(t) tends to be more and more a straight line in this part of the c–t plot. Exotic G(t) and F(t) curves with multiple intersections or superheated regions, as depicted in figures B.1 and B.3, are therefore not likely to take place: G(t) is in fact a function of the form $G(t) \cong t^a$ ($t > 0$, $a = Le_v > 0$), while F(t) is basically of the form $F(t) \cong e^{-1/t}$.

Fog formation condition

We have seen in appendix A that $K > 0$ is assured for $Le_v \geq 1$. In the following it is demonstrated that this is also the case for $Le_v < 1$, since there is always a t_a that is smaller than the temperature which satisfies $K = 0$ (or $Le_v = H(t)$, see equations (A.17) and A(18)).

To the temperature that satisfies $K = 0$, denoted here as $t_{K=0}$, applies:

$$(\mathrm{Le_v} - 1) \left[\left. \frac{dF}{dt} \right|_{t_{K=0}} \right]^2 + \mathrm{Le_v}\,(1 - F(t_a)) \left. \frac{d^2F}{dt^2} \right|_{t_{K=0}} = 0 \quad , \tag{B.7}$$

see equation (A.17). The second derivative of $G(t)$ with respect to t in t_a follows from equations (1.49) and (2.11) as:

$$\left. \frac{d^2G}{dt^2} \right|_{t_a} = \mathrm{Le_v}\,(\mathrm{Le_v} - 1)\, \frac{c_a - 1}{(t_b - t_a)^2} \left[e^{\frac{1}{\mathrm{Le_v}} Ln\left[\frac{1 - c_b}{1 - c_a}\right]} - 1 \right]^2 \quad . \tag{B.8}$$

It can be verified with equations (B.4) and (B.8) that for $0 < \mathrm{Le_v} < 1$:

$$(\mathrm{Le_v} - 1) \left[\left. \frac{dG}{dt} \right|_{t_a} \right]^2 + \mathrm{Le_v}\,(1 - G(t_a)) \left. \frac{d^2G}{dt^2} \right|_{t_a} > 0 \quad . \tag{B.9}$$

Considering the feature of t_a:

$$\left. \frac{d^2F}{dt^2} \right|_{t_a} > \left. \frac{d^2G}{dt^2} \right|_{t_a} \quad , \tag{B.10}$$

and the fact that the left hand side of equation (B.7) is positive for $t < t_{K=0}$, it can be concluded that t_a is greater than t_i, but smaller than $t_{K=0}$. In other words, the saturated region will never attain $t_{K=0}$. Accordingly, in the saturated region $\mathrm{Le_v} > H(t)$ is guaranteed, regardless the value of $\mathrm{Le_v}$.

APPENDIX C: THE SATURATION LINE

In this appendix the saturation function F(t) is derived for a non–condensables vapour mixture, in particular an air water–vapour mixture, as well as the first derivative and inverse of this function. The derivation is based on the saturation pressure equation of a pure substance, on the thermally perfect gas law, and on Gibbs–Dalton's law. The saturation line is furthermore used to compute and depict the fog condition line H(t).

The saturation pressure of a pure substance is commonly described as:

$$\frac{P_{v,sat}(t)}{[\mathrm{bar}]} = A(t) = e^{J(t)} \quad . \tag{C.1}$$

Equation (C.1) is referred to as Antoine's equation when J(t) is represented by:

$$J(t) = \alpha - \frac{\beta}{\gamma \; + \; t/[^{\circ}\mathrm{C}]} \quad , \tag{C.2}$$

while equation (C.1) is referred to as Rankine–Kirchhoff's equation for:

$$J(t) = \alpha - \frac{\beta}{T/[\mathrm{K}]} - \gamma \, Ln(T/[\mathrm{K}]) \quad . \tag{C.3}$$

The Antoine constants of pure liquid water are found in Reid *et al.* (1977); $\alpha = 11.6834$, $\beta = 3816.44$ and $\gamma = 226.87$, the constants of liquid n–butyl alcohol are; $\alpha = 10.5958$, $\beta = 3137.02$ and $\gamma = 178.57$. The Rankine–Kirchhoff constants of liquid nickel follow from Smithells (1976); $\alpha = 32.41$, $\beta = 51578$ and $\gamma = 2.01$. The saturation pressure of a pure liquid is for instance found at the interface of a film of that liquid. In the case there are no other gases present, this pressure is likewise the total pressure.

The mass fraction of vapour is defined as:

$$c = \frac{\rho_v}{\rho_v + \rho_n} \quad . \tag{C.4}$$

Using the law for thermally perfect gases equation (C.4) is transformed into:

$$c = \frac{\dfrac{M_v P_v}{RT}}{\dfrac{M_v P_v}{RT} + \dfrac{M_n P_n}{RT}} \quad . \tag{C.5}$$

In this equation R represents the universal gas constant, R = 8316.94 J/kmoleK, M_n the molecular mass of the non–condensables (air: M_n = 28.96 kg/kmole, helium: M_n = 4.00 kg/kmole), M_v the molecular mass of the vapour (water: M_v = 18.02 kg/kmole, n–butyl alcohol: M_v = 74.12 kg/kmole, nickel: M_v = 58.71 kg/kmole), and T the absolute temperature. The thermally perfect gas law is applicable as the mixtures considered are atmospheric. The partial pressure of the non–condensables can be expressed in the total pressure and the partial vapour pressure with Gibbs–Dalton's law:

$$P_n = P_{tot} - P_v \quad , \tag{C.6}$$

where the total absolute pressure P_{tot} is close to 1.01325 bar (= 1 atm.) in the studied mixtures of nickel and helium, and water–vapour and air. The saturation mass fraction is derived by combining equations (C.1), (C.5) and (C.6):

$$c_{sat}(t) = F(t) = \frac{P_{v,sat}(t)}{P_{v,sat}(t) + \frac{M_n}{M_v}(P_{tot} - P_{v,sat}(t))} \quad . \tag{C.7}$$

This saturation (or equilibrium) line of a water–vapour air mixture is drawn in figure C.1. A mixture is supersaturated when the temperature and vapour mass fraction are situated above F(t), it is saturated when they are situated on F(t), and it is superheated when c and t are situated below F(t). A saturated mixture is found at the interface of a condensate film in the presence of non–condensables, or in the fog layer when thermodynamic equilibrium is assumed.

In this thesis frequently the first and second derivative of F(t) with respect to t is needed. Substituting equation (C.1) and differentiating equation (C.7) with respect to t one finds:

$$\frac{dF}{dt} = \frac{dJ}{dt}\left[1 - (1 - \frac{M_n}{M_v})\, F(t)\right] F(t) \quad . \tag{C.8}$$

Equation (C.8) illustrates that the first derivative is positive definite (as J(t) is monotonically rising and $F(t) \leq 1$), thus F(t) is a strict monotone rising function in t. The second derivative reads:

$$\frac{d^2F}{dt^2} = \frac{dJ}{dt}\left[1 - 2\,(1 - \frac{M_n}{M_v})\, F(t)\right] \frac{dF}{dt} + \frac{d^2J}{dt^2}\left[1 - (1 - \frac{M_n}{M_v})\, F(t)\right] F(t) \quad , \tag{C.9}$$

and it can be verified that it is positive definite as well for the considered air water–vapour mixture. This implies that F(t) of this mixture is a convex function, as illustrated by figure

C.1. Moreover, with F(t) known, the first and second derivative follow directly from equations (C.8) and (C.9) with little computational effort.

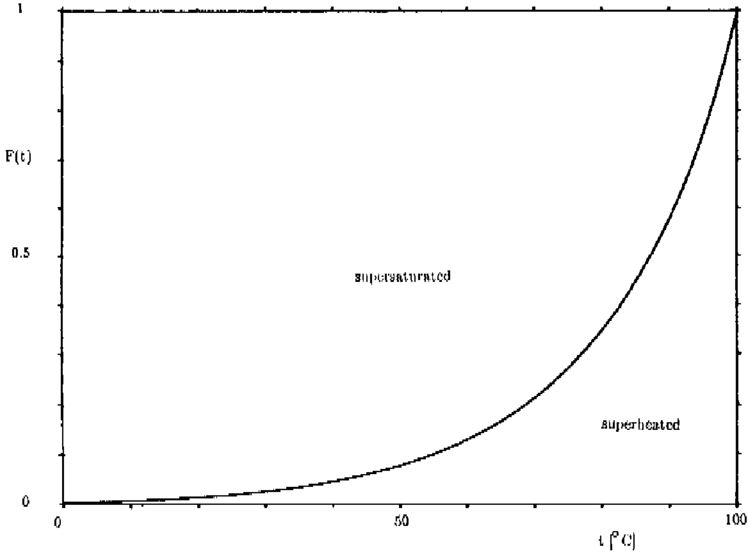

Figure C.1 The saturation line F(t) of water–vapour.

In chapter 4 the saturation temperature of pure steam and the dew point temperature of an air water–vapour mixture are needed to investigate whether condensation takes place. The pure steam saturation temperature follows from the combined equations (C.1) and (C.2) as:

$$\frac{t_{sat}}{[^\circ C]} = A^{inv}(P_v) = \frac{\beta}{\alpha - Ln(P_v/[bar])} - \gamma \quad . \tag{C.10}$$

The dew point temperature is obtained analytically by determining the inverse of the saturation function (C.7), with application of equations (C.1) and (C.2), yielding:

$$\frac{t_{dew}}{[^\circ C]} = F^{inv}(c) = \frac{\beta}{Ln\left[\frac{1 + \frac{M_v}{M_n}(\frac{1}{c} - 1)}{P_{tot}/[\mathrm{bar}]}\right] + \alpha} - \gamma \quad . \qquad (C.11)$$

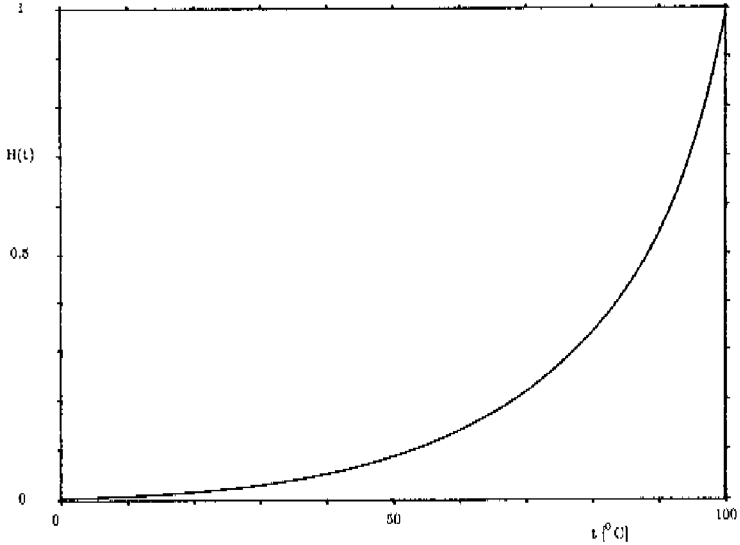

Figure C.2 The fog formation boundary line for an air water–vapour mixture.

In order to examine the possibility of fog formation in the film, in appendix A the fog condition function H(t) has been derived as:

$$H(t) = \frac{\left[\frac{dF}{dt}\right]^2}{\left[\frac{dF}{dt}\right]^2 + (1 - F)\,\frac{d^2F}{dt^2}} \quad , \tag{C.12}$$

which must be smaller than Le_v to permit $K > 0$. In figure C.2 H(t) of the air water–vapour mixture is drawn with the saturation line (C.7) and its derivatives (C.8) and (C.9) substituted. Fog formation spontaneously ends when H(t) in the film's fog layer becomes larger than Le_v. Equation (C.12) and figure C.2 indicate this is never the case when $Le_v \geq 1$, and might be the case when $Le_v < 1$.

APPENDIX D: TRUNCATION ERROR ANALYSIS

In this appendix an error estimation is given of the truncated expansion of Mason's series when it is expanded up to N terms. The error E_N introduced by calculating series (4.20) up to N terms reads:

$$E_N = \frac{1}{NTU_l NTU_g} \sum_{n=N+1}^{\infty} \left[\left(1 - e^{-NTU_g} \sum_{i=0}^{n} \frac{NTU_g^i}{i\,!}\right) \left(1 - e^{-NTU_l} \sum_{i=0}^{n} \frac{NTU_l^i}{i\,!}\right) \right] \quad . \tag{D.1}$$

Substituting the power series of the e–power transforms equation (D.1) into:

$$E_N = \frac{e^{-NTU_l}}{NTU_l} \frac{e^{-NTU_g}}{NTU_g} \sum_{n=N+1}^{\infty} \left(\sum_{i=n+1}^{\infty} \frac{NTU_g^i}{i\,!}\right) \left(\sum_{i=n+1}^{\infty} \frac{NTU_l^i}{i\,!}\right) \quad . \tag{D.2}$$

It can be verified with the power series expansion of the e–power that:

$$\begin{aligned} \sum_{i=n+1}^{\infty} \frac{p^i}{i!} &= \frac{p^{n+1}}{(n+1)!} \left(1 + \frac{p}{n+2} + \frac{p^2}{(n+2)(n+3)} + \ldots\right) \\ &< \frac{p^n}{(n+1)!} (e^p - 1) \quad . \end{aligned} \tag{D.3}$$

Application of equation (D.3) in equation (D.2) yields:

$$E_N < \frac{(1 - e^{-NTU_g})(1 - e^{-NTU_l})}{(NTU_l NTU_g)^2} \sum_{n=N+2}^{\infty} \left(\frac{NTU_l^n}{n!} \frac{NTU_g^n}{n!}\right) . \qquad (D.4)$$

For:

$$NTU_l NTU_g \leq N+2 \quad , \qquad (D.5)$$

it can be validated that:

$$\sum_{n=N+2}^{\infty} \left(\frac{NTU_l^n}{n!} \frac{NTU_g^n}{n!}\right) < \frac{(NTU_l NTU_g)^{N+2}}{(N+2)!} \sum_{n=N+2}^{\infty} \left(\frac{1}{n!}\right) . \qquad (D.6)$$

For most practical situations NTU_l and NTU_g are both smaller than 2. So, even for $N \geq 2$, inequality (D.5) is applicable. Substitution of equation (D.6) into equation (D.4) and employment of the Taylor series expansion of the e–power in unity produces:

$$E_N < \frac{(NTU_l NTU_g)^N (1 - e^{-NTU_g})(1 - e^{-NTU_l})}{(N+2)!} \left(e - \sum_{n=0}^{N+1} \frac{1}{n!}\right) . \qquad (D.7)$$

To calculate the maximum break–off error when series (4.20) is expanded up to five terms, NTU_l and NTU_g are set equal to 2, and $N = 5$ substituted in equation (D.7), yielding a E_N smaller than $0.4 \ 10^{-4}$. This maximum error is a factor 25 times smaller than the propounded error estimation of Mason (1954), which is thus in fact too pessimistic. In the plastic heat exchanger both NTU's are usually smaller than unity, consequently, the truncation error will even be smaller than calculated here.

APPENDIX E: WATER CONDENSATION ON PLASTIC CHANNEL PLATES

In this appendix the maximum condensation mass flux of water–vapour towards a channel plate is assessed. With this maximum mass flux the maximum condensate layer thickness is determined. Even this maximum water layer thickness yields a heat transfer coefficient that is very large compared with the heat transfer coefficient of the plate and consequently, the condensate film can be considered as isothermal.

Maximum mass fluxes towards the plate take place when pure saturated steam (*i.e.* $t_{g,in} = t_{sat}$) condenses on the coldest spot of the plate, that is where the cold liquid enters the plate. With equation (4.48) it can be verified that:

$$\bar{m} \leq \frac{(t_{sat} - t_{l,in})}{\bar{H}_{lat}} \bar{h}_{pl} = 0.032 \text{ kg/m}^2\text{s} \quad , \qquad \text{(E.1)}$$

see table E.1 for the substituted relevant properties. The total heat transfer coefficient of the plate $\bar{h}_{pl}$ follows from equation (4.5) with $\bar{h}_w$ = 950 W/m^{2}K and $\bar{h}_l$ = 3000 W/m^{2}K substituted. This latter value follows from equation (4.7), multiplied by a factor two. This has been done to account for heat transfer through the intermediate walls in the channel plate, though these walls are close to adiabatic for plastic plates. In reality therefore $\bar{h}_l$ and $\bar{h}_{pl}$ will be smaller, resulting in less condensate production and a thinner condensate film.

For an non–isothermal condensate film the physical properties of the film have to be evaluated at a reference temperature that lies between plate surface and t_{sat}. Minkowycz and Sparrow (1966) and Sparrow *et al.* (1967) determined how these properties for a water condensate film should be evaluated. However, in table E.1 and this appendix the physical properties are evaluated at t_{sat}, thus it is assumed *a priori* that the film is isothermal. Substitution of the maximum flux (E.1) and the values of table E.1 into equation (1.26) yields as maximum dimensionless thermal mass flux:

$$\Phi_t \leq 1.18 \quad . \tag{E.2}$$

Actually, the maximum mass flux is smaller, as the driving temperature difference $(t_{sat} - \bar{t}_l)$ decreases because of the temperature rise of the liquid. In the presence of non–condensables the interface temperature t_i is also smaller than t_{sat}, implying a smaller driving temperature difference. Furthermore, the film as such causes an extra, but small, heat resistance that reduces the mass flux.

$\bar{u} = 5$ m/s
$t_{l,in} = 0^\circ$C
$g = 9.81$ m^2/s
$B_{tot} = 75.8$ mm
$\bar{h}_g = 55$ W/m^2K
$k_{con} = 0.677$ W/mK
$c_{p,con} = 4216$ J/kgK
$\rho_{con} = 958.1$ kg/m^3
$\eta_{con} = 282.2\ 10^{-6}$ Pas

$\overline{u^2}/\bar{u}^2 = 6/5$
$t_{sat} = 100^\circ$C
$D_{h,g}\ (\equiv 2d_5) = 4$ mm
$B = 67.2$ mm
$\bar{h}_{pl} = 730$ W/m^2K
$H_{lat} = 2.257\ 10^6$ J/kg
$c_{p,v} = 2034$ J/kgK
$\rho_v = 0.597$ kg/m^3
$\eta_v = 12.28\ 10^{-6}$ Pas

Table E.1 Conditions in heat exchanger, see also figure 4.2, and physical properties of water at state of saturation, according to V.D.I. (1988).

In order to examine the maximum condensate film thickness, attention is paid to the condensate flow along the plate. The film flows under the action of gravity in the direction opposite to the gas flow, which is the most unfavourable condition to obtain a thin film.

For the film the momentum equation in the direction of x yields:

$$\eta_{con}\frac{\partial^2 u_{con}}{\partial y^2} = \rho_{con}g + \frac{dP}{dx} \quad . \tag{E.3}$$

In equation (E.3) the convective terms are not retained. Sparrow and Gregg (1959) demonstrated this so–called Nusselt assumption is valid for all liquids, except low Prandtl number liquids, such as liquid metals. The buoyancy force exerted by the vapour on the film has also been neglected, because ρ_v/ρ_{con} is very small, see table E.1.

Appropriate boundary conditions on u_{con} are:

$$u_{con}(y{=}0) = 0 \quad , \tag{E.4}$$

$$\eta_{con}\frac{\partial u_{con}}{\partial y}\bigg|_{y=\delta_{con}} = \tau \quad . \tag{E.5}$$

The solution of equation (E.3) with application of equations (E.4) and (E.5) reads:

$$u_{con}(y) = \frac{(\rho_{con}g\ +\ dP/dx)}{\eta_{con}}(\tfrac{1}{2}y^2 - y\delta_{con}) + \frac{\tau}{\eta_{con}}y \quad . \tag{E.6}$$

The interfacial shear stress, exerted by the gas on the condensate film, follows from equation (1.30). Combining this equation with equations (1.32), (1.56), (E.1) and the properties of table E.1, yields as maximum non–dimensional frictional mass flux:

$$\phi_u \leq 0.21 \quad , \tag{E.7}$$

and as maximum shear stress:

$$\tau \leq 0.86 \text{ Pa} \quad . \tag{E.8}$$

This shear stress is very small because the flow is laminar. Yet, the interfacial stress cannot be neglected since the film thickness is also very small and hence, the first term in equation (E.6) is small as well. The pressure gradient figuring in equation (E.6) follows from equation (1.42). Applying equations (1.31), (1.32), (1.56), (E.1), and substituting the values listed in table E.1, produces:

$$\frac{dP}{dx} = -\,440 \text{ Pa/m} \quad . \tag{E.9}$$

Applying equations (1.42) and (1.56) it has been assumed the condensate surface velocity $u_{con}(\delta_{con})$ is small in comparison with the vapour velocity $\overline{u}$, this will be verified later on. Moreover, the free flowing area decrement by the presence of the condensate film on the plate surfaces have not been taken into account either. It will be verified later on these films are very thin when compared with the total channel width d_5.

The mean condensate velocity is obtained by integration of equation (E.6):

$$\overline{u}_{con} = \frac{1}{\delta_{con}} \int_{y=0}^{\delta_{con}} u_{con}(y)\, dy = \\ -\frac{\delta_{con}}{\eta_{con}} \left[\frac{\delta_{con}(\rho_{con} g + dP/dx)}{3} - \frac{\tau}{2}\right] \quad . \tag{E.10}$$

A global balance of mass flows towards the condensate film and flowing of the plate yields:

$$\dot{m}B = -\,\rho_{con} \overline{u}_{con} \delta_{con} \quad . \tag{E.11}$$

Substituting equation (E.10) into equation (E.11) produces:

$$\dot{m}B = \frac{\rho_{con}\delta^2_{con}}{\eta_{con}}\left[\frac{\delta_{con}(\rho_{con}g + dP/dx)}{3} - \frac{\tau}{2}\right] \quad . \tag{E.12}$$

Setting δ_{con} dimensionless with respect to the film thickness without shear, thus $\tau = 0$:

$$\Delta = \delta_{con}\left[\frac{\rho_{con}(\rho_{con}g + dP/dx)}{3\dot{m}B\eta_{con}}\right]^{\frac{1}{3}} \quad , \tag{E.13}$$

transforms equation (E.12) into:

$$\epsilon\Delta^3 - \Delta^2 = \epsilon \quad , \tag{E.14}$$

wherein:

$$\epsilon = \left[\frac{8\dot{m}Bg\eta_{con}(\rho_{con}g + dP/dx)}{9\tau^3}\right]^{\frac{1}{3}} = \frac{1}{2.3} \quad . \tag{E.15}$$

In equation (E.15) the values of table E.1 have been substituted, as well as equations (E.1), (E.8), and (E.9). Rather than determining Δ by numerical iteration of equation (E.14), it is asymptotically approximated by substitution of the perturbation expansion:

$$\Delta = \frac{1}{\epsilon}(\Delta_0 + \epsilon^3\Delta_1 + O(\epsilon^6)) \quad , \tag{E.16}$$

into equation (E.14). Solving the zero–order equation yields:

$$\Delta_0 = 1 \quad , \tag{E.17}$$

and the first order equation yields:

$$\Delta_1 = 1 \quad . \tag{E.18}$$

The asymptotic solution, represented by equations (E.15)–(E.18), indicates that the shear, exerted by the vapour, the film thickness enhances with a factor 2.5 ($= (1+\epsilon^3)/\epsilon$). For a free flowing film namely, the dimensionless film thickness Δ equals unity, see equations (E.12) and (E.13). This implies that it is of a major advantage to position the heat exchanger towards gravity such that the condensate flow is not directed opposite to the gas flow. Moreover, for these preferable flow–off situations the pressure gradient, appearing in equation (E.3), is zero as well.

Substitution of equations (E.1), (E.9), and (E.15)–(E.18) into equation (E.13), and the values from table E.1, yields as maximum film thickness:

$$\delta_{con} \leq 1.45\ 10^{-4}\ \mathrm{m} \quad . \tag{E.19}$$

The value of two film thicknesses is about a factor 7 smaller than the channel width d_5, see table E.1. Thus the assumption that the presence of the films is of negligible influence on the available free flowing area, is acceptable. Equation (E.19), combined with table E.1 and equations (E.8) and (E.9), is substituted in equation (E.6) to obtain:

$$u_{con}(\delta_{con}) = 0.08\ \mathrm{m/s} \quad . \tag{E.20}$$

This velocity of the condensate surface is indeed much smaller than the gas velocity $\bar{u}$, see table E.1. Equation (E.20) also indicates that, due to the shear stress exerted by the gas, the surface velocity is opposite to the direction of gravity and mean condensate velocity $\overline{u}_{con}$. As minimum heat transfer coefficient of the plate is obtained with equation (E.19) and table E.1:

$$h_{con} = \frac{k_{con}}{\delta_{con}} \geq 4700\ \mathrm{W/m^2K} \quad . \tag{E.21}$$

This absolute minimum heat transfer coefficient of the water film is about a factor 7 larger than the heat transfer coefficient of the plate $\overline{h}_{pl}$, see table E.1. Furthermore, when the gas flow is not directed in the opposite direction of gravity, the heat transfer coefficient of the film is at least even a factor 2.5 higher than here determined, as the film is the same factor thinner. Accordingly, the water condensate film is approximately isothermal. Its presence is only of importance to relate unambiguously at the vapour condensate interface the partial water–vapour pressure to the interface temperature.

APPENDIX F: THE IMPROVED TANGENCY CONDITION

Introduction

A pioneering article on fog formation in non–condensables vapour mixtures has been published by Johnstone *et al.* (1950). Extensive reviews of subsequent literature on the field of fog formation in gas mixtures have been presented recently by Sekulić (1985) and Koch (1986).

On the basis of a film model analysis, Johnstone *et al.* (1950) derived the tangency condition to determine the critical wall temperature for fog formation in flowing binary mixtures in the presence of wall condensation. This condition followed from a consideration of the vapour pressure and temperature gradients at the wall, which were compared with the slope of the saturation line at wall temperature. Experiments were furthermore performed with mixtures of nitrogen and vapours of sulphur, n–butyl alcohol and water to validate the derived condition.

Two experimental departures from the theoretical predictions of (no) fog formation were observed, namely:

– no fog formation, though predicted, and,

– fog formation, though superheating was proved theoretically.

This former deviation could be attributed to the absence of sufficient nuclei in the gas flow, although in the examined mixtures extra nuclei were generated artificially. The second discrepancy, only found with film condensation of n–butyl alcohol and dropwise condensation of water, could not be explained satisfactory.

In this appendix it will be shown that Johnstone *et al.* (1950) employed an erroneous equation to investigate fog formation; the improved tangency equation will be derived here. Furthermore, the nitrogen water–vapour condensation experiments of Johnstone *et al.*

(1950) are found to correlate excellently with this improved condition.

Basic equations of the film and their solutions

In this section the profiles of the vapour mole fraction and temperature in a stagnant film are derived. The required basic equations of diffusion and energy can be found in Bird *et al.* (1960).

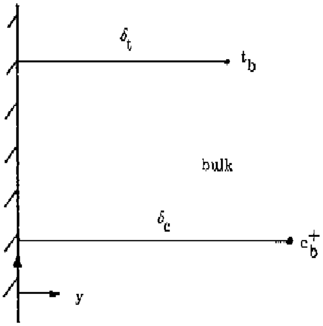

Figure F.1 The film.

In the film, *i.e.* a steady state system wherein variations in the direction of x are not considered, the Fickian diffusion equation reads:

$$v\rho^+ \frac{dc^+}{dy} = \rho^+ \mathbb{D} \frac{d^2c^+}{dy^2} \quad , \tag{F.1}$$

see figure F.1. In this equation v appears as induced velocity:

$$v = -\frac{\mathbb{D}}{1 - c^+} \frac{dc^+}{dy} \quad . \tag{F.2}$$

This velocity is traditionally referred to as "induced velocity", "bulk flow", or "Stefan flow". The boundary conditions on c^+, see figure F.1, read:

$$c^+(y = 0) = c_i^+ \quad , \tag{F.3}$$

$$c^+(y = \delta_c) = c_b^+ \quad , \tag{F.4}$$

where c_i^+ is the vapour mole fraction at the interface and c_b^+ the mole fraction of the bulk. The bulk values of temperature and vapour mole fraction are taken to be the mixed mean values when the film model is applied to closed channel flow, while δ_t and δ_c are considered to be D_h/Nu and D_h/Sh, respectively. Substituting equation (F.2) into equation (F.1), solving the resulting differential equation, and applying equations (F.3) and (F.4), produces:

$$c^+(y) = 1 + (c_i^+ - 1)\, e^{\frac{y}{\delta_c} Ln\left[\frac{1 - c_b^+}{1 - c_i^+}\right]} \quad . \tag{F.5}$$

The energy equation of the film, without viscous dissipation, internal heat sources and radiation, reads:

$$\rho^+ c_p^+ v \frac{dt}{dy} + \rho^+ \mathbb{D} \left(c_{p,n}^+ - c_{p,v}^+\right) \frac{dc^+}{dy} \frac{dt}{dy} = k \frac{d^2 t}{dy^2} \quad . \tag{F.6}$$

In this equation the second term on the left hand side represents the well–known Ackermann term. The boundary conditions on t are:

$$t(y = 0) = t_i \quad , \tag{F.7}$$

$$t(y = \delta_t) = t_b \quad . \tag{F.8}$$

Substituting the relation between the mixtures molar specific heat and its composition:

$$c_p^+ = c^+ \, c_{p,v}^+ + (1 - c^+) \, c_{p,n}^+ \quad , \tag{F.9}$$

and equations (F.2) and (F.5) into equation (F.6), solving the resulting equation and applying boundary conditions (F.7) and (F.8), yields the temperature in the film:

$$t(y) = (t_b - t_i) \left[\frac{e^{\frac{c_{p,v}^+ y}{Le \, c_p^+ \delta_c} Ln\left[\frac{1 - c_b^+}{1 - c_i^+}\right]} - 1}{e^{\frac{c_{p,v}^+ \delta_t}{Le \, c_p^+ \delta_c} Ln\left[\frac{1 - c_b^+}{1 - c_i^+}\right]} - 1} \right] + t_i \quad , \tag{F.10}$$

where:

$$Le = \frac{k}{\rho^+ c_p^+ \mathbb{D}} \equiv \frac{k}{\rho c_p \mathbb{D}} \quad . \tag{F.11}$$

In this section the vapour mole fraction and temperature in a stagnant film have been derived, in the next section they are used to investigate supersaturation in the mixture. Note that equations (A.13) and (F.9) are equivalent.

The fog formation condition

In order to obtain a relation between c^+ and t in the film, which can be compared with the saturation line, the coordinate y/δ_c is eliminated from equations (F.5) and (F.10), yielding:

$$c^+ = G^+(t) = 1 + (c_i^+ - 1) \left[\frac{t - t_i}{t_b - t_i}\left[e^{\frac{c^+_{p,v}\delta_t}{c_p^+ \mathrm{Le}\,\delta_c} Ln\left[\frac{1 - c_b^+}{1 - c_i^+}\right]} - 1\right] + 1\right]^{\frac{\mathrm{Le}\,c_p^+}{c^+_{p,v}}} . \tag{F.12}$$

This relation is a monotonically rising function in t, since the first derivative of $G^+(t)$ with respect to t is positive:

$$\frac{dG^+}{dt} = \frac{\mathrm{Le}\,c_p^+}{c^+_{p,v}}\left[\frac{c_i^+ - 1}{t_b - t_i}\right]\left[e^{\frac{c^+_{p,v}\delta_t}{c_p^+ \mathrm{Le}\,\delta_c} Ln\left[\frac{1 - c_b^+}{1 - c_i^+}\right]} - 1\right] \left[\frac{t - t_i}{t_b - t_i}\left[e^{\frac{c^+_{p,v}\delta_t}{c_p^+ \mathrm{Le}\,\delta_c} Ln\left[\frac{1 - c_b^+}{1 - c_i^+}\right]} - 1\right] + 1\right]^{\frac{\mathrm{Le}\,c_p^+}{c^+_{p,v}} - 1} . \tag{F.13}$$

For $\mathrm{Le}c_p^+/c_{p,v}^+ > 1$ the function $G^+(t)$ is concave, $G^+(t)$ is a straight line for $\mathrm{Le}c_p^+/c_{p,v}^+ = 1$, while $G^+(t)$ is a convex curve for $\mathrm{Le}c_p^+/c_{p,v}^+ < 1$. These properties follow from the second derivative of $G^+(t)$ with respect to t. The vapour mole fraction on the saturation line follows from:

$$c^+ = F^+(t) = \frac{P_{v,sat}(t)}{P_{tot}} . \tag{F.14}$$

Johnstone *et al.* (1950) derived, on basis of a consideration of vapour and temperature profiles, the following slope condition to examine whether supersaturation occurs in a condenser:

$$\frac{\left.\frac{dc^+}{dy}\right|_{y=0}}{\left.\frac{dt}{dy}\right|_{y=0}} = \left.\frac{dG^+}{dt}\right|_{t=t_i} > \left.\frac{dF^+}{dt}\right|_{t=t_i} , \qquad (F.15)$$

which is based on the slopes of $F^+(t)$ and $G^+(t)$ in $t = t_i$.

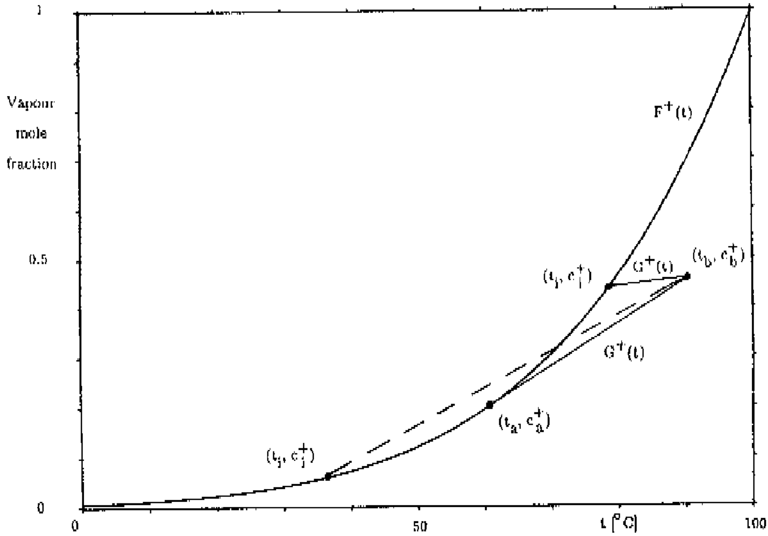

Figure F.2 Determination of t_a and prediction of fog formation, $Lec_p^+/c_{p,v}^+ = 1$ and $\delta_c = \delta_t$, for two (t_i, c_i^+).

With this equation and the saturation condition, thus excluding the possibility of supersaturation, fog formation can be detected. The lowest permissible t_i for which fog is not yet formed, denoted as t_a, is obtained when equation (F.15) is an equality. Applying equations (F.13) and rewriting equation (F.15) yields as tangency condition:

$$\left.\frac{dF^+}{dt}\right|_{t=t_a} = \left.\frac{dG^+}{dt}\right|_{t=t_a} = \frac{\delta_t}{\delta_c}\,\frac{\Theta_c^+}{\Theta_t^+}\,\frac{c_b^+ - c_a^+}{t_b - t_a} \quad , \tag{F.16}$$

where c_a denotes the critical interface mole fraction ($c_a = F(t_a)$). In this equation the thermal Ackermann correction factor is introduced as:

$$\Theta_t^+ = \frac{\dfrac{c_{p,v}^+ \delta_t}{Le\, c_p^+ \delta_c} Ln\left[\dfrac{1 - c_b^+}{1 - c_a^+}\right]}{e^{\dfrac{c_{p,v}^+ \delta_t}{Le\, c_p^+ \delta_c} Ln\left[\dfrac{1 - c_b^+}{1 - c_a^+}\right]} - 1} \quad , \tag{F.17}$$

and the diffusion mass transfer correction factor:

$$\Theta_c^+ = \frac{Ln\left[1 - \dfrac{c_b^+ - c_a^+}{1 - c_a^+}\right]}{-\dfrac{c_b^+ - c_a^+}{1 - c_a^+}} \quad . \tag{F.18}$$

Both (molar) conventional film model correction factors can be found in Bird *et al.* (1960). For $t_i < t_a$, a part of the film is fogging ($t_i \le t \le t_a$), in this part t and c^+ are coupled with equation (F.14). In the superheated part ($t_a \le t \le t_b$) $c^+ = G^+(t)$ prevails. In figure F.2 the physical principles of equations (F.15) and (F.16) are illustrated graphically. Equations

(F.15) and (F.16) have been applied successfully in linearized form by Toor (1971a, 1971b) ($\delta_t/\delta_c = \mathrm{Sh}/\mathrm{Nu} = 1$), Koch (1986) ($\delta_t/\delta_c = 1$) and Hayashi *et al.* (1981) ($\delta_t/\delta_c = \mathrm{Le}^{0.36} = 0.95$) to determine fog formation and assess the boundary of superheated and saturated region in flowing mixtures of dilute wall condensing water—vapour ($\Theta_c^+ \cong \Theta_t^+ \cong 1$) in air.

With equation (F.15) (or with equation (F.16)) fog can be detected. But on the other hand, if equation (F.15) is not fulfilled, superheating in the entire film is not necessarily guaranteed. This aspect of criterion (F.15) is discussed below. For $\mathrm{Le}c_p^+/c_{p,v}^+ \geq 1$ superheating can be examined correctly with equation (F.15), since $G^+(t)$ is a straight line or a concave curve, whereas $F^+(t)$ is convex.

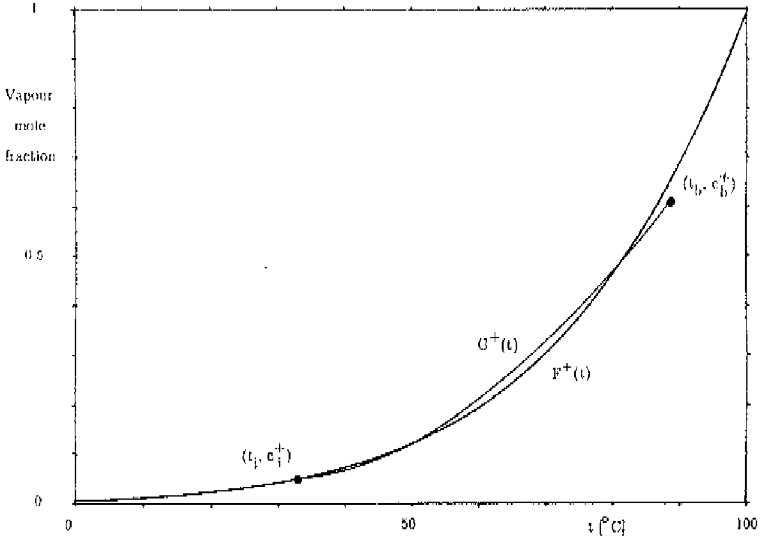

Figure F.3 Erroneous prediction of a superheated film with equation (F.15), $\mathrm{Le}c_p^+/c_{p,v}^+ < 1$ and $\delta_t = \delta_c$.

However, for $\mathrm{Le}c_p^+/c_{p,v}^+ < 1$, it is theoretically possible that equation (F.15) predicts no fog formation, while both convex curves $F^+(t)$ and $G^+(t)$ intersect in the film. In figure F.3 an example of such a supersaturation case in the film is depicted.

The expression of Johnstone *et al.* (1950) ("eq. (9)") is obtained when in equations (F.15)–(F.17) are substituted:

$$\frac{\delta_t}{\delta_c} = \frac{\mathrm{Sh}}{\mathrm{Nu}} = \mathrm{Le}^{\frac{1}{3}} \quad , \tag{F.19}$$

and:

$$c_{p,v}^+ = c_p^+ \quad , \tag{F.20}$$

and:

$$\Theta_c^+ = 1 \quad . \tag{F.21}$$

Equation (F.19) is applicable to turbulent flow (the so–called Chilton–Colburn analogy) and to forced convective laminar flow in the entrance region of a channel. Johnstone *et al.* (1950) examined experimentally laminar flow ($\mathrm{Re} \cong 700$) of binary mixtures in this region of a circular tube. Approximation (F.20) implies $c_{p,v}^+ = c_{p,n}^+$, see equation (F.9), and introduces an unacceptable inaccuracy. This is in particular the case with nitrogen and n–butyl alcohol mixtures (n–butyl alcohol: $c_{p,v}^+ \cong 135$ kJ/kmoleK, water: $c_{p,v}^+ \cong 34$ kJ/KmoleK and nitrogen: $c_{p,n}^+ \cong 28$ kJ/kmoleK). Approximation (F.20) follows actually from a film model analysis where the Ackermann term in energy equation (F.6) is not taken into account. Assumption (F.21) is not correct either, since the diffusion correction factor Θ_c^+ is of the same order of magnitude as the thermal correction factor; they are even identical when $Lec_p^+/c_{p,v}^+ = 1$. Equation (F.21) follows in fact from a film model analysis where the effect of the induced velocity on diffusion is neglected. The introduction of equations (F.20) and (F.21) might be the reason Johnstone *et al.* (1950) observed discrepancies between some experiments and theory. In the next section these cases are discussed in detail.

Condensation experiments

The experimental results of Johnstone *et al.* (1950) are now compared with the correct expression predicting (no) fog formation. We are particularly interested in the cases fog was not predicted with erroneous equations (F.16)–(F.21), though fog formation was observed for some situations. The introduction of equation (F.20) results namely in too high a t_a (since $c_{p,v}^+ > c_p^+$), while assumption (F.21) causes too low a t_a (since $\Theta_c^+ > 1$), see equation (F.16). The net result of both introductions could be too low a t_a, resulting in an erroneous theoretical prediction of a superheated mixture and hence no fog formation. These situations were found only with mixtures of nitrogen and vapours of n–butyl alcohol and water, which are therefore treated here.

In table F.1 the considered experimental data of water–vapour nitrogen mixtures are listed, while in table F.2 those of n–butyl alcohol nitrogen mixtures are summarized. In these tables t_a and (no) fog formation predictions of Johnstone *et al.* (1950) are included.

With equations (F.16)–(F.19) the correct critical temperatures t_a are now re–determined. As the physical properties of air and nitrogen are very similar, the physical properties of air are used here, taken from V.D.I. (1988). The latter is also used to supply the properties of water–vapour. The diffusion coefficient of both gases is given by Edwards *et al.* (1979) as:

$$\mathbb{D}/[\mathrm{m}^2/\mathrm{s}] = 1.758\ 10^{-4}\,\frac{(T/[\mathrm{K}])^{1.685}}{P_{tot}/[\mathrm{Pa}]} \quad . \tag{F.22}$$

The molar specific heat $c^{+}_{p,v}$ of n–butyl alcohol is taken from Reid *et al.* (1977).

	Johnstone *et al.* (1950)					equations (F.16)–(F.19)		
c_b^{+}	t_b [°C]	t_i [°C]	t_a [°C]	prediction	observation	t_a [°C]	prediction	Le
0.101	111.0	12.0	8.0	no fog	no fog	10.1	no fog	0.84
0.101	110.0	10.7	8.3	no fog	no fog	10.3	no fog	0.84
0.098	107.0	9.6	8.5	no fog	no fog	10.3	fog	0.84
0.097	105.0	8.3	8.3	critical value	no fog	10.4	fog	0.84
0.125	110.0	13.7	12.6	no fog	no fog	14.4	fog	0.83
0.123	111.0	12.4	12.4	critical value	fog	13.9	fog	0.83
0.123	112.5	12.0	12.0	critical value	fog	13.7	fog	0.83
0.095	123.5	11.1	5.0	no fog	no fog	7.0	no fog	0.84
0.100	134.0	6.0	4.5	no fog	no fog	6.5	fog	0.84
0.102	136.5	4.7	4.5	no fog	no fog	6.5	fog	0.84
0.096	135.0	4.5	3.7	no fog	fog	5.6	fog	0.84
0.169	129.0	16.5	15.0	no fog	no fog	17.0	fog	0.82
0.172	135.0	15.0	14.5	no fog	fog	16.3	fog	0.82
0.172	137.0	16.0	14.2	no fog	no fog	16.0	critical value	0.81
0.174	139.0	16.0	14.0	no fog	no fog	15.9	no fog	0.81
0.176	140.0	15.0	14.0	no fog	fog	16.0	fog	0.81
0.176	142.0	16.5	13.8	no fog	no fog	15.7	no fog	0.81

Table F.1 Dropwise wall condensation experiments of water–vapour in nitrogen.

The values of k and $\mathbb{D}$ of this vapour, provided by Landolt–Börnstein (1960), are approximated by:

$$k/[\mathrm{W/mK}] = 11.88\ 10^{-3} + t/[^\circ\mathrm{C}]\ (5.54\ 10^{-5} + 2.155\ 10^{-7}\ t/[^\circ\mathrm{C}]) \quad , \quad (\mathrm{F}.23)$$

$$\mathbb{D}/[\mathrm{m}^2/\mathrm{s}] = 0.74\ 10^{-5} \left[\frac{T/[\mathrm{K}]}{273}\right]^{1.72} \quad . \quad (\mathrm{F}.24)$$

The molar densities ρ^+ of all the mixtures are simply determined with the ideal gas law. The Antoine relations for the saturation pressures of both vapours stem from Reid *et al.* (1977). These vapour pressures, in combination with P_{tot} = 1 atmosphere (= 1.01325 bar), yield saturation lines for both mixtures which correspond excellently to the lines drawn by Johnstone *et al.* (1950) ("fig. 2" and "fig. 3").

			Johnstone *et al.* (1950)			equations (F.16)–(F.19)		
c_b^+	t_b [°C]	t_i [°C]	t_a [°C]	prediction	observation	t_a [°C]	prediction	Le
0.181	219.0	33.7	33.7	critical value	fog	31.0	no fog	1.41
0.178	229.0	35.0	32.7	no fog	no fog	29.9	no fog	1.42
0.180	265.0	31.0	30.2	no fog	no fog	27.3	no fog	1.41
0.180	138.0	56.6	44.0	no fog	no fog	41.3	no fog	1.43
0.180	152.0	43.9	41.5	no fog	fog	38.8	no fog	1.42
0.182	167.0	45.9	39.3	no fog	no fog	36.8	no fog	1.41
0.181	212.0	38.7	34.3	no fog	no fog	31.6	no fog	1.41
0.180	292.5	28.2	28.2	critical value	no fog	25.6	no fog	1.40
0.136	95.6	54.8	49.0	no fog	no fog	47.5	no fog	1.63

0.140	162.3	37.0	35.3	no fog	fog	33.5	no fog	1.59
0.136	174.0	34.7	33.3	no fog	fog	31.6	no fog	1.60
0.137	206.5	34.0	30.2	no fog	no fog	28.4	no fog	1.59
0.139	209.0	31.7	30.3	no fog	fog	28.2	no fog	1.58
0.139	210.0	30.3	30.3	critical value	fog	28.3	no fog	1.58
0.139	210.4	33.1	30.2	no fog	no fog	28.2	no fog	1.58
0.138	207.5	32.2	30.5	no fog	fog	28.4	no fog	1.58
0.139	207.5	32.8	30.6	no fog	no fog	28.5	no fog	1.58
0.147	229.0	32.6	29.5	no fog	no fog	27.4	no fog	1.54
0.149	250.0	29.1	28.0	no fog	no fog	26.0	no fog	1.53
0.153	250.0	28.8	28.3	no fog	no fog	26.3	no fog	1.51
0.147	220.8	31.4	30.2	no fog	fog	28.1	no fog	1.54
0.107	122.0	38.7	37.0	no fog	no fog	35.7	no fog	1.77
0.107	122.0	38.5	37.0	no fog	fog	35.7	no fog	1.77
0.110	128.0	42.1	36.3	no fog	no fog	35.1	no fog	1.75
0.106	129.0	38.7	35.3	no fog	fog	34.3	no fog	1.77
0.108	169.0	31.2	30.2	no fog	fog	28.9	no fog	1.75
0.109	180.5	34.4	29.0	no fog	no fog	27.8	no fog	1.74
0.110	190.0	32.9	28.0	no fog	no fog	26.9	no fog	1.73
0.108	195.0	33.7	27.5	no fog	no fog	26.2	no fog	1.74

Table F.2 Filmwise wall condensation experiments of n–butyl alcohol in nitrogen.

The saturation lines in figures F.2 and F.3 are in fact those of water–vapour. The mixtures' molar specific heat is evaluated at the bulk composition (see equation (F.9) with c^+ replaced by c_b^+). The mixtures' thermal conductivity is evaluated at the bulk composition, taking into account its composition following Perry and Green (1984):

$$k = \frac{c_b^+ k_v}{c_b^+ + \left(\frac{M_n}{M_v}\right)^{\frac{1}{2}} (1 - c_b^+)} + \frac{(1 - c_b^+)\ k_n}{1 - c_b^+ + \left(\frac{M_v}{M_n}\right)^{\frac{1}{2}} c_b^+} \quad . \tag{F.25}$$

The properties of the two components are evaluated at bulk temperature. In tables F.1 and F.2 the newly determined t_a and calculated Le are listed. Table F.1 reveals that all correct t_a are larger than those of Johnstone *et al.* (1950), owing to the effect of equation (F.21). Accordingly, for most cases $t_i < t_a$, and hence fog formation is predicted, which is in agreement with the experimental observation. However, in a few situations fog is predicted but not observed. This can be explained from the difference between t_a and t_i, which is a measure for the degree of supersaturation. In general, it follows that fog is not observed when t_i is slightly below t_a, while visible fog formation occurs when t_i exceeds the critical temperature t_a significantly (typically 1°C). Table F.1 also discloses that, according to the improved tangency condition, no inexplicable situations appear where a critical condition ($t_a = t_i$) or even superheating is predicted theoretically, but fog observed experimentally.

The new results in table F.2 indicate however that the re–determined t_a are even lower than those of Johnstone *et al.* (1950). This can be explained from $c_{p,v}^+/c_p^+$ being much larger than unity, typically $c_{p,v}^+/c_p^+ = 3.2$, for all the mixtures considered. This implies an enhancement of Θ_t^+ and reduction of the calculated t_a, see equations (F.16) and (F.17). The observed fog can therefore not be explained with the here derived equations (F.16)–(F.19).

An intersection of $G^+(t)$ and $F^+(t)$ in the bulk, as depicted in figure F.3, may result in fog formation as well. This intersection is possible since $\mathrm{Le}c_p^+/c_{p,v}^+ < 1$ for both mixtures considered (water–vapour air: $\mathrm{Le}c_p^+/c_{p,v}^+ \cong 0.7$, n–butyl alcohol air: $\mathrm{Le}c_p^+/c_{p,v}^+ \cong 0.5$), which implies $G^+(t)$ is a convex curve. A numerical investigation of $G^+(t)$ and $F^+(t)$ with t ranging from t_i to t_b provided evidence for both mixtures that an intersection of both curves does not occur when superheating was predicted by the slope condition. That is to say, $F^{+}(t) > G^{+}(t)$ in the entire film, thus predicted correctly by slope condition (F.15). Summarizing, the experimental results of n–butyl alcohol nitrogen mixtures cannot be explained properly.

The major difference with the water–vapour nitrogen experiments, besides the higher temperatures and different Lewis numbers, is the filmwise condensation of n–butyl alcohol, since no promoter could be found for dropwise condensation. Oleic acid was used by Johnstone *et al.* (1950) to promote the dropwise condensation of water–vapour. This dropwise condensation implies that the measured channel wall temperature better corresponds to the interface temperature, which might be the reason overall agreement is found only between theory and water–vapour nitrogen experiments.

Conclusions

In this appendix an improved tangency condition for predicting supersaturation in condensers has been derived. This condition is based on the slope of the saturation line and film model expressions for the vapour mole fraction and temperature. It has been demonstrated that for $\mathrm{Le}c_p^{+}/c_{p,v}^{+} < 1$ superheating in a mixture cannot be guaranteed by this condition. But a comparison of this condition with a complete examination of temperature and vapour mole fraction profiles in various binary mixtures of nitrogen with vapours of water and n–butyl alcohol, revealed that the condition predicted correctly superheating. A comparison of the condition with experiments of Johnstone *et al.* (1950), concerning dropwise wall condensation of water–vapour in air, yields good agreement. If dropwise condensation of n–butyl alcohol had also been achieved by these investigators, complete agreement with theory might have been obtained.

APPENDIX G: EXPERIMENTAL DATA OF PLASTIC HEAT EXCHANGER

In this appendix the primary experimental data of the plastic heat exchanger are listed. Furthermore, to verify the reliability of the measured quantities, the relative error of a global energy balance is included as well.

The added energy to the primary water reads:

$$Q_l = 48\, w_l c_{p,l} \left(t_{l,out} - t_{l,in}\right) \quad , \tag{G.1}$$

and the extracted latent and sensible heat from the gas is governed by:

$$Q_g = 96\, w_{g,in} c_{p,g,in} t_{g,in} - 96\, w_{g,out} c_{p,g,out} t_{g,out} - w_{con} c_{p,v} t_{con} + w_{con} H_{lat} \quad . \tag{G.2}$$

Employing this expression the cooling of the condensate below the condensation temperature has been neglected. The effect of subcooling is expected to be very modest; in appendix E it has been demonstrated that the condensate film is practically isothermal. In equations (G.1) and (G.2) the factors 48 and 96 appear since the total liquid mass flow and total gas mass flow are divided over 48 plates and 96 gaps of the considered heat exchanger, respectively. The exit gas mass flow simply follows from the mass balance:

$$96\, w_{g,out} = 96\, w_{g,in} - w_{con} \quad , \tag{G.3}$$

where both 96 $w_{g,in}$ and w_{con} are measured. The specific heats of the mixture at the entry and exit are evaluated at their concerning temperatures and compositions. The vapour's specific heat $c_{p,v}$ and latent heat H_{lat}, appearing in equation (G.2), are evaluated at t_{con}.

nr	$48\ w_l$ [kg/s]	$t_{l,in}$ [°C]	$t_{l,out}$ [°C]	$96\ w_{g,in}$ [kg/s]	$t_{g,in}$ [°C]	$t_{g,out}$ [°C]	RH_{in} [–]	RH_{out} [–]
1	0.860	18.2	20.9	0.435	60.5	40.3	0.065	0.128
2	0.860	18.5	20.5	0.376	60.8	39.0	0.067	0.148
3	0.852	18.9	21.0	0.235	64.8	35.0	0.065	0.226
4	0.860	19.7	26.8	0.423	60.0	43.8	0.475	0.802
5	0.860	20.6	33.4	0.423	61.8	52.2	0.865	1.000
6	0.860	19.4	27.4	0.378	59.7	44.3	0.627	1.000
7	0.860	20.4	24.9	0.237	62.0	38.2	0.380	0.846
8	0.860	20.5	32.1	0.379	60.6	50.0	0.868	0.996
9	0.860	20.3	30.5	0.250	61.4	48.6	0.954	1.000
10	0.860	18.0	20.5	0.355	61.0	38.2	0.082	0.212
11	0.860	18.1	20.8	0.395	61.6	37.5	0.061	0.152
12	0.860	18.2	30.6	0.459	59.9	47.4	0.836	0.945
13	0.860	19.0	33.7	0.455	62.1	51.6	0.921	0.997
14	0.860	19.5	28.7	0.264	62.1	42.5	0.693	0.943
15	0.860	19.9	32.8	0.280	61.4	48.9	0.952	0.986
16	0.912	19.7	27.1	0.263	57.7	38.4	0.646	0.911
17	1.670	18.3	19.7	0.435	60.8	40.1	0.065	0.132
18	1.670	18.6	20.0	0.375	61.0	38.7	0.065	0.150
19	1.670	19.0	20.1	0.235	64.8	43.4	0.065	0.238
20	1.670	20.3	24.4	0.430	61.1	43.8	0.446	0.780
21	1.670	20.4	28.0	0.424	61.7	50.9	0.874	1.000
22	1.670	20.0	24.6	0.380	59.3	43.5	0.616	1.000
23	1.670	20.4	23.1	0.236	61.8	37.0	0.382	0.840
24	1.670	20.3	27.0	0.379	60.5	48.6	0.872	0.998
25	1.670	20.4	26.4	0.248	61.8	48.0	0.918	0.996
26	1.656	17.8	19.3	0.446	59.4	39.5	0.080	0.190
27	1.670	18.1	19.5	0.355	60.8	38.0	0.082	0.216
28	1.670	18.4	19.5	0.233	63.8	34.0	0.093	0.402
29	1.670	19.6	23.7	0.244	63.0	40.5	0.510	0.910

nr	w_{con}	t_{con}	P_{tot}	E_Q	NTU_l	NTU_g	Figure
	[kg/s]	[°C]	[Pa]	[–]	[–]	[–]	
1	0.000	——	102950	–0.088	0.040	0.702	4.7
2	0.000	——	102940	0.143	0.039	0.798	–
3	0.000	——	102940	–0.052	0.038	1.223	4.8
4	0.007	34.8	102950	–0.052	0.039	0.689	4.7
5	0.017	46.1	102950	–0.017	0.039	0.661	4.7
6	0.009	36.2	102680	–0.026	0.039	0.749	–
7	0.004	30.6	102670	–0.034	0.037	1.170	4.8
8	0.015	43.2	102680	–0.030	0.039	0.731	–
9	0.014	41.3	102670	0.016	0.037	1.058	4.8
10	0.000	——	103470	–0.091	0.039	0.838	–
11	0.000	——	102680	–0.008	0.039	0.763	–
12	0.016	40.5	102950	0.005	0.040	0.623	4.7
13	0.019	47.4	102950	–0.041	0.040	0.618	4.7
14	0.011	36.1	102940	–0.027	0.037	1.031	4.8
15	0.017	43.0	102940	–0.036	0.038	0.954	–
16	0.009	35.6	100510	–0.040	0.035	1.044	–
17	0.000	——	102950	–0.070	0.021	0.705	–
18	0.000	——	102940	–0.144	0.020	0.803	–
19	0.000	——	102940	–0.059	0.019	1.227	–
20	0.008	33.5	102950	–0.047	0.020	0.684	–
21	0.019	43.8	102950	–0.045	0.020	0.663	–
22	0.010	35.5	102680	–0.047	0.020	0.750	–
23	0.004	30.1	102670	–0.173	0.019	1.179	–
24	0.017	41.5	102680	–0.019	0.020	0.735	–
25	0.015	39.5	102670	–0.046	0.019	1.072	–
26	0.000	——	103480	–0.143	0.021	0.687	–
27	0.000	——	103470	–0.174	0.020	0.841	–
28	0.000	——	103470	–0.083	0.019	1.229	–
29	0.009	31.6	103470	–0.031	0.019	1.130	–

Table G.1 Experimental data for $t_{g,in} \cong 60^{o}C$.

nr	$48\ w_l$ [kg/s]	$t_{l,in}$ [°C]	$t_{l,out}$ [°C]	$96\ w_{g,in}$ [kg/s]	$t_{g,in}$ [°C]	$t_{g,out}$ [°C]	RH_{in} [–]	RH_{out} [–]
1	0.860	20.1	24.0	0.427	84.3	53.2	0.036	0.088
2	0.860	19.6	23.2	0.372	81.8	49.0	0.034	0.096
3	0.865	20.4	23.1	0.236	80.8	41.0	0.040	0.176
4	0.860	19.8	35.6	0.418	80.2	62.0	0.469	0.816
5	0.860	20.2	35.3	0.376	78.8	60.5	0.492	0.824
6	0.860	20.2	34.0	0.249	82.4	58.5	0.452	0.864
7	0.860	20.4	45.2	0.403	83.4	75.4	0.847	0.974
8	0.860	20.5	44.5	0.360	82.3	74.2	0.863	0.988
9	0.860	20.0	42.8	0.277	84.1	74.8	0.859	0.994
10	0.912	18.5	22.3	0.442	82.3	48.7	0.031	0.085
11	0.912	20.5	31.1	0.434	80.1	52.5	0.304	0.670
12	0.912	20.3	40.5	0.443	80.9	66.0	0.703	0.949
13	1.670	20.3	22.3	0.430	78.8	50.6	0.042	0.100
14	1.662	20.0	21.9	0.367	81.2	48.4	0.034	0.098
15	1.662	20.3	21.9	0.232	82.4	41.0	0.038	0.176
16	1.670	20.3	29.5	0.419	80.4	61.0	0.479	0.800
17	1.670	20.1	29.1	0.377	79.1	59.4	0.491	0.428
18	1.670	20.2	28.0	0.251	83.0	57.0	0.456	0.844
19	1.670	20.8	36.2	0.403	83.2	74.0	0.845	0.984
20	1.670	20.7	35.5	0.360	82.6	73.1	0.857	0.990
21	1.670	20.6	34.4	0.274	84.4	73.5	0.845	1.000

nr	w_{con} [kg/s]	t_{con} [°C]	P_{tot} [Pa]	E_Q [–]	NTU_l [–]	NTU_g [–]	Figure
1	0.000	——	102550	–0.038	0.041	0.737	4.9
2	0.000	——	102540	–0.044	0.040	0.829	–
3	0.000	——	102540	–0.023	0.038	1.245	–
4	0.020	51.0	101880	–0.005	0.040	0.667	4.9
5	0.019	48.9	101880	–0.017	0.040	0.733	4.9
6	0.016	46.5	101870	–0.092	0.038	1.063	–
7	0.036	68.4	101880	–0.006	0.040	0.598	–
8	0.034	66.3	101880	–0.030	0.039	0.664	4.9
9	0.033	65.0	101880	–0.009	0.038	0.827	–
10	0.000	——	102680	0.039	0.039	0.712	4.9
11	0.012	42.7	100550	0.007	0.038	0.675	–
12	0.028	61.9	100520	–0.041	0.038	0.594	–
13	0.000	——	102550	–0.125	0.021	0.730	–
14	0.000	——	102540	–0.078	0.021	0.842	–
15	0.000	——	102540	–0.130	0.020	1.272	–
16	0.022	48.9	101880	–0.035	0.021	0.668	–
17	0.021	46.9	101880	–0.067	0.021	0.755	–
18	0.019	44.2	101870	–0.023	0.020	1.061	–
19	0.042	66.3	101880	–0.037	0.021	0.604	–
20	0.041	64.2	101880	–0.021	0.020	0.670	–
21	0.036	61.5	101880	–0.076	0.020	0.844	–

Table G.2 Experimental data for $t_{g,in} \cong 80^\circ C$.

nr	$48\ w_l$ [kg/s]	$t_{l,in}$ [°C]	$t_{l,out}$ [°C]	$96\ w_{g,in}$ [kg/s]	$t_{g,in}$ [°C]	$t_{g,out}$ [°C]	RH_{in} [–]	RH_{out} [–]
1	0.860	19.0	23.9	0.422	97.5	58.8	0.023	0.064
2	0.860	19.6	24.2	0.344	102.0	56.0	0.019	0.072
3	0.865	20.1	24.0	0.235	103.6	48.0	0.019	0.130
4	0.860	20.4	43.5	0.427	101.9	80.2	0.365	0.690
5	0.860	20.5	44.4	0.357	99.2	80.0	0.428	0.768
6	0.860	20.5	43.8	0.296	102.3	81.5	0.431	0.766
7	0.860	20.5	45.1	0.392	99.4	81.8	0.443	0.758
8	0.860	20.7	46.6	0.305	100.5	84.5	0.519	0.846
9	0.938	18.7	23.4	0.428	101.9	57.1	0.018	0.056
10	0.912	20.0	33.7	0.432	102.1	69.3	0.160	0.554
11	0.912	20.4	34.8	0.390	100.2	62.3	0.190	0.614
12	1.670	19.1	21.8	0.423	100.0	58.8	0.019	0.056
13	1.670	19.8	22.3	0.345	101.2	54.5	0.019	0.070
14	1.670	20.2	22.3	0.235	103.4	47.5	0.021	0.138
15	1.670	20.7	34.0	0.426	102.0	79.0	0.361	0.684
16	1.670	20.8	35.3	0.357	98.8	78.2	0.428	0.770
17	1.670	20.7	34.9	0.296	102.7	80.7	0.418	0.772
18	1.670	20.6	36.1	0.392	98.9	80.0	0.448	0.768
19	1.672	20.5	36.6	0.305	100.6	83.3	0.517	0.844

nr	w_{con}	t_{con}	P_{tot}	E_Q	NTU_l	NTU_g	Figure
	[kg/s]	[°C]	[Pa]	[–]	[–]	[–]	
1	0.000	——	103480	–0.059	0.042	0.757	–
2	0.000	——	101480	–0.027	0.041	0.911	–
3	0.000	——	101470	–0.053	0.039	1.285	–
4	0.030	63.6	100810	0.000	0.042	0.602	–
5	0.032	65.5	100810	–0.016	0.040	0.687	4.10
6	0.032	66.6	100810	0.001	0.040	0.792	–
7	0.034	68.9	102810	0.007	0.041	0.628	4.10
8	0.037	71.6	102810	0.006	0.040	0.732	4.10
9	0.000	——	102680	0.056	0.038	0.751	–
10	0.014	46.3	102680	–0.043	0.039	0.682	4.10
11	0.015	48.8	100550	–0.044	0.039	0.738	–
12	0.000	——	101480	–0.062	0.022	0.761	–
13	0.000	——	101480	–0.063	0.021	0.911	–
14	0.000	——	101480	–0.091	0.020	1.288	–
15	0.036	63.2	100810	0.052	0.022	0.610	–
16	0.037	63.8	100810	–0.041	0.021	0.696	–
17	0.037	64.8	100810	–0.029	0.021	0.800	–
18	0.040	66.7	102810	–0.039	0.021	0.635	–
19	0.042	69.3	102810	–0.051	0.021	0.741	–

Table G.3 Experimental data for $t_{g,in} \cong 100^{\circ}C$.

The relative error of the global energy balance is now defined as:

$$E_Q = 2\frac{(Q_g - Q_l)}{(Q_g + Q_l)} \quad . \tag{G.4}$$

In table G.1 the experimental data pertaining to an entry gas temperature $t_{g,in}$ of about 60°C are listed. In table G.2 those pertaining to $t_{g,in} \cong 80^\circ C$ and in table G.3 the data pertaining to $t_{g,in} \cong 100^\circ C$ are included. The entry liquid temperature is always about 20°C. The selected data for figures 4.7–4.10 are marked and the tables furthermore contain NTU_l and NTU_g of the measurement, computed as described in §4.5.

One can readily see that the relative error E_Q increases with increasing liquid flow rates, which in turn imply small differences between entry and exit liquid temperatures and hence a substantial effect of the measurement uncertainty. It is interesting to observe that for most tabled cases the relative error is negative. This indicates that energy is added to the gas (which is theoretically not possible since the gas is hotter) and/or extracted from the water by the surroundings (this is not possible either since for a number of cases the water is colder than the surroundings). Tables G.1–G.3 show that the negative relative error becomes less pronounced, or even positive, for higher temperature levels at the liquid side. One can therefore conclude that heat losses at the primary side cannot be responsible for the negative energy balance. In particular when one realizes that the entry and exit channels are well insulated. Accordingly, it is expected that a negative energy balance is due to uncertainties of flow and temperature measurements.

APPENDIX H: UNCERTAINTY ANALYSIS

The uncertainty analysis presented here follows the procedures described by Kline and McClintock (1953) and Holman (1978). The primary experimental data, such as $t_{l,in}$, $t_{g,out}$ *etc.*, is used to calculate some desired quantities, *e.g.* c_{in}, $\zeta_{l,out}$ and so on. The uncertainty in these calculated results is obtained by considering the uncertainties in the primary measurements and is discussed below.

The uncertainty in a calculated result I, which is a function of the independent variables $i_1, i_2, \ldots, i_n$, reads:

$$\left[\frac{dI}{I}\right]^2 = \left[\frac{\partial I}{\partial i_1}\frac{di_1}{I}\right]^2 + \left[\frac{\partial I}{\partial i_2}\frac{di_2}{I}\right]^2 + \ldots + \left[\frac{\partial I}{\partial i_n}\frac{di_n}{I}\right]^2 \quad , \tag{H.1}$$

where $di_1, di_2, \ldots, di_n$ represent the uncertainties in the quantities $i_1, i_2, \ldots, i_n$. Applying equation (H.1) to equation (4.55) produces:

$$\left[\frac{d\zeta_{l,out}}{\zeta_{l,out}}\right]^2 = \left[\frac{dt_{l,out}}{t_{l,out} - t_{l,in}}\right]^2 + \left[\frac{dt_{g,in}}{t_{g,in} - t_{l,in}}\right]^2 + \left[\frac{(t_{l,out} - t_{g,in})\ dt_{l,in}}{(t_{g,in} - t_{l,in})(t_{l,out} - t_{l,in})}\right]^2 \ . \tag{H.2}$$

This expression constitutes the relative uncertainty in $\zeta_{l,out}$ as a result of the uncertainties in the measured $t_{l,in}$, $t_{g,in}$ and $t_{l,out}$, represented by $dt_{l,in}$, $dt_{g,in}$ and $dt_{l,out}$, respectively. These temperatures are measured with mercury thermometers with uncertainties of 0.1°C.

The relative uncertainty in $\zeta_{g,out}$ follows from equations (4.55) and (H.1) as:

$$\left[\frac{d\zeta_{g,out}}{\zeta_{g,out}}\right]^2 = \left[\frac{dt_{g,out}}{t_{g,out} - t_{l,in}}\right]^2 + \left[\frac{dt_{g,in}}{t_{g,in} - t_{l,in}}\right]^2 + \left[\frac{(t_{g,out} - t_{g,in})\, dt_{l,in}}{(t_{g,in} - t_{l,in})(t_{g,out} - t_{l,in})}\right]^2 . \tag{H.3}$$

The uncertainty $dt_{g,out}$, which is also measured with a mercury thermometer, amounts 0.1°C. The dimensionless exit gas mass flow is defined by equations (4.56) and (G.3). The actual condensate flow follows from:

$$w_{con} = \frac{m}{\Upsilon} \ , \tag{H.4}$$

where m is the water which is weighed in the tank and Υ the time measured. Applying equation (H.1) to equations (4.56), (G.3) and (H.4) yields:

$$\left[\frac{dW_{g,out}}{W_{g,out}}\right]^2 = \left[\left[\frac{dw_{g,in}}{w_{g,in}}\right]^2 + \left[\frac{dm}{m}\right]^2 + \left[\frac{d\Upsilon}{\Upsilon}\right]^2\right] \left[1 - \frac{1}{W_{g,out}}\right]^2 . \tag{H.5}$$

The uncertainty dm of the weighing–machine amounts 0.01 kg and $d\Upsilon$ of the chronometer is 0.2 s. The total entry gas mass flow, which is divided over 96 gaps, is measured with an orifice plate and follows from:

$$96\, w_{g,in} = p\, \frac{\pi}{4}\, D_h^2\, (2\rho\, \Delta P)^{\frac{1}{2}} \ , \tag{H.6}$$

see Eck (1957) and Ward–Smith (1980). In this equation D_h represents the diameter of the orifice (≅ 0.155 m). The coefficient p depends on a number of factors, such as the flow Reynolds number, the cross–sectional area of the orifice divided by the cross–sectional area of the approach pipe ($\cong$ 0.6), and compressibility effects, but does depart appreciably from a value of 0.74. Neglecting the uncertainties in the density of the mixture (which depends weakly on composition and temperature) and the diameter of the orifice, equations (H.1) and (H.6) yield:

$$\left[\frac{dw_{g,in}}{w_{g,in}}\right]^2 = \left[\frac{1}{2}\frac{d\Delta P}{\Delta P}\right]^2 \quad . \tag{H.7}$$

The pressure difference is measured with an U–tube manometer under an angle with an uncertainty $d\Delta P$ of 10 Pa.

The vapour mass fraction is given by:

$$c(t) = \frac{M_v P_{v,sat}(t) RH}{RH\ (M_v - M_n)\ P_{v,sat}(t) + M_n P_{tot}} \quad , \tag{H.8}$$

in which the relative humidity RH and temperature of the gas t are supplied by a Vaisala HMP–135Y device. The absolute total pressure in the tunnel is measured with an U–tube manometer. The saturation pressure of water–vapour is described by equations (C.1) and (C.2). Applying equation (H.1) yields:

$$\left[\frac{dc}{c}\right]^2 = \left[\frac{M_n P_{tot}}{RH\ (M_v - M_n)\ P_{v,sat}(t) + M_n P_{tot}}\right]^2 \left[\left[\frac{dRH}{RH}\right]^2 + \left[\frac{dP_{tot}}{P_{tot}}\right]^2 + \left[\frac{dP_{v,sat}}{dt}\frac{dt}{P_{v,sat}(t)\ t}\right]^2\right] \quad . \tag{H.9}$$

The uncertainties dRH and dt amount 0.01 and 0.1°C, respectively. The uncertainty in total pressure, dP_{tot}, is only 10 Pa ($\equiv$ 0.1 mbar).

With the help of equations (H.2), (H.3), (H.5) and (H.7), and (H.9), the uncertainty bars of figures 4.7—4.10 have been constructed. For the experimental data of figures 4.7 and 4.8 the maximum dc_{in}, $d\zeta_{l,out}$, $d\zeta_{g,out}$ and $dW_{g,out}$ amount 0.0015, 0.0034, 0.0032 and 0.0019, respectively. For figure 4.9 they are 0.0050, 0.0023, 0.0021 and 0.0013. The maximum dc_{in}, $d\zeta_{l,out}$, $d\zeta_{g,out}$ and $dW_{g,out}$ of the experiments depicted in figure 4.10 amount 0.0100, 0.0017, 0.0016 and 0.0012, respectively.

To compare the theoretical results with the experimental data one also needs to know the mass flows of gas and liquid, in dimensionless form represented by NTU_g and NTU_l. The uncertainty $dNTU_g$ depends on $dw_{g,in}$, $dc_{p,g}$, dk_g, dk_l, dk_p, dL, dB, dd_1, dd_4 and dd_5, see equations (4.15), (4.4), (4.6) and (4.7). Neglecting uncertainties in the physical and geometrical properties, which are much smaller than the uncertainty of the gas mass flow, equations (H.1) and (4.15) produce:

$$\left[\frac{dNTU_g}{NTU_g}\right]^2 = \left[\frac{dw_{g,in}}{w_{g,in}}\right]^2 \quad . \tag{H.10}$$

The uncertainty $dw_{g,in}$ follows from equation (H.7).

Neglecting again uncertainties in physical and geometrical properties equations (4.14) and (H.1) yield:

$$\left[\frac{dNTU_l}{NTU_l}\right]^2 = \left[\frac{dw_l}{w_l}\right]^2 \quad . \tag{H.11}$$

The total liquid mass flow is measured with rotameter with an uncertainty 48 dw_l of 0.026 kg/s, since the water is divided over 48 channel plates. For the experimental data of figure 4.7 the maximum $dNTU_l$ and $dNTU_g$ amount 0.001 and 0.011, respectively. For figure 4.8 these values read 0.001 and 0.047, for figure 4.9 they are 0.001 and 0.010, and for figure 4.10 the maximum $dNTU_l$ and $dNTU_g$ amount 0.001 and 0.009.

SYMBOLS

A	vapour pressure function of a pure substance	
Ad	McAdam number, defined by equation (5.31) and (5.46)	
B	net plate width	$[\mathrm{m}]$
b	intermediate distance discretisation points, see figure 4.5	
c	vapour mass fraction	
c_p	specific heat	$[\mathrm{Jkg^{-1}K^{-1}}]$
$\mathbb{D}$	diffusion coefficient	$[\mathrm{m^2s^{-1}}]$
D_h	hydraulic diameter; four times the cross–sectional/the perimeter	$[\mathrm{m}]$
d_i	geometrical property of heat exchanger, see figure 4.2	$[\mathrm{m}]$
E_N	break–off error, equation (D.1)	
E_Q	relative energy balance error, equation (G.4)	
F	saturation function, see equation (C.7)	
f	friction coefficient	
G	relation between c and t in superheated region	
g	acceleration due to gravity	$[\mathrm{ms^{-2}}]$
g_m	mass transfer coefficient	$[\mathrm{kgm^{-2}s^{-1}}]$
H	fog condition function, see equation (A.18)	
H_{lat}	latent heat of condensation	$[\mathrm{Jkg^{-1}}]$
h	heat transfer coefficient	$[\mathrm{Wm^{-2}K^{-1}}]$
K	fog formation	$[\mathrm{kgm^{-3}s^{-1}}]$
Ku_{con}	Kutateladze number, $c_{p,con}(t_{sat} - t_{con,w})/H_{lat}$	
k	thermal conductivity	$[\mathrm{Wm^{-1}K^{-1}}]$
L	net plate length	$[\mathrm{m}]$
Le	Lewis number, $k/\rho c_p \mathbb{D}$	

Le_v	modified Lewis number, $k/\rho c_{p,v}\mathbb{D}$	
M	mass of one kmole of substance	[kg]
$\dot{M}_{con}$	dimensionless condensate formation, defined by equation (5.60)	
$\dot{M}_f$	dimensionless fog formation, defined by equation (2.30)	
m	mass of condensate in weighing tank	[kg]
$\dot{m}$	mass flux at wall	[kgm^{-2}s^{-1}]
$\dot{m}_f$	fog mass flux in film	[kgm^{-2}s^{-1}]
N	number of discretisation points	
NTU	number of transfer units, defined by equations (4.14), (4.15) or (5.30)	
Nu	Nusselt number, hD_h/k	
n	turbulent power–law coefficient	
P	pressure	[bar]
Pr	Prandtl number, $\eta c_p/k$	
Q	heat flow	[W]
q	heat flux at wall	[Wm^{-2}]
R	gas constant	[JK^{-1}kmole^{-1}]
RH	relative humidity	
Re	Reynolds number, $\bar{u}\rho D_h/\eta$	
S	Series, see equation (4.20)	
Sc	Schmidt number, $\eta/\rho\mathbb{D}$	
Sh	Sherwood number, $g_m D_h/\rho\mathbb{D}$	
T	absolute temperature	[K]
t	temperature	[^{o}C]
u	component of velocity in the direction of x	[ms^{-1}]
v	component of velocity in the direction of y	[ms^{-1}]
W	dimensionless mass flow, see equation (5.46)	
w	mass flow	[kgs^{-1}]

X	dimensionless coordinate, $X=x/B$	
x	coordinate	[m]
Y	dimensionless coordinate, $Y=y/\delta_a$	
y	coordinate	[m]
Z	dimensionless coordinate, $Z=x/L$	
z	coordinate	[m]

Greek symbols

α,β,γ	constants Antoine's or Rankine–Kirchhoffs' equation	
Δ	dimensionless film thickness, defined by equations (5.29) and (E.13)	
δ	film thickness	[m]
ϵ	perturbation quantity	
ζ	dimensionless temperature, defined by equations (4.55) or (5.28)	
η	dynamic viscosity	[Pas]
Θ	correction factor	
ρ	density	[kgm^{-3}]
Υ	time	[s]
τ	shear stress	[Nm^{-2}]
ϕ	dimensionless wall mass flux, defined by equations (1.20), (1.26) and (1.32)	

Subscripts

a	border of saturated and superheated region
b	bulk
c	diffusional
con	condensate

dew	dew point
f	fog
f1	pertaining to numerical fog film model
f2	pertaining to asymptotic fog film model
f3	pertaining to fog film model with a negligible induced velocity
f4	pertaining to compound fog film model
g	gas mixture
i	channel plate/gas or condensate/gas interface
in	entry
l	liquid in channel plate
n	non–condensables
out	exit
pl	channel plate
sat	saturation
t	thermal
tot	total
u	frictional
v	vapour
w	channel plate/coolant or channel plate/condensate interface
∞	fully developed flow

Superscripts

inv	inverse
—	mean mixed or "bulk"
*	reference
+	molar

REFERENCES

Ackermann, G. (1937), Wärmeübertragung und molekulare Stoffübertragung in gleichen Feld bei groszen Temperatur– und Partialdruckdifferenzen, V.D.I. – Forschungsheft 382 (in German).

Aref'yev, K.M. and Averkiyev, A.G. (1979), Effect of fog formation at the evaporation surface on coefficients of heat and mass transfer during evaporative cooling of water, Heat Transfer – Soviet Research, 11, 143 – 147.

Baclic, B.S. and Heggs, P.J. (1985), On the search for new solutions of the single–pass crossflow heat exchanger problem, Int. J. Heat Mass Transfer, 28, 1965 – 1976.

Beekmans, S. (1989), Kunststof compact warmtewisselaar: het bouwen en testen van een proefopstelling, Eindhoven University of Technology, Rep. nr. WOP–WET 89.009 (in Dutch).

Berman, A.S. (1953), Laminar flow in channels with porous walls, J. Appl. Physics, 24, 1232 – 1235.

Berman, A.S. (1956), Concerning laminar flow in channels with porous walls, J. Appl. Physics, 27, 1557 – 1558.

Bird, R.B., Stewart, W.E. and Lightfoot, E.N. (1960), Transport phenomena, John Wiley and Sons.

Bromley, L.A. (1952), Effect of heat capacity of condensate, Ind. Eng.Chem., 44, 2966 – 2969.

Bundy, R.D. and Weissberg, H.L. (1970), Experimental study of fully developed laminar flow in a porous pipe with wall injection, Phys. Fluids, 13, 2613 – 2615.

Chen, M.M. (1961), An analytical study of laminar film condensation, Part 1 flat plates, J. Heat Transfer, 83, 48 – 54.

Churchill, S.W. (1986), Laminar film condensation, Int. J. Heat Mass Transfer, 29, 1219 – 1226.

Colburn, A.P. and Drew, T.B. (1937), The condensation of mixed vapours, Trans. A.I.Ch.E., 33, 197 – 212.

Cussler, E.L. (1976), Multicomponent diffusion, Elsevier Scientific Publishing Company.

Dennis, S.R.C., Mercer, A.M. and Poats, G. (1959), Forced heat convection in laminar flow through rectangular ducts, Quart. Appl. Math., 17, 285 – 297.

Eck, B. (1957), Technische Strömungslehre (5. Aufl.), Springer Verlag (in German).

Edwards, D.K., Denny, V.E. and Mills, A.F. (1979), Transfer processes, Hemisphere/ McGraw – Hill Book Company.

Epstein, M. and Rosner, D.E. (1970), Enhancement of diffusion–limited vaporization rates by condensation within the thermal boundary layer, Int. J. Heat Mass Transfer, 13, 1393 – 1414.

Faghri, M. and Sparrow, E.M. (1980), Parallel–flow and counter–flow condensation on an internally cooled vertical tube, Int. J. Heat Mass Transfer, 23, 559 – 562.

Hall, G. and Watt, J.M. (1976), Modern numerical methods for ordinary differential equations, Clarendon Press.

Hayashi, Y., Takimoto, A. and Kanbe, M. (1976), Transport–reaction mechanism of mist formation based on the critical supersaturation model, J. Heat Transfer, 98, 114 – 119.

Hayashi, Y., Takimoto, A. and Kanbe, M. (1978), Mechanism of mist formation based on a critical supersaturation model in a turbulent convective field, Heat Transfer – Jap. Research, 7, 14 – 25.

Hayashi, Y., Takimoto, A. and Yamamoto, Y. (1981), Heat and mass transfer with mist formation in a laminar duct flow, Heat Transfer – Jap. Research, 10, 37 – 51.

Hijikata, K. and Mori, Y. (1973), Forced convective heat transfer of a gas with condensing vapor around a flat plate, Heat transfer – Jap. Research, 2, 81 – 101.

Hills, A.W.D. and Szekely, J. (1964), Notes on vaporization into much colder surroundings, Chem. Eng. Sci., 17, 79 – 81.

Hills, A.W.D. and Szekely, J. (1969), A note on the enhancement of the diffusion limited vaporization rates by condensation within the thermal boundary layer, Int. J. Heat Mass Transfer, 12, 111 – 114.

Holman, J.P. (1978), Experimental methods for engineers (3rd ed.), McGraw – Hill Book Company.

Hwang, C.L. and Fan, L.T. (1964), Finite difference analysis of forced–convection heat transfer in entrance region of a flat rectangular duct, Appl. Sci. Res., Sect. A 13, 401 – 422.

Johnstone, H.F., Kelley, M.D. and McKinley, D.L. (1950), Fog formation in cooler–condensers, Ind. Eng. Chem., 42, 2298 – 2302.

Kinney, R.B. and Sparrow, E.M. (1970), Turbulent flow, heat transfer, and mass transfer in a tube with surface suction, J. Heat Transfer, 92, 117 – 125.

Kline, S.J. and McClintock, F.A. (1953), Describing uncertainties in single–sample experiments, Mech. Eng., 75, 3 – 8.

Koch, P. (1986), Wärme– und Stofftransport bei laminarer freier Konvektion in feuchter Luft an einer gekühlten vertikalen Platte, D.Sc. Thesis, Technische Universität München (in German).

Koch, P. and Straub, J. (1990), Private communications, Technische Universität München.

Koh, J.C.Y. (1961), On integral treatment of two phase boundary layer in film condensation, J. Heat Transfer, 83, 359 – 362.

Koh, J.C.Y., Sparrow, E.M. and Hartnett, J.P. (1961), The two phase boundary layer in laminar film condensation, Int. J. Heat Mass Transfer, 2, 69 – 82.

Krishna, R. and Standart, G.L. (1976), A multicomponent film model incorporating a general matrix method of solution to the Maxwell–Stefan equations, A.I.Ch.E. Journal, 22, 383 – 389.

Kutateladze, S.S. and Gogonin, I.I. (1979), Heat transfer in film condensation of slowly moving vapour, Int. J. Heat Mass transfer, 22, 1593 – 1599.

Landolt–Börnstein (1960), Bd. II/5a and Bd. IV/4b (6. Aufl.), Springer Verlag (in German).

Legay–Desesquelles, F. and Prunet–Foch, B. (1985), Dynamic behaviour of a boundary layer with condensation along a flat plate: comparison with suction, Int. J. Heat Mass Transfer, 28, 2363 – 2370.

Legay–Desesquelles, F. and Prunet–Foch, B. (1986), Heat and mass transfer with condensation in laminar and turbulent boundary layers along a flat plate, Int. J. Heat Mass Transfer, 29, 95 – 105.

Liu, J. (1974), Flow of a Bingham fluid in the entrance region of an annular tube, M.Sc. Thesis, University of Wisconsin – Milwaukee.

Maclean, P. (1989), Heat transfer and distribution phenomena in gas–liquid compact heat exchangers, Eindhoven University of Technology, Rep. nr. WOP–WET 89.022.

Mason, J.L. (1954), Heat transfer in crossflow, Proc. Appl. Mech. 2nd. U.S. Nat. Congress, 801 – 803.

Merk, H.J. (1957), Stofoverdracht in laminaire grenslagen door gedwongen convectie, D.Sc. Thesis, Technische Universiteit Delft (in Dutch).

Mickley, H.S., Ross, R.C., Squyers, A.L. and Stewart, W.E. (1954), Heat, mass, and momentum transfer for flow over a flat plate with blowing or suction, NACA Techn. Note 3208.

Minkowycz, W.J. and Sparrow, E.M. (1966), Condensation heat transfer in the presence of noncondensables, interfacial resistance, superheating, variable properties, and diffusion, Int. J. Heat Mass Transfer, 9, 1125 – 1144.

Mizushina, T., Ito, R., Yamashita, S. and Kamimura, H. (1978), Film condensation of a pure superheated vapor inside a vertical tube, Int. Chem. Eng., 18, 672 – 679.

Mizushina, T., Ogino, F. and Takeshita, S. (1975), Eddy diffusivity in a turbulent pipe flow with uniform fluid injection and suction through a wall, J. Chem. Eng. Japan, 8, 217 – 223.

Neti, S. and Eichhorn, R. (1983), Combined hydrodynamic and thermal development in a square duct, Num. Heat Transfer, 6, 497 – 510.

Nusselt, W. (1911), Der Wärmeübergang im Kreuzstrom, Z. Ver. dt. Ing., 55, 2021 – 2024 (in German).

Nusselt, W. (1916), Die Oberflächenkondensation des Wasserdampfes, Z. Ver. dt. Ing., 60, 541 – 546 and 569 – 575 (in German).

Olson, R.B. and Eckert, E.R.G. (1966), Experimental studies of turbulent flow in a porous circular tube with uniform fluid injection through the tube wall, J. Applied Mechanics, 33, 7 – 17.

Perry, R.H. and Green, D.W. (1984), Perry's chemical engineers' handbook (6th ed.), McGraw – Hill Book Company.

Piening, W. (1933), Die Wärmeübertragung an kalte Flachen bei freier Strömung, Beihefte zum Gesundheits – Ing., 1, 1 – 23 (in German).

Reid, R.C., Prausnitz, J.M. and Sherwood, T.K. (1977), The properties of gases and liquids (3rd ed.), McGraw – Hill Book Company.

Ratiani, G.V. and Shekriladze, I.G. (1964), An experimental study of the heat exchange process on transition from laminar to turbulent flow of the film, Thermal Engng., 11, 101 – 102.

Rohsenow, W.M. (1956), Heat transfer and temperature distribution in laminar–film condensation, Trans. Am. Soc. Mech. Engrs., 78, 1645 – 1648.

Rosner, D.E. (1967), Enhancement of diffusion–limited vaporization rates by condensation within the thermal boundary layer, Int. J. Heat Mass Transfer, 10, 1267 – 1279.

Rosner, D.E. and Epstein, M. (1968), Fog formation conditions near cool surfaces, J. Coll. Interface Sci., 28, 60 – 65.

Sekulić, D.P. (1985), Irreversible condensation conditions near the cryosurface, Int. J. Heat Mass Transfer, 28, 1205 – 1214.

Shah, R.K. and London, A.L. (1978), Laminar flow forced convection in ducts, Academic Press.

Sherwood, T.K., Pigford, R.L. and Wilke, C.R. (1975), Mass transfer, McGraw – Hill Book Company.

Slegers, L. and Seban, R.A. (1970), Laminar film condensation of steam containing small concentrations of air, Int. J. Heat Mass Transfer, 13, 1941 – 1947.

Smithells, C.J. (1976), Metals reference book (5th ed.), Butterworths.

Sparrow, E.M. and Eckert, E.R.G. (1961), Effects of superheated vapor and noncondensable gases on laminar film condensation, A.I.Ch.E. Journal, 7, 473 – 477.

Sparrow, E.M. and Gregg, J.L. (1959), A boundary layer treatment of laminar–film condensation, Trans. Am. Soc. Mech. Engrs., 81, 13 – 17.

Sparrow, E.M., Minkowycz, W.J. and Saddy, M. (1967), Forced convection condensation in the presence of noncondensables and interfacial resistance, Int. J. Heat Mass Transfer, 10, 1829 – 1845.

Stefan, J. (1873), Versuche über die Verdampfung, Sitzgs. – Ber. Akad. Wiss. Wien (2), 68, 385 – 423 (in German).

Steinmeyer, D.E. (1972), Fog formation in partial condensers, Chem. Eng. Progress, 68, 64 – 68.

Stephan, K. (1959), Wärmeübertragung und Druckabfall bei nicht ausgebildeter Laminarströmung in Rohren und in ebenen Spalt, Chemie–Ing.–Techn., 31, 773 – 778 (in German).

Terrill, R.M. (1964), Laminar flow in a uniformly porous channel, Aeronaut. Quart., 15, 299 – 310.

Terrill, R.M. (1965), Laminar flow in a uniformly porous channel with large injection, Aeronaut. Quart., 16, 323 – 332.

Terrill, R.M. and Thomas, P.W. (1969), On laminar flow through a uniformly porous pipe, Appl. Sci. Res., 21, 37 – 67.

Toor, H.L. (1971a), Fog formation in boundary value problems, A.I.Ch.E. Journal, 17, 5 – 14.

Toor, H.L. (1971b), Fog vaporization and condensation in boundary value problems, Ind. Eng. Fundam., 10, 121 – 131.

Turkdogan, E.T. (1964), The theory of enhancement of diffusion–limited vaporization rates by a convection–condensation process, Part 1 Theoretical, Trans. metall. Soc. A.I.M.E., 230, 740 – 750.

Turkdogan, E.T. and Mills, K.C. (1964), The theory of enhancement of diffusion–limited vaporization rates by a convection–condensation process, Part 2 Experimental, Trans. metall. Soc. A.I.M.E., 230, 750 – 753.

Ünsal, M. (1988), Effect of waves on Nusselt condensation, Int. J. Heat Mass Transfer, 31, 1944 – 1947.

Van Dyke, M. (1975), Perturbation methods in fluid mechanics, The Parabolic Press.

Van Vredendaal (1990), Meting aan warmte–overdracht en distributieverschijnselen bij condensatie op een PVDF compact warmtewisselaar, Eindhoven University of Technology, Rep. nr. WOC–WET 90.011 (in Dutch).

V.D.I. (1988), V.D.I. – Wärmeatlas (5. Aufl.), V.D.I. Verlag GmbH (in German).

Wang, C.Y. and Tu, C.J. (1988), Effects of non–condensable gas on laminar film condensation in a vertical tube, Int. J. Heat Mass Transfer, 31, 2339 – 2345.

Ward–Smith, A.J. (1980), Internal fluid flow, Clarendon Press.

Webb, D.R., Panchal, C.B. and Coward, I. (1981), The significance of multicomponent diffusional interactions in the process of condensation in the presence of a non condensable gas, Chem. Eng. Sci., 36, 87 – 95.

Webb, D.R. and Sardesai, R.G. (1981), Verification of multicomponent mass transfer models for condensation inside a vertical tube, Int. J. Multiphase Flow, 7, 507 – 520.

Yuan, S.W. (1956), Further investigation of laminar flow in channels with porous walls, J. Appl. Physics, 27, 267 – 269.

Yuan, S.W. and Finkelstein, A.B. (1956), Laminar pipe flow with injection and suction through a porous wall, Trans. Am. Soc. Mech. Engrs., 78, 719 – 724.

SUMMARY

In this thesis the heat and mass transfer in gas–liquid plastic heat exchangers, made up of channel plates, is examined both theoretically and experimentally. To describe the transfer, use is made of averaged (or bulk) temperatures and vapour mass fraction in the channels. The employment of these quantities results in two–dimensional crossflow models for processes which are, in fact, three–dimensional. In the simplest case, heat transfer without condensation, this approach yields equations whose solution is put forward in the literature.

For pure steam condensation and partial water–vapour condensation on the channel plates the heat and mass transfer follows from a local balance of energy fluxes to and from the condensate surface, resulting in an implicit equation that relates the bulk states of both fluids. The mass flux, induced by the vapour (corresponding to suction through a porous wall), towards the condensate enhances the heat, mass and momentum transfer. The classical film model, which provides local correction factors, has been used to take this effect into account. In chapter 1 these correction factors have been derived, as are expressions for the alteration of bulk temperature, mass flow and pressure in a closed channel. On account of its originality the latter equation has been compared extensively with experimental and theoretical results of previous investigators, and found in good agreement.

Formation of fog, which may occur upon partial condensation of water–vapour in the heat exchanger, has been described in the chapters 2 and 3 by means of a film analysis and the saturation condition (*i.e.* excluding the possibility of supersaturation). In chapter 2 the exact conditions for fog formation have been determined, while the coupled energy and diffusion equation of the fog layer has first been solved numerically. Subsequently, an asymptotic approximation solution of this non–linear differential equation has been

derived, resulting in analytical expressions for the correction factors.

In chapter 3 a fogged film is considered in the case of a negligibly small induced velocity, yielding analytical correction factors as well. It is demonstrated heuristically that the product of the resulting correction factors (for fog only) and those of the classical film model (for induced velocity only) correspond to the correction factors of chapter 2 (for the combined situation of fog and induced velocity). On the basis of this insight simple compound correction factors have been introduced. Both fog film models lead to new procedures for computing condensers and evaporators, and to new expressions for the alteration of bulk temperature and vapour mass fraction in combination with the creation of bulk fog.

In the case of wall condensation and fog formation the fog models predict an enhancement of sensible heat transfer and a reduction of latent heat transfer, with the total heat transfer remaining unchanged. In addition, a comparison has been made between the basic fog film models and the theoretical and experimental results of foregoing studies, concerning fog formation in the presence of free and forced convection. This important comparison confirms the heat and mass transfer predictions of the fog film model, thus permitting the film model approach to fog formation.

In chapter 4 the theoretical and experimental investigations of heat and mass transfer in plastic heat exchangers are described for cases in which there is no condensation, partial water–vapour condensation or pure steam condensation. In the case of partial water–vapour condensation the classical film model, the asymptotic fog film model of chapter 2, and the compound fog film model of chapter 3, have been applied and compared mutually. As the heat exchanger operates in crossflow and multiple liquid passes in the heat exchanger are conceivable, the exit properties need not necessarily be in thermodynamic equilibrium (this applies generally to mixed gases of different compositions). Universally applicable equations which describe the transition towards a stable state have therefore been derived, resulting in practice in fog formation or dissolution.

Numerous computations reveal that a substantial part of the vapour entering the heat exchanger condenses on the channel walls, and that the produced fog is less than about 10 % of the total amount of condensed vapour. It is furthermore observed that the predictions of the asymptotic and compound fog model are identical, but that the latter requires less computer time. The computer time of all the models is such that use can be made of a personal computer. The experiments performed ($0 \leq c_{in} \leq 0.40$, $60^\circ C \leq t_{g,in} \leq 100^\circ C$ and $t_{l,in} \cong 20^\circ C$) confirm quantitatively the predicted exit properties of the heat exchanger and qualitatively the formation of bulk fog. An important feature of partial water–vapour and pure steam condensation is a negligible heat resistance of the condensate layer. This implies that the heat exchanger models are applicable to all practical orientations to the vertical. However, for vapours other than water–vapour, one cannot assume an isothermal condensate film.

Hence, chapter 5 deals with the condensation of an arbitrary pure vapour on a channel plate, including the interaction between condensate, plate, coolant and orientation to the vertical. This analysis is an extension of the classical Nusselt condensation model, which proceeds from an isothermal plate. To describe cocurrent, countercurrent and crosscurrent condensation, non–linear differential equations have been derived and solved in closed form. For all the three processes holds that they are governed by two dimensionless numbers. A thorough asymptotic analysis yields a compact approximation solution for the exit temperature of the coolant and formed condensate as a function of both dimensionless numbers. For a broad range of both numbers the models are found to be in good agreement with the results of experiments performed.

SAMENVATTING

In dit proefschrift wordt de warmte– en stofoverdracht in gas–vloeistof kunststof warmtewisselaars, opgebouwd uit kanaalplaten, theoretisch en experimenteel onderzocht. Voor de beschrijving van de overdracht wordt gebruik gemaakt van over de kanaalhoogten gemiddelde (of bulk) temperaturen en dampmassafractie. Het gebruik van deze grootheden resulteert in tweedimensionale kruisstroom modellen van eigenlijk driedimensionale processen. Voor het meest eenvoudige geval, warmteoverdracht zonder condensatie, leidt deze aanpak tot vergelijkingen waarvan de oplossing in literatuur wordt aangedragen.

Bij pure stoomcondensatie en partiele waterdampcondensatie op de kanaalplaten volgt de warmte– en stofoverdracht uit een locale balans van energiestromen van en naar het condensaatoppervlak, resulterend in een impliciete vergelijking tussen de bulkgrootheden van beide media. De stofflux van damp naar condensaat (corresponderend met afzuiging door een poreuze wand) leidt tot een verhoging van de warmte– en stofoverdracht en uitgeoefende frictie. Voor de beschrijving van dit effect is gekozen voor het klassieke "filmmodel", dat voorziet in locale correctiefactoren voor de uitgeoefende frictie en overdracht van warmte en stof. In hoofdstuk 1 zijn deze correctiefactoren afgeleid, alsmede uitdrukkingen voor de verandering van bulktemperatuur, massastroom en druk in een gesloten kanaal. Vanwege zijn originaliteit is de laatstgenoemde uitgebreid vergeleken met experimentele en theoretische resultaten van eerdere onderzoekers, en in goede overeenstemming daarmee bevonden.

Mistvorming, bij partiele waterdampcondensatie in de warmtewisselaar kan dit fenomeen optreden, is in de hoofdstukken 2 en 3 met een filmanalyse en de verzadigings–conditie (dat wil zeggen: uitsluiting van oververzadiging) beschreven. In hoofdstuk 2 zijn de precieze condities voor mistvorming vastgelegd, terwijl de gekoppelde energie– en diffusievergelijking van de mistlaag in eerste instantie numeriek is opgelost. Van deze

niet–lineaire differentiaalvergelijking is vervolgens een asymptotische benaderingsoplossing bepaald, welke leidt tot analytische uitdrukkingen voor de correctiefactoren.

In hoofdstuk 3 wordt een mistfilmmodel beschouwd met een verwaarloosbaar kleine stofflux, eveneens leidend tot analytische correctiefactoren. Heuristisch wordt aangetoond dat het produkt van deze correctiefactoren (alleen voor mist) en die van het klassieke filmmodel (alleen voor stofflux) overeenstemt met de correctiefactoren van hoofdstuk 2 (voor mist en stofflux). Op basis van dit inzicht zijn samengestelde eenvoudige correctiefactoren geintroduceerd. Beide mistfilmmodellen leiden tot nieuwe procedures voor het berekenen van condensors en verdampers, en tot alternatieve uitdrukkingen voor de verandering van bulktemperatuur en bulkmassafractie van de damp in combinatie met het ontstaan van bulkmist.

De mistmodelllen voorspellen bij wandcondensatie en mistvorming een verhoging van de voelbare warmteoverdracht en een reductie van de latente warmteoverdracht, terwijl de totale warmteoverdracht ongewijzigd blijft. Een vergelijking is verder gemaakt tussen de mistfilmmodel correctiefactoren en theoretische en experimentele resultaten van voorgaande studies over mistvorming bij gedwongen en vrije convectie. Deze belangrijke vergelijking bevestigt de voorspellingen van warmte– en stofoverdracht door de mist–correctiefactoren en daarmee de toelaatbaarheid van de filmmodelaanpak van mistvorming.

In hoofdstuk 4 is daadwerkelijk de stof– en warmteoverdracht in kunststof warmtewisselaars onderzocht voor het geval dat er geen condensatie, partiele waterdamp–condensatie, of pure stoomcondensatie optreedt. Bij partiele waterdampcondensatie zijn het klassieke filmmodel, het asymptotische mistfilmmodel van hoofdstuk 2, en het samengestelde mistfilmmodel van hoofdstuk 3, toegepast en onderling vergeleken. Vanwege het kruisstroomprincipe en de mogelijkheid van meerdere vloeistof passages in de warmtewisselaar behoeven de uittredegrootheden niet in thermodynamisch evenwicht te zijn (dit geldt in het algemeen voor gassen van verschillende samenstelling die worden gemengd). Universeel toepasbare vergelijkingen zijn daarom afgeleid die de overgang naar een stabiele eindsituatie beschrijven, in de praktijk resulterend in mistvorming of mistoplossing.

Uit talloze berekeningen blijkt dat een substantieel deel van de binnentredende damp condenseert aan de wand, en dat de hoeveelheid gevormde mist minder dan ongeveer 10 % van de totaal gecondenseerde damp bedraagt. Verder blijkt dat de voorspellingen van het asymptotische en het samengestelde mistmodel identiek zijn, maar dat de benodigde rekentijd van de laatste veel geringer is. De rekentijd van alle modellen is dusdanig dat de berekeningen door een personal computer kunnen worden uitgevoerd.

Uitgevoerde experimenten ($0 \leq c_{in} \leq 0.40$, $60^\circ C \leq t_{g,in} \leq 100^\circ C$ en $t_{l,in} \cong 20^\circ C$) bevestigen kwantitatief de voorspelde uittredegrootheden van de warmtewisselaar en kwalitatief het ontstaan van bulkmist. Een belangrijk kenmerk van partiele waterdampcondensatie en pure stoomcondensatie is de verwaarloosbaar kleine warmteweerstand van de condensaatlaag. Dit houdt in dat de warmtewisselaarmodellen geldig zijn voor alle in de praktijk voorkomende standen ten opzichte van de gravitatie. Voor andere dampen dan waterdamp kan echter niet worden aangenomen dat de condensaatfilm isotherm is.

Hierop inhakend is daarom in hoofdstuk 5 de condensatie van een willekeurige pure damp op een kanaalplaat onderzocht, met inbegrip van de interactie tussen condensaat, plaat, koelvloeistof en orientatie ten opzichte van de gravitatie. Deze analyse is een uitbreiding van het klassieke Nusselt condensatiemodel, dat uitgaat van een isotherme plaat. Voor meestroom–, tegenstroom– en kruisstroomcondensatie, zijn niet–lineaire differentiaalvergelijkingen afgeleid en analytisch opgelost. Voor de drie processen geldt dat ze worden beschreven door twee dimensieloze getallen. Een asymptotische analyse leidt tot een handzame benaderingsoplossing voor de uittredetemperatuur van de koelvloeistof en het gevormd condensaat als functie van beide dimensieloze getallen. Voor een brede reeks van beide getallen blijken de modellen goed met de resultaten van uitgevoerde experimenten overeen te stemmen.

CURRICULUM VITAE

De auteur werd op 6 juni 1963 te Maastricht geboren. Na de lagere school doorlopen te hebben bezocht hij het Jeanne d'Arc Lyceum te Maastricht, alwaar hij in juni 1981 het eindexamen Atheneum–B aflegde. In september 1981 werd hij aan de faculteit Werktuigbouwkunde van de Technische Universiteit Eindhoven ingeschreven, waar hij in juli 1984 slaagde voor het kandidaatsexamen en in juni 1986 voor het ingenieursexamen bij prof.dr.ir. D.H. van Campen van de vakgroep Technische Mechanica (WFW). Het afstudeerwerk, uitgevoerd onder begeleiding van dr.ir. M.T.M. Crooijmans en dr.ir. A. de Kraker, betrof een niet–lineaire stabiliteitsanalyse van een hydrodynamisch glijlager. Vanaf 1 september 1986 is de auteur werkzaam bij Akzo Research Laboratories Arnhem. Bij de afdeling mechanische/fysische research (CDM) heeft hij zich beziggehouden met het modelleren van kunststof warmtewisselaars, extruders, filters en vloeipersen. De onderzoekingen aan de kunststof warmtewisselaars hebben geleid tot dit proefschrift.

STELLINGEN

behorende bij het proefschrift

FILM MODELS FOR TRANSPORT PHENOMENA WITH FOG FORMATION

with application to plastic heat exchangers and condensers

van H.J.H. Brouwers

1. Door de keuze van $Le_v = 1$ blijkt achteraf de aanname van een volledig verzadigde film en mistvorming in de gehele film ($K > 0$) van Aref'yev en Averkiyev (1979) juist te zijn.
   - Aref'yev, K.M. en Averkiyev, A.G. (1979), Effects of fog formation at the evaporation surface on coefficients of heat and mass transfer during evaporative cooling of water, Heat Transfer – Soviet Research, 11, 143 – 147.
   - Hoofdstuk 2 en appendices A–C van dit proefschrift.

2. Omdat de warmteweerstand van het condensaat veel kleiner is dan die van de kunststof kanaalplaat kan de aanwezigheid van de eerste buiten beschouwing worden gelaten. Een bijkomend voordeel is dat de condensatiemodellen geldig zijn voor iedere stand van de kunststof warmtewisselaar ten opzichte van de gravitatie.
   - Hoofdstuk 4 en appendix E van dit proefschrift.

3. De differentiaalvergelijkingen die de meestroom en tegenstroom condensatie van een pure damp op platen en pijpen beschrijven kunnen, in tegenstelling tot de bewering van Faghri en Sparrow (1980), analytisch worden opgelost.
   - Faghri, M. en Sparrow, E.M. (1980), Parallel–flow and counter–flow condensation on an internally cooled vertical tube, Int. J. Heat Mass Transfer, 23, 559 – 562.
   - §5.1–§5.3 van dit proefschrift.

4. Voor pure verzadigde dampcondensatie op platen en pijpen geldt dat de hoeveelheid opgenomen warmte door het koelwater slechts gelijk is aan het produkt van gevormd condensaat en latente warmte indien de onderkoeling van het condensaat verwaarloosbaar is (ofwel het Kutateladze getal $Ku << 1$).
   - Brouwers, H.J.H. (1989), Film condensation on nonisothermal vertical plates, Int J. Heat Mass Transfer, 32, 655 – 663.
   - §5.2 en §5.3 van dit proefschrift.

5. De afbreekfout van Mason's reeksontwikkeling is kleiner dan deze zelf verwachtte.
   - Mason, J.L. (1954), Heat transfer in crossflow, Proc. Appl. Mech. 2nd. U.S. Nat. Congress, 801 – 803.
   - Appendix D van dit proefschrift.

6. De weglating door Johnstone e.a. (1950) van de filmmodel correctiefactor voor diffusie in de hellingconditie voor mistvorming verklaart de discrepantie van deze conditie met hun waarnemingen van mistvorming in waterdamp–stikstof mengsels.
   - Johnstone, H.F., Kelley, M.D. en McKinley, D.L. (1950), Fog formation in cooler–condensers, Ind. Eng. Chem., 42, 2298 – 2302.
   - Appendix F van dit proefschrift.

7. In de impulsbalans wordt de acceleratieterm/deceleratieterm gerepresenteerd door $(\rho u^2)_m$, en niet door ρu_m^2 zoals voorgesteld door Wang en Tu (1988), hoewel de geïntroduceerde fout slechts een paar procent is voor incompressibele turbulente stroming.
   - Wang, C.Y. en Tu, C.J. (1988), Effects of non–condensable gas on laminar film condensation in a vertical tube, Int. J. Heat Mass Transfer, 31, 2339 – 2345.
   - Ward–Smith, A.J. (1980), Internal fluid flow, Clarendon Press.

8. Dat iemand een proefschrift kan schrijven wil niet altijd zeggen dat de promovendus stellingen kan formuleren die geen betrekking hebben op het proefschriftonderwerp. Het vereisen van deze stellingen bij een proefschrift dient dan ook heroverwogen te worden.

9. Een as in een hydrodynamisch glijlager kan eerder instabiel worden dan men op grond van een lineaire stabliteitsanalyse zou mogen verwachten.
   - Crooijmans, M.T.M., Brouwers, H.J.H., van Campen, D.H. en de Kraker, A. (1990), Limit cycle predictions of a nonlinear journal–bearing system, Journal of Engineering for Industry, 112, 168 – 171.

10. Het verdient aanbeveling numerieke methoden niet te gebruiken voor het oplossen van fysische problemen alvorens een asymptotische analyse een benaderingsoplossing heeft uitgesloten.

11. Onderzoekers dienen bedacht te zijn op het toepassen van denkbeelden en theorieën op een breder terrein dan waarvoor ze oorspronkelijk zijn ontwikkeld en getoetst.

12. De omvang van de overheidsbemoeienis waarmee de samenleving wordt geconfronteerd staat in schril contrast met het geringe aantal effectiviteits–onderzoeken dat eraan wordt vastgekoppeld.

Arnhem, september 1990